frontiers | Research Topics

Broadband seafloor sediment acoustic property and multi-parameter geoacoustic model

Edited by
Guangming Kan, Xingsen Guo, Jingqiang Wang and Baohua Liu

Published in
Frontiers in Marine Science

ISSN 1664-8714
ISBN 978-2-8325-6330-4
DOI 10.3389/978-2-8325-6330-4

About Frontiers

Frontiers is more than just an open access publisher of scholarly articles: it is a pioneering approach to the world of academia, radically improving the way scholarly research is managed. The grand vision of Frontiers is a world where all people have an equal opportunity to seek, share and generate knowledge. Frontiers provides immediate and permanent online open access to all its publications, but this alone is not enough to realize our grand goals.

Frontiers journal series

The Frontiers journal series is a multi-tier and interdisciplinary set of open-access, online journals, promising a paradigm shift from the current review, selection and dissemination processes in academic publishing. All Frontiers journals are driven by researchers for researchers; therefore, they constitute a service to the scholarly community. At the same time, the *Frontiers journal series* operates on a revolutionary invention, the tiered publishing system, initially addressing specific communities of scholars, and gradually climbing up to broader public understanding, thus serving the interests of the lay society, too.

Dedication to quality

Each Frontiers article is a landmark of the highest quality, thanks to genuinely collaborative interactions between authors and review editors, who include some of the world's best academicians. Research must be certified by peers before entering a stream of knowledge that may eventually reach the public - and shape society; therefore, Frontiers only applies the most rigorous and unbiased reviews. Frontiers revolutionizes research publishing by freely delivering the most outstanding research, evaluated with no bias from both the academic and social point of view. By applying the most advanced information technologies, Frontiers is catapulting scholarly publishing into a new generation.

What are Frontiers Research Topics?

Frontiers Research Topics are very popular trademarks of the *Frontiers journals series*: they are collections of at least ten articles, all centered on a particular subject. With their unique mix of varied contributions from Original Research to Review Articles, Frontiers Research Topics unify the most influential researchers, the latest key findings and historical advances in a hot research area.

Find out more on how to host your own Frontiers Research Topic or contribute to one as an author by contacting the Frontiers editorial office: frontiersin.org/about/contact

Broadband seafloor sediment acoustic property and multi-parameter geoacoustic model

Topic editors

Guangming Kan — First Institute of Oceanography, Ministry of Natural Resources, China

Xingsen Guo — University College London, United Kingdom

Jingqiang Wang — First Institute of Oceanography, Ministry of Natural Resources, China

Baohua Liu — National Deep Sea Center (NDSC), China

Citation

Kan, G., Guo, X., Wang, J., Liu, B., eds. (2025). *Broadband seafloor sediment acoustic property and multi-parameter geoacoustic model*. Lausanne: Frontiers Media SA. doi: 10.3389/978-2-8325-6330-4

Table of contents

frontiers | Frontiers in Marine Science

TYPE Editorial
PUBLISHED 28 April 2025
DOI 10.3389/fmars.2025.1518989

OPEN ACCESS

EDITED AND REVIEWED BY
Eric 'Pieter Achterberg,
Helmholtz Association of German Research Centres (HZ), Germany

*CORRESPONDENCE
Jingqiang Wang
wangjqfio@fio.org.cn

RECEIVED 29 October 2024
ACCEPTED 24 March 2025
PUBLISHED 28 April 2025

CITATION
Kan G, Liu B, Guo X and Wang J (2025) Editorial: Broadband seafloor sediment acoustic property and multi-parameter geoacoustic model. *Front. Mar. Sci.* 12:1518989. doi: 10.3389/fmars.2025.1518989

Editorial: Broadband seafloor sediment acoustic property and multi-parameter geoacoustic model

Guangming Kan[1,2], Baohua Liu[3], Xingsen Guo[4,5] and Jingqiang Wang[1,2]*

[1]Key Laboratory of Marine Geology and Metallogeny, First Institute of Oceanography, Ministry of Natural Resources, Qingdao, China, [2]Key Laboratory of Submarine Acoustic Investigation and Application of Qingdao(Preparatory), Qingdao, China, [3]Laboratory for Marine Geology, Laoshan Laboratory, Qingdao, China, [4]Department of Civil, Environmental, Geomatic Engineering, University College London, London, United Kingdom, [5]Shandong Provincial Key Laboratory of Marine Environment and Geological Engineering, Ocean University of China, Qingdao, China

KEYWORDS

sediment acoustic property, geoacoustic model, geoacoustic inversion, seafloor sediment acoustic *in-situ* measurement, sound speed and attenuation in sediment

Editorial on the Research Topic
Broadband seafloor sediment acoustic property and multi-parameter geoacoustic model

The seafloor is an important boundary of the ocean sound field, and the acoustic property of seafloor sediment and its spatial distribution are important factors that affect the propagation and variation of sound waves in the ocean. The research of seafloor sediment acoustic property (geoacoustic property) is an interdisciplinary subject involving marine geology, marine geophysics, and marine acoustics. The research of geoacoustic property mainly includes measurement techniques on geoacoustic property, the impacting factors on the geoacoustic property, the relationship between geoacoustic property and the physical-mechanical parameters (geoacoustic model), application of geoacoustic property, and so on. The research of geoacoustics has important practical value and significance in many fields such as ocean sound field prediction, marine engineering construction, marine resources exploration, marine disaster prevention, etc. With the development of new technology such as *in-situ* measurement technology, low-frequency geoacoustic inversion, deep-towed multichannel seismic technology, and prediction methods based on artificial intelligence technologies such as machine learning and neural networks, research on broadband geoacoustic property from low to high-frequency and multi-parameter geoacoustic models have received more attention. In light of these considerations, we have proposed the Research Topic, *Broadband Seafloor Sediment Acoustic Property and multi-parameter Geoacoustic Model*, to compile the latest advancements in the aforementioned critical areas.

This Research Topic comprises 10 original research papers contributed by 63 authors. The research within encompasses a spectrum of Measurement technologies for acoustic and physical properties of seabed sediments, geoacoustic inversion, Artificial intelligence and Multi-parameter Geoacoustic Model. These approaches collectively offer valuable insights into the realms of Seafloor sediment acoustic property and geoacoustic model. In this summary, we highlight key findings derived from the 10 research papers featured in this Research Topic.

Measurement technologies for acoustic and physical properties of seabed sediments

Jiao et al. conducted cyclic shear tests of the natural marine clay of the South China Sea, with varying the cyclic stress ratio (CSR), overpressure consolidation ratio (OCR), consolidation ratio (Kc), and loading frequency. They found that the CSR, OCR, and Kc significantly impact the cumulative dynamic strain in deep-sea soft clay during undrained cyclic dynamic tests. Higher CSR values lead to increased dynamic strain and structural failure risk. They also proposed a dynamic strain-dynamic pore pressure development model, which can effectively capture the cumulative plastic deformation and dynamic pore pressure development, showing correlations with the CSR, OCR, and Kc, thus providing insights into the deformation and pore pressure trends in deep-sea clay under high cyclic dynamic loading conditions. This study not only furnishes essential background information but also addresses a critical gap in understanding the behavior of deep-sea soft clay under cyclic loading, thereby enhancing the safety and stability of seabed structures.

Li et al. presented an array geometry inversion method suitable for complex seafloors to address the challenge of precise source-receiver positioning with deep-towed multichannel seismic systems. An objective function of the deep-towed seismic array geometry inversion was built using the shortest path algorithm according to the travel times of direct waves and seafloor reflections, and the high-precision inversion of the source-receiver position was achieved by using the particle swarm optimization (PSO) algorithm. The results verified the effectiveness of the method proposed in this paper, especially its applicability in scenarios with dramatic changes in seabed topography. This study provides insights into the accuracy and reliability of the proposed geometric shape inversion method for deep-towed seismic arrays in practical applications to meet the requirements of near-bottom acoustic detection for fine imaging of deep-sea seabed strata and precise inversion of geoacoustic parameters.

Wang et al. designed and developed a Seabed Cone Penetration Test (CPT) and Sampling System, which can be used to perform multi-parameter *in situ* testing and low-disturbance sampling of 3000 m deep-sea seabed sediments. The system adopts electrohydraulic proportional position control and a fuzzy PID controller to precisely control the position of the piston of the hydraulic circuit, which can improve the accuracy of the cone test data and reduce the interference of the sampling tube with the original sediment during the sampling process. Moreover, electrohydraulic co-simulation of the hydraulic control system was conducted with AMESim and Simulink software, and the position control and speed control effects of the system were verified. The system was tested on site in the Shenhu Sea area of the South China Sea, and obtained 9 *in-situ* parameters, including physical and chemical parameters, for sediments within a depth range of 2.66 m on the seabed surface at a depth of 1820 m. The testing results of the system accurately and efficiently reflect the property characteristics of seafloor sediments in an *in situ* environment, indicating the system can be widely used in marine engineering geological investigations and measurement of physical parameters of seafloor sediment.

Zhen et al. developed an acoustic reflection measurement system using a self-developed, high-precision, high-frequency shallow stratigraphic profiler to perform the sediment grain size classification. In this study, they utilized this system to analyze six sandy sediments with different grain sizes in the laboratory. The result shows a positive correlation between the amplitude of the acoustic reflection echo and grain size, and the amplitude of the reflection peaks increased with increasing grain size. By analyzing the amplitude of the reflection peaks and echo waveform, sediment grain sizes can be distinguished in a more precise manner. This study provides a valuable guide for the fine-grained classification of sediment grain size.

Geoacoustic inversion

Lee et al. estimate the geoacoustic parameter values at low frequency for the two-layer geoacoustic bottom model by comparing the dispersion curves extracted from the replicas predicted by the KRAKEN normal-mode program with dispersion curves extracted from airgun sounds received in the East Siberian Sea. The result revealed the best-fit values for the sediment sound speed and density in the surficial layer to be approximately 1422.4 m/s and 1.58 g/cm^3, respectively. For the lower layer, these values were estimated to be 1733.6 m/s and 1.84 g/cm^3, respectively, and the surficial sediment thickness was estimated to be ~ 4.1 m. Subsequently, the distances between the airgun and the receiver system in the 18.6 to 121.5 km range were calculated by comparing the measured modal curves and the model replicas predicted using the estimated geoacoustic parameters. In order to mitigate the distance errors, they employed an adiabatic approximation for model propagation in the range-dependent environment. The modeled modal travel times were calculated by dividing the source-receiver distance into range-independent segments, each based on a 1-m change in water depth, and then summed. The result shows that the re-estimated distance error is reduced to within 10%, indicating the method of geoacoustic inversion presented in this study is effective.

Artificial intelligence

Meng et al. established a machine learning model for predicting the shear wave speed of seafloor sediments in the northwest South China Sea, using the eXtreme Gradient Boosting (XGBoost) algorithm. By optimizing the hyperparameters of the model, the best fit of the XGBoost algorithm is obtained when the n_estimator and max_depth are 115 and 6, respectively. The mean absolute error and the goodness of fit between the predicted values and validation data are 3.366 m/s and 9.90%, respectively. They compared the multi-parameter shear wave speed prediction model established in this study with the single-parameter prediction models, the dual-parameter prediction models, and the GS prediction model, and the result indicates that the multi-parameter shear wave speed prediction model based on the XGBoost algorithm has the lowest MAE and MAPE between the test data and the predicted values, which are 4.04 m/s and 14.3%, respectively. This study indicates that the multi-parameter shear wave speed prediction model based on the XGBoost algorithm has a higher accuracy for predicting the shear wave speed in the northwest South China Sea.

Multi-parameter geoacoustic model

Zou et al. established a porosity-based effective density fluid model (P-EDFM) to analyze the variation of acoustic properties with the porosity of seafloor sediments. They employed P-EDFM to investigate the influence of physical parameters, including porosity and density, as well as temperature environment, and measurement frequency on the *in situ* sound velocity and sound attenuation coefficient of seafloor sediments. According to the P-EDFM, the *in situ* sound velocity ratio decreases with increasing bulk porosity and with decreasing bulk density. After considering the influence of temperature in the P-EDFM, the prediction of *in situ* sound velocity aligns well with the measured dataset. The acoustic attenuation coefficient exhibits an inflection point, increasing initially and then decreasing with changes in porosity, similar to the observed pattern in Hamilton's observation and estimation. Overall, P-EDFM can predict the *in situ* sound velocity and sound attenuation coefficient under different temperatures and frequencies, with a lower prediction error for sound velocity compared to the sound attenuation coefficient.

Tian et al. measured the acoustic and physical properties of marine cold spring carbonate rock samples gathered from the Chaoshan Depression in the South China Sea, which is different from the ordinary seafloor sediments and can be regarded as a special type of sediment distributed on or in the ordinary seafloor sediments. In this study, the Wyllie time-average equation, Voigt model, Reuss model, and Voigt-Reuss-Hill model were used to predict the characteristics of the sound speed for four states of seafloor sediments containing cold spring carbonate mineral particles or rocks. For these four states of marine cold spring carbonate mineral particles existing on or in seafloor sediments, the sound speed and reflection coefficient of a mixture of seafloor surface sediments containing cold spring carbonate mineral particles or rocks decrease with an increase in the volume ratio of the seafloor sediment. This method for predicting the reflection coefficient provides evidence to explain the high and low reflection coefficients observed in Chirp sub-bottom profiles of cold spring seepage areas.

Liu et al. compared the deviations between the sound velocities of seafloor sediments measured on-site(on the deck of the research vessel) and in the laboratory ($V_{p\text{-}f}/V_{p\text{-}l}$) and analyzed their mechanisms by combining the on-site and laboratory measurements obtained in the southern Huanghai Sea in 2009 with that acquired in 2014 from the northern Huanghai Sea and Bohai Sea. The result shows that the deviations of the ratio of $V_{p\text{-}f}/V_{p\text{-}l}$ among different sediment types were significant and the changes in temperature and disturbance during the transport of the samples were the key environmental factors causing deviations to exist in the measured sound velocities. The dynamic liquefaction, re-consolidation, and thixotropic resumption processes that occurred during transport and the standing of samples were the most important dynamical mechanisms of acoustic deviations, all of which were caused by disturbances during sample transport. Sandy silts and silty sands exhibited dynamic liquefaction and re-consolidation, while the clayey silts exhibited thixotropy, and resumption and the silts showed dynamic liquefaction, re-consolidation, thixotropy and then resumption. The dynamic formation mechanisms of the deviations between on-site and at-laboratory measured sound velocities were the changes in the properties of sediments by external actions.

Zhang et al. analyze the influence of physical parameters (including density, porosity, and grain size) on the acoustic velocity of the sediments in the land slope of the northern South China Sea (SCS). The single-parameter and dual-parameter regression equations based on the data from all of the sites in the whole land slope of the northern SCS are established to further examine this influence. Further, this study also establishes single-parameter and dual-parameter regression equations suitable for the upper, middle, and lower land slopes to better study the relationships between each parameter. The results show that the influence of each parameter on the prediction of the acoustic velocity of the sediment is in the following order: porosity>density>grain size. This study analyzed and revealed the reason why the seafloor sediments in the local area cause the acoustic properties to change greatly, which may be caused by changes in the sediment type, and lithology along depth. And the other reason is the development of inter-layer in the land slope of the northern SCS.

Author contributions

GK: Writing – original draft, Writing – review & editing. BL: Writing – original draft, Writing – review & editing. XG: Writing – original draft, Writing – review & editing. JW: Writing – original draft, Writing – review & editing.

Funding

The author(s) declare that financial support was received for the research and/or publication of this article. Funding for the research has been supported by the National Natural Science Foundation of China under Grant Nos. 42376076, U2006202, and 42176191.

Conflict of interest

The authors declare that the research was conducted in the absence of any commercial or financial relationships that could be construed as a potential conflict of interest.

Generative AI statement

The author(s) declare that no Generative AI was used in the creation of this manuscript.

Publisher's note

frontiers | Frontiers in Marine Science

TYPE Original Research
PUBLISHED 28 August 2023
DOI 10.3389/fmars.2023.1243780

OPEN ACCESS

EDITED BY
Guangming Kan,
Ministry of Natural Resources, China

REVIEWED BY
Yanliang Pei,
Ministry of Natural Resources, China
Gil Young Kim,
Korea Institute of Geoscience and Mineral Resources, Republic of Korea

*CORRESPONDENCE
Dapeng Zou
anthonyzou@gdut.edu.cn
Zhong Chen
chzhsouth@scsio.ac.cn

RECEIVED 21 June 2023
ACCEPTED 07 August 2023
PUBLISHED 28 August 2023

CITATION
Tian Y, Wu L, Zou D, Chen Z, Jiang Y, Yan P and Fan C (2023) Predicting the acoustic characteristics of seafloor sediments containing cold spring carbonate rocks.
Front. Mar. Sci. 10:1243780.
doi: 10.3389/fmars.2023.1243780

Predicting the acoustic characteristics of seafloor sediments containing cold spring carbonate rocks

Yuhang Tian[1,2], Lei Wu[3], Dapeng Zou[3,4]*, Zhong Chen[1]*, Yongjun Jiang[3], Pin Yan[1] and Chaoyan Fan[1]

[1]Key Laboratory of Ocean and Marginal Sea Geology, South China Sea Institute of Oceanology, Chinese Academy of Sciences, Guangzhou, China, [2]Sanya Institute of Ocean Eco-Environmental Engineering, Sanya, China, [3]School of Electromechanical Engineering, Guangdong University of Technology, Guangzhou, China, [4]Guangdong Key Laboratory of Advanced Manufacturing Technology of Marine Energy Equipment, Guangzhou, China

The acoustic and physical properties of two valuable marine cold spring carbonate rock samples gathered from the Chaoshan Depression in the South China Sea were measured. The Wyllie time-average equation was applied to analyze the measured sound speeds and their trend under different porosities, and the sound speeds of marine cold spring carbonate rocks were found to be consistent with those of terrestrial carbonate rocks. The Voigt model, Reuss model, and Voigt-Reuss-Hill model were used to predict the characteristics of the sound speed for four states of seafloor sediments containing cold spring carbonate mineral particles or rocks. For these four states of marine cold spring carbonate mineral particles existing on or in seafloor sediments, the sound speed and reflection coefficient of a mixture of seafloor surface sediments containing cold spring carbonate mineral particles or rocks decrease with an increase in the volume ratio of the seafloor sediment. This method for predicting the reflection coefficient provides evidence to explain the high and low reflection coefficients observed in Chirp sub-bottom profiles of cold spring seepage areas.

KEYWORDS

cold spring, carbonate rocks, seafloor sediments, sound speed, reflection coefficient

1 Introduction

Since 12 Ma BP, the Earth's climate has been marked by frequent cold spring activities (Callender and Powell, 1999). Cold springs characterized by a sufficient gas source and continuous overflow lead to the formation of chemoautotrophic communities, which are recorded in carbonate sediments. Therefore, the deposition of carbonate rocks indicates the existence of natural gas hydrates and the occurrence and persistence of natural gas seepage (Chen et al., 2007; Wu et al., 2015; Wang et al., 2019; Shan et al., 2020). Cold spring carbonate rocks are usually deposited on the seafloor surface with angular, spherical, and

ellipsoidal shapes and massive, lamellar, tubular and columnar habits. These rocks generally reach sizes of 3 to 8 cm but can sometimes be as large as 22 cm (Chen et al., 2008; Tong et al., 2012; Xue and Huang, 2016; Xi et al., 2017), and some grow even larger in the form of different structures that accumulate on the seafloor (Wang et al., 2019; Shan et al., 2020).

Cold spring carbonate rocks have been mainly studied by biogeochemical methods with a focus on their lithological characteristics (Chen et al., 2005; Chen et al., 2007; Chen et al., 2008; Han et al., 2008; Wu et al., 2009; Xue and Huang, 2016; Liu et al., 2017; Lu et al., 2020; Zhao et al., 2020). These rocks are directly related to the existence of seepage-associated natural gas hydrates and cold springs. For example, carbonate rocks are distributed across the seafloor of the Shenhu Sea area and Dongsha Island in the northern South China Sea, and drilling yielded gas hydrate samples at a depth of 183 m in the Shenhu Sea area (Zhang et al., 2007). Yan et al. (2011) found evidence of seepage-associated hydrates based on sub-bottom geophysical surveys across a suspected mud diapir area of the Baiyun Depression in the northern South China Sea. Based on the analysis of these sub-bottom profiles, the reflections from most areas of the seafloor are weak, but there are obvious abnormal reflection characteristics in some areas with strong reflection intensities (Yan et al., 2014; Liu et al., 2015; Chen et al., 2016; Shan et al., 2020). The samples obtained in this area were found to contain carbonate rock fragments, which indicates that these strong reflections may originate from cold spring carbonate rocks. The reflection coefficients also indicate the different states under which these cold spring carbonate rocks exist. Unlike sand, silt, clay, and mixed-type seafloor surface sediments, cold spring carbonate rocks form clumps because of their crystalline and compacted structure, and their acoustic characteristics typically show high sound speeds and low attenuation. However, due to their special natural shapes and varying structures, it is difficult to obtain proper samples of marine cold spring carbonate rocks to carry out acoustic measurements. As a result, few direct measurements of the acoustic characteristics of marine cold spring carbonate rocks have been reported.

In this article, based on two valuable marine cold spring carbonate rock samples gathered from the Chaoshan Depression, we measured some of the physical properties and sound speeds of the two samples, compared them with the properties of terrestrial carbonate rocks, analyzed the relationship between the sound speed and porosity of cold spring carbonate rocks using the Wyllie time-average equation, and predicted the acoustic characteristics of seafloor surface sediments containing cold spring carbonate rocks. Detecting and predicting the acoustic characteristics of marine cold spring carbonate rocks both on the seafloor and in seafloor surface sediments can provide evidence to explain the strong reflection characteristics of cold spring carbonate rocks and help develop an effective method for the exploration of seepage-associated natural gas hydrates.

2 Materials and methods

The samples of marine cold spring carbonate rocks were gathered from the Chaoshan Depression (Figure 1), the largest Mesozoic residual basin in the northern South China Sea with a sedimentary thickness exceeding 6000 m. Our samples were extracted from the seafloor surface sediments at a seawater depth of approximately 470 m. Their main component was determined to be ferruginous dolomite (Chen et al., 2006; Yan et al., 2014). Based on a Chirp sub-bottom profiling survey near Dongsha Island in the northern South China Sea, Chen et al. (2016) found reflection coefficients of the seabed ranging from 0.1 to 0.8.

The two samples used in this article are named TSYC1 and TSYC2. Both samples (Figure 1) were cut into two parts. One part of each sample was used to measure the physical and acoustic properties reported in this study. These parts were split at both

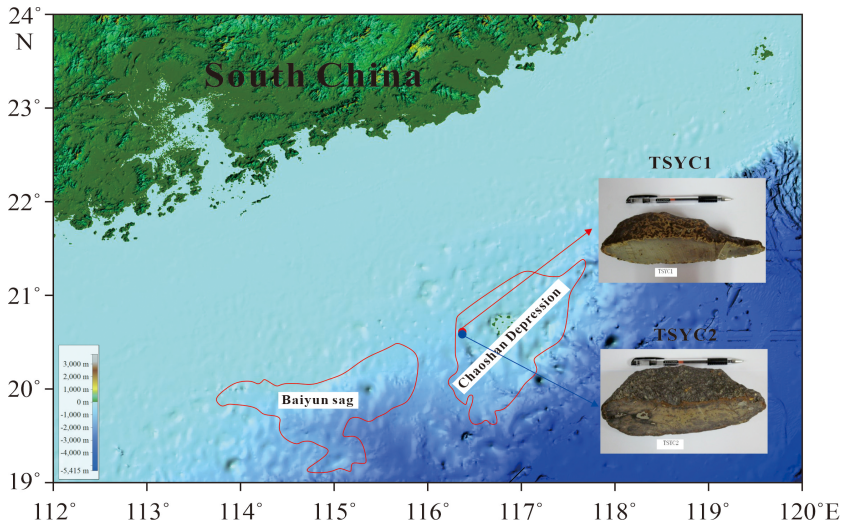

FIGURE 1
Samples of cold spring carbonate rocks from the northern South China Sea. The red dot is the sample of TSYC1, and the bule dot is the sample TSYC2.

ends, and the two edges of the main part were cut flat for acoustic measurements, and the cut segments were used to detect the physical properties. The samples were very dense overall, with an approximately 3 mm thick brown coating on the surface. The sample interior was gray and displayed an uneven texture with a small amount of unconsolidated soil. Miniscule individual pores were identified on the cutting surface of each sample.

The samples were preserved and saturated in seawater. The cut segments were used to measure the wet weight and volume by using the volume product method. Then, the cut segments were dried in an oven at 108°C for 24 hours to measure the dry weight by using the weight removal method. An electronic balance with an accuracy of 0.01 g was used to record the weight, and a high-precision measuring cylinder with an accuracy of ±0.1 ml was used for bulk measurements. Then, the wet density and porosity were calculated 2.239 g/cm^3 and 3.904%, respectively, for TSYC1 and 2.748 g/cm^3 and 10.027%, respectively, for TSYC2.

The lengths of the main segments employed for the acoustic measurements were 100.92 mm and 139.89 mm for TSYC1 and TSYC2, respectively. The acoustic measurement principle is based on the time-of-fight method, as shown in Figure 2. A DB4 ultrasonic apparatus was used to excite electrical signals, drive the acoustic emitter, amplify the signal of the acoustic receiver, and store the sound pressure signals. The sampling frequency of the acoustic instrument was 5 MHz. A Lenovo laptop with a good human-computer interface was employed as the control and analysis system, and the data were analyzed in MATLAB 2009. The length of each sample was measured by a Vernier caliper with an accuracy of 0.02 mm. Transducers with dominant frequencies of 20 kHz, 40 kHz and 100 kHz were applied to study the characteristics of the longitudinal wave velocity (hereinafter referred to as the sound speed) under both seawater- and air-saturated conditions. The total absolute acoustic measurement precision was less than 1.2%.

3 Results

3.1 Measured sound speeds of the marine cold spring carbonate rocks

The measured sound speeds of the marine cold spring carbonate rocks (shown in Table 1) are 166 m/s on average higher in the seawater-saturated rocks than in the air-saturated rocks. In addition, the sound speeds of the marine cold spring carbonate rocks exhibit dispersion characteristics, with the sound speed of the seawater-saturated samples being 261 m/s on average higher at 100 kHz than at 20 kHz and 162 m/s on average higher than at 40 kHz. Because the acoustic properties of marine carbonate rocks have not been reported, we compare the above measured data with those of terrestrial carbonate rocks. Liu (1985) pointed out that the sound speeds of terrestrial liquid-saturated carbonates range from 3,200 to 7,000 m/s due to differences in the sample area and formation and are higher than those of air-saturated carbonates by 300 to 2,000 m/s. The sound speeds of dolomite (a carbonate rock) from Sichuan and other regions of China range from 4,991.41 to 7,019.84 m/s (Hang et al., 2004). Moreover, carbonate rocks are characterized by obvious anisotropy, and thus, the sound speed varies in different directions from 4,590 to 7,230 m/s (Chen et al., 2017). Both water- and air-saturated rocks usually display dispersion characteristics (Wei et al., 2015; Guo et al., 2018; Ma et al., 2019), and carbonate rocks differ in terms of their lithology, diagenetic history, structure and degree of saturation. Therefore, the sound speeds of the marine cold spring carbonate rocks are in the range of those of terrestrial carbonates.

The sound speed-porosity relationships of the two air-saturated cold spring carbonate rock samples at different frequencies with those of terrestrial limestone and dolomite measured by Rafavich et al. (1984) and Sayers (2008), respectively. The sound speeds of TSYC1 and TSYC2 are consistent with that of the terrestrial

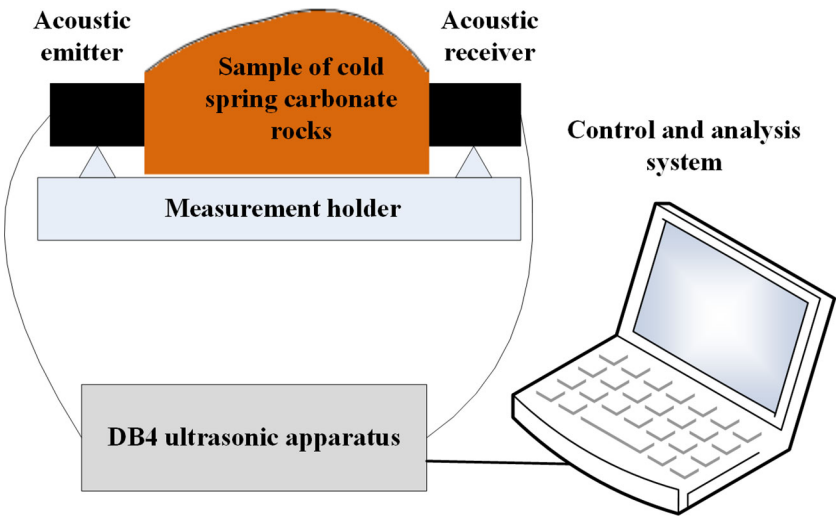

FIGURE 2
Schematic diagram of acoustic measurements in the laboratory for the samples of marine cold spring carbonate rocks.

TABLE 1 Sound speeds of the samples of cold spring carbonate rocks.

Samples	Dominant frequency (kHz)	Sound speed (m/s)	
		Air-saturated	Seawater-saturated
TSYC1	20	5,371	5,607
	40	5,577	5,546
	100	5,615	5,834
TSYC2	20	5,470	5,554
	40	5,511	5,813
	100	5,665	5,849

carbonate rocks, while the sound speed of TSYC1 is slightly lower. The sound speeds of the marine cold spring carbonate rocks seem to be similar to those of terrestrial carbonate rocks. Baechle et al. (2008) pointed out that microporosity (proportion of micropores to total pores) scatters the sound speed of terrestrial carbonate rocks. As shown in Figure 3, the higher the overall porosity is, the lower the sound speed; likewise, the higher the microporosity is, the lower the sound speed. These properties suggest that the microporosity of TSYC1 may be higher than that of TSYC2. In fact, some small unevenly distributed microcracks were found on the cutting surfaces of the two samples, and some clay holes with a low degree of consolidation were also identified. In another respect, the anisotropic characteristics in three different directions of terrestrial water-saturated carbonate rocks changed in the anisotropy coefficient of the wave velocity ranging from 1.671% to 24.699%(Chen et al., 2017). These two cold spring carbonate rock samples also appeared slight anisotropy in the structure.

3.2 Analysis of the sound speed based on the Wyllie time-average equation

According to the Wyllie time-average equation (Wyllie et al., 1956; Ma et al., 2010), the acoustic interval transit time of a rock can be expressed as follows:

$$\Delta t = (1 - n)\Delta t_{ma} + n\Delta t_f \tag{1}$$

where Δt is the interval transit time; n is the porosity; and the subscripts ma and f denote the rock skeleton and pore fluid, respectively.

When analyzing the sound speed c_{pcr} of marine cold spring carbonate rocks, Eq. (1) can be rewritten as follows:

$$\frac{1}{c_{pcr}} = \frac{1 - n}{c_{ma}} + \frac{n}{c_f} \tag{2}$$

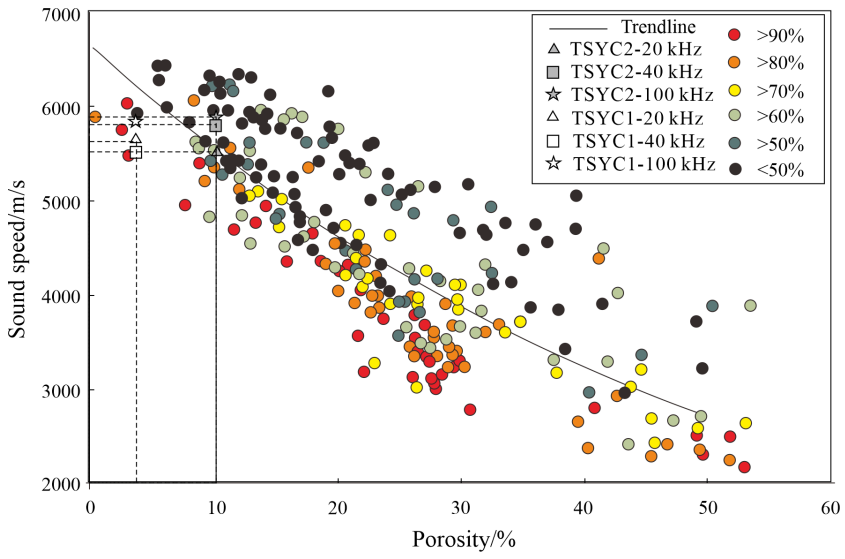

FIGURE 3
Comparison of the sound speeds between water-saturated cold spring carbonate rocks and terrestrial carbonate rocks. The dots are the porosity and these different colors of the dots represent different percentages of micropores (Baechle et al., 2008).

The sound speed of the interior of the frame is expressed as

$$c_{ma} = \sqrt{\frac{k_{ma} + 4\frac{\mu_{ma}}{3}}{\rho_{ma}}} \quad (3)$$

where k_{ma}, μ_{ma} and ρ_{ma} are the bulk modulus, shear modulus, and density of the frame, respectively.

Moreover, the density ρ_{pcr} of marine cold spring carbonate rocks can be written as

$$\rho_{pcr} = (1 - n)\rho_{ma} + n\rho_f \quad (4)$$

The marine cold spring carbonate rocks near Dongsha Island contain ferriferous dolomite, siderite, and small amounts of aragonite and calcite (Chen et al., 2008). However, due to the lack of details on the mineral composition, for the analyses of the acoustic and other physical properties, the frame is presumed to be made entirely of either dolomite or calcite. The elastic properties of the minerals (Sayers, 2008) and seawater are shown in Table 2.

The Wyllie time-average equation is used to calculate the relationship between the sound speed and the porosity of the cold spring carbonate rocks. As shown in Figure 4, the sound speeds of the cold spring carbonate rocks decrease with increasing porosity. Porosity is the main factor affecting the acoustic characteristics of carbonate rocks (Li et al., 2002). The measured properties of the marine cold spring carbonate rocks in the northern South China Sea, that is, the measured sound speeds of samples TSYC1 and TSYC2, are close to the theoretically calculated values.

4 Discussion

4.1 Prediction of the sound speed characteristics

According to the existing states of natural deposits of sediment and authigenic carbonate minerals (Chen et al., 2007; Wang et al., 2019), the mixed states of marine cold spring carbonate rocks and seafloor sediments can be simplified into four states: a) seafloor sediments without cold spring carbonate minerals (named SA); b) a scattered distribution of small cold spring carbonate minerals in seafloor sediments (named SB); c) an accumulation of cold spring carbonate minerals in seafloor sediments (named SC); and d) consolidated marine cold spring carbonate rocks isolated from seafloor sediments (named SD). For simplification, spherical particles are used to represent the most general from of the cold spring carbonate rocks and the four states are illustrated in Figure 5.

SA is the basic state of seafloor sediment without marine cold spring carbonate rocks (Chen et al., 2016), while SD is the diagenetic state of large marine cold spring carbonate rocks (Wang et al., 2019). SB and SC signify the growth and accumulation states of authigenic carbonate minerals, respectively, in seafloor sediments (Wang et al., 2019). For SB and SC, carbonate minerals may grow into small- or medium-sized carbonate rocks. When samples TSYC1 and TSYC2 were separately measured in the laboratory, they were in the state of SD; when they were distributed on the seafloor, they were in the state of either SB or SC; and when they grew into a large carbonate rock on the seafloor, they were in the state of SD.

The seafloor sediment sample collected from the marine cold spring carbonate rock area is a clayey silt. The sound speed measured at 40 kHz is 1,578 m/s, and its main physical parameters are a porosity of 41.46%, a wet density of 1.88 g/cm^3, an average grain size of 7.685 and a silt content of 60.76%. The parameters of TSYC2 are selected to represent the marine cold spring carbonate rocks in this area with a sound speed of 5,813 m/s at 40 kHz, a porosity of 10.027%, and a density of 2.748 g/cm^3. Because the measured temperature of the marine cold spring carbonate rocks and sediments was 24°C, this temperature is used for the pore water in the following calculations.

4.1.1 Predicting the sound speeds of SA and SD

For SA, the sound speed of the clayey silt without marine cold spring carbonate rocks was measured to be 1,578 m/s. In contrast, SD represents marine cold spring carbonate rocks. Due to differences in their diagenetic history, these rocks may have different degrees of cementation and thus different porosities and fracture networks. The measured porosity of a natural terrestrial carbonate rock does not exceed 55% (Baechle et al., 2008), so the porosity of the marine cold spring carbonate rocks is also set to be no greater than 55%. Eqs. (2) and (3) are used to predict the sound speed. As seen in Figure 4, the sound speed of the marine cold spring carbonate rock decreases as its porosity increases. When the porosity (pure dolomite) increases from 0 to 55%, its sound speed is predicted to decrease from 7,051 m/s to 2,367 m/s. The sound speeds of both TSYC1 and TSYC2 are within this range.

4.1.2 Predicting the sound speeds of SB and SC

The mixture of seafloor sediments with marine cold spring carbonate rocks can be considered equivalent to a stratified model of two components according to the Wyllie time-average equation. Because seafloor sediments are much softer than cold spring carbonate rocks, the former component is assumed to be the fluid filling the pore space between cold spring carbonate minerals or

TABLE 2 Elastic moduli and density of minerals (Sayers, 2008) and seawater.

Composition		Bulk modulus (GPa)	Shear modulus (GPa)	Density (g/cm^3)
Minerals	Dolomite	76.4	49.7	2.87
	Calcite	76.8	32.0	2.71
Seawater		2.365	0	1.023

10.3389/fmars.2023.1243780

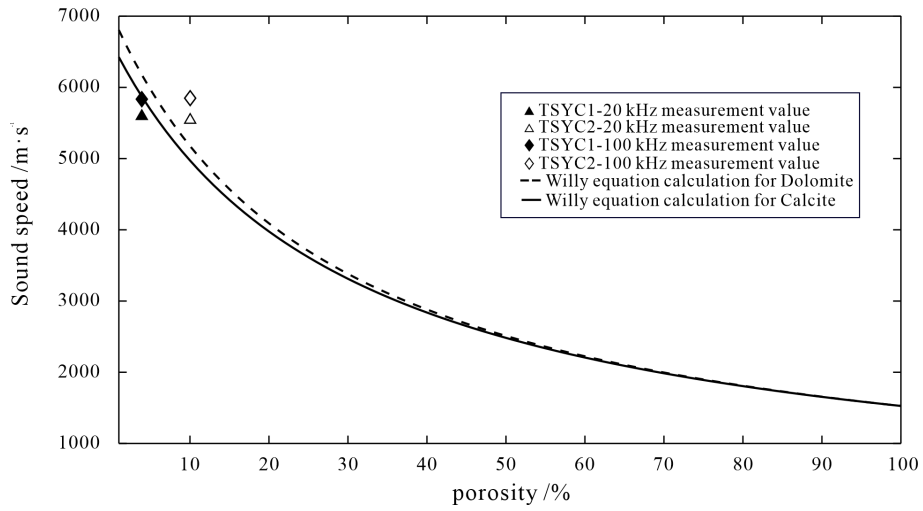

FIGURE 4
Comparison between the theoretically calculated and actually measured properties of the cold spring carbonate rock samples.

rocks. When the volume ratio of seafloor sediments in the entire mixture varies, the mixture exhibits different acoustic and other physical properties.

For SB and SC, the mixing form of marine cold spring carbonate mineral particles (or rocks) in the seafloor sediments is more complex because of the different porosities, shapes, sizes and ratios of the cold spring carbonate mineral particles (or rocks) in the seafloor sediment. Hence, for the following calculations, the equivalent elastic modulus is adopted as a necessary parameter. To predict the equivalent elastic modulus of a mixture of mineral particles and sediments, it is usually necessary to know the volume content, elastic moduli, and spatial and geometric distributions of each component. However, marine cold spring carbonate rocks have rarely been studied, and thus, their sizes and spatial and

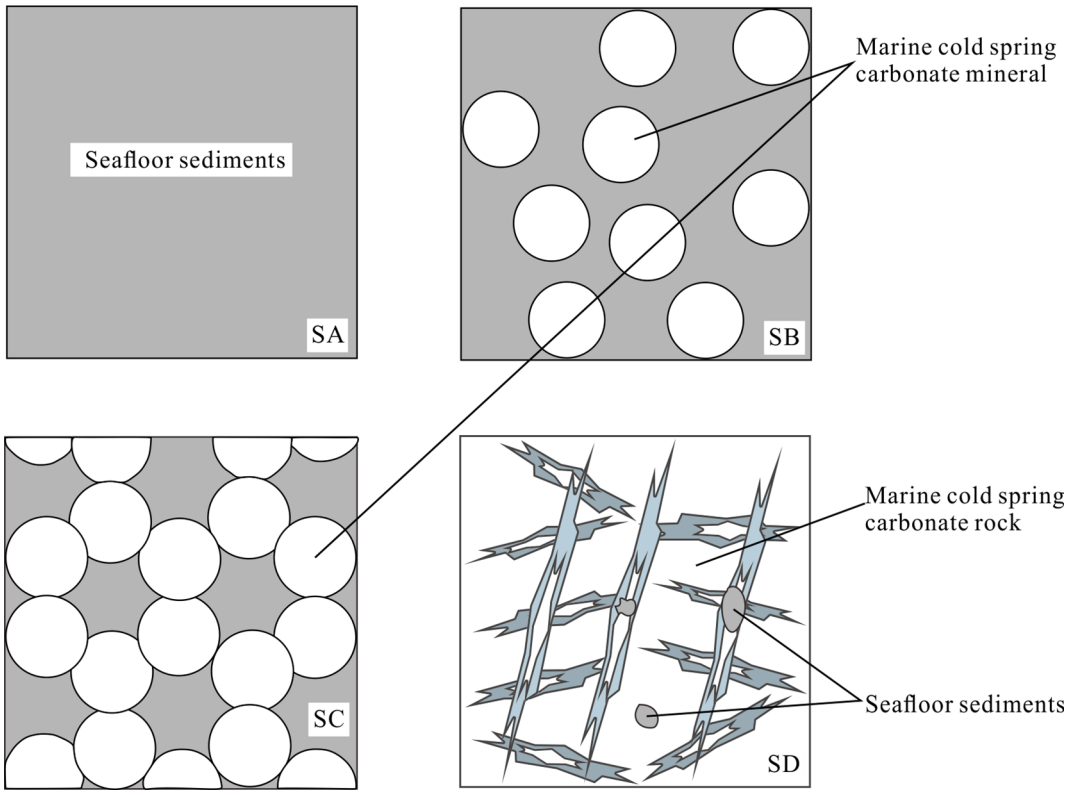

FIGURE 5
Four states of cold spring carbonate rocks in sediments.

geometric distributions are not fully understood. Hill (1952) developed a method to average the upper and lower limits calculated by the Voigt and Reuss models to obtain the Voigt-Reuss-Hill model, which can be used to calculate the elastic properties of mixtures such as SB and SC. The equivalent elastic modulus E_H of sediments containing cold spring carbonate mineral particles (or rocks) can be written as

$$E_{s-cr} = (E_V + E_R)/2 \tag{5}$$

where $E_V = \varnothing E_s + (1-\varnothing)E_{cr}$ and $\frac{1}{E_R} = \frac{\varnothing}{E_s} + \frac{1-\varnothing}{E_{cr}}$ are the equivalent elastic moduli calculated by the Voigt and Reuss models, respectively; $\varnothing$ is the volume ratio of seafloor sediments in the entire mixture; and E_s and E_{cr} are the equivalent elastic moduli of seafloor sediments and cold spring carbonate mineral particles (or rocks), respectively.

The equivalent density ρ_{s-cr} seafloor sediments containing cold spring carbonate rocks is calculated as follows:

$$\rho_{s-cr} = \varnothing \rho_s + (1-\varnothing)\rho_{cr} \tag{6}$$

where ρ_{cr} and ρ_s are the densities of cold spring carbonate rocks and seafloor sediments, respectively.

Then, the sound speed c_{ps-cr} of the seafloor sediments containing cold spring carbonate mineral particles (or rocks) can be calculated as

$$c_{ps-cr} = (E_{s-cr}/\rho_{s-cr})^{1/2} \tag{7}$$

The sound speeds of seafloor sediments containing cold spring carbonates calculated with the Voigt, Reuss, and Voigt-Reuss-Hill models (Eqs. (5–7)) are shown in Figure 6. When seafloor sediments do not contain cold spring carbonate mineral particles (or rocks), that is, when the volume ratio of seafloor sediment is 100% (SA), the sound speed depends entirely on the acoustic properties of the seafloor sediment. In this case, the sediment is equivalent of clayey silt. When the volume ratio of seafloor sediment is zero (SD), the sound speed depends entirely on the acoustic properties of the marine cold spring carbonate rocks. In this case, the rock is equivalent to sample TSYC2. When the volume ratio is small or moderate, authigenic cold spring carbonate mineral particles accumulate in the seafloor sediments, which fill in the pore space of the cold spring carbonate mineral skeleton (SC). As the consolidation of authigenic mineral particles continues, the mineral particles contact each other and grow into small- and large-sized cold spring carbonate rocks (with larger rocks yielding SD), although some small particles may remain separated by sediments (such as in SB). When the volume ratio is large, marine cold spring carbonate mineral particles are distributed and wrapped mainly in seafloor sediments (SB). Based on the Voigt and Reuss models, the upper and lower limits of the possible sound speed of seafloor sediments containing cold spring carbonate rocks are predicted. Based on the Voigt-Reuss-Hill model, the intermediate sound speed characteristics of seafloor sediments containing cold spring carbonate rocks are also predicted. However, when considering an uneven pore distribution, complex cold spring carbonate rock states, shapes and structures, and different seafloor sediment types, the sound speed distribution becomes highly complicated and should be studied in greater detail and depth in future research.

4.2 Predicting the reflection characteristics

When both the incident angle and the reflection angle are 0° (representing vertical incidence), the reflection coefficient can be written as Eq.(8), which is seafloor Rayleigh reflection coefficient.

$$R = 1 - \frac{2k}{1+k} \tag{8}$$

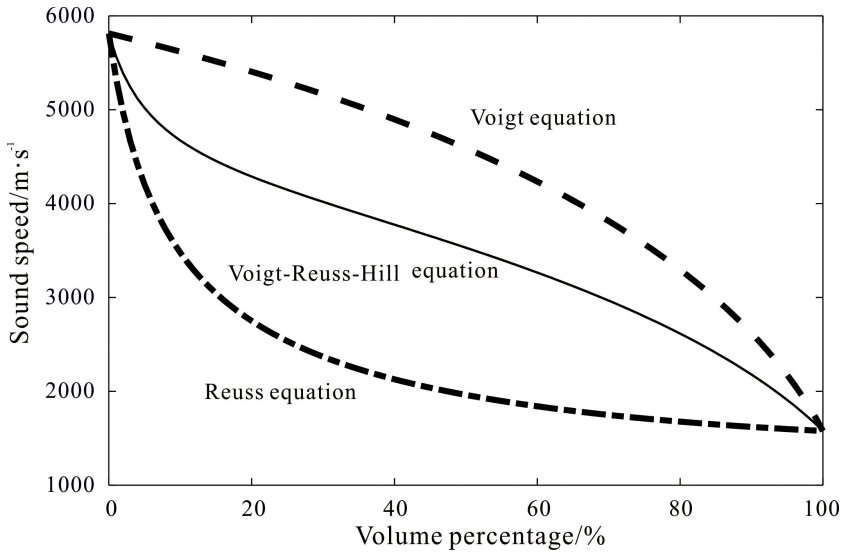

FIGURE 6
Relationship between the sound speed and volume percentage of seafloor sediments containing cold spring carbonate rocks.

where $k = \rho_w c_w / \rho_s c_\rho = (c_w / c_p)(1/(n + (1 - n)\rho_g / \rho_w))$ and the subscript w denotes bottom seawater.

4.2.1 Predicting the reflection characteristics of SA and SD

For SA, the reflection coefficient of clayey silt without cold spring carbonate rocks is calculated as 0.308. In contrast, SD represents the encrustation of cold spring carbonate rocks. According to the analysis of the sound speed, the porosity of the cold spring carbonate rock encrustation is no more than 55%. As shown in Figure 7, upon calculating the sound speed using Eqs. (2) and (3), the density using Eq. (4), and the reflection coefficient using Eq. (8), the predicted reflection coefficient of the cold spring carbonate rock (with dolomite as the constituent mineral) decreases from 0.856 to 0.473 as its porosity increases from 0 to 55%. The reflection coefficient of TSYC2 is 0.821, which is within this range.

4.2.2 Predicting the reflection characteristics of SB and SC

Based on the Voigt, Reuss, and Voigt-Reuss-Hill models, the reflection coefficients of seafloor sediments containing marine cold spring carbonate mineral particles (or rocks) are analyzed. As shown in Figure 8A, when the volume ratio is close to 0, the sediment contains only cold spring carbonate rocks (TSYC2), and the reflection coefficient reaches as high as 0.821. When the volume ratio is close to 1, the sediment contains only clayey silt, and the reflection coefficient is only 0.308. When the volume ratio is between 0 and 1, namely, when cold spring carbonate mineral particles (or rocks) and seafloor sediments are mixed together, the reflection coefficient varies from 0.308 to 0.821. Considering that the abovementioned porosity of natural carbonate rocks cannot exceed 55%, the reflection coefficient of seawater-saturated cold spring carbonate rocks (composed mainly of dolomite) must be greater than 0.473, as illustrated in Figure 7. On the other hand, the reflection coefficient of seafloor surface sediments on continental slopes without cold spring carbonate mineral particles is usually no greater than the reflection coefficient of coarse-grained sand (0.410) (Liu et al., 2015). Consequently, seafloor sediments with a reflection coefficient between 0.410 and 0.473 in cold spring seepage areas are likely to contain cold spring carbonate mineral particles (or rocks) in an accumulated or suspended state.

Based on a sub-bottom profiling survey near the Baiyun Depression in the northern South China Sea, the reflection coefficient inverted from Chirp sub-bottom data ranges from 0.2 to 0.8 as shown in Figure 8B (Chen et al., 2016). And the porosity inversion is illustrated in Figure 8C. The inversion results predicted the presence of obvious high-velocity, high-density, and low-porosity seafloor sediments inside the Mud Volcano Zone and low-velocity, low-density, and high-porosity seafloor sediments outside the Mud Volcano Zone. It can be explained by the mixture of cold spring carbonate rock and seafloor sediment as the kind of SA and SD shown in Figure 7 and the kind of SB and SC shown in Figure 8A. Clayey silt containing carbonate rock fragments and cold spring carbonate rock encrustations was collected at several nearby sampling points, so cold spring carbonate mineral particles must be mixed into the seafloor sediments (as in SB) when the reflection coefficient is between 0.41 and 0.473. When the reflection coefficient ranges from 0.473 to 0.821, the cold spring carbonate mineral particles are very likely to grow into cold spring carbonate rocks, which may form a mixture (SB), an accumulation (SC) or an encrustation (SD).

5 Conclusions

An increasing number of cold spring carbonate mineral particles and rocks have been found in different states throughout

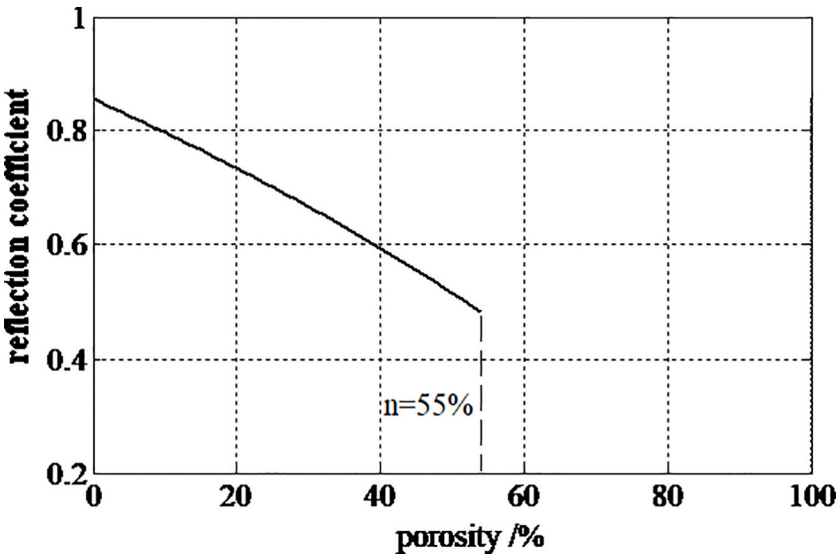

FIGURE 7
Reflection characteristics of a cold spring carbonate rock encrustation based on the Wyllie time-average equation.

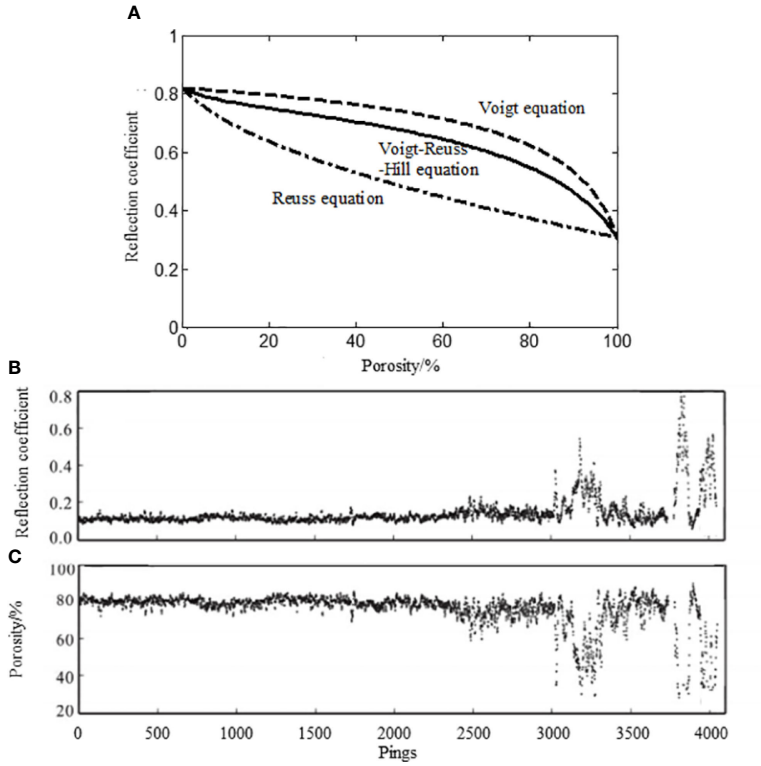

FIGURE 8
Reflection characteristics and porosities of the seafloor sediments containing cold spring carbonate rocks. The **(A)** is the relationship between the reflection coefficient and porosity, the **(B, C)** is the inverted reflection coefficient and porosity from the Chirp sub-bottom data, respectively.

the northern South China Sea. These cold spring carbonate rocks can be regarded as a special type of sediment distributed on or in seafloor surface sediments.

When cold spring carbonate mineral particles exist in seafloor sediments, the sound speed of the mixture is less than that of cold spring carbonate encrustations and cold spring carbonate rocks but greater than that of the clayey silt sediment. The same is true for the Rayleigh reflection coefficient of the mixture. Upon analyzing the measurement and calculation results with the Wyllie time-average equation and Voigt-Reuss-Hill model, the sound speeds and Rayleigh reflection coefficients of the seafloor sediments containing cold spring carbonate rocks are predicted. Some meaningful conclusions are as follows:

1) The relationship between the sound speed and porosity of marine cold spring carbonate rocks is consistent with that of terrestrial carbonate rocks. Taking sample TSYC2 as a reference, the measured sound speed of the seawater-saturated marine cold spring carbonate rock sample is 5,813 m/s, and the Rayleigh reflection coefficient is 0.821 at 40 kHz.
2) The sound speeds in marine cold spring carbonate rocks are dispersive, with the sound speed at 100 kHz being 261 m/s on average higher than that at 20 kHz, and the sound speed of seawater-saturated cold spring carbonate rocks is 166 m/s on average higher than that of air-saturated cold spring carbonate rocks.
3) For marine cold spring carbonate rocks, the sound speed decreases as the porosity increases. When the porosity (with dolomite as the constituent mineral) of seawater-saturated marine cold spring carbonate rocks increases from 0 to 55%, its sound speed is predicted to decrease from 7,051 m/s to 2,367 m/s.
4) For the four states of marine cold spring carbonate mineral particles existing on or in seafloor sediments, the sound speed and the Rayleigh reflection coefficient of a mixture of seafloor surface sediments containing cold spring carbonate mineral particles or rocks decrease with an increase in the volume ratio of the seafloor sediment. The reflection coefficient is predicted to vary from 0.308 (clayey silt) to 0.821 (marine cold spring carbonate rocks).

Data availability statement

The datasets presented in this study can be found in online repositories. The names of the repository/repositories and accession number(s) can be found in the article/supplementary material.

Author contributions

YT: Writing – original draft. DZ: Writing – review & editing. ZC: Review & editing. CF: Review & editing. PY: Review & editing.

YJ: Review & editing. LW: Review & editing. All authors contributed to the article and approved the submitted version.

Funding

We are also thankful for the financial support of the National Natural Science Foundation of China (42227803, 41976065, 91855101 and 42006071), Special Support Program for Cultivating High-level Talents in Guangdong Province (2019BT02H594), and 2020 Research Program of Sanya Yazhou Bay Science and Technology City (SKJC-2020-01-012), National Key R&D Program of China (2021YFC3100600).

Acknowledgments

We wish to thank the other members of the Guangdong University of Technology and the South China Sea Institute of Oceanology, Chinese Academy of Sciences, for carrying out the measurements and experiments, analyzing the datasets, and discussing this research.

Conflict of interest

The authors declare that the research was conducted in the absence of any commercial or financial relationships that could be construed as a potential conflict of interest.

Publisher's note

References

Baechle, G. T., Colpaert, A., Eberli, G. P., and Weger, R. J. (2008). Effects of microporosity on sonic velocity in carbonate rocks. *Leading Edge.* 27, 1012–1018. doi: 10.1190/1.2967554

Callender, W. R., and Powell, E. N. (1999). Why did ancient chemosynthetic seep and vent assemblages occur in shallower water than they do today? *Int. J. Earth Sci.* 88, 377–391. doi: 10.1007/s005310100196

Chen, D. F., Huang, Y. Y., Yuan, X. L., and Cathles, III, L. M. (2005). Seep carbonates and preserved methane oxidizing archaea and sulfate reducing bacteria fossils suggest recent gas venting on the seafloor in the Northeastern South China Sea. *Mar. petroleum Geology.* 22, 613–621. doi: 10.1016/j.marpetgeo.2005.05.002

Chen, C., Lou, Z. H., and Jin, A. M. (2017). Acoustic anisotropy of water-saturated and desiccated carbonate rocks. *Lithologic Reservoirs.* 29, 131–137. doi: 10.3969/j.issn.1673-8926.2017.04.016

Chen, Z., Yan, W., Chen, M. H., and Wang, S. H. (2006). Discovery of seep authigenic carbonate nodules on northern continental slope of South China Sea: new evidence of gas hydrate. *J. Trop. Oceanography.* 25, 83–83.

Chen, S., Yan, P., and Wang, Y. L. (2016). Inversion of the physical properties of the seabed using Chirp sub-bottom data in Mud Volcanoes field of the Southwest of Dongsha Islands. *Earth Science.* 41, 425–432. doi: 10.3799/dpkx.2016.034in Chinese with English abstract

Chen, Z., Yang, H. P., Huang, Q. Y., Lu, J., and Yan, W. (2007). Characteristics of cold seeps and structures of chemoauto-synthesis-based communities in seep sediments. *J. Trop. Oceanography.* 26, 73–82.

Chen, Z., Yang, H. P., Huang, Q. Y., Yan, W., and Lu, J. (2008). Diagenetic environment and implication of seep carbonate precipitations from the southwestern Dongsha area South China Sea. *Geoscience.* 22, 382–389.

Guo, M. Q., Ba., J., Ma., N. P., Chen, T. S., Zhang, L., Pang, M. Q., et al. (2018). P-wave velocity dispersion and attenuation in fluid-saturated tight sandstones: Characteristics analysis based on a double double-porosity structure model description. *Chin. J. Geophysics.* 61, 1053–1068. doi: 10.6038/cjg2018L0678

Han, X., Suess, E., Huang, Y., Wu, N., Bohrmann, G., Su, X., et al. (2008). Jiulong methane reef: microbial mediation of seep carbonates in the South China Sea. *Mar. Geology.* 249, 243–256. doi: 10.1016/j.margeo.2007.11.012

Hang, L. J., Li, Z. K., Yan, J., Sun, J. J., Geng, Y. C., Shi, H. J., et al. (2004). Test and application of sonic properties of carbonate rock. *Chin. J. Rock Mechanics Eng.* 14, 2444–2447.

Hill, R. (1952). The elastic behaviour of a crystalline aggregate. *Proc. Phys. Soc. Section A.* 65, 349–355. doi: 10.1088/0370-1298/65/5/307

Li, Y. H., Chu, Z. H., and Wang, H. (2002). On the experimental relation between clay-bearing carbonate rock acoustical and lithological characters. *Well Logging Technology.* 26, 269–227. doi: 10.16489/j.issn.1004-1338.2002.04.002

Liu, D. H. (1985). Testing of carbonate reservoir and its acoustic characteristics. *Oil Explor. Ser.* 06, 49–56.

Liu, B. R., Song, H. B., Guan, Y. X., Bai, Y., Chen, J. X., Geng, M. H., et al. (2015). Characteristics and formation mechanism of cold seep system in the northeastern continental slope of South China Sea from sub-bottom profiler data. *Chin. J. Geophysics.* 58, 247–256. doi: 10.6038/cjg20150122 (in Chinese with English abstract

Liu, X. J., Tang, D. H., Yan, P., Ge, C. D., and Wang, Y. L. (2017). Characteristics of authigenic carbonates from a mega-pockmark on the eastern side of Baiyun Sag, South China Sea and their geological significance. *Mar. Geo. Quaternary Geo.* 37, 119–127. doi: 10.16562/j.cnki.0256-1492.2017.06.013

Lu, Y., Chu, F. Y., Dong, Y. H., Zhu, Z. M., Zhu, J. H., and Lu, J. G. (2020). Formation of nodules on continental slopes in the northeast of the South China Sea and its implications for cold seep. *J. Mar. Sci.* 38, 16–25. doi: 10.3969/j.issn.1001-909X.2020.02.03

Ma, R. P., Ba, J., Carcione, J. M., Zhou, X., and Li, F. (2019). Dispersion and attenuation of compressional waves in tight oil reservoirs: Experiments and simulations. *Appl. Geophysics.* 16, 33–45. doi: 10.1007/s11770-019-0748-3

Ma, S. F., Han, D. K., Gan, L. D., and Yang, H. (2010). A review of seismic rock physics models. *Prog. Geophys* 2, 460–471. doi: 10.3969/j.issn.1004-2903.2010.02.012

Rafavich, F., Kendall, C. S. C., and Todd, T. P. (1984). The relationship between acoustic properties and the petrographic character of carbonate rocks. *Geophysics.* 49, 1622–1636. doi: 10.1190/1.1441570

Sayers, C. M. (2008). The elastic properties of carbonates. *Leading Edge.* 8, 1020–1024. doi: 10.1190/1.2967555

Shan, C. C., Deng, X. G., Wen, M. M., Feng, Q. Q., Syed, W. H., and Huang, W. (2020). Application of parametric sub-bottom profile in gas plumes detection: ATLAS P70 in Makran area as an example. *Prog. Geophysics.* 35, 1183–1190. doi: 10.6038/pg2020DD0148

Tong, H. P., Feng, D., and Chen, D. F. (2012). Progresses on petrology, mineralogy and geochemistry of cold seep carbonates in the northern South China Sea. *J. Trop. Oceanography.* 31, 45–56. doi: 10.3969/j.issn.1009-5470.2012.05.007

Wang, B., Luan, Z. D., Zhang, X., Xi, S. C., Li, L. F., Lian, C., et al. (2019). Topographic and geomorphological features of the Formosa Ridge cold seep system, the Southwestern Taiwan Island. *Mar. Sci.* 43, 51–59. doi: 10.11759/hykx20171120003

Wei, X., Wang, S. X., and Zhao, J. G. (2015). Laboratory study of velocity dispersion of the seismic wave in fluid-saturated sandstones. *Chin. J. Geophysics.* 58, 3380–3388. doi: 10.6038/cjg20150930

Wu, X. T., Liu, L. H., Wu, N. Y., and Cheng, J. W. (2015). Geochemistry of early diagenesis in marine sediments: research progress. *Mar. Geology Frontiers.* 31, 17–26. doi: 10.16028/j.1009-2722.2015.12003

Wu, D. D., Wu, N. Y., Ye, Y., Han, X. Q., Huang, Y. Y., and Suess, E. (2009). Petrographic characteristics of authigenic carbonates from Jiulong methane reef of northern South China Sea. *J. Trop. Oceanography*, 74–81.

Wyllie, M. R. J., Gregory, A. R., and Gardner, L. W. (1956). Elastic wave velocities in heterogeneous and porous media. *Geophysics.* 21, 41–70. doi: 10.1190/1.1438217

Xi, S. C., Zhang, X., Wang, B., Luan, Z. D., Chen, C. A., and Yan, J. (2017). The indicators of seabed cold seep and comparison among main distribution areas. *Mar. Geol. Front.* 33, 7–18. doi: 10.16028/j.1009-2722.2017.02002

Xue, Y. S., and Huang, J. H. (2016). Advances in study of cold seep deposition and palaeoclimatic and palaeoenviromental significance. *Geological Sci. Technol. Information.* 35, 97–104.

Yan, P., Wang, Y. L., and Zheng, H. B. (2011). Characteristics of deep water sedimentation revealed by sub-bottom profiler survey over the Baiyun Sag-Southwest Dongsha Island Waters in the norther South China Sea. *J. Trop. Oceanogr.* 30, 115–122.

Yan, P., Wang, Y. L., Zheng, H. B., Zou, D. P., and Chen, Z. (2014). Geophysical features of mud volcanoes in the waters southwest of Dongsha Islands. *Acta Oceanologica Sinica.* 36, 142–148. doi: 10.3969/j.issn.0253-4193.2014.07.016 (in Chinese with English abstract

Zhang, H., Yang, S., Wu, N. Y., Su, X., Holland, M., Schultheiss, P., et al. (2007). Successful and surprising results for China first gas hydrate drilling expedition. *Fire Ice* 7, 6–9.

Zhao, J., Liang, Q. Y., Wei, J. G., Tao, J., Yang, S. X., Liang, J. Q., et al. (2020). Seafloor geology and geochemistry characteristic of methane seepage of the "Haima" cold seep, northwestern slope of the South China Sea. *Geochimica.* 49, 108–118. doi: 10.19700/j.0379-1726.2020.01.009

frontiers | Frontiers in Marine Science

TYPE Original Research
PUBLISHED 27 September 2023
DOI 10.3389/fmars.2023.1283061

OPEN ACCESS

EDITED BY
Baohua Liu,
National Deep Sea Center (NDSC), China

REVIEWED BY
Peng Guo,
Commonwealth Scientific and Industrial Research Organisation (CSIRO), Australia
Lei Xing,
Ocean University of China, China
Xiangchun Wang,
China University of Geosciences, China

*CORRESPONDENCE
Kai Liu
liuk@fio.org.cn

RECEIVED 25 August 2023
ACCEPTED 11 September 2023
PUBLISHED 27 September 2023

CITATION
Li J, Pei Y, Liu C, Zhang L, Luo X, Liu K and Li W (2023) A robust array geometry inversion method for a deep-towed multichannel seismic system with a complex seafloor.
Front. Mar. Sci. 10:1283061.
doi: 10.3389/fmars.2023.1283061

A robust array geometry inversion method for a deep-towed multichannel seismic system with a complex seafloor

Jing Li[1,2,3], Yanliang Pei[1,2,3], Chenguang Liu[1,2,3], Liancheng Zhang[4], Xiaohu Luo[1,2,3], Kai Liu[1,2,3]* and Weilu Li[5]

[1]Key Laboratory of Marine Geology and Metallogency, First Institute of Oceanography, Ministry of Natural Resources, Qingdao, Shandong, China, [2]Laboratory of Marine Geology, Laoshan Laboratory, Qingdao, Shandong, China, [3]Key Laboratory of Submarine Acoustic Investigation and Application of Qingdao (Preparatory), First Institute of Oceanography, Ministry of Natural Resources, Qingdao, Shandong, China, [4]Key Laboratory of Fluid Transmission Technology of Zhejiang Province, Zhejiang Sci-Tech University, Hangzhou, Zhejiang, China, [5]Marine Data Center, National Marine Data and Information Service, Tianjin, China

Deep-towed multichannel seismic exploration technology has better applicability and more development potential when utilized to invert the geoacoustic properties of deep-sea sediment. The accurate geometric inversion results of the receiving array are crucial for fine submarine sediment imaging and physical property parameter inversion based on deep-towed multichannel seismic data. Thus, this study presents an array geometry inversion method suitable for complex seafloors to address the challenge of precise source-receiver positioning. The objective function of the deep-towed seismic array geometry inversion is built using the shortest path algorithm according to the traveltimes of direct waves and seafloor reflections, and the particle swarm optimization algorithm is used to achieve high-precision inversion of the source-receiver position. The results showed that the proposed method is shown to have incomparable applicability and effectiveness in obtaining exact source-receiver positions for deep-towed multichannel seismic systems. Regardless of the complexity of the seabed morphology, seismic image processing techniques using the source-receiver position data obtained by the suggested method produce fine seismic imaging profiles that clearly and accurately reflect the structural characteristics of sediments. These findings provide insights for the accuracy and reliability of the proposed geometric shape inversion method for deep-towed seismic arrays in practical applications to meet the requirements of near-bottom acoustic detection for fine imaging of deep-sea seabed strata and precise inversion of geoacoustic parameters.

KEYWORDS

near-bottom acoustic detection technology, deep-towed multichannel seismic system, array geometry inversion, complex seafloor, fine seismic imaging, accurate geoacoustic parameters inversion

1 Introduction

A deep-towed multichannel seismic system is a novel deep-sea near-bottom acoustic detection technology that drags an artificial high-frequency seismic source and seismic receiving streamer placed near the seabed to acquire seismic data (Breitzke and Bialas, 2003; Gettrust et al., 2004). This system has better lateral and vertical resolution, better signal-to-noise ratio (SNR), and deeper stratigraphic detection capacity than traditional high-resolution multichannel seismic systems. Moreover, this system has better applicability and more development potential when utilized to invert the geoacoustic properties of deep-sea sediment.

Researchers in many countries worldwide have conducted research on deep-towed seismic exploration technology to improve their deep-sea near-bottom investigation capabilities and have successfully developed representative deep-towed multichannel seismic systems. In the 1980s, the United States Naval Research Laboratory (NRL) designed and produced the deep-towed acoustic geophysical system (DTAGS) (Gettrust et al., 1988; Rowe and Gettrust, 1993; Wood et al., 2003), which consists of a Helmholtz resonator source (220-820 Hz) and a 622 m hydrophone cable. At the beginning of this century, the French Research Institute for Exploitation of the Sea (Ifremer) developed the SYstème SIsmique Fond de mer (SYSIF) (Marsset et al., 2010; Marsset et al., 2014), which includes two sets of Helmholtz resonators with different frequency bands, 580-2200 Hz and 220-1050 Hz, and a seismic streamer composed of 52 digital hydrophones arranged with a channel spacing of 2 m. Recently, researchers at the First Institute of Oceanography of Ministry of Natural Resources (FIO, MNR) developed the Kuiyang-ST2000 (Pei et al., 2022), which includes a deep-towed sparker source (150-1200 Hz) and a 48-channel digital seismic streamer. Moreover, the Research and Development Partnership for Next Generation Technology of Marine Resources Survey (J-MARES) developed the deep-towed autonomous cable seismic (ACS) system (Hutapea et al., 2020). The seismic source in this system is based on the iXBlue Echos 1500 subbottom profiler (700-2250 Hz), and the data acquisition device utilizes a 32-channel seismic receiving cable with a channel spacing of 5 m. In addition, deep-towed multichannel seismic systems are usually equipped with ultrashort baselines (USBLs), depth transducers, altimeters and attitude sensors to monitor the attitude and positioning of the systems in real time.

Given the unparalleled advantages of deep-towed seismic data acquisition systems, such as their high resolution and SNR, deep-towed multichannel seismic exploration technology has played an increasingly important role in deep-sea mineral resource surveys, marine engineering exploration, and deep-sea geohazard evaluation and has achieved remarkable application results (Talukder et al., 2007; Ker et al., 2014; Riboulot et al., 2018). For example, Marsset et al. (2010) confirmed that SYSIF can effectively optimize the imaging quality of submarine stratigraphic structures such as pockmarks, carbonate mounds, submarine landslides and underground faults and is thus very suitable for deep-sea geohazard studies. Sultan et al. (2014) utilized high-resolution seismic imaging profiles obtained by SYSIF to assess pockmark formation and evolution in deep water in Nigeria; in addition, they combined their results with seafloor drill rig data, *in situ* geotechnical measurements, and pore water analyses. Colin et al. (2020a); Colin et al. (2020b) developed a fine velocity model of gas hydrate-bearing sedimentary layers using SYSIF data acquired in the western Black Sea, revealing an anomalous free gas distribution, which might suggest the ongoing migration of the base of the gas hydrate stability zone (GHSZ). Chapman et al. (2002) and He et al. (2009) employed high-resolution DTAGS data to finely image the structure of a hydrate-related cold vent offshore Vancouver Island, assessed the amount of gas hydrate and underlying free gas, and determined the associated seismic velocities, which were used to estimate the gas hydrate concentration. Wood et al. (2008) studied the gas and gas hydrate distributions near seafloor seeps in Mississippi Canyon in the northern Gulf of Mexico using deep-towed high-resolution seismic imaging technology based on DTAGS. Hutapea et al. (2020) used high-resolution ACS data acquired in the Joetsu Basin in Niigata, Japan, and seismic attribute analysis technology to effectively identify natural gas hydrates, free gas and gas chimneys. Pei et al. (2023) utilized Kuiyang-ST2000 to conduct natural gas hydrate surveys in the Qiongdongnan and Shenhu areas of the South China Sea and finely imaged the sedimentary and structural features of geohazards related to natural gas hydrates.

Ultrahigh-resolution seismic detection technology has higher requirements for the source-receiver positioning accuracy. Therefore, accurate geometric inversion results of the receiving array are crucial for fine submarine sediment imaging and physical property parameter inversion based on deep-towed multichannel seismic data. In recent years, to address this issue, scholars have proposed a variety of array geometry inversion methods. Rowe and Gettrust (1993) used the real-time depth measurement values obtained by four engineering nodes configured at the source of the DTAGS and the 28th, 38th and 48th channels of the receiving cable and directly calculated the positions of the receivers with a linear interpolation model. Because the linear interpolation result is not sufficiently accurate, Walia and Hannay (1999) evaluated the depths of the source and receivers by introducing the traveltime of the sea-surface reflection to constrain the nonlinear array geometry. On the basis of previous studies, He et al. (2009) constrained the inversion according to engineering node depth measurements and the joint traveltime of the direct wave and sea-surface reflection and used a genetic algorithm and polynomial interpolation to determine the globally optimized source-receiver positioning information. Each digital hydrophone in the SYSIF receiving array is equipped with an attitude sensor; hence, Marsset et al. (2014); Marsset et al. (2018) reconstructed the array geometry according to the attitude sensor pitch angle measurement values. Considering the impact of pitch angle measurement errors and error accumulation on the accuracy of array geometry inversion, Colin et al. (2020a) improved the accuracy of array geometry reconstruction with the pitch angles acquired by the attitude sensors as the reference initial values and the traveltimes of the direct wave and seafloor reflection as constraints to optimize the inversion of the pitch angle

parameters. Pei et al. (2023) directly calculated the position of the receivers using the traveltime of the direct wave and sea-surface reflection and corrected the array geometry results with a polynomial curve fitting method in accordance with the deep-water towed morphological characteristics of Kuiyang-ST2000 obtained by dynamic simulations (Zhu et al., 2020).

In summary, the existing technology mainly depends on the attitude sensors in the receiving array and the seismic traveltime; hence, the attitude measurement error and the traveltime accuracy are the main factors leading to inaccurate source-receiver positions in deep-towed seismic arrays. According to analyses of deep-towed seismic data, the traveltime accuracy of the seafloor reflection is better than that of the sea-surface reflection due to the stronger energy, higher SNR and better waveform consistency of the seafloor reflection. However, because of the high complexity of the seafloor, previous studies on seafloor reflection traveltime positioning methods are generally best suited for gentle seabed working environments with small slopes. Moreover, influencing factor analyses of array geometry inversion methods are lacking. To address this issue, we propose a robust array geometry inversion method for arbitrarily complex seafloors. By introducing the traveltimes of direct waves and seafloor reflections, we establish an objective function for array geometry inversion that is applicable to complicated seabeds and apply a nonlinear optimization algorithm to realize high-precision inversion of the geometric representation parameters and acquire highly accurate and reliable source-receiver positioning results. Furthermore, the accuracy and reliability of the proposed method are evaluated by means of Monte Carlo uncertainty analyses through numerical experiments, focusing on factors such as the seismic traveltime, seawater velocity and seabed morphology. Additionally, the applicability of field data processing with Kuiyang-ST2000 proves that this method can efficiently address the issue of precise source-receiver positioning with deep-towed multichannel seismic systems while ensuring that the SNR and resolution of this type of seismic data meet the requirements of deep-sea fine stratigraphic imaging and geoacoustic parameter inversion.

2 Methods

2.1 Geometric representation of the deep-towed seismic array

To enhance the stability of the objective function for array geometry inversion with deep-towed multichannel seismic systems while accounting for the constraints of the inherent properties of deep-towed seismic streamers, we characterize the relative position relationship between the source and receivers using the known channel spacing and the pitch angle parameters to be obtained. In the solution of the objective function, only the pitch angle parameters need to be optimized to reconstruct the geometric shape of the deep-towed seismic array.

Because the deep-sea current velocity is smaller than the towing speed of the deep-towed multichannel seismic system, no significant feather angles occur in the deep-towed seismic array during deep water operations. As shown in Figure 1, taking the Kuiyang-ST2000 engineering design scheme as an example, when only two dimensions are considered, the receiving cable can be divided into multiple segments according to the offset and channel spacing, and the pitch angle is considered the geometric shape representation parameter. Based on the length and pitch angle of each segment, the horizontal and vertical offsets of each receiver in the deep-towed multichannel seismic streamer relative to the source position can be characterized as follows:

$$\begin{cases} X_1 = l_0^x + l_1 \cos\theta_1 \\ Z_1 = l_0^z + l_1 \sin\theta_1 \\ X_r = X_1 + \sum_{i=2}^{r} l \cos\theta_i \\ Z_r = Z_1 + \sum_{i=2}^{r} l \sin\theta_i \end{cases} \tag{1}$$

where l_1 represents the distance between the towing point and the 1st receiver in the deep-towed seismic streamer, l is the distance between adjacent receivers along the cable, namely, the channel spacing, and θ_1 and θ_i are the pitch angles of the 1st and i th segments in the deep-towed seismic streamer, respectively. A

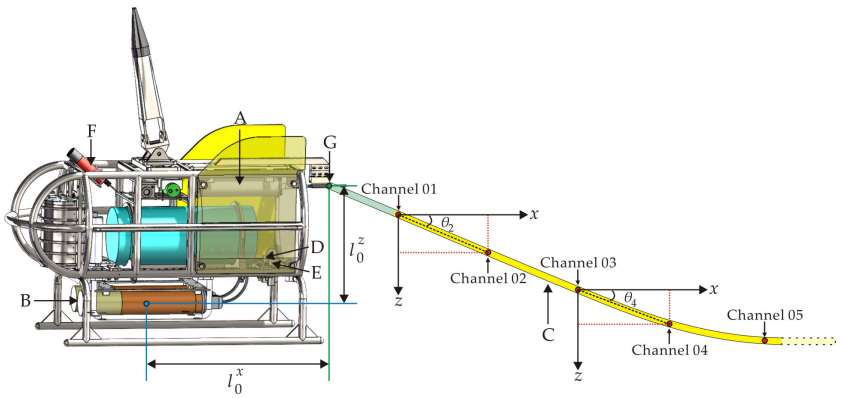

FIGURE 1
Schematic diagram of the geometric representation of a deep-towed seismic array. **(A)** operating control center; **(B)** deep-towed sparker source; **(C)** deep-towed seismic streamer; **(D)** depth transducer; **(E)** altimeter; **(F)** ultrashort baseline beacon; **(G)** towing point of deep-towed seismic streamer; θ_i: pitch angle.).

rectangular coordinate system is established with the deep-towed seismic source position as the origin, where l_0^x and l_0^z denote the horizontal and vertical offsets between the source and the towing point of the seismic streamer, respectively, X_1 and Z_1 are the horizontal and vertical coordinates of the 1st receiver, X_r and Z_r are the horizontal and vertical coordinates of the r th receiver, where $r = 2, \ldots, N$, and N is the number of acquisition channels in the seismic streamer. Notably, the measured pitch angle is not needed for the initial model by the method proposed in this paper, and the global optimal solution for the geometric representation parameters, namely, the pitch angles, of the deep-towed seismic array can be obtained.

2.2 Determination of the seafloor reflection propagation path

Source-receiver positioning methods based on seismic traveltime often require that the propagation path of the seismic waves is relatively clear; thus, the sea-surface reflection traveltime is usually selected for inversion processing. In addition, the seawater velocity is a key parameter that affects the seismic traveltime. The seawater layer is not a homogeneous medium, and it has obvious heterogeneity in the longitudinal direction, which could hinder the use of the sea-surface reflection traveltime to precisely locate the source-receiver positions for deep-towed seismic arrays. Moreover, the sea-surface reflection data acquired by the deep-towed multichannel seismic system might exhibit low SNR and even waveform distortion, deteriorating the accuracy of the determined traveltime. In contrast, the seafloor reflection has stronger energy, higher SNR, and better waveform consistency and is thus more convenient for obtaining an accurate traveltime. Therefore, developing a geometric shape inversion method for deep-towed seismic arrays based on the traveltimes of direct waves and seafloor reflections has good applicability and high application value. The key is to solve the problem of determining the propagation path of seafloor reflections for complex seabeds.

As shown in Figure 2, in the case of a flat seabed interface, the propagation path of the seafloor reflection can be easily determined through simple spatial geometric relationships based on Snell's law. Thus, the expression for the traveltime of the seafloor reflection can be obtained as follows:

$$t_r^{F\_cal\_f} = \frac{\sqrt{X_r^2 + (2H_{st} - Z_r)^2}}{v_w} \tag{2}$$

The expression for the traveltime of the direct wave is formulated as follows:

$$t_r^{D\_cal} = \frac{\sqrt{X_r^2 + Z_r^2}}{v_w} \tag{3}$$

where $t_r^{D\_cal}$ and $t_r^{F\_cal\_f}$ represent the traveltimes of the direct wave and seafloor reflection acquired by the r th receiver in the case of a flat seabed interface, respectively, H_{st} is the altitude of the source, and v_w is the seawater velocity.

Furthermore, as shown in Figure 2, the determination of the propagation path of the seafloor reflection is related to the slope angle in the case of a slanted seabed interface. Similarly, on the basis of Snell's law, by introducing coordinate rotation and intermediate quantities, the following expression for the traveltime of the seafloor reflection can be obtained:

$$\begin{cases} t_r^{F\_cal\_s} = \frac{\sqrt{(2H_{st}^* - Z_r^*)^2 + X_r^{*2}}}{v_w} \\ H_{st}^* = H_{st}\cos\alpha \\ X_r^* = (X_r - Z_r\tan\alpha)\cos\alpha \\ Z_r^* = \sqrt{X_r^2 + Z_r^2 - X_r^{*2}} \end{cases} \tag{4}$$

where $t_r^{F\_cal\_s}$ represents the traveltime of the seafloor reflection acquired by the r th receiver in the case of a slanted seabed interface, α denotes the slope angle of the inclined seabed interface, and X_r^*, Z_r^* and H_{st}^* are the intermediate variables during the calculation process.

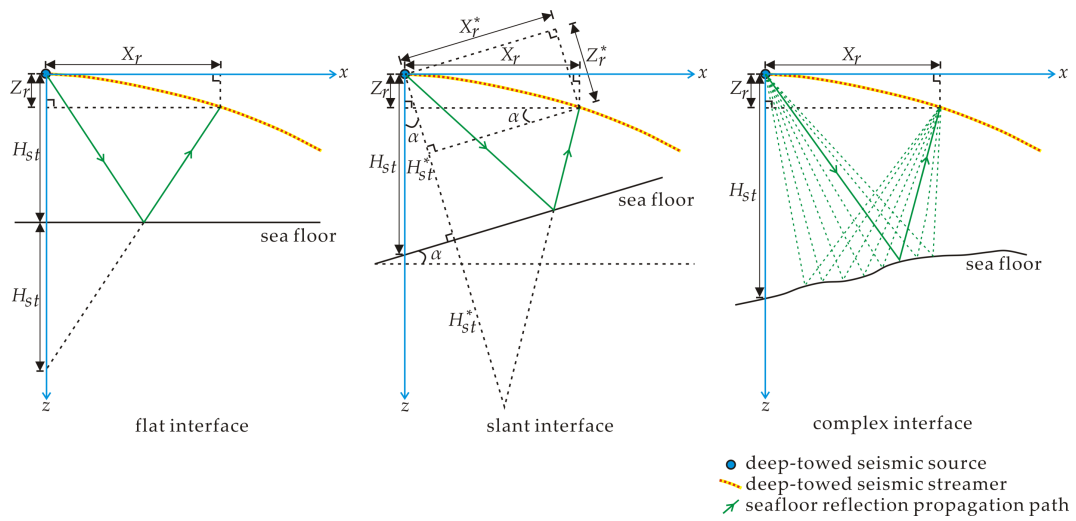

FIGURE 2
Schematic diagram of the seafloor reflection propagation path determination strategy for different seabed interfaces.

However, the morphological changes in the seabed may be complicated in real situations, and it is difficult to determine the exact propagation path of the seafloor reflection with Snell's law using simple spatial geometry. To address this issue, we employ the shortest path algorithm based on Fermat's principle to identify the reflection point of the seafloor reflection. The shortest path algorithm can be used to determine the ray path and the corresponding traveltime of the seafloor reflection for complex velocity interfaces. This algorithm has the advantages of high calculation accuracy, fast operation speed and good robustness. In this paper, as demonstrated in Figure 2, we discretized the seabed interface at certain intervals and assumed that the area near the operating depth of the deep-towed multichannel seismic system on the seabed could be regarded as an isotropic medium. Then, we connected the source, the discrete points on the seabed interface and the receivers. With this approach, multiple seafloor reflection propagation paths were constructed, and the shortest ray path was found to be an accurate and reliable propagation path of the seafloor reflection. Therefore, for the complex seabed interface, the expression for the seafloor reflection traveltime is formulated as follows:

$$\begin{cases} t_r^{F\_cal\_c} = \dfrac{\min(path_r^m)}{v_w} \\ path_r^m = \sqrt{x_m{}^2 + z_m{}^2} + \sqrt{(x_m - X_r)^2 + (z_m - Z_r)^2} \\ z_m = D_m - S_z \end{cases} \tag{5}$$

where $t_r^{F\_cal\_c}$ represents the traveltime of the seafloor reflection acquired by the r th receiver in the case of a complex seabed interface, and S_z indicates the depth of the source. Taking the position of the source as the origin, the rectangular coordinate system shown in Figure 2 was established, where x_m and z_m are the abscissa and ordinate values of the m th discrete point on the seabed interface, respectively, and D_m denotes the depth of the m th discrete point on the seabed interface. The depth variation curve of the seabed interface can be derived according to the measured values of the depth and the altitude of the deep-towed source along the direction of the survey line. When the m th discrete point on the seabed interface is set as the reflection point, $path_r^m$ is the distance of the seafloor reflection propagation path to be determined acquired by the r th receiver, where $m = 1, \ldots, M$, and M is the total number of discrete points on the seabed interface.

2.3 Construction and solution of the objective function

Based on the geometric representation of the deep-towed seismic array and the determination of the seafloor reflection propagation path, the objective function of the geometric representation parameter inversion is built as follows:

$$\hat{\boldsymbol{\theta}} = \arg\min_{\boldsymbol{\theta}} \sum_{r=1}^{N} \left\{ (t_r^{D\_cal} - t_r^{D\_obs})^2 + (t_r^{F\_cal} - t_r^{F\_obs})^2 \right\} \tag{6}$$

where $\theta = [\theta_1, \theta_2, \theta_3, \ldots, \theta_N]$ are the parameters to be optimized; $\theta_1, \theta_2, \theta_3, \ldots, \theta_N$ represent the pitch angles of each segment in the deep-towed seismic array, constituting the geometric shape representation parameters; $t_r^{D\_cal}$ and $t_r^{D\_obs}$ are the theoretical and observed values of the direct wave traveltime to the r th receiver, respectively; and $t_r^{F\_cal}$ and $t_r^{F\_obs}$ are the theoretical and observed values of the seafloor reflection traveltime to the r th receiver, respectively. Notably, $t_r^{F\_cal}$ should be replaced by $t_r^{F\_cal\_c}$ in the method proposed in this paper. $\hat{\theta}$ is the optimal solution of the objective function, $\hat{\theta} = [\hat{\theta}_1, \hat{\theta}_2, \hat{\theta}_3, \ldots, \hat{\theta}_N]$; in other words, $\hat{\theta}_1, \hat{\theta}_2, \hat{\theta}_3, \ldots, \hat{\theta}_N$ are the optimal geometric shape representation parameters for the deep-towed seismic array.

Based on Equations (1), (3), (5) and (6), we adopt the particle swarm optimization (PSO) algorithm to solve the optimization problem of the objective function without relying on the initial model. The PSO algorithm, which applies a group information sharing mechanism, has the advantages of fast convergence and good robustness. Then, the high-precision inversion of the array geometry for a deep-towed multichannel seismic system suitable for an arbitrarily complex seabed is realized.

3 Numerical experiments

3.1 Numerical model and evaluation criteria

To verify the effectiveness of the proposed method, we employ the method to the array geometry inversion problem for a numerical model for a deep-towed multichannel seismic system. The model is established according to the engineering design scheme of Kuiyang-ST2000, in which there are 48 seismic traces with a trace interval of 3.125 m. The distance between the towing point of the deep-towed seismic streamer and the 1st receiver is 12.5 m. Because of its length, it is split into four 3.125 m segments, resulting in three additional node pitch angles and a total of 51 geometric representation parameters that need to be reversed. The deep-towed streamer's towing point is offset from the sparker source emission array center by 2.0 m and -0.6 m in the horizontal and vertical directions, respectively. Figure 3A shows the numerical model of the array geometry and seabed interface established based on the above parameters. The immersion depth of the source is 1104.69 m, and the height above the seabed is 120.00 m. The seabed interface is set to be close to a real complex seabed. The seismic velocity of seawater is set to 1488 m/s. The theoretical traveltimes of the direct wave and the seafloor reflection, as illustrated in Figure 3B, can be derived using the seismic ray-tracing method. Based on the numerical model, the reliability and accuracy of the proposed method are assessed according to an influencing factor analysis of uncertainty sources such as the seismic traveltime, seawater velocity and seabed morphology. In addition, to quantitatively evaluate the quality of the array geometry inversion results, the root mean square error (RMSE) is introduced as the evaluation criterion:

$$RMSE = \sqrt{\frac{1}{n} \sum_{i=1}^{n} \left(\sqrt{(X_i - \tilde{X}_i)^2 + (Z_i - \tilde{Z}_i)^2} \right)^2} \tag{7}$$

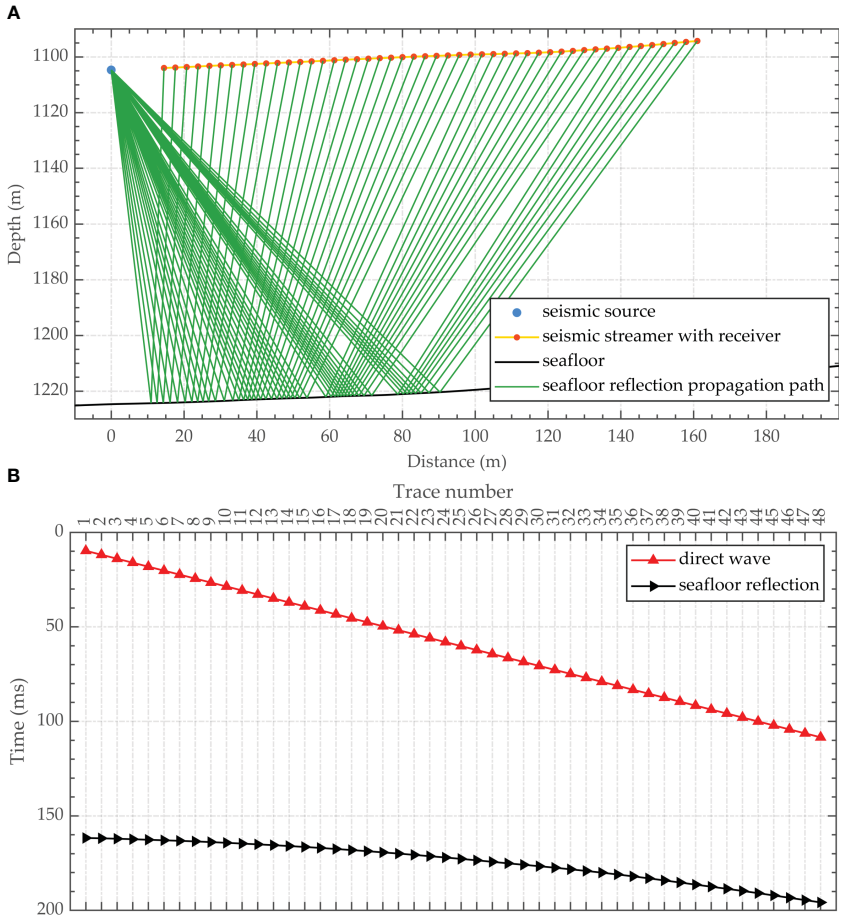

FIGURE 3
Numerical model of a deep-towed seismic array and its theoretical seismic traveltimes. ((**A**) Numerical model of the array geometry and seabed interface; **(B)** Theoretical traveltimes of the direct wave and seafloor reflection).

where X_i and Z_i are the reference values of the i th receiver position in the numerical model, $\tilde{X}_i$ and $\tilde{Z}_i$ are the predicted values of the i th receiver position obtained by the inversion method, $\sqrt{(X_i - \tilde{X}_i)^2 + (Z_i - \tilde{Z}_i)^2}$ represents the positioning error of the i th receiver, and n is the total number of receivers in the numerical model.

Three different strategies for determining the propagation path of the seafloor reflection described in Section 2.2 are utilized to invert the geometric shape of the array model, namely, replacing t_r^{F-cal} in Equation (6) with $t_r^{F-cal\_f}$, $t_r^{F-cal\_s}$ and $t_r^{F-cal\_c}$. The hypothesis of a flat seabed interface is that the seabed interface is approximated as a horizontal interface based on the height of the deep-towed source above the seafloor. The assumption of a slanted seabed interface is that the seabed interface within the lateral spacing of 80 m is approximated as an inclined interface by taking the horizontal position of the source as the origin. The proposed method does not need an approximate representation of the seabed interface and can accurately calculate the traveltime of the seafloor reflection with the shortest path algorithm. As shown in Figure 4, the source-receiver positioning result obtained by the suggested method is the most consistent to the model reference value among the considered models, followed by the slanted interface assumption model and finally the flat interface assumption model. The accuracy of the array geometry inversion method with the assumption of a slanted interface relies on the degree of fitting between the inclined interface and the seabed at the current position. Thus, the inversion accuracy improves when the seabed topography changes gradually. However, when the seabed interface is rugged and the topographical changes are more severe, the inversion precision is greatly reduced. Therefore, the inversion strategy proposed in this paper demonstrates excellent applicability in the case of complex seabeds. Figure 5 shows the relationship among the RMSE of the source-receiver positioning determined by the numerical model, the computational efficiency of the inversion and the discrete interval of the seabed interface. Accounting for both the accuracy and efficiency of the inversion, the discrete interval of the seabed interface was set to 1.0 m in the subsequent numerical model experiments and field data processing.

3.2 Influencing factors analysis

3.2.1 Uncertainty of the traveltime

Due to the influence of the SNR of the data and the decision criterion of the waveform starting point, several errors impact seismic traveltime results (Liu et al., 2022). Referring to the suggestions of

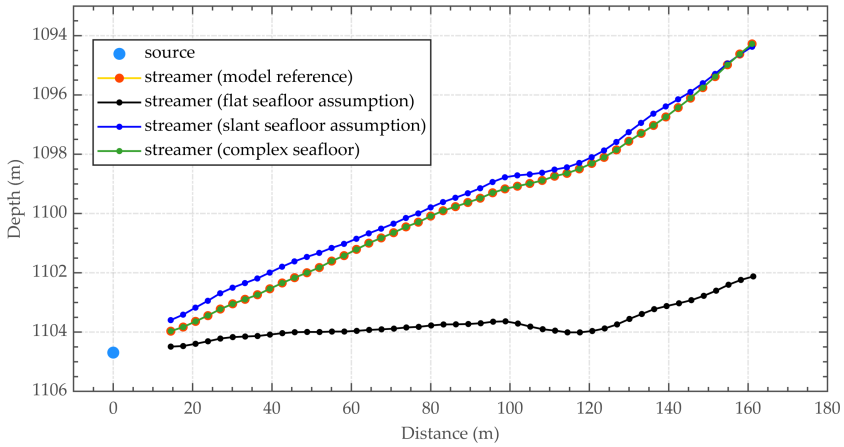

FIGURE 4
Results of the array geometry inversion of the numerical models based on different strategies for determining the seafloor reflection propagation path.

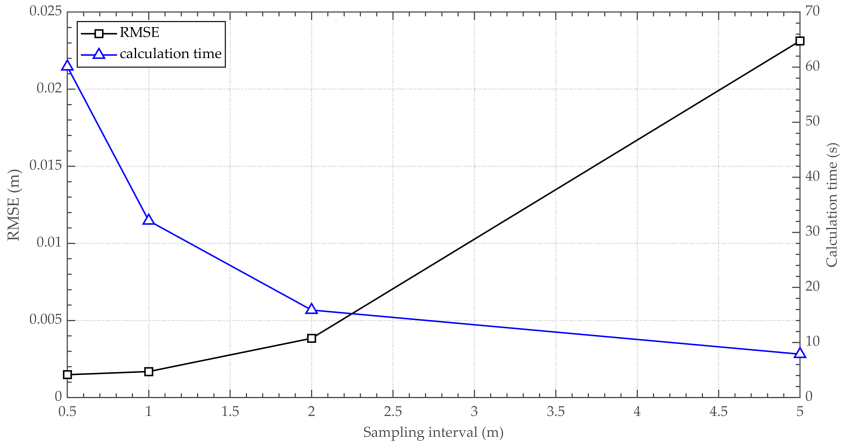

FIGURE 5
Relationship among the RMSE, inversion efficiency and seabed interface dispersion interval.

Zhang and Toksöz (1998) and Korenaga et al. (2000), the overall traveltime error should be divided into two types: common phase errors and individual errors. The common phase errors are related to the determination of the initial point of the same seismic phase (similar to systematic errors), and the individual errors are equivalent to adding Gaussian noise to the acquired data. This data randomization method is used due to the highly correlated nature of real seismic data to reliably model the uncertainty of the determined traveltime.

To evaluate the impact of the traveltime uncertainty on the accuracy of the geometric inversion of the deep-towed seismic array, four groups of traveltime data for direct waves and seafloor reflections with different errors are constructed, named Picking Error 01, Picking Error 02, Picking Error 03 and Picking Error 04. Considering the dominant frequency of the seismic source, the common phase errors are sequentially set to -0.25 ms, -0.125 ms, 0.125 ms and 0.25 ms in the four datasets. The individual errors for the Picking Error 01 and Picking Error 04 sets are set to ±0.25 ms, and the individual errors for the Picking Error 02 and Picking Error 03 sets are set to ±0.125 ms. In other words, the total traveltime error for the Picking Error 01 and Picking Error 04 sets is 0.50 ms, while that for the Picking Error 02 and Picking Error 03 sets is 0.25 ms. Figure 6 shows the influence of the traveltime uncertainty on the array geometry inversion results. Figure 6A displays the traveltime errors for direct waves and seafloor reflections in the four datasets mentioned above. Figure 6B shows the inversion results of the array geometry obtained by the proposed method for these test groups. Figure 6C presents the receiver positioning errors corresponding to the inversion results shown in Figure 6B. The RMSEs of the inversion results for the Picking Error 01, Picking Error 02, Picking Error 03 and Picking Error 04 sets are 0.45 m, 0.23 m, 0.20 m and 0.42 m, respectively.

As shown in Figure 6, the common phase errors lead to deviations in the overall position in the array geometry inversion results, with larger common phase errors causing larger positioning

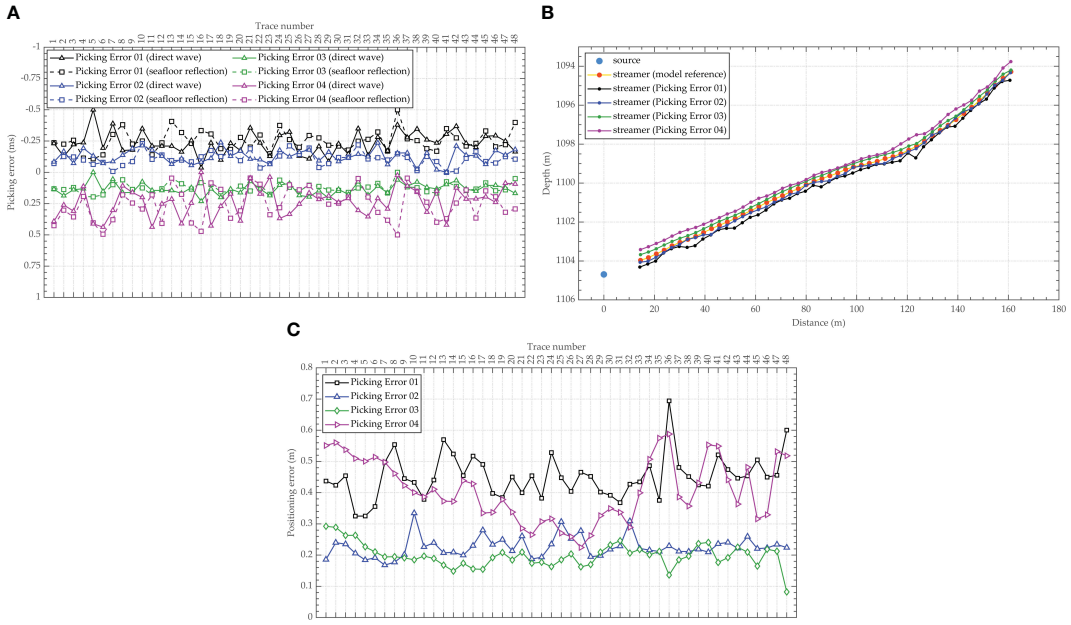

FIGURE 6
Influence of traveltime uncertainty on the array geometry inversion results. ((**A**) Traveltime errors; (**B**) Array geometry inversion results; (**C**) Receiver positioning errors).

errors. Larger traveltime values cause the inversion position of the seismic array to move upward; in contrast, smaller traveltime values cause the inversion position to move downward, leading to slightly noticeable array geometry jitter. On the basis of the common phase error, adding Gaussian noise to the individual errors leads to jitter distortion in the array geometry inversion results. Moreover, as the individual error increases, the jitter and nonsmoothness of the array geometry inversion results become more severe.

3.2.2 Uncertainty in the seawater velocity

The seawater velocity is related to the temperature, salinity and pressure of seawater. Due to the heterogeneity of seawater, the seawater velocity varies over time in different places, which introduces uncertainty to the seawater velocity value utilized in the geometric shape inversion of the deep-towed seismic array. In previous works, several expendable conductivity-temperature-depth (XCTD) profilers were usually employed to analyze the vertical and lateral changes in the seawater velocity in the study area as a reference for the value during near-bottom multichannel seismic surveys. The accurate seawater velocity value in the numerical model is known to be 1488.0 m/s. To analyze the influence of seawater velocity errors on the accuracy of the array geometry inversion, we set the seawater velocity to 1486.0 m/s, 1487.0 m/s, 1489.0 m/s and 1490.0 m/s, named Velocity Error 01, Velocity Error 02, Velocity Error 03 and Velocity Error 04, respectively. As shown in Figure 7, the array geometry of the numerical model is inverted by using accurate seismic traveltime and seabed morphology data with the proposed method, and the inversion results and positioning errors are obtained in scenarios with different seawater velocity values. The RMSEs of the receiver positions are 0.35 m, 0.18 m, 0.19 m and 0.38 m.

As shown in Figure 7, as the absolute error of the seawater velocity increases, the positioning errors of the array geometry inversion results increase, and the positioning errors of the far-end receivers are slightly greater than those of the near-end receivers. The locations of the receivers determined by the proposed method move upward with larger seawater velocity values and downward with smaller seawater velocity values. Moreover, when the seawater velocity is smaller than the true value, jitter distortion occurs in the middle section of the array, with larger seawater velocity errors leading to more severe and wider range jitter. In addition, when the seawater velocity is larger than the true value, the array geometry obtained by inversion is relatively smooth.

As a comparison, we utilize the sea-surface reflection traveltime fitting term $(t_r^{S-cal} - t_r^{S-obs})^2$ to replace the seafloor reflection traveltime fitting term $(t_r^{F-cal} - t_r^{F-obs})^2$ in Equation (6), namely, the sea-surface reflection traveltime positioning method, and invert the array geometry based on the aforementioned seawater velocity error test groups to obtain the corresponding inversion results and positioning errors, as shown in Figure 8. The RMSEs of the receiver positions are 2.98 m, 1.49 m, 1.47 m and 2.93 m. The accuracy of the inversion results is sensitive to the uncertainty in the seawater velocity; that is, the same degree of seawater velocity error leads to greater receiver positioning errors than the proposed method. Therefore, the seawater velocity is a significant factor that seriously affects the precision of the array geometry inversion method utilizing the sea-surface reflection traveltime.

3.2.3 Uncertainty in the seabed morphology

The measured values of the immersion depth and the height above the seabed for the deep-towed source are determined by the depth transducer and altimeter. These two measurements can be used to

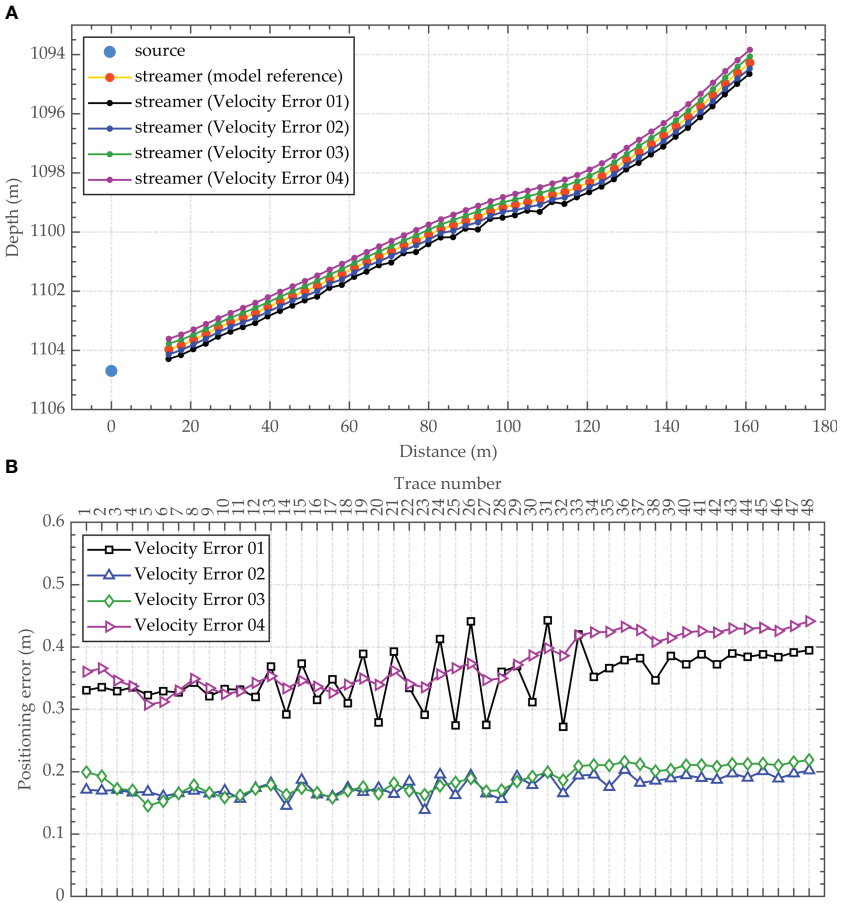

FIGURE 7
Influence of seawater velocity uncertainty on the array geometry inversion results (proposed method). ((**A**) Array geometry inversion results; (**B**) Receiver positioning errors).

obtain the seabed topography at the survey line. The precision of measurement equipment affects the precision of the data; that is, uncertainties in the seabed morphology affect the accuracy of the array geometry inversion results. Given the characteristics of sensor measurement errors, we divide the seabed topography errors into systematic errors and random errors that distort the shape of the input seabed interface to varying degrees.

To evaluate the influence of seabed morphology uncertainties on the accuracy of the array geometry inversion results, four groups of seabed topography data with different error levels are constructed and denoted as Topography Error 01, Topography Error 02, Topography Error 03 and Topography Error 04. Considering the measurement precision of the depth transducer and the altimeter, the systematic errors of the seabed topography data are set to -0.2 m, -0.1 m, 0.1 m and 0.2 m. For random errors, ± 0.2 m Gaussian noise is added to the seabed topography data for Topography Error 01 and Topography Error 04, and ±0.1 m Gaussian noise is added to Topography Error 02 and Topography Error 03. In other words, the overall errors of the seabed morphology are 0.4 m for Topography Error 01 and Topography Error 04 and 0.2 m for Topography Error 02 and Topography Error 03. Since the seabed topography data must be smooth for use in the proposed method, the final seabed morphology used as the input to the proposed array geometry inversion method is shown in Figure 9A. Figures 9B, C show the inversion results and the positioning errors obtained when varying degrees of distortion were introduced in the seabed morphology. The RMSEs of the inversion results for Topography Error 01, Topography Error 02, Topography Error 03 and Topography Error 04 are 0.40 m, 0.20 m, 0.20 m and 0.42 m, respectively.

As shown in Figure 9, the inversion accuracy of the geometric shape of the deep-towed seismic array decreases as the seabed topography data errors increase. When the overall bathymetric topography deviates toward the shallower side, the positions of the receivers shift upward. When the overall bathymetric topography deviates toward the deeper side, the positions of the inverted receivers move downward. Larger seabed morphology errors lead to greater RMSEs for the inversion results. Systematic errors in the seabed topography data are the main influencing factor on the results, which cause the receivers to deviate from their true positions, and the positioning errors of different receivers are similar. However, random errors in the seabed topography data could also distort the geometric shape of the deep-towed seismic streamer, and the distortion from the true shape is positively correlated with the magnitude of the random errors.

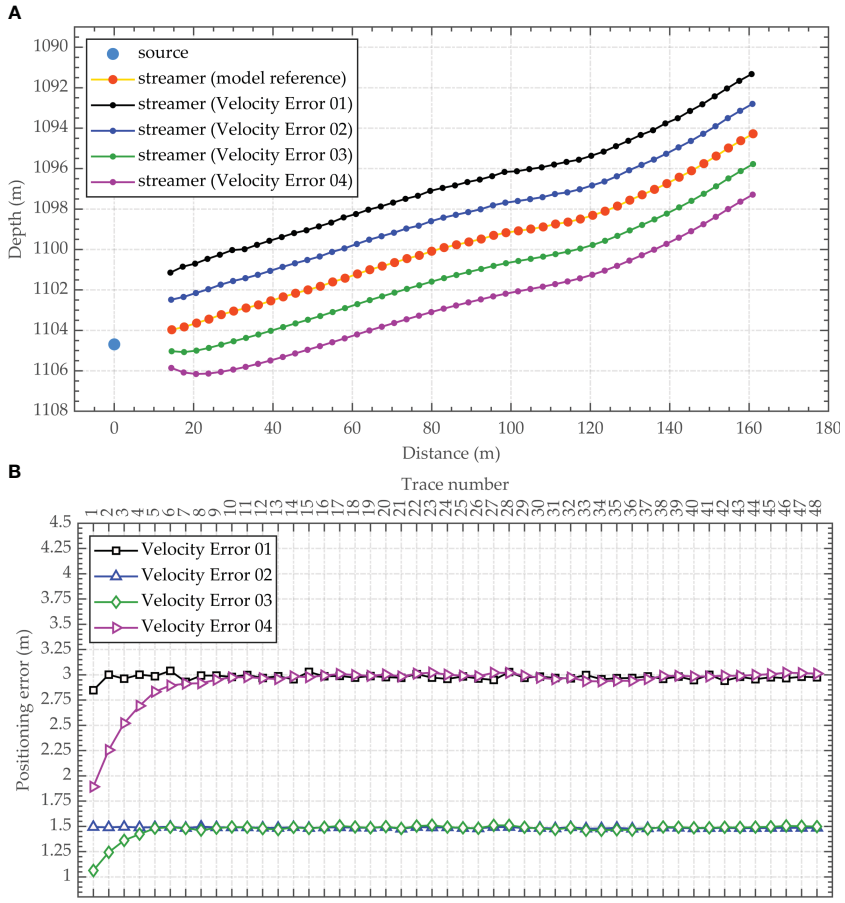

FIGURE 8
Influence of the uncertainty in the seawater velocity on the array geometry inversion results (sea-surface reflection traveltime positioning method). (**(A)** Array geometry inversion results; **(B)** Receiver positioning errors).

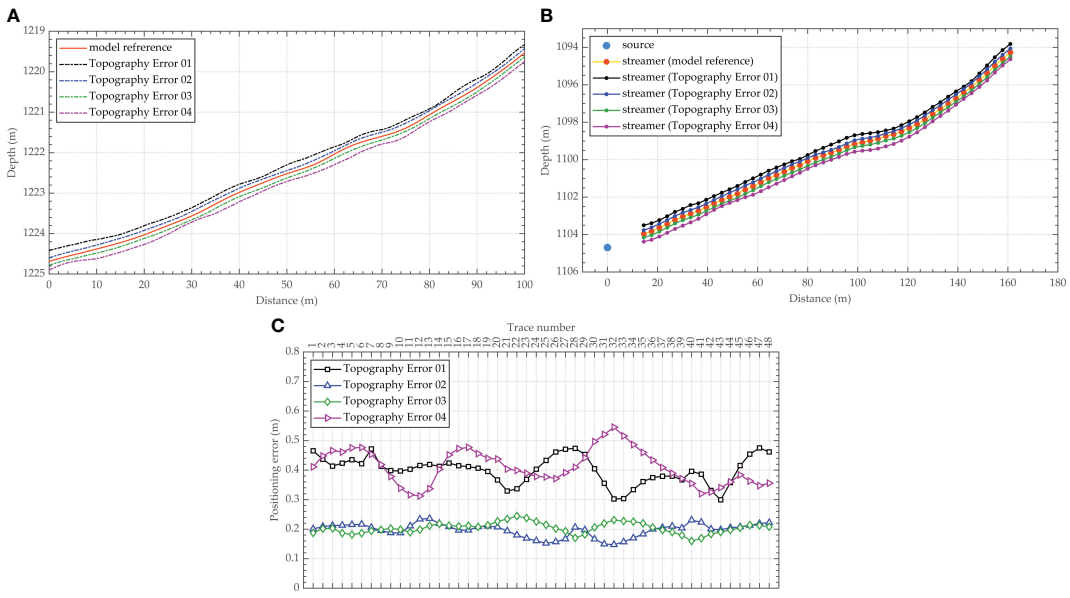

FIGURE 9
Influence of the seabed interface morphology uncertainty on the array geometry inversion results. (**(A)** Seabed interface morphology after smoothing; **(B)** Array geometry inversion results; **(C)** Receiver positioning errors).

3.3 Uncertainty analysis

To comprehensively evaluate the influence of uncertainty sources on the inversion results of the deep-towed array geometry using the method proposed in this paper, we use Monte Carlo uncertainty analysis to quantify the reliability and accuracy of the inversion results. In this case, according to the operating mode of the deep-towed multichannel seismic system and the signal-to-noise characteristics of the collected seismic data, the input data to the inversion process, including the seismic traveltime, seawater velocity, and seabed morphology, are perturbed on the basis of the numerical model presented in Section 3.1. The overall error in the seismic traveltime is set to ±0.25 ms (common phase error of ±0.125 ms and individual error of ±0.125 ms), the error in the seawater velocity is set to ±1 m/s, and the overall error in the seabed morphology is set to ±0.4 m (systematic error of ±0.2 m and random error of ±0.2 m). Accordingly, the method proposed in this paper is utilized to invert the geometric shape of the deep-towed seismic array for a total of 100 input datasets constructed with different perturbations, which have random seismic traveltime errors, seawater velocity deviations and seabed morphology deviations. The Monte Carlo uncertainty analysis results are shown in Figure 10A. As a contrast, we also performed Monte Carlo uncertainty analysis using the same perturbation datasets with the array geometry inversion method based on the sea-surface reflection traveltime discussed in Section 3.2.2, and the results are shown in Figure 10B. Figure 11 shows the statistical results of the RMSE of the array geometry inversion results obtained by the above two methods.

As shown in Figures 10 and 11, the proposed method greatly reduces the uncertainty in the array geometry inversion results for the deep-towed multichannel seismic system, and the RMSE of the receiver location is approximately in the range of 0.1 to 0.3 m. The maximum positioning error of the receivers determined with the proposed method is 0.73 m, and the maximum RMSE is 0.49 m, while the maximum positioning error of the receivers determined with the sea-surface reflection traveltime positioning method is 1.64 m, and the maximum RMSE is 1.54 m. In addition, considering the low SNR of sea-surface reflections in real deep-towed seismic data, waveform distortion could seriously affect the accuracy of the identified waveform starting point, leading to increased common phase errors. The uncertainty analysis results in scenarios closer to the real situation are worse than those shown in Figure 10B.

In summary, the numerical results confirm that the proposed method can effectively solve the problem of high-precision array

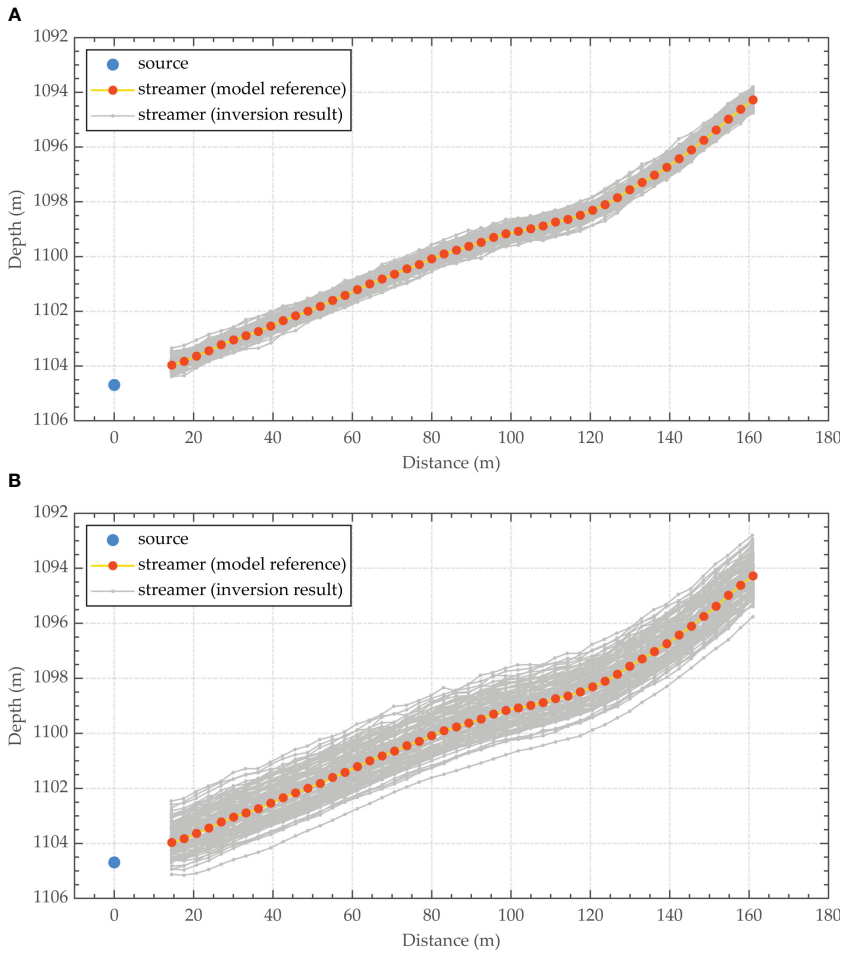

FIGURE 10
Monte Carlo uncertainty analysis results of the numerical model. (**(A)** Proposed method; **(B)** Sea-surface reflection traveltime positioning method).

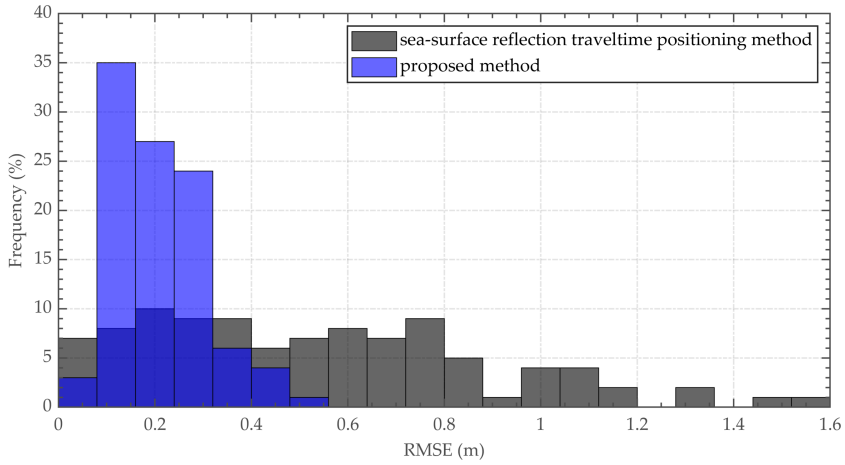

FIGURE 11
RMSE statistics of the Monte Carlo uncertainty analysis results.

geometry inversion for deep-towed multichannel seismic systems in scenarios with complex seabeds. On this basis, influencing factor and uncertainty analyses are used to systemically study the effects of errors in the seismic traveltime, seawater velocity and seabed topography on the array geometry inversion results. Furthermore, the sensitivity of the inversion accuracy to seismic traveltime errors, seawater velocity deviations and seabed topography errors is evaluated. The results of the numerical experiments are of great significance for the improvement of deep-towed multichannel seismic data processing and field investigation methods, so as to obtain high-quality near-bottom acoustic detection data. For example, the determination of the initial seismic waveform point could be appropriately modified to improve the seismic traveltime data, and a self-contained sound velocity profiler could be introduced to obtain continuous and accurate measurements of the seawater velocity. Moreover, the accuracy of the seabed morphology could be verified and evaluated by comprehensively comparing the seabed topography synthesized according to depth transducer and altimeter data and the multibeam bathymetric data extracted by the ultrashort baseline positioning of the deep-towed vehicle.

4 Application to real data

Given the good performance of the proposed method in the numerical experiments, we apply the proposed approach to invert the array geometry of real data acquired during sea experiments with Kuiyang-ST2000 to verify the effectiveness of the proposed method. Furthermore, we evaluate the accuracy and stability of our method through velocity spectra analyses and seismic imaging quality assessments after floating datum correction (He et al., 2009).

The prestack shot gathers in the sea experiments with Kuiyang-ST2000 conducted in 2020 in the Shenhu area in the South China Sea are selected, and the change in the seabed topography at the selected survey line is relatively severe, as shown in Figure 12. The main acquisition parameters of the deep-towed multichannel seismic datasets are as follows: the source energy is 3000 J, shot spacing is 6.25 m, trace spacing is 3.125 m, minimum offset is 14.5 m, trace number is 48, recording duration is 3000 ms, and sampling rate is 8 kHz. We utilize the sea-surface reflection traveltime positioning method discussed in Section 3.2.2, the piecewise approximate slanted interface processing mentioned in Section 3.1, and the method proposed in this paper to invert the array geometry based on the above real data. Then, based on the inverted source-receiver positioning results, we carry out subsequent seismic image processing without residual time difference correction. Figure 13 shows the velocity spectra acquired at the common midpoint (CMP) based on the processed sea trial data. Figure 14 shows the seafloor sedimentary characteristics and structural details in the seismic imaging profile at the selected survey line.

The velocity spectra shown in Figure 13 were obtained in a region in which the seabed morphology undergoes drastic changes. Figures 13A, B show that the hyperbolic features in the seismic reflection records are not well recovered after floating datum correction with the array geometry inversion results obtained by the two methods, resulting in poor focusing of the velocity spectra. However, the velocity spectra obtained by the proposed method is more focused, as shown in Figure 13C, which is conducive to establishing fine velocity structures and improving the seismic imaging quality. The seismic imaging profile shown in Figure 14A was produced using the array geometry inversion technique based on the sea-surface reflection traveltime, while the seismic imaging profiles shown in Figures 14B, C were generated employing the technique based on the seafloor reflection traveltime. Moreover, the result shown in Figure 14B was obtained using the piecewise approximate slanted interface processing strategy, while the result shown in Figure 14C was obtained utilizing the method proposed in this paper. The comparison shows that the seismic imaging profile obtained by the proposed method has the best overall quality, the clearest wave group features, and the best event continuity, particularly in areas in which the seafloor topography varies significantly. As shown in Figure 14A, the array geometry inversion results based on the sea-surface reflection traveltime are more sensitive to input data errors, leading to the worst SNR and

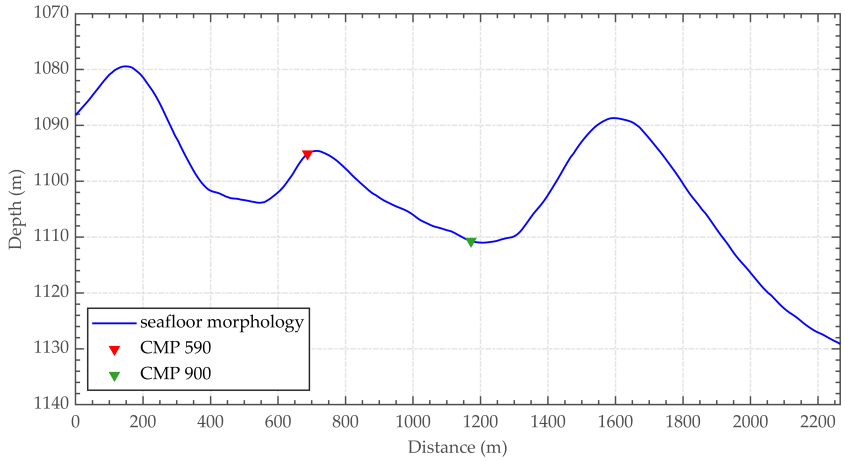

FIGURE 12
Seafloor morphology of sea trial datasets.

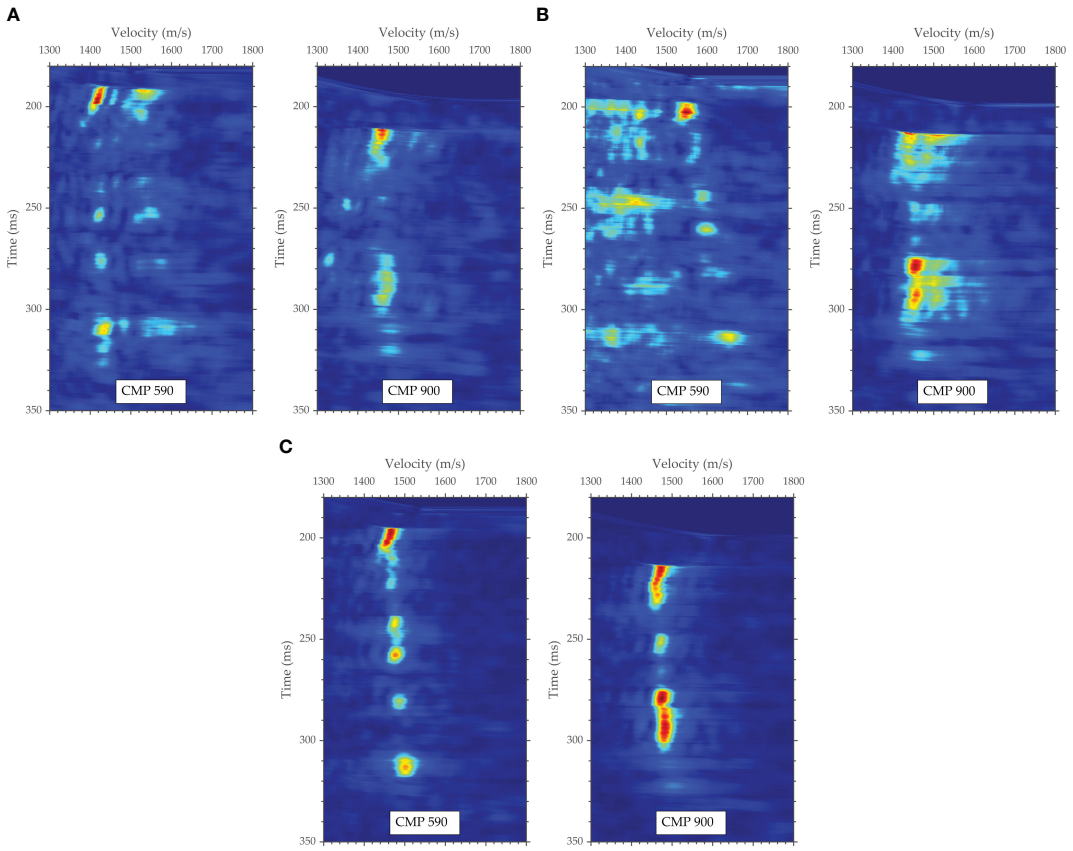

FIGURE 13
Velocity spectra comparison of sea trial datasets corresponding to different inversion methods. ((**A**) Sea-surface reflection traveltime positioning method; **(B)** Piecewise approximate slanted interface processing strategy; **(C)** Proposed method).

resolution in the seismic imaging profile. The seafloor strata shown in Figure 14C have a finer image quality than those shown in Figure 14B, and there is no imaging loss or distortion in the areas with dramatic seabed topography changes, which is compatible with the circumstances presented in Figure 13.

In conclusion, the array geometry inversion method described in this study has greatly improved accuracy, enabling effective detection and imaging of regions with large seabed topographic variations. The proposed method is shown to have incomparable applicability and effectiveness in obtaining exact source-receiver

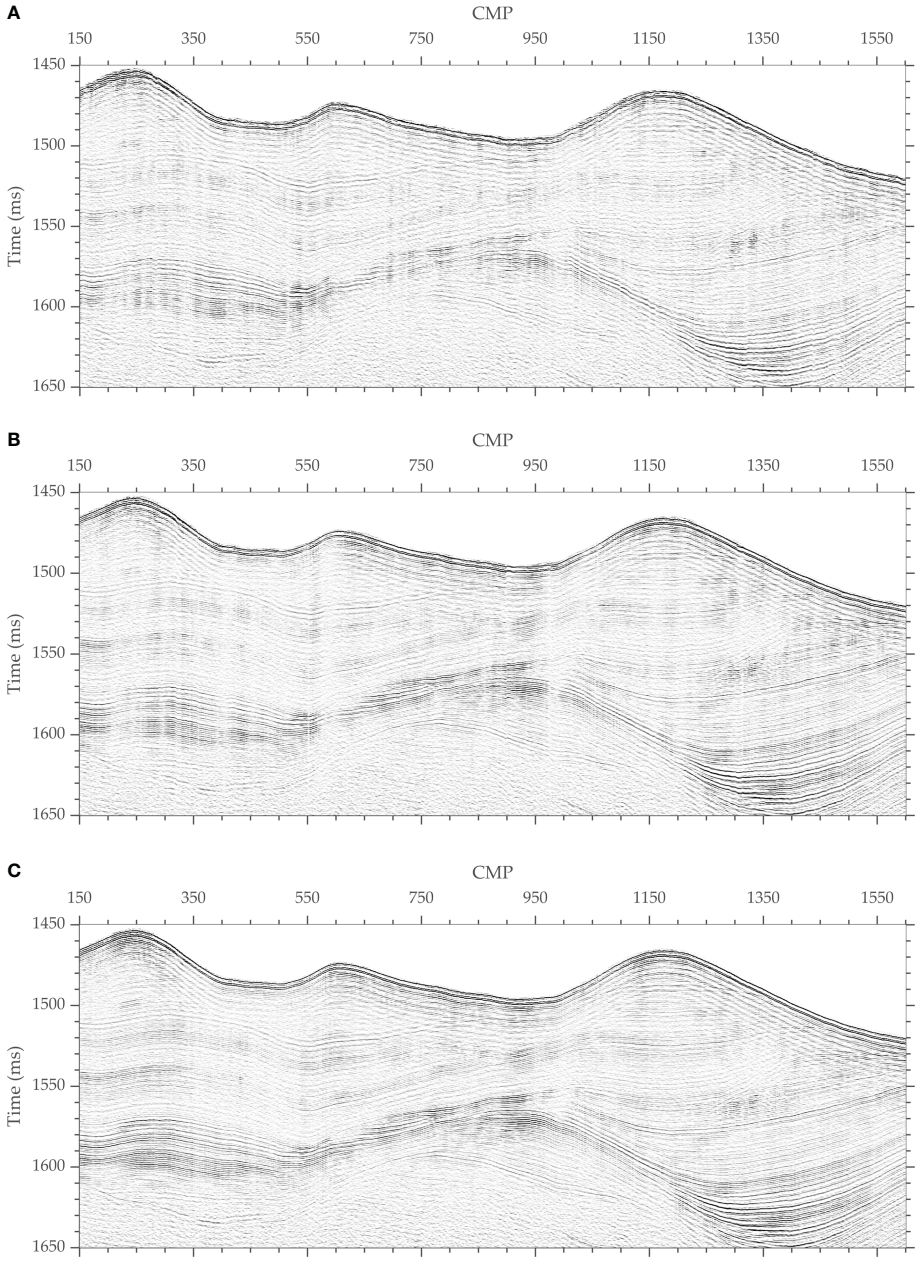

FIGURE 14
Comparison of deep-towed multichannel seismic imaging profiles of sea trial datasets corresponding to different inversion methods. ((**A**) Sea-surface reflection traveltime positioning method; **(B)** Piecewise approximate slanted interface processing strategy; **(C)** Proposed method).

positions for deep-towed multichannel seismic systems. Regardless of the complexity of the seabed morphology, seismic image processing techniques using the source-receiver position data obtained by the suggested method produce fine seismic imaging profiles that clearly and accurately reflect the structural characteristics of sediments. Additionally, despite the limited accuracy of the array geometry inversion associated with the processing strategy based on the piecewise approximate slanted interface, this method could be used because of its high computational efficiency to quickly obtain field seismic processing results in the near-bottom acoustic investigations conducted in flat seabed areas, thereby realizing on-site monitoring of the performance of deep-towed multichannel seismic systems and the quality of the data.

5 Conclusions

We present an array geometry inversion method suitable for complex seafloors to address the challenge of precise source-receiver positioning with deep-towed multichannel seismic systems. Our method does not rely on an initial model, and the objective function of the deep-towed seismic array geometry inversion is built using the shortest path algorithm according to

the traveltimes of direct waves and seafloor reflections. Moreover, the PSO algorithm is used to achieve high-precision inversion of the source-receiver position. The numerical analyses and field data application results verify the effectiveness of the method proposed in this paper, especially its applicability in scenarios with dramatic changes in seabed topography. Moreover, influencing factor and uncertainty analyses are used to evaluate the dependence of the accuracy of the proposed inversion method on seismic traveltime, seawater velocity and seabed morphology errors. The results provide insights for the accuracy and reliability of the proposed geometric shape inversion method for deep-towed seismic arrays in practical applications to meet the requirements of near-bottom acoustic detection for fine imaging of deep-sea seabed strata and precise inversion of geoacoustic parameters. As a future work, the proposed algorithm can be modified to estimate the optimal seawater velocity while recovering the array geometry of deep-towed multichannel seismic systems, and the computational efficiency needs to be improved due to the massive deep-towed seismic data.

Data availability statement

The original contributions presented in the study are included in the article/supplementary material. Further inquiries can be directed to the corresponding author.

Author contributions

JL: Methodology, Visualization, Writing – original draft, Investigation. YP: Conceptualization, Methodology, Writing – review & editing. CL: Investigation, Supervision, Writing – review & editing. LZ: Investigation, Writing – review & editing. XL: Investigation, Writing – review & editing. KL: Conceptualization, Methodology, Supervision, Writing – review & editing. WL: Investigation, Writing – review & editing.

Funding

The authors declare financial support was received for the research, authorship, and/or publication of this article. This study was supported by the special funds of Laoshan Laboratory (No. LSKJ202203604), the National Key Research and Development Program of China (No. 2016YFC0303901), and the National Natural Science Foundation of China (No. 42206226).

Conflict of interest

The authors declare that the research was conducted in the absence of any commercial or financial relationships that could be construed as a potential conflict of interest.

Publisher's note

All claims expressed in this article are solely those of the authors and do not necessarily represent those of their affiliated organizations, or those of the publisher, the editors and the reviewers. Any product that may be evaluated in this article, or claim that may be made by its manufacturer, is not guaranteed or endorsed by the publisher.

References

Breitzke, M., and Bialas, J. (2003). A deep-towed multichannel seismic streamer for very high-resolution surveys in full ocean depth. *First Break* 21 (12), 59–65. doi: 10.3997/1365-2397.21.12.25738

Chapman, N., Gettrust, J., Walia, R., Hannay, D., Spence, G., Wood, W., et al. (2002). High-resolution, deep-towed, multichannel seismic survey of deep-sea gas hydrates off western Canada. *Geophycics* 67 (4), 1038–1047. doi: 10.1190/1.1500364

Colin, F., Ker, S., and Marsset, B. (2020a). Fine-scale velocity distribution revealed by datuming of very-high-resolution deep-towed seismic data: Example of a shallow-gas system from the western Black Sea. *Geophycics* 85 (5), B181–B192. doi: 10.1190/geo2019-0686.1

Colin, F., Ker, S., Riboulot, V., and Sultan, N. (2020b). Irregular BSR: Evidence of an ongoing reequilibrium of a gas hydrate system. *Geophys. Res. Lett.* 47 (20), 1–10. doi: 10.1029/2020GL089906

Gettrust, J., Grimm, M., Madosik, S., and Rowe, M. (1988). Results of a deep-tow multichannel survey on the Bermuda Rise. *Geophys. Res. Lett.* 15 (12), 1413–1416. doi: 10.1029/GL015i012p01413

Gettrust, J., Wood, W., and Spychalski, S. (2004). High-resolution MCS in deepwater. *Leading Edge* 23 (4), 374–377. doi: 10.1190/1.1729234

He, T., Spence, G., Wood, W., Riedel, M., and Hyndman, R. (2009). Imaging a hydrate-related cold vent offshore Vancouver Island from deep-towed multichannel seismic data. *Geophycics* 74 (2), B23–B36. doi: 10.1190/1.3072620

Hutapea, F., Tsuji, T., Katou, M., and Asakawa, E. (2020). Data processing and interpretation schemes for a deep-towed high-frequency seismic system for gas and hydrate exploration. *J. Nat. Gas Sci. Eng.* 83, 103573. doi: 10.1016/j.jngse.2020.103573

Ker, S., Le Gonidec, Y., Marsset, B., Westbrook, G., Gibert, D., and Minshull, T. (2014). Fine-scale gas distribution in marine sediments assessed from deep-towed seismic data. *Geophys. J. Int.* 196 (3), 1466–1470. doi: 10.1093/gji/ggt497

Korenaga, J., Holbrook, W. S., Kent, G. M., Kelemen, P. B., Detrick, R. S., Larsen, H.-C., et al. (2000). Crustal structure of the southeast Greenland margin from joint refraction and reflection seismic tomography. *J. Geophys. Res.* 105 (B9), 21591–21614. doi: 10.1029/2000JB900188

Liu, H. W., Liu, H. S., Xing, L., and Li, Q. Q. (2022). A new method for OBS relocation using direct water wave arrival time and accurate bathymetric data. *Mar. Geophys. Res.* 43 (2), 1–17. doi: 10.1007/s11001-022-09482-0

Marsset, B., Ker, S., Thomas, Y., and Colin, F. (2018). Deep-towed high resolution seismic imaging II: determination of P-wave velocity distribution. *Deep-sea Res. Pt. I* 132, 29–36. doi: 10.1016/j.dsr.2017.12.005

Marsset, T., Marsset, B., Ker, S., Thomas, Y., and Le Gall, Y. (2010). High and very high resolution deep-towed seismic system: performance and examples from deep water Geohazard studies. *Deep-sea Res. Pt. I* 57, 628–637. doi: 10.1016/j.dsr.2010.01.001

Marsset, B., Menut, E., Ker, S., Thomas, Y., Regnault, J. P., Leon, P., et al. (2014). Deep-towed high resolution multichannel seismic imaging. *Deep-sea Res. Pt. I* 93, 83–90. doi: 10.1016/j.dsr.2014.07.013

Pei, Y. L., Wen, M. M., Wei, Z. R., Liu, B. H., Liu, K., and Kan, G. M. (2023). Data processing of the Kuiyang-ST2000 deep-towed high-resolution multichannel seismic system and application to South China Sea data. *J. Oceanol. Limnol.* 41 (2), 644–659. doi: 10.1007/s00343-022-2049-6

Pei, Y. L., Wen, M. M., Zhang, L. C., Yu, K. B., Kan, G. M., Zong, L., et al. (2022). Development of a high-resolution deep-towed multi-channel seismic exploration

system: Kuiyang ST2000. *J. Appl. Geophys.* 198, 104575. doi: 10.1016/j.jappgeo.2022.104575

Riboulot, V., Ker, S., Sultan, N., Thomas, Y., Marsset, B., Scalabrin, C., et al. (2018). Freshwater lake to salt-water sea causing widespread hydrate dissociation in the Black Sea. *Nat. Commun.* 9, 117. doi: 10.1038/s41467-017-02271-z

Rowe, M., and Gettrust, J. (1993). Fine structure of methane hydrate-bearing sediments on the Blake Outer Ridge as determined from deep-tow multichannel seismic data. *J. Geophys. Res.* 98 (B1), 463–473. doi: 10.1029/92JB01706

Sultan, N., Bohrmann, G., Ruffine, L., Pape, T., Riboulot, V., Colliat, J. L., et al. (2014). Pockmark formation and evolution in deep water Nigeria: rapid hydrate growth versus slow hydrate dissolution. *J. Geophys. Res.-Sol. Ea.* 119 (4), 2679–2694. doi: 10.1002/2013JB010546

Talukder, A., Bialas, J., Klaeschen, D., Buerk, D., Brueckmann, W., Reston, T., et al. (2007). High-resolution, deep tow, multichannel seismic and sidescan sonar survey of the submarine mounds and associated BSR off Nicaragua pacific margin. *Mar. Geol.* 241, 33–43. doi: 10.1016/j.margeo.2007.03.002

Walia, R., and Hannay, D. (1999). Source and receiver geometry corrections for deep towed multichannel seismic data. *Geophys. Res. Lett.* 26 (13), 1993–1996. doi: 10.1029/1999GL900402

Wood, W., Gettrust, J. F., and Spychalski, S. (2003). A new deep-towed, multi-channel seismic system. *Sea Technol.* 44 (9), 44–49. doi: 10.1016/S0029-8018(02)00149-X

Wood, W., Hart, P., Hutchinson, D., Dutta, N., Snyder, F., Coffin, R., et al. (2008). Gas and gas hydrate distribution around seafloor seeps in Mississippi Canyon, Northern Gulf of Mexico, using multi-resolution seismic imagery. *Mar. Petrol. Geol.* 25 (9), 952–959. doi: 10.1016/j.marpetgeo.2008.01.015

Zhang, J., and Toksöz, M. N. (1998). Nonlinear refraction traveltime tomography. *Geophysics* 63 (5), 1726–1737. doi: 10.1190/1.1444468

Zhu, X. Q., Wang, Y. F., Yu, K. B., Pei, Y. L., Wei, Z. R., and Zong, L. (2020). Dynamic analysis of deep-towed seismic array based on relative-velocity-element-frame. *Ocean Eng.* 218 (6), 108243. doi: 10.1016/j.oceaneng.2020.108243

frontiers | Frontiers in Marine Science

TYPE Original Research
PUBLISHED 29 November 2023
DOI 10.3389/fmars.2023.1270673

OPEN ACCESS

EDITED BY
Xianbiao Lin,
Ocean University of China, China

REVIEWED BY
Xuebo Zhang,
Northwest Normal University, China
Jiawang Chen,
Zhejiang University, China

*CORRESPONDENCE
Xiangmei Meng
mxmeng@fio.org.cn
Han Sun
sunhan_iori@hotmail.com

RECEIVED 01 August 2023
ACCEPTED 09 October 2023
PUBLISHED 29 November 2023

CITATION
Zou D, Xie J, Meng X, Sun H, Feng J and Kan G (2023) Analysis of the variation of *in situ* seafloor sediments acoustic characteristics with porosity based EDFM. *Front. Mar. Sci.* 10:1270673. doi: 10.3389/fmars.2023.1270673

Analysis of the variation of *in situ* seafloor sediments acoustic characteristics with porosity based EDFM

Dapeng Zou[1], Jin Xie[1], Xiangmei Meng[2,3]*, Han Sun[1]*, Jingchun Feng[4,5] and Guangming Kan[2,3]

[1]Provincial Key Laboratory of Advanced Manufacturing Technology for Marine Energy Equipment, Guangdong University of Technology, Guangzhou, Guangdong, China, [2]Key Laboratory of Marine Geology and Metallogeny, First Institute of Oceanography, Ministry of Natural Resources (MNR), Qingdao, Shandong, China, [3]Key Laboratory of Seafloor Acoustic Detection Technology and Application, Qingdao (Preparatory), Qingdao, Shandong, China, [4]School of Ecology, Environment and Resources, Guangdong University of Technology, Guangzhou, China, [5]Research Centre of Ecology & Environment for Coastal Area and Deep Sea, Southern Marine Science and Engineering Guangdong Laboratory, Guangzhou, China

Numerous factors influence the acoustic characteristics of seafloor sediments, necessitating a comprehensive study that combines theoretical analysis, laboratory measurements and *in situ* measurements to support acoustic prediction and inversion. In this study, a porosity-based effective density fluid model (P-EDFM) is established to analyze the variation of acoustic properties with the porosity of seafloor sediments. On the biases of P-EDFM, the attribute of measured sound velocity and acoustic attenuation coefficient of seafloor sediment in Series 9B of the SAX99 was well interpreted within the frequency range of 25-100 kHz. The *in situ* measured sound velocity ratio was well predicated by the P-EDFM in the East China Sea and Yellow Sea. It reveals that the *in situ* sound velocity ratio decreases with increasing bulk porosity and with decreasing bulk density. The scattering and differences in the acoustic attenuation coefficient measured *in situ* in seafloor sediments are found to be greater than those observed for sound velocity. After considering the influence of temperature in the P-EDFM, the prediction of *in situ* sound velocity aligns well with the measured dataset. While, the acoustic attenuation coefficient exhibits an inflection point, increasing initially and then decreasing with changes in porosity, similar to the observed pattern in Hamilton's observation and estimation. By incorporating temperature and frequency influences, the *in situ* measurements of sound velocity of seafloor sediments are corrected into laboratory sound velocities by using the P-EDFM. The result reveals the sediment samples' sampling and transmitting process has a much greater impact on the sound velocity of sandy sediment in the East China Sea compared to muddy sediment. Overall, P-EDFM can predict the *in situ* sound velocity and sound attenuation coefficient under different temperatures and frequencies, with a lower prediction error for sound velocity compared to sound attenuation coefficient.

KEYWORDS

sound velocity, porosity, seafloor sediment, *in situ* measurement, EDFM

1 Introduction

The sound velocity and acoustic attenuation coefficient of seafloor sediments are crucial parameters in the fields of underwater acoustics, geo-acoustics, and sedimentary acoustics (Kim et al., 2018a; Buckingham, 2020; Yang and Jackson, 2020). They determine wave speed, acoustic impedance, path and distance of sound wave propagation. They are closely related to the sediment physical and mechanical properties, as well as to the measurement methods and environmental conditions. Currently, three primary methods are employed for obtaining the acoustic properties of seafloor sediments: geoacoustic inversion, laboratory acoustic measurement, and *in situ* acoustic measurement (Tao et al., 2006; Jackson and Richardson, 2007; Liu et al., 2019; Zou et al., 2022). Due to these methods differing in terms of measurement technology, frequency and environmental conditions, challenges arise on how to effectively apply different methods, diverse measurement datasets, and various fitting empirical equations from different sea areas. As *in situ* acoustic measurement technology improves, a series of *in situ* measurements were conducted within the frequency range of 1 kHz to 50 kHz (Kim et al., 2018b; Megan et al., 2019; Li et al., 2020; Wang et al., 2020; Wang et al., 2023) to establish a connection between high-frequency laboratory acoustic measurements ranging from 30 kHz to 1 MHz (Henfer et al., 2009; Zimmer et al., 2010; Wang et al., 2018b; Tang et al., 2019) and low-frequency geoacoustic inversion ranging from 0.1 Hz to 1 kHz (Ballard et al., 2018; Li et al., 2019; Belcourt et al., 2020). *In situ* acoustic measurement causes significantly less disturbance to seafloor sediments than laboratory acoustic measurement but with the complex process and long operation period. Furthermore, to obtain the physical characteristics of seafloor sediment and acoustic characteristics across a wider frequency range, it is necessary to collect sediment samples and transport them to the laboratory for measurement and analysis (Buckingham and Richardson, 2002; Kim et al., 2018c), conduct controlled environmental state measurement research (Kan et al., 2019; Zhou et al., 2019; Zou et al., 2021), and perform acoustic characteristic measurements at various frequencies (Zimmer et al., 2010; Yu et al., 2017; Wang et al., 2018b). The aforementioned research emphasizes the significance of factors such as physical properties of seafloor sediments, measurement frequency and measurement environmental state in understanding the differences in acoustic properties of seafloor sediments. These factors play a crucial role in comparing, applying, and enhancing the three marine acoustic detection methods.

Considering the influence of numerous factors on the acoustic characteristics of seafloor sediments, there is a need to minimize the impact of measurement methods by promoting *in situ* acoustic measurements. *In situ* measurements are highly valuable, but they still have limitations when it comes to complex marine environments, deep-layered detection and diverse wave propagation states. Laboratory measurements, on the other hand, are widely employed to conduct simultaneous physical and acoustic measurements (Hou et al., 2015; Wang et al., 2023), especially when precise control over real seafloor sediment samples is required. However, even with state-controlled measurement techniques, laboratory measurements alone do not provide a complete understanding of the different acoustic characteristics of seafloor sediments. By combining theoretical model calculations and analysis with limited *in situ* acoustic measurements and laboratory acoustic measurements, it becomes possible to obtain the general regularity and the specific differences of acoustic characteristics of various seafloor sediments across broad seafloor areas. Among of the various theories and models available (Jackson and Richardson, 2007; Yu et al., 2017; Wang et al., 2018b), the grain shearing model (GSM) (Buckingham, 1998) and the effective density fluid model (EDFM) (Williams, 2001) are widely used for analyzing seafloor sediment acoustics. The GSM effectively explains sound speed dispersion and attenuation coefficients of seafloor sediments observed in the SAX99 (Buckingham and Richardson, 2002). It also reveals the relationships between porosity and the physical/acoustic properties of seafloor sediments (Buckingham, 2005). However, it is seldom employed to analyze the influencing factors of sediment physical parameters and environmental state. On the other hand, the EDFM can well explain dispersion and attenuation characteristics observed in the SAX99 (Williams et al., 2002) and at Jiaozhou Bay (Wang et al., 2018b). It can also well reveal the influence of the environmental sates on the sound velocity (Zou et al., 2015; Kan et al., 2019), as well as the relationship between sound velocity and porosity (Zou et al., 2018). However, even as a simplified model based on the Biot theory (Biot, 1956a, 1956b), the EDFM still involves numerous parameters and challenges associated with difficult-to-measure parameters (Williams et al., 2002; Jackson and Richardson, 2007). Schock (2005) proposed an approach based on porosity and average particle size to express complex parameters like tortuosity factor, permeability, and pore size, aiming to invert the acoustic physical properties of seafloor sediments using the Biot model and Chirp sonar measurement reflection loss. Since several parameters in the theoretical model are related to the representative physical parameter of porosity, expressing challenging-to-measure parameters in terms of porosity can reduce measurement errors and value-selected errors. This approach leads to simplified model calculation relationships.

This research aims to elucidate the mechanisms, changes and influences on the acoustic characteristics of seafloor sediments in their true *in situ* state. To achieve this, a porosity-based effective density fluid model (P-EDFM) is established to investigate the influence of *in situ* acoustic characteristics of seafloor sediments and their associated influencing factors. Using P-EDFM, the impact of changes in porosity and density on the *in situ* sound velocity ratio of the seafloor sediment is analyzed, along with their relationships. Furthermore, the relationships between *in situ* sound velocity, acoustic attenuation coefficient, and porosity in different sea areas are explored. The study also addresses the influence of temperature and frequency dispersion on sound velocity and proposes a correction method to investigate the disparities between the *in situ* acoustic measurement and the laboratory acoustic measurement. The findings of this research provide valuable support for acoustic prediction, geoacoustic inversion, and underwater detection.

2 Principle of P-EDFM

EDFM adopts effective elastic modulus K_{eff} and effective density ρ_{eff} establishes the expression of sound velocity (m/s) and sound attenuation coefficient (dB/m) as follows:

$$c_p = \mathrm{Re}\left[\sqrt{K_{eff}/\rho_{eff}}\right] \tag{1}$$

$$\alpha_p = 8.686{*}\omega{*}\,\mathrm{Im}\left[\sqrt{\rho_{eff}/K_{eff}}\right] \tag{2}$$

$$K_{eff} = ((1-n)/K_g + n/K_w)^{-1} \tag{3}$$

$$\rho_{eff} = \rho_w \frac{\alpha(1-n)\rho_g + n(\alpha-1)\rho_w + i(n\rho_s F\eta/\rho_w\omega k)}{n(1-n)\rho_g + (\alpha-2n+n^2)\rho_w + i(nF\eta/\omega k)} \tag{4}$$

Where, η is the viscosity of the pore water, k is its permeability, and α is the tortuosity. K_g and K_w are the bulk modulus of solid grains and the bulk modulus of pore water, respectively, and n is the bulk porosity of the sediment. ρ_w, ρ_g, *and* ρ_s are the bulk densities of the pore water, solid grains, and sediment, respectively, $\rho_s = n\rho_w + (1-n)\rho_g$. i is the imaginary part factor of the complex number, Re[] and Im[] represents the real part and imaginary part of the measurement result. F is a dynamic viscosity correction factor (Biot, 1956b; Williams, 2001), which is related to the detected angular frequency ω, pore size a, porosity n, pore water density ρ_w.

The relationship between tortuosity and porosity (Boudreau, 1996) is as follows,

$$\alpha = \sqrt{1 - 2\ln(n)} \tag{5}$$

The permeability expression (6a) is the correction of Hovem and Ingram formula by Schock (2005). According to the previous model analysis and data process, here the correction formula for the permeability can be written as Eq. (6b).

$$k = \frac{1}{180\sqrt{10}} \frac{d^2 n^3}{(1-n)^2} \tag{6a}$$

$$k = \frac{n}{180(1-n)} \frac{d^2 n^3}{(1-n)^2} \tag{6b}$$

Based on the linearization transformation of the average particle diameter d (unit: mm) and the porosity n of Schock (2005), an E1 formula can be obtained as

$$d = 2^{5.5315-18.44n} \quad 0.299 < n < 0.841 \tag{7}$$

The EDFM considering the porosity relationships of equations (5)-(7) is defined as porosity based EDFM (P-EDFM). Compared with the 9-parameter EDFM, P-EDFM has six parameters, the reference value of particle bulk modulus K_g is 36GPa with a referred range of 0.7~57GPa (Williams et al., 2002; Jackson and Richardson, 2007). Porosity n and the density of solid particles of seafloor sediment ρ_g can be directly measured. The density ρ_w, viscosity η, and the bulk elastic modulus of pore seawater K_w can be calculated directly by applying the seawater state equation formula (Jackson and Richardson, 2007) using the *in situ* measured environmental state parameters.

The analysis of the measurement data of seafloor sediment in Series 9B of SAX99 was performed using the porosity value of 0.37 and a particle volume elastic modulus of 36 GPa, as provided by Buckingham (2002). The laboratory standard measurement temperature conditions (23°C, 1 atm.) were considered, and the P-EDFM was employed for calculations. Equations (6a) and (6b) were compared, and Figure 1 demonstrates their ability to simultaneously explain the frequency dispersion characteristics of sound velocity within the range of 25-100 kHz and the relationships between the acoustic attenuation coefficient and frequency for the sandy seafloor sediment in Series 9B. However, certain calculation errors were still present in both sound velocity and acoustic attenuation coefficient. To account for the measured porosity

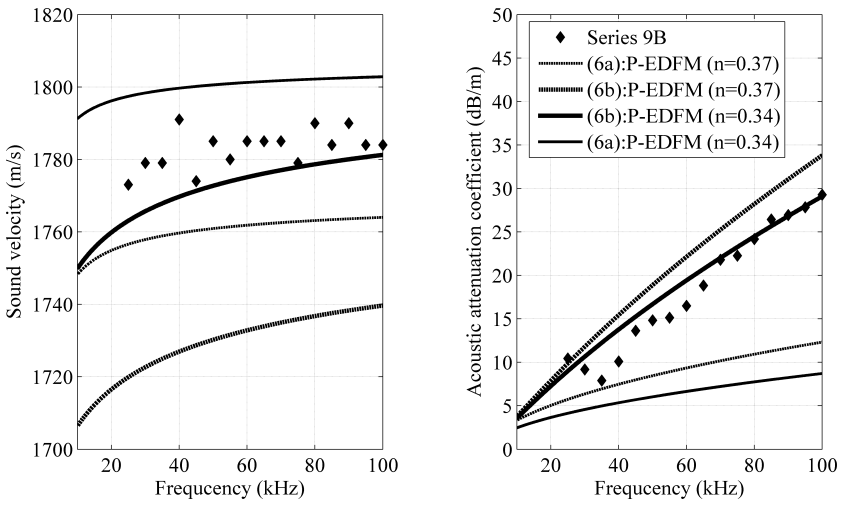

FIGURE 1
The acoustic characteristics of Series 9B in SAX99 (Buckingham and Richardson, 2002) based on P-EDFM.

ranges reported in the same experimental area of SAX99 (0.359-0.387, 0.34-0.48, and 0.41-0.52 for different measurement methods) (Williams et al., 2002), the lower limit value of 0.34 was selected for comparison, as shown in Figure 1. This selection reduced the errors between the model-calculated sound velocity and acoustic attenuation coefficient and the measured data, resulting in a higher precision in explaining the measured acoustic characteristic in Series 9B. Eq. (6b) provided higher precision compared to Eq. (6a). Consequently, the P-EDFM successfully explain the sound velocity and attenuation coefficient of Series 9B in SAX99 using 6 parameters, supporting the validity of acoustic prediction and inversion based on theoretical models derived from Biot Theory.

3 Relationships between *in situ* sound velocity ratio and porosity, density

The *in situ* sound speed at 17 representative sites was measured in the East China Sea (ECS) during spring voyage in 2021, funded by the National Natural Science Foundation of China Open Research Cruise (Cruise No. NORC2021-02+NORC2021-301). The seafloor sediment samples include various sediment types, such as sand, sandy silt, silt, clayey silt, and silty clay. The *in situ* sound speed ratio and physical parameters are listed in Table 1.The depth of the ECS generally does not exceed 100 m. The temperature of the bottom seawater varies at different depths and during different seasons. For instance, the temperature at a depth of 60 m is approximately 3.6°C higher compared to that at 90 m. And the bottom water temperature in autumn is around 4.7°C higher than that in spring. Regarding the *in situ* and laboratory measurements of seafloor sediments in the ECS, environmental factors primarily change in temperature, with the pressure change being neglected (considering 1 MPa for 100 m, which has a minimal impact of about 1‰ on the sound velocity of seawater and seafloor sediments). These sediment types exhibit porosity ranging from 0.384 to 0.692, and sound velocity ratio ranging from 0.974 to 1.070 (Wang et al., 2023). These values align with the measurement datasets recorded on the continental shelf and continental slope of the North Pacific Ocean (Hamilton, 1971), the datasets in the South China Sea (SCS) (Wang et al., 2018a; Liu et al., 2019) and the datasets in the Yellow Sea (YS) (Kan et al., 2011; Liu et al., 2019). By utilizing the sound velocity ratio to analyze the relationships between acoustic and physical characteristics of different seafloor sediment types, the influence of *in situ* temperature variations at different measurement stations can be mitigated (Kan et al., 2019; Zou et al., 2021). Moreover, the wide ranges in porosity, density, and sand content in Table 1 also provide indicators of the scattering and complexity of seafloor sediment acoustic properties. Regression fitting reveals the following empirical relationships between the *in situ* sound velocity ratio R_v and porosity n and density ρ_s in the ECS (Wang et al., 2023) as follows:

$$R_v = 0.8394n^2 - 1.212n + 1.4108 \quad R^2 = 0.8559 \tag{8}$$

$$R_v = 0.2397\rho_s^2 - 0.6425\rho_s + 1.3891 \quad R^2 = 0.8621 \tag{9}$$

The relationship between the average particle diameter d (unit: mm) and porosity n of the ECS samples is expressed as Eq. (10). The P-EDFM with Eq. (10) being applied is called ED group P-EDFM. The E1 group P-EDM with Eq. (7) is used as a comparison.

$$d = 2^{2.2775-14.732n} \quad R^2 = 0.8968 \quad 0.384 \le n \le 0.692 \tag{10}$$

Based on the results illustrated in Figure 2, the calculation curve of the ED group P-EDFM exhibits high consistency with the measured values in the ECS and closely aligns with the empirical relationships expressed by Eq. (8). Although the E1 group P-EDFM does not exhibit as high interpretation accuracy as the ED group, it effectively explains the variations of *in situ* acoustic values with respect to porosity. The *in situ* dataset in the YS is taken as a comparison, as shown in Figure 2. The relationships between the *in situ* sound velocity ratio and porosity in the ECS and YS slightly differ, and generally conform to the rule that the *in situ* sound velocity ratio decreases with increasing porosity. Porosity is a comprehensive parameter that plays a crucial role in characterizing the physical and acoustic characteristics of seafloor sediments. Density, which is closely related to porosity, is another important parameter for describing the physical and acoustic characteristics of seafloor sediments. The relationship between density and the *in situ* sound velocity ratio in the two sea areas exhibits similarity. P-EDFM also can explain the trend of the *in situ* sound velocity ratio increasing with increasing density. Additionally, the interpretation accuracy of the sound velocity ratio and density obtained by ED group P-EDFM closely matches the empirical relationships expressed by Eq. (10), surpassing the calculation curve of E1 group P-EDFM, as depicted in Figure 2.

The above observations indicate that the physical and acoustic characteristics of seafloor sediments exhibit both similarities and regularities across different sea areas, albeit with minor numerical differences. Through the application of the P-EDFM with the ED group's fitted empirical equation, the interpretation accuracy of the ECS's measurement data surpasses that of the E1 group, further

TABLE 1 Characteristics of 17 *in situ* acoustic measurement samples of seafloor sediments in the ECS.

Items	Porosity	Density (g/cm^3)	Sand content (%)	Sound velocity ratio
Maximum	0.692	2.01	80.50	1.070
Minimum	0.384	1.53	0.30	0.974
Average ± Standard deviation	0.526±0.114	1.80±0.18	36.18±34.63	1.016±0.036

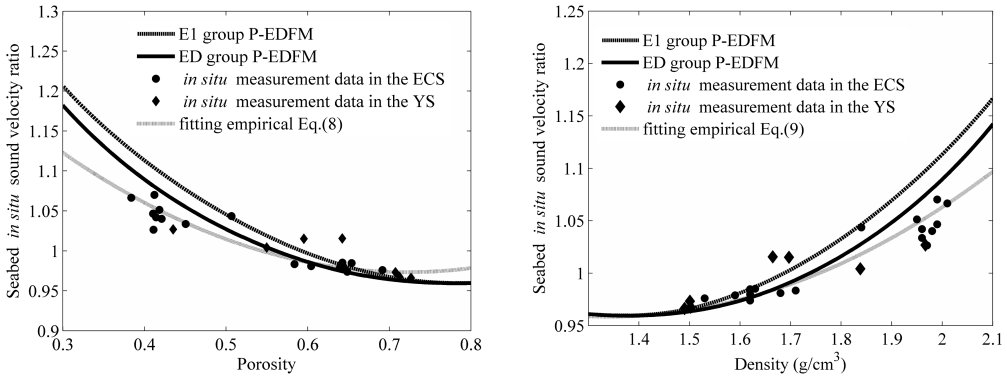

FIGURE 2
Relationships between *in situ* sound velocity ratio and porosity/density analyzed by P-EDFM.

confirming the overall similarity exists in the empirical relationships of physical and acoustic characteristics of seafloor sediments, but numerical differences exist among different sea areas. Therefore, in the application, on the one hand, the empirical relationships should be applied with the fitting formula obtained from the domestic sea area as far as possible; on the other hand, this difference also reveals the slight variations and scattering in the seafloor sediment characteristics of different sea areas.

Based on the analysis provided, it is evident that P-EDFM can effectively explain the variation of sound velocity and porosity measured in the laboratory, as well as the relationships between sound velocity ratio and porosity and density measured in situ. However, porosity, as a macro parameter, can only partially represent the general trends and common differences in seafloor sediments, and it may not fully capture the individual differences among sediment samples. The heterogeneity and anisotropy of factors such as pore size, pore channel connectivity, particle size, and particle shape within individual samples can lead to differences in density, elastic modulus, and sound transmission losses along the actual acoustic wave propagation path. These variations contribute to the disparities and scattering observed in the acoustic characteristics among different seafloor sediment samples. The scattering of the *in situ* sound velocity ratio in different sea areas can be accurately predicted by adjusting and optimizing parameters such as permeability, tortuosity factor, or pore size in the EDFM. However, P-EDFM limits the adjustment of these parameters and does not allow for arbitrary optimization. Although it may be challenging to accurately explain the specific differences among each seafloor sediment sample, P-EDFM can be applied to describe the overall trends of the porosity/density and acoustic characteristics of seafloor sediments, eliminating the ambiguity and subjectivity associated with manually adjusting or optimizing. Additionally, the establishment and application of empirical relationships usually should be restricted with the influence of environmental state and measurement frequency both in laboratory and in situ. Compared with the empirical relationships, the prediction and calculation of P-EDFM consider the effects of environmental conditions and measurement frequency and eliminate their influences to some extent.

4 *In situ* acoustic characteristics of seafloor sediments and its influencing factors

4.1 *In situ* acoustic characteristic analysis based on P-EDFM

Physical parameters, such as porosity and density of seafloor sediments, are typically obtained in laboratory conditions at room temperature. However, variations in seasons and geographical locations can introduce temperature differences in these physical parameters. To account for this, measurements are often standardized or assumed to be at 23°C. *In situ* measurements of seafloor sediment in the YS and ECS typically utilize similar methods and are conducted at a main frequency of 30-33 kHz (Liu et al., 2019) using similar methods. The dataset for *in situ* measurements reveals that the temperature of bottom seawater ranges from 8.5-17.9°C. Figure 3 illustrates the relationships between porosity and sound velocity and attenuation at different *in situ* temperatures. This analysis takes into account the impact of temperature, which is a significant factor to consider when comparing results obtained in different seasons and at various seafloor depths. Currently, there is no effective method to correct for the temperature effect on the sound attenuation coefficient, as the velocity ratio correction method is used specifically to address the impact on sound velocity (Zou et al., 2021).

In the *in situ* acoustic measurements conducted in the YS and ECS, the temperatures were 10.00±0.91°C and 16.96±1.06°C, respectively. The YS exhibited a lower average temperature and a smaller temperature scattering. There was a slight difference and small scattering in the *in situ* sound velocity data obtained from the two sea areas, with 0.095±0.026 in the YS and 1.016±0.036 in the ECS. But there were observed significant differences and large scattering in the *in situ* sound attenuation coefficient with 6.29±2.37 dB/m in the YS and 4.24±3.87 dB/m in the ECS. For sediments with the same porosity, the sound attenuation coefficient of sediments was generally higher in the YS compared to the ECS.

The influences of different *in situ* temperature and its range were taken into account of the actual *in situ* measurement data in

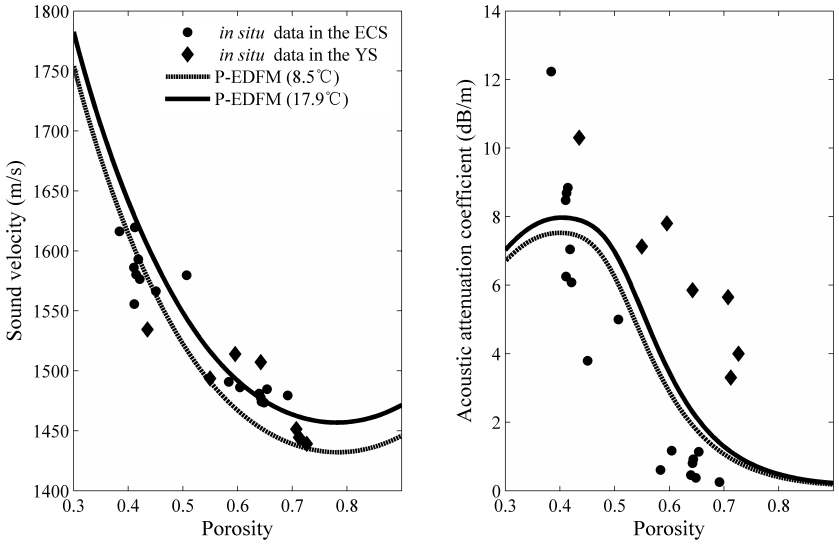

FIGURE 3
Calculation of the relationships between *in situ* sound velocity/acoustic attenuation coefficient and porosity of seafloor sediment based on P-EDFM within *in situ* temperature range.

the two sea areas in the ED group P-EDFM, as shown in Figure 3. Within the temperature range, the *in situ* sound velocity exhibits good conformity in measurement with the P-EDFM prediction, while the interpretation of the *in situ* acoustic attenuation coefficient varies significantly. An inflection point is observed at porosity of approximately 0.45, which aligns with previous observations and estimations made by Hamilton (1980) and Liu et al. (2019). While this analysis offers theoretical model support for the *in situ* measurement dataset, it does not effectively explain the scattering characteristics of the acoustic attenuation coefficient for porosities around 0.4, which are 10dB/m larger than the theoretical prediction. The scattering and measurement error of the acoustic attenuation coefficient may be larger than those of the sound velocity of seafloor sediments. This highlights the need for more comprehensive discussions and verifications regarding measurement accuracy and the factors influencing acoustic attenuation. Therefore, considering environmental factors, conducting more extensive and in-depth measurements of the acoustic attenuation coefficient will yield more comprehensive datasets. These data will help to clarify the *in situ* acoustic attenuation characteristics of seafloor sediments and test the applicability of P-EDFM.

4.2 Difference of sound velocity characteristics between *in situ* measurement and laboratory measurement

During the spring survey in the ECS, laboratory measurements were conducted on 17 samples to determine the sound velocity following the *in situ* measurement. As shown in Figure 4, the measured sound velocity in the laboratory was found to be higher than the *in situ* sound velocity. Among the 17 samples, the absolute difference between the laboratory and *in situ* sound velocities was much larger for the 9 sandy samples compared to the other 8 muddy samples (ie. silty and clayey sediments). The original *in situ* measurements at each station in the ECS had similar depths and temperatures, with an average *in situ* measurement temperature of 16.96±1.06°C and a measurement frequency of 33 kHz. In the laboratory, the collected samples were measured at a temperature of 22.0°C and a frequency of 100 kHz. As mentioned previously, the influence of pressure factors can be disregarded due to the shallow water depth. Therefore, apart from the disturbances caused by transitioning from the *in situ* to the laboratory measurements, differences in temperature and frequency also contribute to the influence of dispersion, temperature effect, and sample disturbance on the physical and acoustic properties of seafloor sediments.

A fixed sound velocity ratio correction method is employed to adjust the *in situ* temperature sate to the laboratory temperature state (Kan et al., 2019; Zou et al., 2021). The temperature-corrected *in situ* sound velocity values, compared with the laboratory-measured sound velocities, are presented in Figure 4. Even the temperature correction eliminates the influence of temperature differences between the seafloor *in situ* and laboratory measurements, significant differences still exist in the original measurements of sandy seafloor sediment samples.

Due to lacking measured values of sound velocity variations at different frequencies in the same state, theoretical calculations are used to obtain the theoretical sound velocity ratio, which is then applied to frequency correction. Only general regularities are examined, without conducting specific correction analyses for each sample. Each porosity of the 17 samples is inputted into the P-EDFM to obtain the theoretical sound velocities at 100 kHz and 33 kHz respectively. The theoretical sound velocity ratio, R_{ft}, is then obtained, based on that all the original *in situ* measurement values

10.3389/fmars.2023.1270673

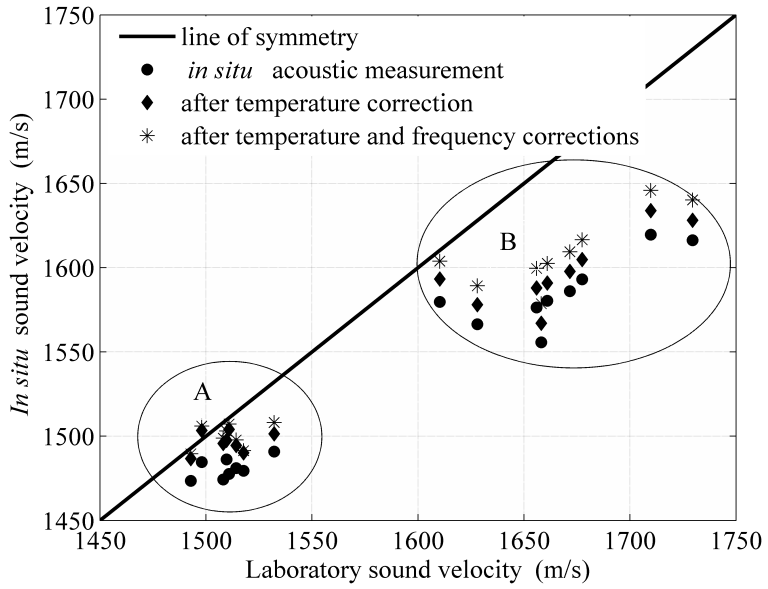

FIGURE 4
Comparison of sound velocity measured *in situ* and in laboratory before and after temperature correction and frequency correction.

are corrected to the laboratory measurement values using the following formula:

$$R_{ft} = c_{pf1}{}' / c_{pf2}{}' \tag{11}$$

$$R = k_f R_{ft} \tag{12}$$

$$c_{pf1} = R \times c_{pf2} \tag{13}$$

Where, R_{ft} is the theoretical sound velocity ratio at two frequencies of f_1 and f_2, where f_1 corresponds to high frequency of 100 kHz and f_2 corresponds to low frequency of 33 kHz. $c_{pf1}{}'$ and $c_{pf2}{}'$ are the theoretical calculated sound velocities of high and low frequencies respectively. k_f is the correction coefficient of sound velocity ratio at different frequencies, which represents the difference between theoretical calculation and actual measurement, where the value here selects 1. c_{pf1} and c_{pf2} are respectively the sound velocity of seafloor sediment after frequency correction and the sound velocity of seafloor sediment under the actually measured frequency state. Here c_{pf2} is the *in situ* measured sound velocity at 33 kHz.

After frequency corrections based on equations (11)-(13), the *in situ* measured sound velocity of muddy sediments closely matched the laboratory measured sound velocity, as depicted by type A in Figure 4. However, sediments primarily composed of sandy material still exhibit significant differences, as shown by type B in Figure 4. The physical properties of the sediments in the two zones are presented in Table 2. The two types exhibit significant variations in the porosity and composition content even there are from the same sea area. Considering the substantial difference in sandy particle percentage and the sound velocity variations after temperature and frequency corrections between the two types, it becomes evident that sandy sediments are more susceptible to disturbance due to their loose particle packing and are more affected by perturbations. The pore water in sandy sediments is more likely to flow, and the loose framework is prone to deformation and reconstruction, resulting in more significant errors caused by disturbance effects. Compared to sandy sediments, muddy sediments are denser, more viscous and firmly fixed in the sampling pipe. As a result, the disturbance effect is relatively weaker, making corrections easier between the *in situ* and laboratory states. This observation aligns with the fact that sampling sandy sediments is challenging due to their susceptibility to seawater erosion, vibration, and detachment, making it difficult to obtain more effective and intact samples. Li et al. (2013) highlighted that the processes of sample collection, transportation, and truncation have an impact on *in situ* and laboratory measurements. However, due to the difficulty in qualitatively and quantitatively analyzing patterns, these processes are typically handled with great care to minimize disturbances in the samples. Specifically, efforts are made to measure the samples as soon as possible after collection to reduce disturbances resulting from subsequent transportation, partitioning, and other procedures. Hence, sandy sediments are more suitable for *in situ* measurements or *in situ* simulation measurement experiments to

TABLE 2 Characteristics of type A and B of 17 *in situ* samples of seafloor sediments in ECS.

Parameter	Average ± Standard deviation	
	8 samples of type A	9 samples of type B
porosity	0.638±0.001	0.425±0.001
silt and clay content (%)	98.89±0.94	32.66±8.68

reduce influences of sampling disturbances. This enables the further correction of measured data more precisely to apply for other various measurement environments and frequency states.

5 Conclusions

This study employed P-EDFM to investigate the influence of physical parameters, including porosity and density, as well as temperature environment, and measurement frequency on the *in situ* sound velocity and sound attenuation coefficient of seafloor sediments. P-EDFM offers a less parametric theoretical model for analyzing the acoustic and physical properties of seafloor sediments. P-EDFM elucidates the relationships between the *in situ* sound velocity ratio, acoustic attenuation coefficient, and porosity of seafloor sediments. It also analyzes the influence of temperature and frequency dispersion, providing a novel approach for evaluating, predicting, correcting and inverting acoustic and physical property parameters of seafloor sediments. These advancements offer convenience and contribute to the progress in this field of research. Some meaningful conclusions are drawn as follows:

(1) The sound velocity ratio of seafloor sediments and bottom seawater measured *in situ* in the ECS and YS exhibits decreases with increasing porosity and with decreasing density. This characteristic can be well explained by P-EDFM.

(2) The scattering and variation of the *in situ* acoustic attenuation coefficient of seafloor sediments are significantly greater than those observed in the sound velocity. Based on the ED group P-EDFM calculation, the interpretation of the *in situ* sound velocity using the empirical relationships between the average particle size and porosity in the ECS is highly accurate. However, the interpretation of the *in situ* acoustic attenuation coefficient is slightly less accurate. It is also observed that the acoustic attenuation coefficient initially increases and then decreases with changes in porosity.

(3) By comparing and analyzing the *in situ* and laboratory measurement results in the ECS and YS, P-EDFM is used to consider the effect of temperature variation and frequency dispersion, enabling the prediction of sound velocity and acoustic attenuation coefficient at different temperatures and frequencies more precisely. And the prediction error of sound velocity is lower than that of the sound attenuation coefficient.

(4) After applying temperature correction and frequency correction, the sound velocity of muddy seafloor sediments demonstrates consistency between laboratorial and *in situ* measurements. Conversely, for sandy seafloor sediments in the ECS, the sound velocity remains higher than the *in situ* measurements even after correction. This indicates that the disturbing factors in the sampling and laboratory measurement of sandy seafloor sediments cannot be disregarded. Therefore, when studying sandy seafloor sediments, it is advisable to utilize *in situ* measurement techniques or conduct *in situ* simulation experiments.

Data availability statement

The original contributions presented in the study are included in the article/supplementary materials. Further inquiries can be directed to the corresponding author.

Author contributions

DZ: Writing – original draft. JX: Writing – review & editing. XM: Writing – review & editing, Investigation. HS: Writing – review & editing. JF: Writing – review & editing. GK: Writing – review & editing.

Funding

The author(s) declare financial support was received for the research, authorship, and/or publication of this article. We would like to acknowledge the financial support received from the National Key Reasearch and Development Program of China (2021YFF0501200, 2021YFF0501201), and the National Natural Science Foundation of China (42227803, 42049902). Additionally, a portion of the data used in this research was made possible through the National Natural Science Foundation of China Open Research Cruise (NORC2021-02+NORC2021-301), which was funded by the Shiptime Sharing Project of the National Natural Science Foundation of China.

Acknowledgments

We would like to extend our gratitude to the team members from Guangdong University of Technology and the First Institute of Oceanography, Ministry of Natural Resources, who actively participated in the sampling of seafloor sediment samples, as well as the acoustic and physical measurements. We are also thankful for the First Institute of Oceanography, Ministry of Natural Resources, China, for conducting the cruise aboard R/V "XiangYangHong 18" and facilitating the collection of valuable data for our study.

Conflict of interest

The authors declare that the research was conducted in the absence of any commercial or financial relationships that could be construed as a potential conflict of interest.

Publisher's note

References

Ballard, M. S., Costley, R., Sagers, J. D., Lee, K. M., McNeese, A. R., Hathaway, K. K., et al. (2018). A comparison between directly measured and inferred wave speeds from an acoustic propagation experiment in Currituck Sound. *J. Acoust. Soc. Am.* 143 (1), 237–247. doi: 10.1121/1.5021244

Belcourt, J., Holland, C. W., Dosso, S. E., Dettmer, J., and Goff, J. A. (2020). Depth-dependent geoacoustic inferences with dispersion at the New England mud patch via reflection coefficient inversion. *IEEE J. Ocean Eng.* 45 (1), 69–91. doi: 10.1109/JOE.2019.2900115

Biot, M. A. (1956a). Theory of elastic waves in a fluid-saturated porous solid, I. Low-frequency range. *J. Acoust. Soc. Am.* 28, 168–178. doi: 10.1121/1.1908239

Biot, M. A. (1956b). Theory of elastic waves in a fluid-saturated porous solid, II. High-frequency range. *J. Acoust. Soc. Am.* 28, 179. doi: 10.1121/1.1908239

Boudreau, B. P. (1996). The diffusive tortuosity of fine-grained unlithified sediments. *Geochim. Cosmochim. Acta* 60 (16), 3139–3142. doi: 10.1016/0016-7037(96)00158-5

Buckingham, M. J. (1998). Theory of compressional and shear waves in fluidlike marine sediments. *J. Acoust. Soc. Am.* 103 (1), 288–299. doi: 10.1121/1.421091

Buckingham, M. J. (2005). Compressional and shear wave properties of marine sediments: comparisons between theory and data. *J. Acoust. Soc. Am.* 117 (1), 137–152. doi: 10.1121/1.1810231

Buckingham, M. J. (2020). Wave speed and attenuation profiles in a stratified marine sediment: Geo-acoustic modeling of seabed layering using the viscous grain shearing theory. *J. Acoust. Soc. Am.* 148 (2), 962–974. doi: 10.1121/10.0001778

Buckingham, M. J., and Richardson, M. (2002). On tone-burst measurements of sound speed and attenuation in sandy marine sediments. *IEEE J. Ocean Eng.* 27 (3), 429–453. doi: 10.1109/JOE.2002.1040929

Hamilton, E. L. (1971). Elastic properties of marine sediments. *J. Geophys. Res.* 76 (2), 579–604. doi: 10.1029/JB076i002p00579

Hamilton, E. L. (1980). Geoacoustic modeling of the sea floor. *J. Acoust. Soc. Am.* 48 (5), 1313–1340. doi: 10.1121/1.385100

Henfer, B. T., Jackson, D. R., Williams, K. L., and Thorsos, E. I. (2009). Mid-to high-frequency acoustic penetration and propagation measurements in a sandy sediment. *IEEE J. Ocean Eng.* 34 (4), 372–387. doi: 10.1109/joe.2009.2028410

Hou, Z. Y., Guo, C. S., Wang, J. Q., Chen, W. G., Fu, Y. T., and Li, T. G. (2015). Seafloor sediment study from South China Sea: acoustic & physical property relationship. *Remote Sens.* 7 (9), 11570–11585. doi: 10.3390/rs70911570

Jackson, D. R., and Richardson, M. D. (2007). *High-Frequency Seafloor Acoustics* (New York: Springer).

Kan, G. M., Zhao, Y. X., Li, G. B., Han, G. Z., and Meng, X. M. (2011). Comparison on the sound speeds of seafloor sediments measured by *in-situ* and laboratorial technique in Southern Yellow Sea. *J. Ocean Technol.* 30 (1), 52–56. doi: 10.3969/j.issn.1003-2029.2011.01.013

Kan, G. M., Zou, D. P., Liu, B. H., Wang, J. Q., Meng, X. M., Li, G. B., et al. (2019). Correction for effects of temperature and pressure on sound speed in shallow seafloor sediments. *Mar. Geores. Geotechnol.* 37 (10), 1217–1226. doi: 10.1080/1064119X.2018.1545812

Kim, G. Y., Narantsetseg, B., Lee, J. Y., Chang, T. S., Lee, G. S., Dong, G. Y., et al. (2018a). Physical and geotechnical properties of drill core sediments in the Heuksan Mud Belt off SW Korea. *Quat. Int.* 468, 33–48. doi: 10.1016/j.quaint.2017.06.018

Kim, G. Y., Park, K. J., Lee, G. S., Dong, G. Y., Young, K. S., and Kim, I. H. (2018b). KISAP: A new *In-situ* seafloor velocity measurement tool. *Mar. Geores. Geotechnol.* 36 (3), 264–270. doi: 10.1080/1064119X.2016.1236858

Kim, S., Lee, G. S., Kim, D., Hahn, J., and Ryang, W. (2018c). Variation of temperature-dependent sound velocity in unconsolidated marine sediments: Laboratory measurements. *Mar. Geores. Geotechnol.* 36 (3), 280–287. doi: 10.1080/1064119X.2016.1277442

Li, G. B., Kan, G. M., Meng, X. M., Liu, B. H., and Han, G. Z. (2013). Influence of environmental condition variations on laboratory acoustic velocity measurements of submarine sediments. *Adv. Mar. Sci.* 31 (03), 360–366. doi: 10.3969/j.issn.1671-6647.2013.03.008

Li, G. B., Wang, J. Q., Liu, B. H., Meng, X. M., Kan, G. M., Han, G. Z., et al. (2020). *In-situ* acoustic properties of fine-grained sediments on the northern continental slope of the South China Sea. *Ocean Eng.* 218 (108244), 1–8. doi: 10.1016/j.oceaneng.2020.108244

Li, M. Z., Li, Z. L., and Li, Q. Q. (2019). Geoacoustic inversion for bottom parameters in a thermocline environment in the northern area of the South China Sea. *Acta Acustica* 44 (03), 321–328. doi: 10.15949/j.cnki.0371-0025.2019.03.006

Liu, B. H., Kan, G. M., Li, G. B., and Yu, S. Q. (2019). *Measurement Techniques and Applications of Acoustic Properties of Submarine Sediments* (Beijing: Science Press).

Megan, S. B., Kevin, M. L., Andrew, R. M., Preston, S. W., Jason, D. C., John, A. G., et al. (2019). *In-situ* measurements of compressional wave speed during gravity coring operations in the New England Mud Patch. *IEEE J. Ocean Eng.* 45 (1), 26–38. doi: 10.1109/JOE.2019.2924560

Schock, S. G. (2005). A method for estimating the physical and acoustic properties of the sea bed using chirp sonar data. *IEEE J. Ocean Eng.* 29 (4), 1200–1217. doi: 10.1109/JOE.2004.841421

Tang, C., Zheng, X. Y., Li, Y. F., Liu, X., and Xia, Z. (2019). Geoacoustic properties measurement and analysis of gravity cores using MSCL in the Southern Beibu Gulf. *Mar. Sci.* 43 (10), 88–95. doi: 10.11759/hykx20190316001

Tao, C. H., Wang, D., and Jin, X. L. (2006). *Marine Sediments Properties and In Situ Acoustic Measurements* (Beijing: Ocean Press).

Wang, J. Q., Kan, G. M., Li, G. B., Meng, X. M., Zhang, L. Q., Chen, M. J., et al. (2023). Physical properties and *in situ* geoacoustic properties of seafloor surface sediments in the East China Sea. Front. *Mar. Sci.* 10, 1195651. doi: 10.3389/fmars.2023.1195651

Wang, J. Q., Li, G. B., Kan, G. M., Liu, B. H., and Meng, X. M. (2020). Experiment study of the *in-situ* acoustic measurement in seafloor sediments from deep sea. *Chin. J. Geophys.* 63 (12), 4463–4472. doi: 10.6038/cjg2020N0427

Wang, J. Q., Li, G. B., Liu, B. H., Kan, G. M., Sun, Z. W., Meng, X. M., et al. (2018a). Experimental study of the ballast *in situ* sediment acoustic measurement system in South China Sea. *Mar. Geores. Geotechnol.* 36 (5), 515–521. doi: 10.1080/1064119X.2017.1348413

Wang, J. Q., Liu, B. H., Kan, G. M., Li, G. B., Zheng, J. W., and Meng, X. M. (2018b). Frequency dependence of sound speed and attenuation in fine-grained sediments from 25 to 250 kHz based on a probe method. *Ocean Eng.* 160, 45–53. doi: 10.1016/j.oceaneng.2018.04.078

Williams, K. L. (2001). An effective density fluid model for acoustic propagation in sediments derived from Biot theory. *J. Acoust. Soc. Am.* 110 (5), 2276–2281. doi: 10.1121/1.1412449

Williams, K. L., Jackson, D. R., Thorsos, E. I., Tang, D., and Schock, S. G. (2002). Comparison of sound speed and attenuation measured in a sandy sediment to predictions based on the Biot theory of porous media. *IEEE J. Ocean Eng.* 27 (3), 413–428. doi: 10.1109/JOE.2002.1040928

Yang, J., and Jackson, D. R. (2020). Measurement of sound speed in fine-grained sediments during the seabed characterization experiment. *IEEE J. Ocean Eng.* 45 (1), 39–50. doi: 10.1109/JOE.2019.2946004

Yu, S. Q., Liu, B. H., Yu, K. B., Kan, G. M., and Yang, Z. G. (2017). Study on sound-speed dispersion in a sandy sediment at frequency ranges of 0.5–3 kHz and 90–170 kHz. *China Ocean Eng.* 31 (1), 103–113. doi: 10.1007/s13344-017-0013-6

Zhou, J. P., Tao, C. H., Li, H. X., Jin, X. L., Qiu, L., Zhang, G. Y., et al. (2019). The physical model with temperature and pressure controlled for measuring acoustic velocity of marine sediments. *Mar. Geores. Geotechnol.* 37 (5), 633–640. doi: 10.1080/1064119X.2018.1469057

Zimmer, M. A., Bibee, L. D., and Richardson, M. D. (2010). Measurement of the frequency dependence of the sound speed and attenuation of seafloor sands from 1 to 400 kHz. *IEEE J. Ocean Eng.* 35 (3), 538–557. doi: 10.1109/JOE.2010.2056230

Zou, D. P., Liu, W., and Long, J. J. (2018). Relationship of sound speeds between compressional wave and shear wave of seafloor sediments. *Acta Acustica* 43 (6), 951–960. doi: 10.15949/j,cnki.0371-0025.2018.06.010

Zou, D. P., Williams, K. L., and Thorsos, E. I. (2015). Influence of temperature on the acoustic sound speed and attenuation of sand sediment. *IEEE J. Ocean Eng.* 40 (4), 969–980. doi: 10.1109/JOE.2014.2365072

Zou, D. P., Ye, G. C., Liu, W., Sun, H., Li, J., and Xiao, T. B. (2022). Effect of temperature on the acoustic reflection characteristics of seafloor surface sediments. *J. Ocean Univ. China* 21 (1), 62–68. doi: 10.1007/s11802-022-4874-9

Zou, D. P., Zeng, Z. W., Kan, G. M., Liu, W., and Xiao, T. B. (2021). Influence of environmental conditions on the sound velocity ratio of seafloor surficial sediment. *J. Ocean Univ. China* 20 (3), 573–580. doi: 10.1007/s11802-021-4628-0

frontiers | Frontiers in Marine Science

TYPE Original Research
PUBLISHED 21 February 2024
DOI 10.3389/fmars.2024.1307768

OPEN ACCESS

EDITED BY
Martin F. Soto-Jimenez,
National Autonomous University of Mexico, Mexico

REVIEWED BY
Masanao Shinohara,
The University of Tokyo, Japan
Lei Xing,
Ocean University of China, China

*CORRESPONDENCE
Guangming Kan
kgming135@fio.org.cn

RECEIVED 05 October 2023
ACCEPTED 16 January 2024
PUBLISHED 21 February 2024

CITATION
Meng W, Meng X, Wang J, Li G, Liu B, Kan G, Lu J, Zhao L and Zhi P (2024) Prediction of the shear wave speed of seafloor sediments in the northern South China Sea based on an XGBoost algorithm.
Front. Mar. Sci. 11:1307768.
doi: 10.3389/fmars.2024.1307768

Prediction of the shear wave speed of seafloor sediments in the northern South China Sea based on an XGBoost algorithm

Wenjing Meng[1,2,3,4], Xiangmei Meng[2,3,4], Jingqiang Wang[2,3,4], Guanbao Li[2,3,4], Baohua Liu[2,3,4], Guangming Kan[1,2,3,4]*, Junjie Lu[2,4], Lihong Zhao[1] and Pengyao Zhi[1]

[1]College of Earth Science and Engineering, Shandong University of Science and Technology, Qingdao, Shandong, China, [2]Key Laboratory of Marine Geology and Metallogeny, First Institute of Oceanography, Ministry of Natural Resources, Qingdao, Shandong, China, [3]Laboratory for Marine Geology, Laoshan Laboratory, Qingdao, Shandong, China, [4]Key Laboratory of Submarine Acoustic Investigation and Application of Qingdao (preparatory), Qingdao, Shandong, China

Based on data on the shear wave speed and physical properties of the shallow sediment samples collected in the northwest South China Sea, the hyperparameter selection and contribution of the characteristic factors of the machine learning model for predicting the shear wave speed of seafloor sediments were studied using the eXtreme Gradient Boosting (XGBoost) algorithm. An XGBoost model for predicting the shear wave speed of seafloor sediments was established based on four physical parameters of the sediments: porosity (n), water content (w), density (ρ), and average grain size (M_Z). The result reveals that: (1) The shear wave speed has a good correlation with n, w, ρ, and M_Z, and their Pearson correlation coefficients are all above 0.75, indicating that they can be used as the suitable characteristic parameters for predicting the shear wave speed based on the XGBoost model; (2) When the number of weak learners (n_estimators) is 115 and the maximum depth of the tree (max_depth) is 6, the XGBoost model has a very high goodness of fit (R^2) of the validation data of 0.914, the very low mean absolute error (MAE) and mean absolute percentage error (MAPE) of the predicted shear wave speed are 3.366 m/s and 9.90%, respectively; (3) Compared with grain-shearing (GS) model and single- and dual-parameter regression equation prediction models, the XGBoost model for the shear wave speed of seafloor sediments has higher fitting goodness and lower prediction error.

KEYWORDS

seafloor sediments, shear wave speed, machine learning, XGBoost model, the northwest South China Sea

Introduction

As one of the important parameters of seafloor geoacoustic properties, sediment shear wave speed has important applications in marine sound field prediction, geoacoustic model research, and marine engineering investigation. The geoacoustic properties of shallow sediments from several meters to tens of meters below the seafloor are closely related to the geological environment of the seafloor, and the relationship between their acoustic and physical properties has been a focus of research (Hou, 2016). For the research of marine acoustics, the characteristics of shear waves in seafloor sediments are of great significance for the interpretation of experimental results of marine acoustic propagation and the accurate prediction of sound fields (Lu et al., 2004). In the field of marine engineering investigation, measurements of sediment shear wave speed and shear modulus are widely used in the study of foundation-bearing capacity, sand liquefaction caused by earthquakes, and consolidation behavior (Jackson and Richardson, 2007; Guo et al., 2023). In addition, sediment shear wave speed is an indispensable parameter for establishing a complete geoacoustic model (Buckingham, 2005).

Many scholars have studied the correlation between shear wave speed and physical parameters of seafloor sediments and built empirical equations based on single or dual physical parameters of seafloor sediment. Richardson and Briggs (1996) studied the difference in shear wave speed between muddy and sandy sediments but did not build the corresponding empirical equations of the correlation between shear wave speed and the physical parameters of seafloor sediments. Lu et al. (2004) analyzed a small number of shallow seafloor sediment samples from the Yellow Sea, East China Sea, and South China Sea and established single-parameter regression empirical equations for shear wave speed, sediment density, and liquid limit, respectively. Pan et al. (2006) measured the shear wave speed of 10 seafloor sediment samples collected at seven stations located in different marine areas and established single-parameter regression equations between the shear wave speed and water content, density, porosity, plastic limit, and liquid limit, respectively. Kan et al. (2014) established single empirical equations between the shear wave speed and the density, water content, compression coefficient, and shear strength of the sediments in the central area of the South Yellow Sea. However, the single-parameter prediction equation cannot fully reflect the relationship between shear waves and physical properties. In order to overcome the shortcomings of single-parameter analysis, some scholars have also carried out dual-parameter analysis of shear wave speed and physical and mechanical properties of sediments. Lu and Liang (1991) established the dual-parameter regression equations between the shear wave speed and the dual-parameter pair of unconfined compression strength and strength sensitivity of sediments and pointed out that the dual-parameter equations have higher correlation coefficients than the single-parameter equations. Kan et al. (2020) established dual-parameter regression empirical equations of shear wave speed with porosity and average grain size at different frequencies based on data from the northern part of the South China Sea, and the correlation coefficient was significantly improved compared to the single-parameter empirical equation.

The single- or dual-parameter prediction equations cannot fully reflect the relationship between shear waves and physical properties. Acoustic properties such as the shear wave speed of seafloor sediments are often controlled by multiple physical parameters, and the use of multiple physical parameters for acoustic property prediction modeling is essential to improving prediction accuracy. Machine learning algorithms can automatically analyze the multidimensional known data to obtain a prediction model and use the model to predict the unknown data. Using machine learning algorithms, it is possible to establish a prediction model for sediment acoustic properties based on multiple physical parameters. Chen et al. (2022; 2023) established a multiparameter sound speed prediction model for the seafloor sediment in the middle of the South Yellow Sea and the East China Sea, using a machine learning algorithm, and the prediction error was significantly reduced compared with the single- and dual-parameter regression empirical equations. Hou et al. (2023) developed a sound speed prediction model of seafloor sediment using deep neural networks. The shear wave speed prediction models in the northern part of the South China Sea are based on a single physical parameter or two physical parameters that have been established, but there is a lack of shear wave speed prediction models using machine learning algorithms based on multiple physical properties of sediments. The aim of this paper is to establish a multiparameter shear wave speed prediction model based on the XGBoost algorithm to achieve an accurate prediction of the shear wave speed of the seafloor sediment in the northern part of the South China Sea. This study is beneficial for enriching the marine geoacoustic model library and presenting models for seafloor sediment shear wave speed.

Study area and data source

Location of the study area

The study area is located in the northern area of the South China Sea between 14°N–20°N and 108°E–115°E, where the submarine geomorphology is continental shelf and continental slope. The main sources of seafloor sediments in this area are continental and island rivers. The continental shelf is dominated by terrigenous clastic sediments; the sediments are mainly composed of clayey sand, silty sand, and sandy silt. The sediments on the continental slope are mainly composed of silty clay and clayey silt.

Data sources

The samples were collected by using a gravity corer, and sediment columnar samples were obtained from 21 stations; 16 stations were taken from the continental slope, and five stations were taken from the continental shelf. Shear wave speed measurements were carried out in the laboratory using a piezoelectric ceramic bending element test system to obtain shear wave speed with an excitation frequency of 2 kHz. The physical properties were measured in the geotechnical laboratory to obtain

different types of sediment physical properties, namely porosity (n), water content (w), density (ρ), average grain size (M_Z), sand content (S), silt content (T), and clay content (Y). The results of the shear wave speed and physical parameter measurement are shown in Table 1. The seafloor sediments in the study area include coarse silt, silty sand, silty clay, sand–silt–clay, sandy silt, clayey silt, clayey sand, and medium silt, among which there are more silty clay and clayey sand and less coarse silt, sand–silt–clay, and medium silt. Table 1 shows that the density of the sediments in the study area ranges from 1.3 g/cm^3 to 1.98 g/cm^3, the porosity ranges from 42.4% to 82.4%, the water content ranges from 26.1% to 173.0%, the average grain size ranges from 4.18 to 8.59ϕ (ϕ=log$_2d$, d is the grain size in millimeters), the sand content ranges from 0.5% to 74.7%, the silt content ranges from 10.9% to 86.6%, the clay content ranges from 6.08% to 73.9%, and the shear wave speed ranges from 15.81 m/s to 75.55 m/s. Among them, the silty clay has the lowest shear wave speed, and the sandy silt has the highest. The physical properties of the different sediment types are different. Silt, sandy silt, and sandy clay have higher density, larger average grain size, lower porosity, and lower water content. On the contrary, silty clay, clay silt, coarse silt, medium silt, and sand–silt–clay have lower densities, smaller average grain size, and higher porosity and water content.

Shear wave speed prediction based on the XGBoost algorithm

XGBoost algorithm

eXtreme Gradient Boosting (XGBoost) is an integrated learning algorithm based on the Gradient Boosting Decision Tree (GBDT) algorithm. The basic idea of the XGBoost is to train a new model based on the errors in the old model, which is a weak classifier, generate a series of models in an iterative serial fashion, and sum these models in a linearly weighted fashion to form a powerful integrated model which is a strong classifier (Qian et al., 2020). The XGBoost algorithm introduces a regularization term, which controls the complexity of the model and prevents overfitting (Chen and Guestrin, 2016). In addition, the XGBoost algorithm has higher efficiency for optimal solutions because it performs second-order Taylor expansions on the loss function, while traditional GBDT only utilizes first-order derivative information (Li et al., 2018). So, the XGBoost algorithm was chosen to build the prediction model of the shear wave speed. For the XGBoost algorithm, the dataset for training to build the integrated model is assumed to have n samples and m features, and the ith sample of the training dataset can be represented as (x_i,y_i). Here, x_i denotes the feature vector of the ith sample, representing the physical parameters of sediments, and y_i denotes the label of the ith sample, representing the shear wave speed of sediments. After K iterations, the predicted value (Y_i^K) of the integrated model for the ith sample can be expressed as:

$$Y_i^K = \sum_{k=1}^{K} T_k(x_i) \tag{1}$$

In Equation 1, $T_k(x_i)$ denotes the function that maps the features to the weights of the leaf nodes of the tree structure, which can be expressed as $T_k(x_i) = w_{q(xi)}$. w is the weight of the leaf nodes. $q(x_i)$ denotes the position of the ith sample in the K decision trees. The objective function of the XGBoost algorithm is:

$$Obj^K = \sum_{i=1}^{n} l(y_i, Y_i^K) + \sum_{k=1}^{K} \Omega(T_k) \tag{2}$$

In Equation 2, $l(y_i, Y_i^k)$ is the loss function representing the error between the predicted values from the model and the real values for the ith sample. $\sum_{k=1}^{k} \Omega(T_k)$ is the regularization item, which is used to limit the number of leaf nodes to prevent the fitting phenomenon in the training process. It can be expressed as:

$$\Omega(T_k) = \gamma T + \frac{1}{2}\lambda \sum_{j=1}^{T} w_j^2 \tag{3}$$

In Equation 3, $\gamma$is the learning rate used to control the number of leaf nodes. T is the number of young leaf nodes. λ is a regular parameter used to control the score of the leaf node.

The XGBoost model is a front-oriented distribution algorithm, and the iterative form of the target function can be expressed as:

$$Obj^K = \sum_{i=1}^{n} l\left(y_i, Y_i^{K-1} + T_K(x_i)\right) + \Omega(T_K) \tag{4}$$

TABLE 1 Measurement results of shear wave speed and physical parameters of sediment samples in the study area.

Sediment type	V_S (m/s)	n (%)	W (%)	ρ (g/cm^3)	M_Z (ϕ)	S (%)	T (%)	Y (%)
Coarse silt	22.17–55.66	44.0–76.4	31–118.6	1.39–1.98	5.56–6.10	3.9–8.7	75.4–86.6	9.5–17.6
Silty sand	51.61–71.92	43.3–49.5	26.8–38.2	1.86–1.94	4.18–5.19	45.8–74.7	13.4–37.7	10.7–20.5
Silty clay	15.81–45.10	64.0–81.8	63.7–159.9	1.30–1.62	6.31–8.59	1.9–43.5	17.1–57.9	6.52–73.9
Sand–silt–clay	19.93–32.35	73.0–79.2	97.0–140.4	1.37–1.47	6.04–6.22	28.9–30.5	29.4–37.0	34.1–41.0
Sandy silt	62.68–75.55	43.1–50.5	27.5–35.4	1.81–1.96	4.89–5.66	28.5–35.4	44.0–50.1	17.0–21.8
Clayey silt	16.17–59.44	42.5–82.4	26.3–173.0	1.30–1.96	5.99–8.01	0.5–65.6	20.4–74.4	6.08–49.1
Clayey sand	53.14–73.29	42.4–52.5	26.1–40.4	1.80–1.96	4.29–4.86	61.7–74.5	10.9–18.4	14.6–20.2
Medium silt	17.47–28.81	76.9–80.6	121.1–153.3	1.33–1.98	6.54–6.79	2.1–4.6	76.7–78.5	16.9–21.2

10.3389/fmars.2024.1307768

In order to find the minimum value of the target function, the second order of (Equation 4) Taylor at $T_k = 0$ is:

$$Obj^K = \sum_{i=1}^{n}\left[l(y_i, Y_i^{K-1}) + g_i T_K(x_i) + \frac{1}{2}h_i(T_K(x_i))^2\right] + \Omega(T_K) \quad (5)$$

$$g_i = \frac{\partial l(y_i, Y_i^{K-1})}{\partial Y_i^{K-1}} \quad (6)$$

$$h_i = \frac{\partial^2 l(y_i, Y_i^{K-1})}{\partial^2 Y_i^{K-1}} \quad (7)$$

In Equation 5, g_i is the first-order guide, calculated by Equation 6; h_i is the second order guide, calculated by Equation 7.

XGBoost achieves the generation of the learning device by optimizing the structured losses and improves the performance of the algorithm by utilizing the first-order and second-order derivative values of the loss function and through preorder and weighted seminars. Substituting the regularization term expression into Equation 5, the final minimum value of the objective function is obtained, as in Equation 8.

$$Obj^* = -\frac{1}{2}\sum_{m=1}^{k}\left(\frac{G_m^2}{H_m + \lambda}\right) + \gamma T \quad (8)$$

The smaller the target function, the smaller the gap between the real values and the model-predicted values, and the better the model fit.

Characteristic parameter selection

After removing outliers and missing values, a total of 226 datasets were obtained, and eight parameters were included in each set: shear wave speed at 2 kHz, sediment n, w, ρ, M_Z, S, T, and Y. Thus, the dimension of the sample data is (226, 8). The number of data samples is similar to that used to predict sediment sound speed based on the machine learning algorithm in the following literature (Hou et al., 2019; Hou et al., 2023; Chen et al., 2022, 2023) and can be used to train the machine learning prediction model for predicting shear wave speed of seafloor sediments.

In machine learning, the Pearson correlation coefficient is commonly used for feature selection, which helps us find the features with high correlation in the dataset, reducing the number of features, improving the generalization ability of the model, and reducing the computation time (Qi et al., 2023). The Pearson correlation coefficient was used to determine the correlation between the sediment shear wave speed and physical parameters. If the coefficient is negative, it means that the two features are negatively correlated, and if the coefficient is positive, the two features are positively correlated. The closer the absolute value of the coefficient is to 1, the greater the degree of correlation. The Pearson correlation coefficient between X and Y variables can be expressed by Equation 9.

$$\rho_{X,Y} = \frac{E(XY) - E(X)E(Y)}{\sqrt{E(X^2) - E^2(X)}\sqrt{E(Y^2) - E^2(Y)}} \quad (9)$$

The Pearson correlation coefficient of the physical parameters and shear wave speed was calculated for the 226 sets of data, and the correlation coefficients of seafloor sediment shear wave speed with n, w, ρ, M_Z, S, T, and Y are −0.88, −0.81, 0.86, −0.76, −0.55, 0.15, and 0.48, respectively, as shown in Figure 1. According to Figure 1, the n, w, ρ, and M_Z have high correlation coefficients with the shear wave speed and are selected as the input parameters for the model.

Dataset segmentation

Four physical parameters and the shear wave speed are selected to participate in the subsequent model establishment, and the dimension of the sample data is (226, 5). Firstly, the sample is divided into two parts: one part is used for model building, and the other part is not involved in model building and is used for testing after model building. Subsequently, the dataset used for model building is divided into a training dataset and a validation dataset. The training dataset is used to establish the initial hyperparameters of the model. The validation dataset is used to adjust the hyperparameters in XGBoost in the model to prevent overfitting and select the optimal model. The test dataset is used to evaluate the performance of the model through a comparison between the measured shear wave speed and the prediction of the model. Using random numbers, 166 datasets are randomly selected for model training with a data dimension of (166, 5), 30 datasets are randomly selected for model validation with a data dimension of (30, 5), and the remaining 30 datasets are randomly selected for model testing with a data dimension of (30, 5). As shown in Figure 2, the sediment types in the study area are diverse, and the physical properties and shear wave speeds of different sediment types are different. The datasets of training data, validation data, and test data all contain multiple

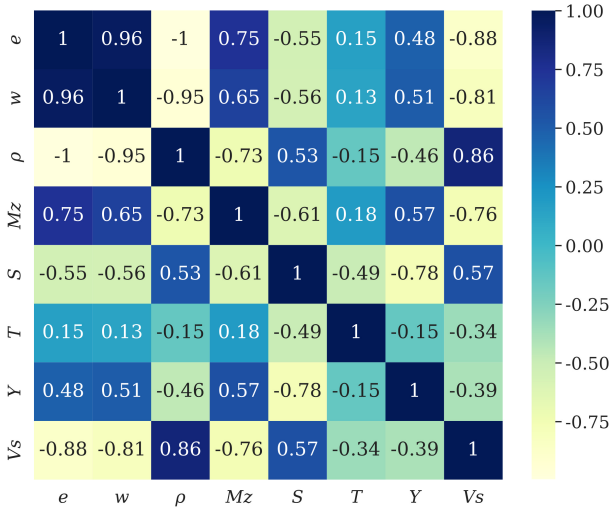

FIGURE 1
Pearson correlation coefficient matrix for each factor. The last column shows the Pearson correlation coefficient between the shear wave speed of the sediments and physical parameters.

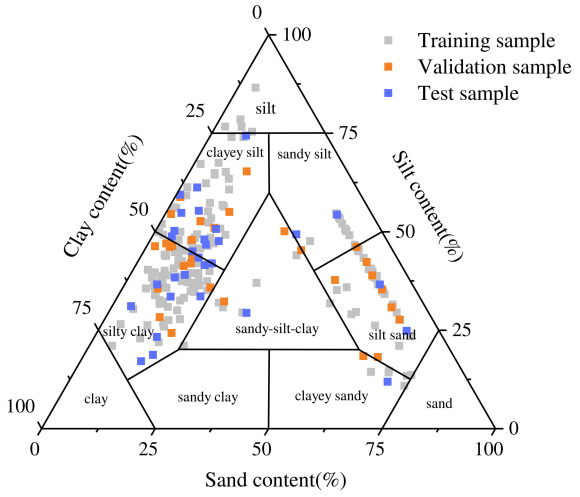

FIGURE 2
Sediment triangulation map of dataset delineation results in this paper. The gray data points in the figure represent the training data, the orange data points represent the validation data, and the blue data points represent the test data.

sediment types, which can ensure the applicability of the model to different types of sediments.

Results

Indicators for assessing the results of model predictions

The mean absolute error (MAE), mean absolute percentage error (MAPE), and goodness of fit (R^2) are selected as indicators to evaluate the predictive ability. The MAE and MAPE reflect the mean absolute error and mean absolute percentage error between the predicted values and the real values, respectively. R^2 reflects the degree of goodness of fit of the model. They are expressed as:

$$MAE = \frac{1}{n}\sum_{i=1}^{n}|y_i - Y_i| \tag{10}$$

$$MAPE = \frac{100\,\%}{n}\sum_{i=1}^{n}\left|\frac{y_i - Y_i}{y_i}\right| \tag{11}$$

$$R^2 = 1 - \frac{\sum_{i=1}^{n}(Y_i - y_i)^2}{\sum_{i=1}^{n}(\overline{y_i} - y_i)^2} \tag{12}$$

In Equations 10–12, n is the number of the sample, Y_i is the predicted value, y_i is the real value, and $\overline{y_i}$ is the mean of the real values.

Model building and optimization

At first, the 166 sets of training data were substituted into the model for training by using the default hyperparameters in XGBoost to train the data, which was called Model0. Substituting the validation data into Model0, the validation goodness of fit of Model0 was 0.902, and the MAE and MAPE between the validation data and the real values were 3.926 m/s and 12.2%, respectively. In order to obtain a better fitting effect, some hyperparameters were adjusted using a random search method and crossvalidation function. The results are shown in Table 2. The adjusted parameters were entered into the model, and the model was retrained, which was called Model1. Now, the MAE, MAPE, and R^2 for the validation data were 3.41 m/s, 10.1%, and 0.913, respectively. Compared with the results of Model0, the prediction performance of Model1 was improved with a smaller MAE and higher R^2.

In addition to the hyperparameters mentioned above, two other hyperparameters, n_estimators and max_depth, are very important for the accuracy of the model training. The n_estimators indicates the number of weak learners (regression trees) in the model; a smaller number of learners will lead to insufficient model performance, and a larger number may improve model performance but will increase training time and memory consumption. The max_depth parameter indicates the maximum depth of the tree, specifying the weak learners. A deeper tree can capture more complex interactions between the features, but the deeper the tree, there greater the risk of overfitting. The n_estimators and max_depth were manually adjusted and optimized according to the curves of MAE changing with the n_estimators and max_depth for the training and validation sets, shown in Figures 3, 4, respectively. As shown in Figure 3, when the value of n_estimators is 115, the MAE of the validation data and the real values are the smallest. As shown in Figure 4, when the value of max_depth is 6, the MAE is the smallest.

The value of the hyperparameters of the XGBoost model was finally obtained through the adjustment and optimization using the random search, crossvalidation function, and manual optimization. When the adjusted parameters were substituted into the model, it was the best-fitted model for the prediction of the shear wave speed in the study area and can be called Model2. The coefficient of determination of the validation data was 0.914, and the MAE and MAPE of the predicted values of the training data and the measured data were 3.366 m/s and 9.90%, respectively. Figure 5 shows the comparison between the model's predicted values and the real values. The predicted data are closely matched with the real data, and the multiparameter shear wave speed prediction model constructed based on the XGBoost algorithm has a small difference between the predicted values and the real values, and the model prediction accuracy is high.

TABLE 2 Optimization results for the hyperparameters of the random search section.

Model parameter	Search area	Optimization results
reg_alpha	[0.1,0.2,0.3,0.4,0.5,0.6,0.7,0.8,0.9,1]	0.4
reg_lambda	[0.1,0.2,0.3,0.4,0.5,0.6,0.7,0.8,0.9,1]	0.5
subsample	[0.1,0.2,0.3,0.4,0.5,0.6,0.7,0.8,0.9,1]	0.5
colsample_bytree	[0.1,0.2,0.3,0.4,0.5,0.6,0.7,0.8,0.9,1]	0.5
colsample_bylevel	[0.1,0.2,0.3,0.4,0.5,0.6,0.7,0.8,0.9,1]	0.7
learning_rate	[0.1,0.2,0.3,0.4,0.5,0.6,0.7,0.8,0.9,1]	0.1

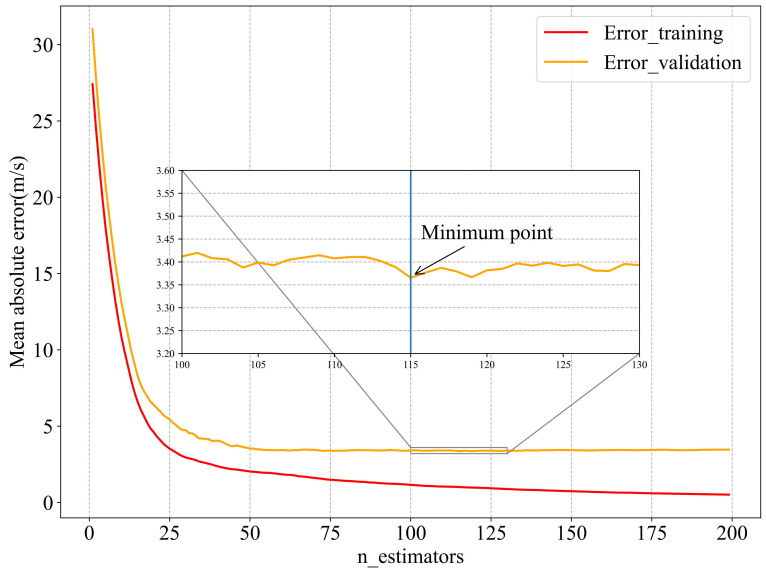

FIGURE 3
Trend of MAE with n_estimators hyperparameter in model training and validation. The red solid line is the iteration change of the model training error, and the orange solid line is the iteration change of the validation result error.

Analysis of the contribution of characteristic parameters

Lundberg and Lee (2017) proposed the SHapley Additive exPlanations (SHAP) method to explain the machine learning model and evaluated the importance of features by calculating the average value of the absolute value of each feature in the sample data. Figure 6 shows the average value of the absolute SHAP value of each feature variable as the importance of this feature. It can be seen that the main influencing factors on shear wave speed in the XGBoost model are porosity and water content, followed by density and average grain size.

Discussion

In order to analyze the predictive performance of the multiparameter shear wave speed prediction model based on the

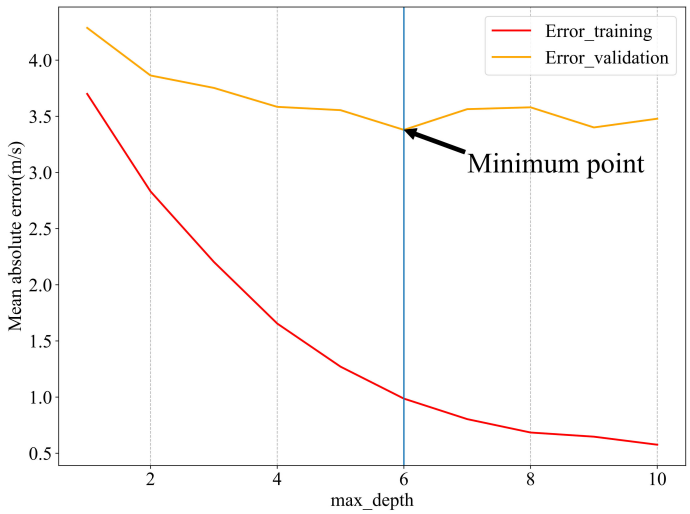

FIGURE 4
Trend of MAE with max_depth hyperparameter in model training and validation. The red solid line is the iteration change of the model training error, and the orange solid line is the iteration change of the validation result error.

10.3389/fmars.2024.1307768

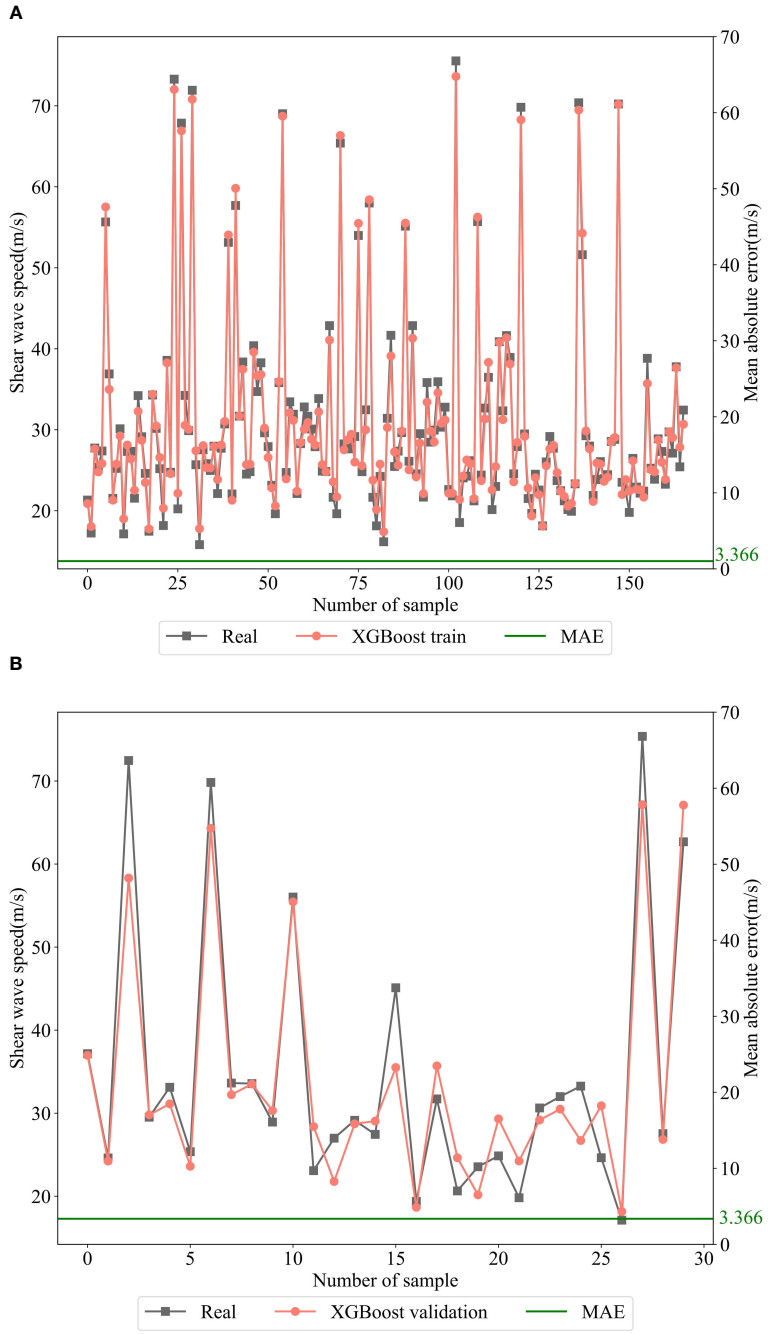

FIGURE 5
Comparison of predicted and real values: **(A)** 166 sets of training sample; **(B)** 30 sets of validation sample. The solid green line represents the MAE between each prediction value and the real values.

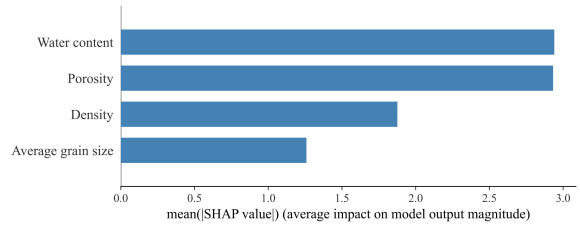

FIGURE 6
Ranking the average influence values of the model output.

XGBoost algorithm, the following section will use the same 166 sets of training data to build the single- and dual-parameter prediction models and the GS prediction model and compare the prediction errors and the magnitude of the coefficients of determination of the models.

Single-parameter prediction model

The 166 sets of training data were used to establish four single-parameter prediction models. The mathematical relationship

between the physical parameters of the sediment and the shear wave speed was fitted using the least squares method to establish the corresponding single-parameter empirical equations listed in Table 3. As shown in Table 3, the shear wave speed has high correlations with the porosity, water content, density, and average grain size, whose goodness of fit is all greater than 0.66. The predicted shear wave speed using the single-parameter prediction equations in Table 3 and the real values are compared and shown in Figure 7. According to Figure 7 and Table 3, the MAEs of the single-parameter prediction equations are all higher than 5 m/s, and the prediction equation based on porosity is the lowest with an MAE of 5.014, while that of the prediction equation based on average grain size is the highest with an MAE of 5.427.

Dual-parameter prediction model

The same 166 sets of training data were used to establish six dual-parameter prediction models. The mathematical relationship between the physical parameters of the sediment and the shear wave speed was fitted using the least squares method, and the corresponding dual-parameter empirical equations were established and listed in Table 4. Similarly, the predicted shear wave speed using the dual-parameter prediction equations in Table 4 and the real values are compared and shown in Figure 8. The results show that the goodness of fit of the dual-parameter prediction equations is all greater than 0.78, which is higher than that of the single-parameter prediction equations established in this paper. The MAEs of the dual-parameter prediction equations are all less than 4.8 m/s, which is lower than that of the single-parameter equations. This indicates that the dual-parameter equations have a higher prediction accuracy than the single-parameter equations.

GS model

In recent years, researchers have studied the propagation mode of sound waves in sediments and summarized models for predicting sound speed in different theoretical media. Buckingham (1997) proposed the grain-shearing (GS) model, which introduced the sticky-slip mechanism between sediment grains, and believed that saturated, unconsolidated particle media have dual properties of fluid and elastic solid, and grains do not cement each other although they contact each other. Furthermore, it is believed that the stiffness of the sediment is generated by the mutual sliding of the grains, and the stiffness supports the existence of shear waves in the sediment. The equation for calculating the shear wave speed is as follows:

$$V_s = \sqrt{\frac{\gamma_s}{\rho}} \frac{(\omega T)^{\frac{n}{2}}}{cos(\frac{n\pi}{4})} \tag{13}$$

Where, γ_s is the shear stiffness coefficient, which is used to describe the viscous sliding mechanism and characterize the shear action between grains, calculated by Equation 14. ρ is the density of deposited objects, calculated by Equation 15. ω is the angular frequency. T is any time variable, which can be set to 1 s. n is the strain hardening index, which represents the strain hardening degree of intergranular contact when sediment grains slip.

$$\gamma_s = \gamma_{s0}\left(\frac{1-\beta)u_g d}{(1-\beta_0)u_{g0}d_0}\right)^{\frac{2}{3}} \tag{14}$$

Where, γ_{s0} is the initial value of γ_s. β, u_g, and d represent measured sediment fraction porosity, grain size, and buried depth, respectively. β_0, u_{g0}, and d_0 are the reference values of fractional porosity, grain size, and buried depth of sediments, and the specific values are shown in Table 5.

$$\rho = (1-\beta)\star\rho_g + \beta\star\rho_f \tag{15}$$

$$u_g = 2^{-\phi} \tag{16}$$

Where, ρ_g is the particle density, ρ_f is the pore fluid density, and ϕ represents the grain size in Equation 16; here, the average grain size of the sediment is selected.

The 166 sets of training data are substituted into Equation 13 to obtain the minimum value of the mean absolute error between the predicted and real values of the shear wave speed, which leads to the optimal values of the shear coefficient and strain hardening index. The values of the input parameters of GS for best fitting are shown in Table 5. Substituting the parameter values into the model, the results of the predicted and real values are shown in Figure 9. The goodness of fit of the model was 0.678; the MAE and MAPE between the real values and the predicted values were 5.253 m/s and 18.09%, respectively.

TABLE 3 Single-parameter prediction models.

Relate parameter	Prediction equation	Goodness of fit (R^2)	MAE (m/s)	MAPE (%)
n	$y = 0.0194n^2 - 3.5293n + 183.3$	0.774	5.014	17.0
w	$y = 0.002w^2 - 0.7547w + 79.717$	0.721	5.338	18.4
ρ	$y = 74.127\rho^2 - 177.71\rho + 130.09$	0.753	5.195	17.3
M_z	$y = 3.4991\ M_z^2 - 54.473M_z + 238.16$	0.661	5.427	18.9

10.3389/fmars.2024.1307768

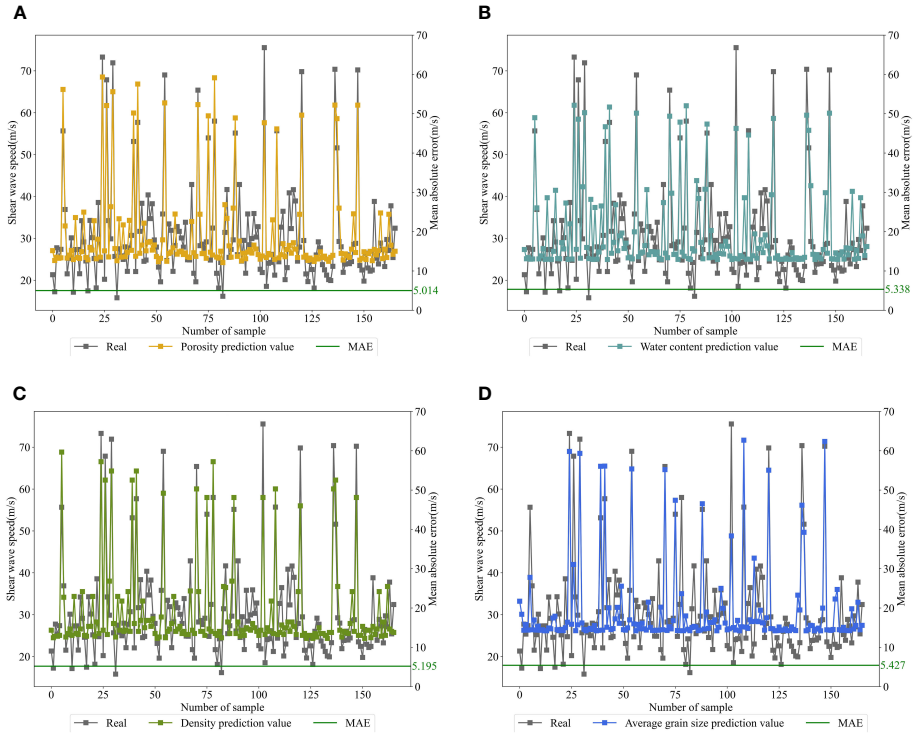

FIGURE 7
Comparison of predicted shear wave speed from the single-parameter prediction models with real values: **(A)** porosity, **(B)** water content, **(C)** density, and **(D)** average grain size. The gray curve in the figures represents the real values. The solid green lines show the MAE between the predicted and real values of the 166 training samples.

Comparison of predicted results of each model

To check the accuracy of model fitting, 30 groups of test data that were not involved in model building were substituted into each prediction model, and the difference between the predicted values and the real values of different models was analyzed. The MAEs and the MAPEs between the predicted values and the real values of each model were calculated, and the results are shown in Figure 10. It can be seen that the XGBoost model has the smallest MAE and MAPE and the highest goodness of fit compared to the single-parameter prediction models, dual-parameter prediction models, and GS prediction model.

Conclusions

In this paper, using the seafloor sediments obtained in the northern part of the South China Sea, the correlation between the

TABLE 4 Dual-parameter prediction models.

Related parameter	Prediction equation	Goodness of fit (R^2)	MAE (m/s)	MAPE (%)
n, w	$y = 0.0529n^2 - 7.4559n - 0.00346w - 1.0373w + 0.017nw + 304.0410$	0.8137	4.4217	15.2
n, ρ	$y = 0.3296n^2 - 98.997n + 888.0952\rho^2 - 5108.5\rho + 33.6063n\rho + 7483.2$	0.7851	4.7904	16.5
n, M_z	$y = -0.0207n^2 - 1.5186n - 1.9425\ M_z^2 - 11.6252M_z + 0.5203nM_z + 163.0088$	0.8084	4.4310	15.0
w, ρ	$y = -0.0045w^2 + 2.7236w + 34.7296\rho^2 + 22.4522\rho - 1.3387w\rho - 109.0748$	0.7878	4.7829	16.0
w, M_z	$y = -0.0014w^2 - 1.1059w - 1.5879\ M_z^2 + 2.7548M_z + 0.1710wM_z + 96.57632$	0.8252	4.0967	13.8
ρ, M_z	$y = -63.1273\rho^2 + 430.0906\rho - 1.5759\ M_z^2 + 61.9130M_z - 28.1868\rho M_z - 530.3517$	0.7954	4.6084	15.5

10.3389/fmars.2024.1307768

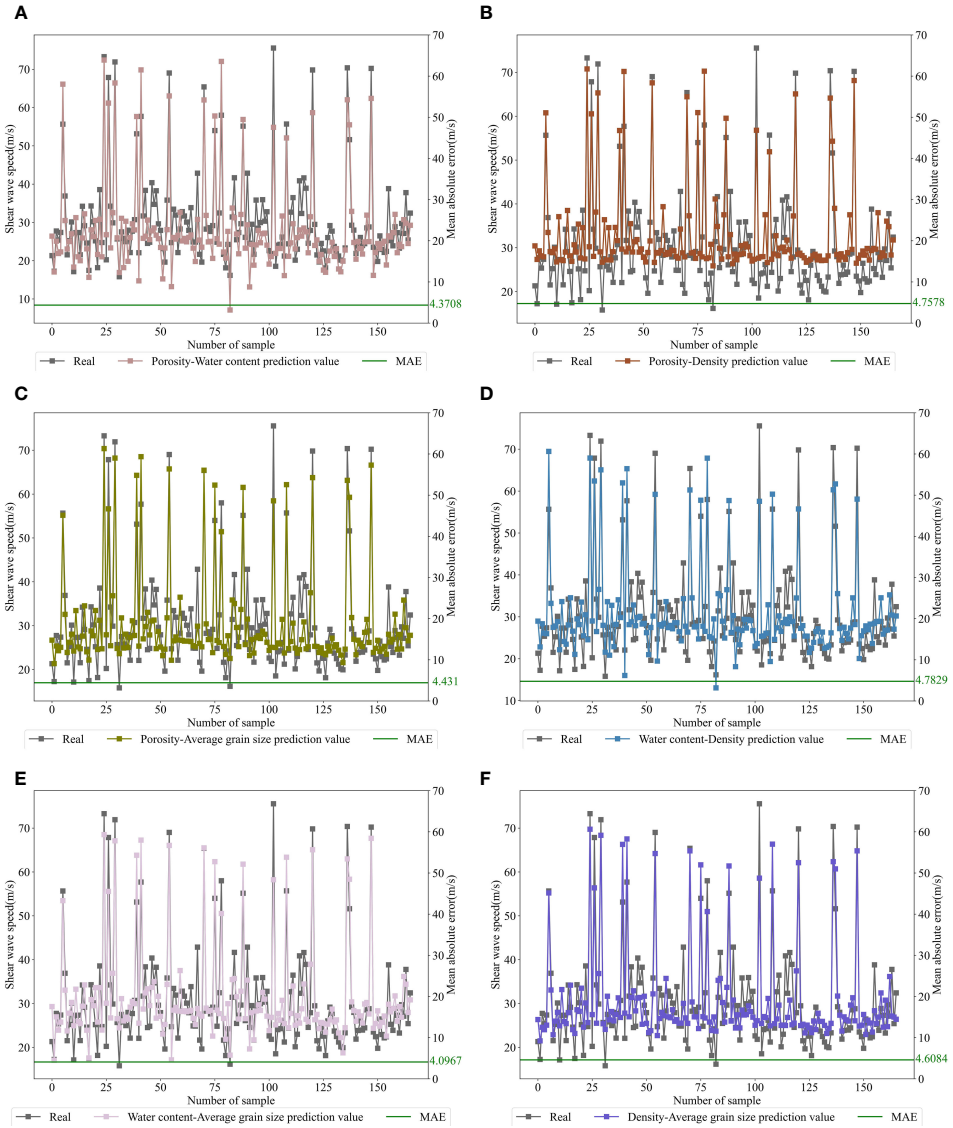

FIGURE 8
Comparison of predicted shear wave speed from the dual-parameter prediction models with real values: **(A)** porosity—water content, **(B)** porosity—density, **(C)** porosity—average grain size, **(D)** water content—density, **(E)** water content—average grain size, and **(F)** density—average grain size. The gray curve in the figures represents the real values, and the solid green lines show the mean absolute error between the predicted and real values of the 166 training samples.

TABLE 5 Input parameters of GS model.

Parameter	Symbol	Units	Value
Reference grain diameter[a]	u_{g0}	μm	1,000
Reference depth in sediment[a]	d_0	m	0.3
Reference porosity[a]	β_0	–	0.37
Average grain size[b]	u_g	μm	Measured
Depth in sediment[b]	d	m	Measured
Porosity[b]	β	–	Measured

(Continued)

TABLE 5 Continued

Parameter	Symbol	Units	Value
Shear coefficient[c]	γ_{s0}	Pa	4.705×10^7
Strain-hardening index[c]	n	–	0.065
Density of grain[a]	ρ_g	kg·m^{-3}	2,730
Density of pore water[a]	ρ_f	kg·m^{-3}	1,005

[a]Physical parameter indicating the value reference (Buckingham, 1997).
[b]For these physical parameters, refer to Table 1 for the range of values.
[c]Physical parameters that were obtained by fitting measured data.

10.3389/fmars.2024.1307768

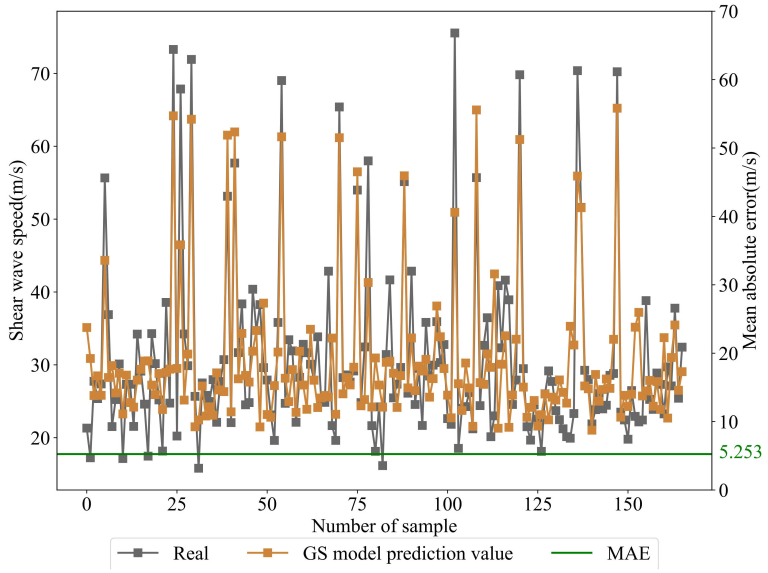

FIGURE 9
Comparison of predicted shear wave speed from the GS model with real values. The gray curve in the figure represents the real values, the brown curve represents the adjusted GS model predicted values, and the solid green lines show the mean absolute error between the predicted and real values of the 166 training samples.

sediment shear wave speed and the physical properties was investigated, the multi-parameter shear wave speed prediction model based on the XGBoost algorithm was established, and the predicted results of the XGBoost model were compared with the single- and dual-parameter models and the GS model. The conclusions are summarized as follows:

(1) The shear wave speed of shallow sediments in the study area has a good correlation with porosity, water content, density, and average grain size. By optimizing the hyperparameters of the model, the best fit of the XGBoost algorithm is obtained when the n_estimator and max_depth are 115 and 6, respectively. The mean absolute error and the goodness of fit between the predicted values and validation data are 3.366 m/s and 9.90%, respectively.

Compared with the single-parameter prediction models, the dual-parameter prediction models, and the GS prediction model, the multiparameter shear wave speed prediction model based on the XGBoost algorithm has the lowest MAE and MAPE between the test data and the predicted values, which are 4.04 m/s and 14.3%,

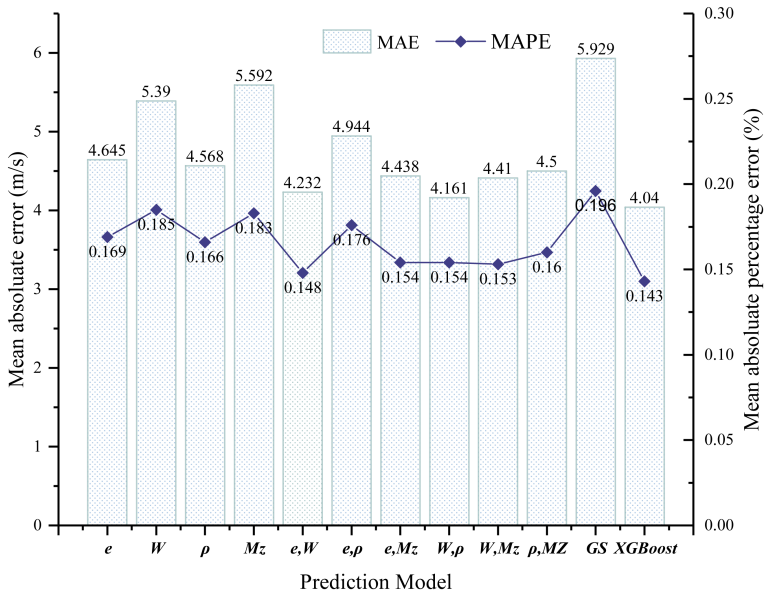

FIGURE 10
Comparison of the error of predicted results of 30 groups of test data substituted into each model.

respectively. It indicates that the multiparameter shear wave speed prediction model based on the XGBoost algorithm has a higher accuracy for predicting the shear wave speed in this area (2).

Data availability statement

The raw data supporting the conclusions of this article will be made available by the authors, without undue reservation.

Author contributions

WM: Writing – original draft, Writing – review & editing. XM: Writing – review & editing. JW: Writing – review & editing. GL: Writing – review & editing. BL: Writing – review & editing. GK: Writing – original draft, Writing – review & editing. JL: Writing – review & editing. LZ: Writing – review & editing. PZ: Writing – review & editing.

Funding

The author(s) declare financial support was received for the research, authorship, and/or publication of this article. This study was supported by the National Key R&D Program of China under Grant No. 2021YFF0501200, in part by the Central Public-Interest Scientific Institution Basal Research Fund under Grant No. GY0220Q09, and in part by the National Natural Science Foundation of China under Grant No. U2006202, No. 42376076, and No. 41706062.

Acknowledgments

We thank all those involved in the marine surveys that collected the data used in this study. Thanks to Mujun Chen from Ocean University of China for helpful discussions on machine learning methods.

Conflict of interest

The authors declare that the research was conducted in the absence of any commercial or financial relationships that could be construed as a potential conflict of interest.

Publisher's note

References

Buckingham, M. J. (1997). Theory of acoustic attenuation, dispersion, and pulse propagation in unconsolidated granular materials including marine sediments. *J. Acoustical Soc America* 102 (5), 2579–2596. doi: 10.1121/1.420313

Buckingham, M. J. (2005). Compressional and shear wave properties of marine sediments: comparisons between theory and data. *J. J. Acoustical Soc. America* 1171, 137–152. doi: 10.1121/1.1810231

Chen, T., and Guestrin, C. (2016). XGBoost: A scalable tree boosting system. [C]// Proceedings of the 22nd ACM SIGKDD International Conference on Knowledge Discovery and Data Mining, August 13 -17, 2016, San Francisco, California. New York: ACM, 2016:785–794. doi: 10.1145/2939672.2939785

Chen, M. J., Meng, X. M., Kan, G. M., Wang, J. Q., Li, G. B., Liu, B. H., et al. (2022). Predicting the sound speed of seafloor sediments in the east China sea based on an XGBoost algorithm. *J. J. Mar. Sci. Eng.* 10 (10), 1366. doi: 10.3390/jmse10101366

Chen, M. J., Meng, X. M., Kan, G. M., Wang, J. Q., Li, G. B., Liu, B. H., et al. (2023). Predicting the sound speed of seafloor sediments in the middle area of the Southern Yellow Sea based on a BP neural network model. *J. Mar. Georesour. Geotechnol.* 41 (6), 662–670. doi: 10.1080/1064119X.2022.2085216

Guo, X. S., Liu, X. L., Li, M. Q., and Lu, Y. (2023). Lateral force on buried pipelines caused by seabed slides using a CFD method with a shear interface weakening model. *J. Ocean Eng.* 280, 114663. doi: 10.1016/j.oceaneng.2023.114663

Hou, Z. Y. (2016). *The Correlation of Seafloor Sediment Acoustic Properties and Physical Parameters in the Southern South China Sea* (Chinese Academy of Sciences: Institute of Oceanology).

Hou, Z. Y., Wang, J. Q., Chen, Z., Yan, W., and Tian, Y. H. (2019). Sound velocity predictive model based on physical properties. *Earth and Space Science* 6, 1561–1568. doi: 10.1029/ 2018EA000545

Hou, Z. Y., Wang, J. Q., and Li, G. B. (2023). A sound velocity prediction model for seafloor sediments based on deep neural networks. *J. Remote Sens.* 15, 4483. doi: 10.3390/rs15184483

Jackson, D. R., and Richardson, M. D. (2007). *High-frequency seafloor acoustics* (New York: Springer).

Kan, G. M., Cao, G. L., Wang, J. Q., Li, G. B., Liu, B. H., Meng, X. M., et al. (2020). Shear wave speed of shallow seafloor sediments in the northern South China Sea and their correlations with physical parameters. *J. Earth Space Sci.* 7 (3). doi: 10.1029/2019ea000950

Kan, G. M., Zhang, Y. F., Su, Y. F., Li, G. B., and Meng, X. M. (2014). Shear wave speeds measured for sediments from the middle of the southern Yellow Sea and their correlation with physical-mechanical parameter. *J. Adv. Mar. Sci. (in Chinese)* 32 (03), 335–342. doi: 10.3969/j.issn.1671-6647.2014.03.005

Li, Y. Z., Wang, Z. Y., Zhou, Y. L., and Han, X. Z. (2018). Improvement and application of xgboost algorithm based on Bayesian optimization. *J. J. Guangdong Univ. Technol.* 35 (01), 23–28. doi: 10.12052/gdutxb.170124

Lu, B., Li, G. X., and Huang, S. J. (2004). A preliminary study of shear wave in seafloor surface sediments. *J. J. Trop. Oceanogr. (in Chinese)* 23 (4), 11–18. doi: 10.1080/1064119x.2022.2085216

Lu, B., and Liang, Y. B. (1991). Correlation between sound velocity and physical-mechanical parameters of marine sediments. *J. Trop. Ocean* 10 (3), 96–100.

Lundberg, S., and Lee, S. I. (2017). *A unified approach to interpreting model predictions. 31st Annual Conference on Neural Information Processing Systems* Vol. 30 (Long Beach: NIPS), 4768–4777.

Pan, G. F., Ye, Y. C., and Lai, X. H. (2006). Shear wave speed of seabed sediment from laboratory measurements and its relationship with physical properties of sediment. *J. Acta Oceanol. Sin. (in Chinese)* 28 (5), 64–68. doi: 10.3321/j.issn:0253-4193.2006.05.008

Qi, W., Sun, R., Zheng, T., and Qi, J. (2023). Prediction and analysis model of ground peak acceleration based on XGBoost and SHAP. *J. Chin. J. Geotech. Eng.* 45 (09), 1934–1943. doi: 10.11779/CJGE20220417

Qian, N., Wang, X. S., Fu, Y. C., Zhao, Z. C., Xu, J. H., and Chen, J. J. (2020). Predicting heat transfer of oscillating heat pipes for machining processes based on extreme gradient boosting algorithm. *J. Appl. Thermal Eng.* 164, 114521. doi: 10.1016/j.applthermaleng.2019.114521

Richardson, M. D., and Briggs, K. B. (1996). *In situ* and laboratory geoacoustic measurements in soft mud and hard-packed sand sediments: Implications for high-frequency acoustic propagation and scattering. *J. Geo Marine Lett.* 16 (3), 196–203. doi: 10.1007/BF01204509

frontiers | Frontiers in Marine Science

TYPE Original Research
PUBLISHED 26 February 2024
DOI 10.3389/fmars.2024.1261164

OPEN ACCESS

EDITED BY
Preston Wilson,
The University of Texas at Austin,
United States

REVIEWED BY
Megan Ballard,
The University of Texas at Austin,
United States
Hu Wang,
Tianjin University, China

*CORRESPONDENCE
Jiewen Zheng
jwzheng@qnlm.ac
Xiaolei Liu
xiaolei@ouc.edu.cn

RECEIVED 19 July 2023
ACCEPTED 02 February 2024
PUBLISHED 26 February 2024

CITATION
Liu B, Zheng J, Wang J, Sun L and Liu X (2024) On-deck vs. laboratory analyses of the sound velocity of sediments from the Huanghai and Bohai seas. *Front. Mar. Sci.* 11:1261164. doi: 10.3389/fmars.2024.1261164

On-deck vs. laboratory analyses of the sound velocity of sediments from the Huanghai and Bohai seas

Baohua Liu[1], Jiewen Zheng[1*], Jingqiang Wang[2], Lei Sun[2] and Xiaolei Liu[3*]

[1]Laoshan Laboratory, Qingdao, China, [2]First Institute of Oceanography, Ministry of Natural Resources, Qingdao, China, [3]Shandong Provincial Key Laboratory of Marine Environment and Geological Engineering, Ocean University of China, Qingdao, China

One popular method of obtaining the acoustic parameters of seabed sediments is by measuring the sound velocity of sediment samples in a laboratory. However, the effects of environmental variation and physical perturbation on acoustic properties are typically neglected in the application of such measured acoustic parameters. In this study, sediment samples were collected from the Huanghai and Bohai seas to measure sound velocity both on the deck and in the laboratory using a digital sonic measuring system. Additionally, sediment compositions, physical and mechanical properties and microstructures were determined. Sound velocity comparisons between on-deck and laboratory measurements indicate that laboratory-measured velocities are generally higher than those measured on the deck, with differences ranging from 1.45 m/s to 130.05 m/s, due to the water loss and densification of sedimentary particles in laboratory settings. The discrepancy of sound velocities measured in the laboratory and on the deck also differ based on the types of sediments sampled. Overall, the discrepancy increases with measurement frequency, increasing average grain diameter and sand content, as well as with decreasing clay content.

KEYWORDS

sound velocity, on-deck measurement, laboratory measurement, seafloor sediment, Huanghai Sea, Bohai Sea

1 Introduction

The seafloor sedimentary environment, as an important part of the ocean, is complex and heterogeneous, and little is known across different spatial scales at the sediment–water interface than for the seawater environment above (Liu et al., 2022). In marine geological research, acoustic measurements may be considered as the most effective means of exploration due to the excellent propagation characteristics of sound waves through the water column (e.g., as compared to optical and electromagnetic technologies) (Chadwick

et al., 2012). The history of geoacoustics can be traced to 1950s, when measurements of the velocity and attenuation of sound waves in sediments were first being conducted in the United States (Hamilton, 1956). Since the 1970s, geoacoustics has developed as an interdisciplinary method applied to hydroacoustic, geological, geophysical and oceanographic investigations (Zhang, 1997). In the 1980s, seafloor sound propagation and sedimentary properties in marine engineering were joined in China (Liang and Lu, 1991), and in the 21st century, a series of related national projects were funded, such as the National Natural Science Foundation projects, publically funded science and technology marine research and the 863 high-technology projects (Han et al., 2011; Kan et al., 2011; Liu et al., 2013). Presently, measurements of the geoacoustic properties of compression wave velocities (namely sound velocity) and shear wave velocities have been necessary components of studies of marine areas.

A detailed understanding of acoustic wave propagation in marine sediments can ultimately lead to improved geoacoustic models and better geotechnical predictions from high-resolution acoustic datasets. Accurate and reliable measurements of geoacoustic parameters over a broad frequency range are key to advancing our knowledge in this area, given that different sediment types may exhibit different characteristics (Best et al., 2001). Sediment acoustic properties are of great importance to the study of acoustic transfer theory, which includes the parameters of sound velocity, shear wave velocity and sound attenuation, among other factors. In the studies of many fields, such as in marine engineering and construction, marine geological hazard analyses and prediction and marine resource exploration, knowledge of seafloor acoustics is essential (Zheng et al., 2014). The direct measurement methods of geoacoustic properties can be classified into three categories:

1. *In situ* measurements: Since the 1990s, several *in situ* techniques have been developed and used to measure acoustic properties, including the *in situ* sediment geoacoustic measurement system (Richardson and Briggs, 1996), sediment acoustic and physical property apparatus (Best et al., 2001), *in situ* sound speed and attenuation probe (ISSAP) (Kraft et al., 2002), acoustic lance (AL) (Fu et al., 2004), sediment acoustic speed measurement system (Yang et al., 2008), multifrequency *in situ* geoacoustic measurement system (Tao et al., 2009), hydraulic-driven *in situ* sediment acoustic measurement system (HSISAMS) (Kan et al., 2011), drag-type *in- situ* acoustic measurement system (Hou et al., 2014), the ballast *in situ* sediment acoustic measurement system (BISAMS) (Wang et al., 2018). These can obtain the closest approximation to the real data, but at the highest cost and with complex operational processes; currently, such measurements have only been applicable to the shallow seafloor. Most of these measurement systems can only insert acoustic transducers into the shallow seafloor sediment, and the operation of *in situ* device are inconvenient such that the system has low working efficiency.

2. On-deck measurements: Sediment samples collected on a research vessel can obtain a close approximation of the real, *in situ* data. Baldwin et al. (1981) made a marine acoustic measurement device that could measure the sound velocity of the seafloor sediment onto the ship's deck. Kan et al. (2011) carried out the sediment measurement on the deck and compared sound speeds of seafloor sediments measured by *in- situ* with the deck laboratorial technique in Southern Yellow Sea. Hou et al. (2013) used the coaxial gap measurement method to take a deck acoustic measurement of the seabed sediments in the Nansha sea area and obtained the sound velocity.

3. Laboratory measurements: As early as 1956, Hamilton (1965) used the resonance chamber technique in the laboratory to test the sound velocity and sound attenuation of sediments in the shallow sea of San Diego. Hamilton and Bachman (1982) measured the compressional wave velocity of sediment from the Bering Sea, North Sea, Mediterranean Sea, equatorial Pacific, and other areas, in the laboratory by a pulse technique (operating at about 200 kHz). Lu and Liang (1994) measured the sound velocity of marine sediments in the southeast coast of China in the laboratory and established its statistical relationship with physical parameters. Best et al. (2001) measured velocity and attenuation in the laboratory at 200-800 kHz on a 1 m long sediment core taken from the Lough Hyne, Ireland, and compared the laboratory and *in situ* measurement results. McCann et al. (2013) described a new laboratory technique for measuring the compressional wave velocity and attenuation of jacketed samples of unconsolidated marine sediments within the acoustic (sonic) frequency range 1-10 kHz. Zheng et al. (2017) measured the sediment from coastal areas of Jiaozhou Bay in the laboratory, and analysed the correlation between sediment acoustics and geotechnical properties. These measurements are widely used in submarine investigations, but the data obtained can be influenced by the measurement conditions.

The deviations of laboratory-measured data should not be neglected when analysing and using such data in the construction of geoacoustic models and the inversion of physical properties. To solve the problem of such deviations between laboratory and on-deck data due to the changes in measuring conditions, three questions should be considered. First, how much do the laboratory geoacoustic data deviate from the real (*in)situ* value? Secondly, what is the cause of such deviations? Finally, how might laboratory measurements be calibrated to generate a closer approximation of the real data? In this study, sound velocity, as one important parameter of sedimentary geoacoustic properties, was chosen to compare the differences between measurements made in the field (on-board a research vessel) and those made in the laboratory. Together with the analyses of sediment composition, physical and mechanical properties and microstructure, the mechanism underlying the discrepancy between the two methods was determined, and suggestions were made regarding the calibration of laboratory data for sediment sound velocities in the Huanghai and Bohai seas.

2 Study area

Twenty-five box-type sediment samples with lengths of ~20–30 cm were collected using a box corer ($47 \times 47 \times 114$ cm^3) from the Bohai Sea and the north part of the Huanghai Sea, over a longitudinal range of 36–40°E and a latitudinal range 119–124° 30'N on the spring voyage of the Dongfanghong II in 2014 (Figure 1). After the seafloor sediments were collected, we

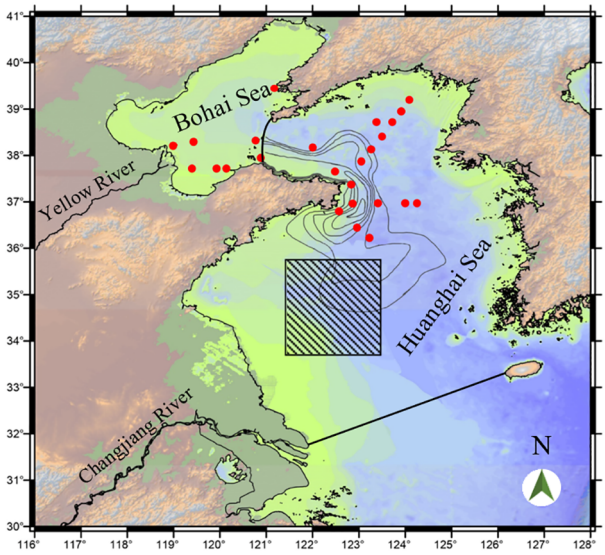

FIGURE 1
Distribution of sampling sites in the Bohai and northern Huanghai seas in the spring voyage of Dongfanghong II in 2014 (red circles), and the sampling area in the southern Huanghai Sea in the first investigation of sediment acoustics in China in 2009 (square shadow).

inserted 110.0-mm-diameter PVC tubes into the box corer to collect short cylindrical samples to preserve the sediment microstructure. These sediment cores were packaged in PVC liner tubes and stored in a sample room with constant temperature and humidity. In order to further analyse the application of the obtained differences between sound velocities measured on the deck and in the laboratory for different types of sediments, data on the sound velocities of sediment samples collected from the southern Huanghai Sea in 2009 are also presented, with the sampling area shown in Figure 1. The sediment samples of the southern Huanghai Sea in 2009 were collected using the gravity sampler, and the top half meter sediment samples were measured using the acoustic transmission method. The detailed collecting and measuring method of sediment in 2009 can be referenced from Kan et al. (2011).

Sediments distributed offshore of China display the characteristics of terrigenous debris deposits, which are the product of interactions among fluvial transport, seafloor erosion and deposition, hydrodynamic processes and biological activities. The Huanghai and Bohai seas are mainly dominated by mud and sandy mud, due to their isolation, complex profiles and the high intensity of terrestrial runoff and tidal currents. The Bohai Sea is an enclosed shallow sea, deep with the Asian continent, and with a mean water depth of 18 m; it is connected to the Huanghai Sea via Bohai Bay in the east and is bordered by neighbouring lands on its other three sides. Liaodong Bay, Bohai Bay and Laizhou Bay are located in the north, west and south of the Bohai Sea, respectively. The main rivers discharged into the Bohai Sea are the Huanghe, Haihe, Luanhe and Liaohe. The thickness of quaternary deposits ranges from 300–500 m, and these sediments are composed of terrigenous debris from runoff. Irregular patches of sediments are distributed on the seafloor of the Bohai Sea, and there is a significant discrepancy between the three main bays and the central zone (Meng et al., 2015).

Sediments discharged into the Huanghai Sea are subjected to the interactions of winds, waves, the circulations of a warm current, coastal current and cold water masses, as well as the tidal current. There are three depositional zones each of coarse and fine sediments, and a transitional depositional zones in the Huanghai Sea, which are mainly composed of modern deposits. The coarse depositional zones are located in the eastern Huanghai Sea, Bohai Bay and Haizhou Bay, while the fine, and dominantly modern, depositional zones are located in the middle of the northern and southern regions of the Huanghai Sea, as well as in the old Yellow River subaqueous delta.

3 Materials and methods

3.1 Measurement of sound velocity

The sound velocities of twenty-five sediment samples were measured, both on the research vessel and in the laboratory, and the data for sixteen typical sediment samples are presented here. The sound velocity measurement on the deck were carried out immediately after the sediment cores were collected from seafloor and the time elapsed between the collecting and the measurement was about 30-60 minutes. The sound speed were measured using the whole sediment sample core on the deck and in the laboratory, respectively. The sound velocities of sediment samples were measured at temperatures ranging from ~18.0–20.5°C on the deck and ~19.5–21.5°C in the laboratory. The measurements were conducted using the same equipment, at frequencies ranging from 25–250 kHz, both in the deck and laboratory (Figure 2). The field bench-top acoustic system was composed of a portable bench and a digital sonic meter, with a measurement accuracy equal to ±0.1 mm of the sample length. Meanwhile, the laboratory bench-top acoustic system was composed of an automatic bench and a digital sonic meter, with the same measurement accuracy as in the field tests. The digital sonic meter was equipped with a handheld computer, Bluetooth and a high-speed analogue-to-digital data converter (A/D), with a low-power consumption and a small volume and weight (http://www.cqbtsk.com.cn/english/Sonic/WSD-3.htm). The portable field bench included a dismountable bottom beam, two fixed units and two support units, and the laboratory bench included a movable and locatable slide platform, a fixed holder, guide rail, sliding holder, V-shaped support and a dividing ruler. The purpose of the beams, the platform, and the support units are to fix and support the sediment cores. During the measurement, the sediment core was placed on the measuring platform at first. The acoustic measurements were conducted along with the length of the cores. The planar emitting transducer was pressed onto one side of the sample core section and the receiving transducer was pressed onto the other side of the sample core. A pulse signal was emitted at the central frequency of each emitting transducer. This method uses travel time differences between the acoustic signal through sediment samples and

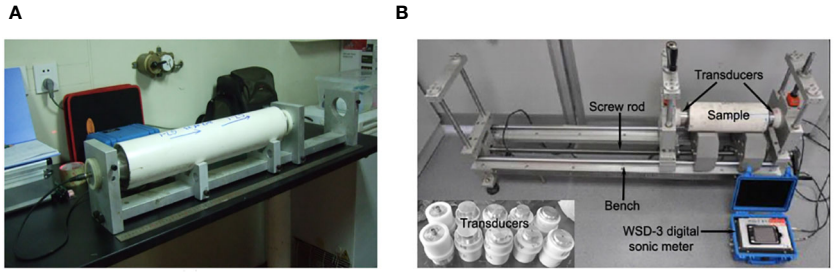

FIGURE 2
Apparatuses used for the measurement of sound velocities in **(A)** on the deck and in **(B)** in the laboratory.

identical reference cores filled with water to measure compressional wave phase speed. The take-off point of a sound wave signal were point out using the conventional manual identification method. The measurement accuracy of the sediment core length of the bench was 0.1 mm, and the digital sonic instrument had a sampling rate of 10 MHz (that is, the accuracy of travel time is ± 0.1 μs) and a sampling length of 4,096 samples. So, the accuracy of sound speed of bench-top acoustic system was estimated to be better than ± 0.1% for a typical sample with a length of 30 cm and velocity of 1500 m/s.

3.2 Measurement of bulk properties

Together with the measurement of the sound velocities of sediment samples, the particle composition, physical and mechanical properties and microstructure were analysed in the laboratory. Laboratory procedures to determine the geotechnical properties of the sediment samples followed the specifications for oceanographic survey GB/T 12763.8-2007 and the standard for geotechnical testing method GB/T 50123-1999, belonging to National Standard of the People's Republic of China. A laser particle analyser (Malvern 2000, UK) was used to determine the composition, mean grain size, sand content, clay content and sorting coefficient; the sediments were then classified using Shepard's (1954) ternary diagram based on the obtained sand and clay contents. The physical properties analysed included the wet bulk density, dry bulk density, water content, porosity, permeability coefficient and plasticity index. The wet bulk density is the weight of the mineral solids and porewater per unit volume and was measured using a cutting-ring method using a steel ring sampler (diameter 6 cm, height 2 cm) which was pushed into the sediment sample (Zhou et al., 2008). The water content was measured via oven-drying. The dry bulk density was calculated from the wet bulk density and water content (Zheng et al., 2011). Porosity was calculated by the specific gravity and dry bulk density (Zheng et al., 2011), and the permeability coefficient was measured using the water head difference from the permeability test (Clearman, 2007). The parameters mechanical properties measured in laboratory were the penetration and shear strengths, wherein the penetration strength was measured using a penetrometer (Lei and Xiao, 2002), and shear strength was measured using a miniature Vane shear apparatus (Xu et al., 2017). The liquid limit and plastic limit of sediments were measured using liquid-plastic limit combined tester (Meng et al., 2015), and the plasticity index is the difference of liquid limit and plastic limit. Microstructural observation were performed using a scanning electron microscope (SEM; QUANTA 200, Thermo Fisher Scientific, USA), at the magnifications of ×100, ×800 and ×1500.

4 Results

4.1 Sound velocity

At different frequencies, the differences in the sound velocities of the silty sand samples collected from the northern Huanghai Sea and Bohai Sea measured on-site and in the laboratory were generally ~85–130 m/s, and those measured in the laboratory were significantly higher than those measured on the deck. The discrepancies in the sound velocities were slightly different at different frequencies. Meanwhile, it was also found that the dispersion of the sound velocity at different measurement frequencies, which was obtained in the two measurement methods, was consistent (Figures 3A–C).

4.1.1 Silty sand

In this study, a total of three samples of silty sand were collected; the mean particle sizes were 8.20 μm, 7.20 μm and 6.70 μm, respectively, and contents of sand were 62.4%, 57.28% and 49.04%. The clay contents were 15.08%, 11.51% and 7.3%. As can be seen in Figures 3A–C, the larger the mean particle size was, the higher the sand and silt content, and the greater the difference between the sound velocities measured on-site and in the laboratory.

For the same sediment samples, as the measurement frequency differed, the difference between the sound velocities measured on-site and in the laboratory also differed. In order to facilitate the statistical and comparative analysis of sound measured velocities, the ratio of the measured sound velocity on the deck ($V_{p\text{-}f}$) to that measured in the laboratory ($V_{p\text{-}l}$) was analysed, and it was found that for the samples of silty sand, V_{p-f}/V_{p-l} ranged from 0.92–0.94. For the same set of sediment samples, V_{p-f}/V_{p-l} was essentially the same when measured at different frequencies. For silty sand samples, the higher the sand content was, the greater the value of V_{p-f}/V_{p-l}, and there was no clear effect of the clay content on V_{p-f}/V_{p-l}.

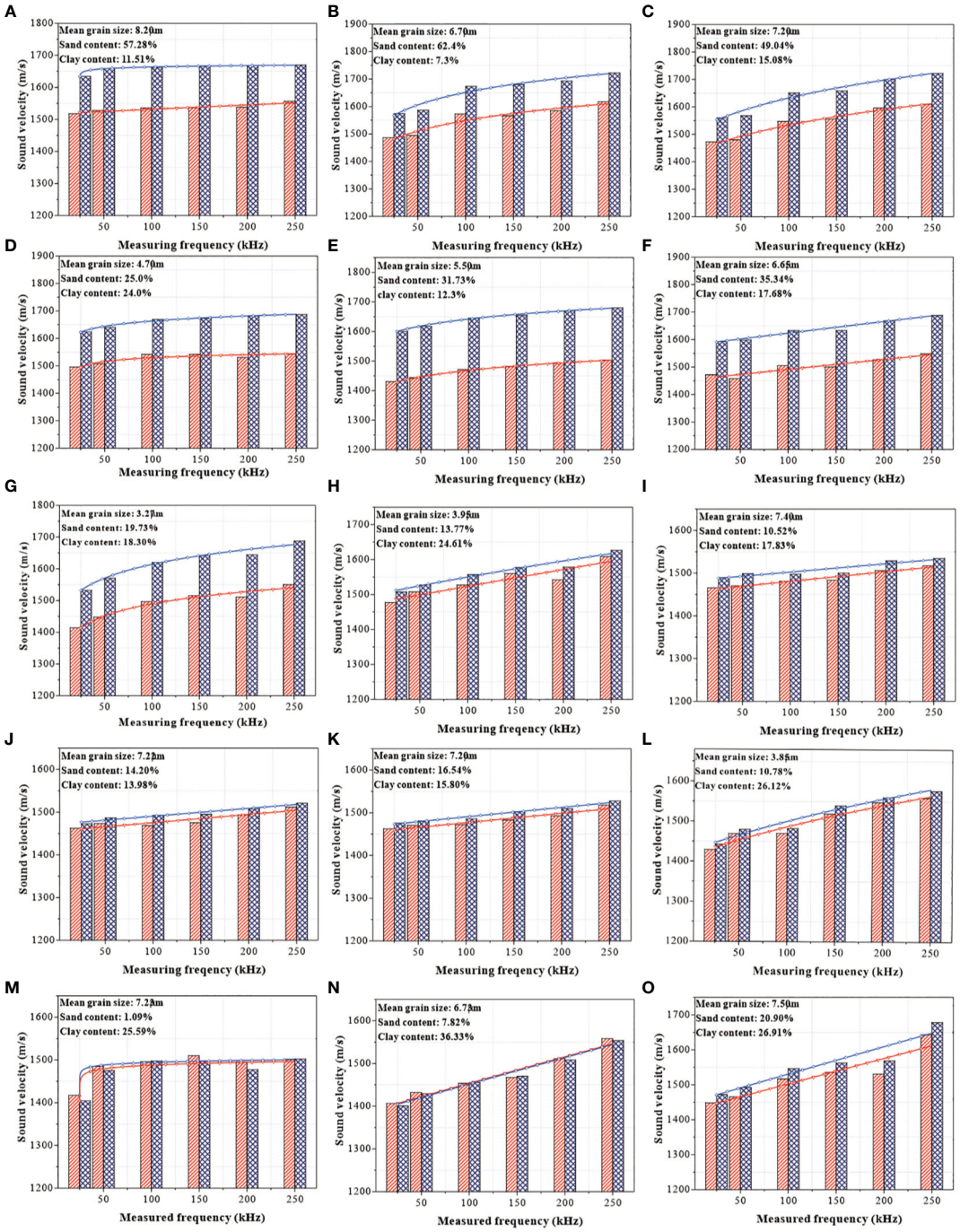

FIGURE 3
Sound velocities of **(A–C)** silty sand, **(D–G)** sandy silt, **(H–K)** silt and **(L–O)** clayey silt sediment samples measured on the deck (red bars) and in the laboratory (blue bars), along with their lines of best fit (red = field data; blue = laboratory data).

4.1.2 Sandy silt

At different frequencies, the difference between the sound velocities in the sandy silts collected from the northern Huanghai Sea and Bohai Sea that were measured on-site and in the laboratory was generally ~120–180 m/s, which is obviously higher than that of the silty sands. However, what was consistent was the fact that the sound velocities measured in the laboratory were significantly higher than those measured on the deck; the difference between these sound velocities was slightly different at different measurement frequencies. It was also found that the dispersion of the sound velocities at different frequencies were consistent (Figures 3D–G).

In this study, a total of 12 samples of sandy silt were collected, and four typical sediment samples were selected for analyses. The mean particle sizes were 6.65 μm, 5.50 μm, 70 μm, and 3.27 μm, respectively, and the contents of sand were 19.73%, 25.0%, 31.73% and 35.34%. The clay contents were 24.0%, 12.30%, 17.68% and 18.30%. From Figures 3D–G, it can be seen that the higher the clay

content of the sandy silt was, the higher the degree of dispersion of sound velocities measured on-site and in the laboratory. Meanwhile, the higher the sand and silt contents were, the higher the differences were in the sound velocities measured on-site and in the laboratory.

Comparing and analysing the ratio of the measured sound velocities on the deck ($V_{p\text{-}f}$) to those measured in the laboratory ($V_{p\text{-}l}$), it was found that the V_{p-f}/V_{p-l} of the sandy silt sediments ranged from 0.90–0.92, which is slightly lower than the range of the silty sand samples. However, this finding was consistent with the silty sand samples in that the sound velocity V_{p-f}/V_{p-l} measured at different frequencies was basically the same for the same sediment samples. For the sandy silt samples, the higher the sand and silt contents were (i.e., the lower the clay content), the greater the value of V_{p-f}/V_{p-l} was, and the effect of clay content on V_{p-f}/V_{p-l} was more pronounced than for the silty sand.

4.1.3 Silt

The difference in sound velocities of the silt samples collected from the northern Huanghai Sea and Bohai Sea measured on-site and in the laboratory differed by measurement frequency, and was generally ~10–40 m/s, which is obviously lower than the ranges of the sandy silt and silty sand samples. However, consistent with the silty sand samples was the fact that the measured sound velocities in the laboratory were significantly higher than those measured on the deck, but the difference was not large, and the differences varied by measurement frequency. Additionally, it was found that the dispersion of the sound velocities at different frequencies was consistent (Figures 3H–K).

In this study, a total of 10 samples of silt were collected, and four typical samples were selected for analyses. The mean particle sizes were 7.40 μm, 7.29 μm, 7.22 μm and 3.95 μm, respectively, and the sand contents were 16.54%, 14.20%, 13.77% and 10.52%. The clay contents were 24.61%, 17.83%, 15.80% and 13.98%. As can be seen from Figures 3H–K, the higher the clay contents of the silt samples were, the lower the degree of dispersion there was in the sound velocities measured on-site and in the laboratory, and the smaller the difference between the two. Meanwhile, the higher the sand and silt contents were, the higher the differences were in the sound velocities measured on-site and in the laboratory. Compared with the silty sand and sandy silt samples, the degree of dispersion on the deck and in the laboratory was much lower.

By comparing and analysing the ratio of the sound velocities measured on the deck ($V_{p\text{-}f}$) to those measured in the laboratory ($V_{p\text{-}l}$), we found that the V_{p-f}/V_{p-l} of the sandy silt samples ranged from 0.98–0.99, which is notably higher than the ranges for silty sand and sandy silt samples. However, in agreement with these sediments, the sound velocity V_{p-f}/V_{p-l} measured at different frequencies was essentially the same for the same sediment samples. Nevertheless, the effects of mean particle size, sand content and clay content on the value of V_{p-f}/V_{p-l} was not statistically significant.

4.1.4 Clayey silt

At different frequencies, the difference in the sound velocities of the clayey silt samples collected from the northern Huanghai and Bohai seas and measured on-site and in the laboratory was generally approximately -15–40 m/s, which is obviously lower than that of the sandy silt and silty sand samples. Additionally, these samples were also inconsistent with the those of the first three sediment types, as the difference between the measured sound velocities in the laboratory and on the deck was not significant, and not all of the laboratory measurements were higher than those from the field. However, it was found that the dispersion of the sound velocities at different measurement frequencies was consistent across all sediment types (Figures 3L–O).

In this study, a total of 4 samples of clayey silt were collected, for which the particle size composition is shown in Figures 3L–O. Based on comparative analyses between the sound velocities measured in the laboratory and on the deck, it was found that when the clay content was very high, the difference between the two methods was very small, and the degree of dispersion was also very low. Conversely, when the sand content was high, the difference between the two methods was large.

Comparing and analysing the ratio of the sound velocities measured on the deck ($V_{p\text{-}f}$) to those measured in the laboratory ($V_{p\text{-}l}$), it was found that the V_{p-f}/V_{p-l} of the clayey silt samples ranged from 0.99–1.01, which is not only higher than the ranges of silty sand, sandy silt and silt, but the ratio is also >1.0, which indicates that during the measurement of clayey silt, there were some sound velocities measured on the deck that were higher than those measured in the laboratory. Meanwhile, consistent with the former sediment types, the sound velocity V_{p-f}/V_{p-l} measured at different frequencies was basically the same for the same sediment samples. The effect of mean particle size, sand content and clay content on the value of V_{p-f}/V_{p-l} was not significant.

4.2 Compositions of different sediments

There were four types of sediments collected in the study area of the Yellow Sea and Bohai Sea – silty sand, sandy silt, silt and clayey silt. These different types of sediments exhibited different degrees of granularity in terms of sand content, clay content, mean particle size and the sorting coefficient (Figure 4). For the sand content, samples of silty sand had significantly higher concentrations, ranging from 48.5–63.2%, while samples of silt and clayey silt had much lower concentrations, ranging from 0.2–21.7%, and samples of silt exhibited a moderate concentration in the range of 21.4–37.0%. With respect to clay content, samples of clayey silt had substantially higher concentrations, ranging from 26.6–36.9%. Meanwhile, samples of silty sand had much lower concentrations, ranging from 7.1–15.9%, and samples of sandy silt and silt had middling concentrations, ranging from 12.7–24.7% and 13.8–24.8%, respectively.

The mean particle sizes in samples of silty sand were generally higher, ranging from 6.8–8.4 μm, while those of other types of sediments were substantially lower. This was the most obvious for the samples of sandy silt and clayey silt, which ranged in size from 3.4–6.6 μm and 3.9–7.6 μm, respectively. For the samples of silt, the average sizes of individual grains were generally concentrated in the range of 7.0–7.5 μm. With respect to the sorting coefficient, the

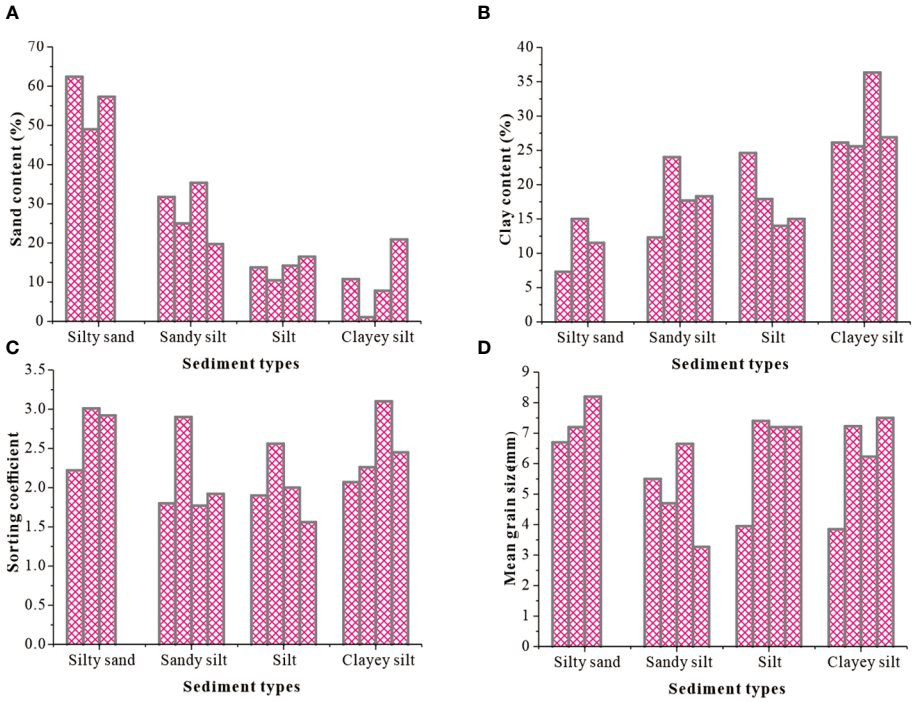

FIGURE 4
Compositions of different sediments types: **(A)** sand content; **(B)** clay content; **(C)** mean grain size; **(D)** sorting coefficient.

different types of sediments in the study area were >1.0 and the silty sand had the highest average sorting coefficient, ranging from 2.2–3.1. The silty sand was poorly sorted with good gradation. The sorting coefficient of the clayey silt range from a similar 2.1–3.2. Compared with the other types of sediments in the study area, the sorting coefficients of the sandy silt and silty sediments were generally lower, while the degree of sorting was generally higher.

This study is focused on the sediments collected in the northern Huanghai and Bohai seas, which mainly comprise silty sand, sandy silt, silt and clayey silt. The sediment samples that Meng et al. (2012) collected in the southern Huanghai Sea involved 10 types of sediment, including super-fine sand, silty sand, clayey sand, sandy silt, coarse silt, medium silt, clayey silt, silty clay, clay and sand–silt –clay. Therefore, compared with the characteristics of the sediments in the southern Huanghai Sea, where the sand content ranged from ~0.3–77.3%, clay content ranged from ~8.9–89.5% and the mean particle size ranged from ~0.002–0.129 mm, the sediments in the northern Huanghai and Bohai seas represent a narrower scope and are generally concentrated. However, in terms of the silty sand, sandy silt, silt and clayey silt, the scope of the granular characteristics of the sediment samples collected in this study is broader than in the study of the southern Huanghai Sea by Meng et al. (2012). These differences are related to the quantitative restrictions imposed by the sediment sampling in this work. Nevertheless, on it can be preliminarily estimated that the distributions of the sediments in the northern Yellow Sea and Bohai Sea are typical (Wang et al., 1996).

4.3 Physical properties of different sediments

Different types of sediments in the northern Huanghai Sea and Bohai Sea have physical properties that are obviously different based on the measured wet bulk density, dry bulk density, water content, porosity, plasticity index and permeability coefficient (Figure 5). For wet bulk density and dry bulk density, the samples of different sediment types were arranged in the order of: silty sand > sandy silt > silt > clayey silt, and respectively in the range of 1.58–2.06 g/cm^3 and 1.07–1.53 g/cm^3. The water contents of different types of sediments in the study area were high, and the moisture content of the clayey silt was the highest. The difference in the water contents among the other three types of sediments was not obvious, as they ranged from 35–45%. With respect to the porosity, clayey silt sediments exhibited the highest porosity and a low degree of consolidation, while the silty sand has the lowest porosity and a high degree of consolidation. Preliminary results showed that it these traits were closely related to the water lost from sediment samples, wherein the samples of sandy silt were more discrete and changed within a wider range. The difference between silt and sandy silt samples was insignificant, and they changed within a standard range.

For the plasticity index, different types of sediments showed more obvious regularity, which increased in the order of: silty sand< sandy silt< silt< clayey silt. The plasticity index of silty sand was in the range of ~6.5–8.5, while for sandy silt it was ~9.0–11.0, for silt,

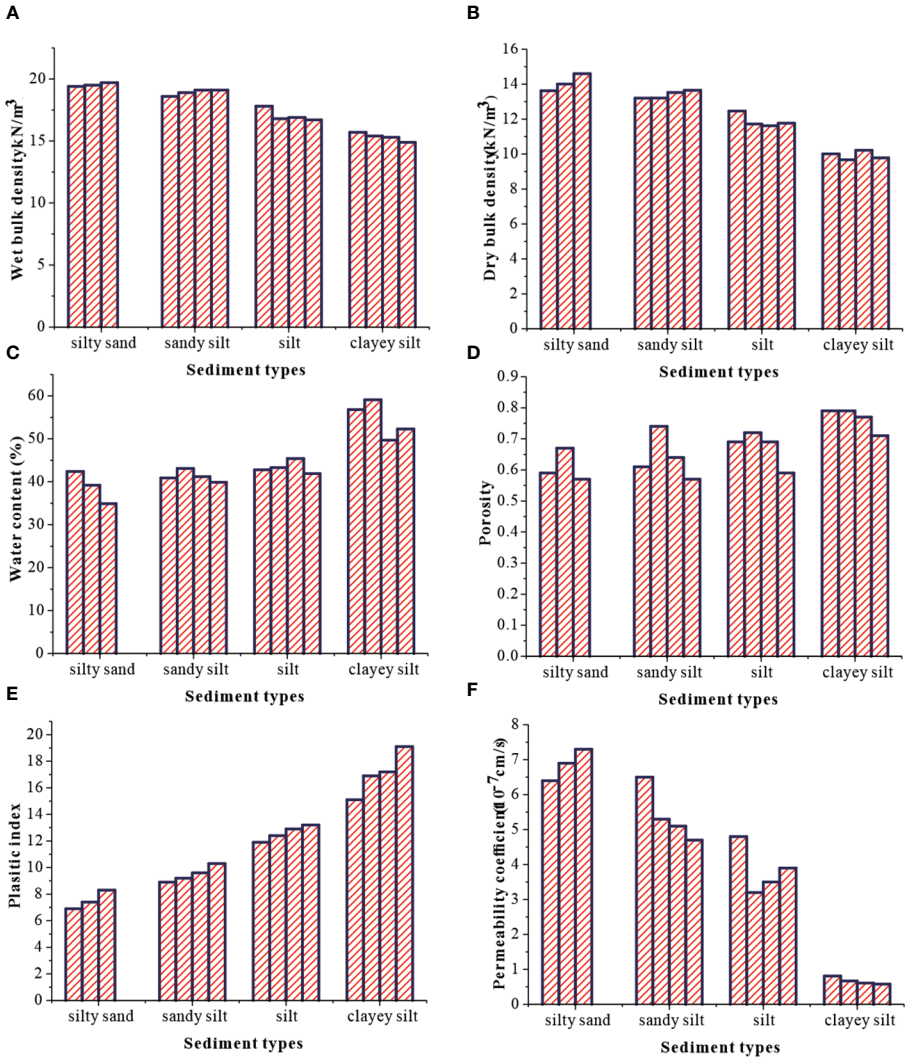

FIGURE 5
Physical properties of different types of sediment samples: **(A)** wet bulk density; **(B)** dry bulk density; **(C)** water content; **(D)** porosity; **(E)** plasticity; **(F)** permeability coefficient.

the range was ~12.5–14.0, and clayey silt ranged from ~14.5–19.5. Finally, the permeability coefficient showed different degrees of regularity for different types of sediments, which increased in the order of clayey silt<silt<sandy silt<silty sand. The permeability of silty sand was in the range of 6.0×10^{-7}–7.5×10^{-7} cm/s, while for sandy silt, it ranged from 4.5×10^{-7}–6.8×10^{-7} cm/s; the permeability range for silt was 3.2×10^{-7}–5.0×10^{-7} cm/s and that of clayey silt was 3.5×10^{-7}–5.5×10^{-8} cm/s.

Compared with the physical properties of the sediments collected in the northern Huanghai and Bohai seas, the sediment types in the southern Huanghai are complex and their properties vary widely. Meng et al. (2012) analysed 10 sediment samples collected from this region in a laboratory, and found a wet bulk density of 1.50–2.07 g/cm^3, a water content of 25.0–107.4%, a porosity of 0.40–0.74 and a permeability coefficient ranging from 9.0×10^{-8}–1.5×10^{-7} cm/s. The consistency of the results between our two studies may be seen in the fact that the physical properties of seafloor sediments correspond well to their types, and coarser sediments have higher values for bulk density and permeability, and lower ones for water content and porosity.

4.4 Mechanical properties of different sediments

The penetration and shear strengths of sediments are important parameters to characterize their macroscopic mechanical properties, which are vital for marine geotechnical engineers. The penetration strength indicates the vertical bearing capacity of the sediment, which is determined by the degree of compaction. The shear strength indicates the maximum shear force that the sediment can bear, which is mainly affected by the adhesion and friction angle of the sediment. Based on laboratory measurements of penetration and shear strength for different types of sediment samples from the northern Huanghai and Bohai seas (Figure 6), it was found that those of silty sand were the highest. The sandy silt and silt exhibited

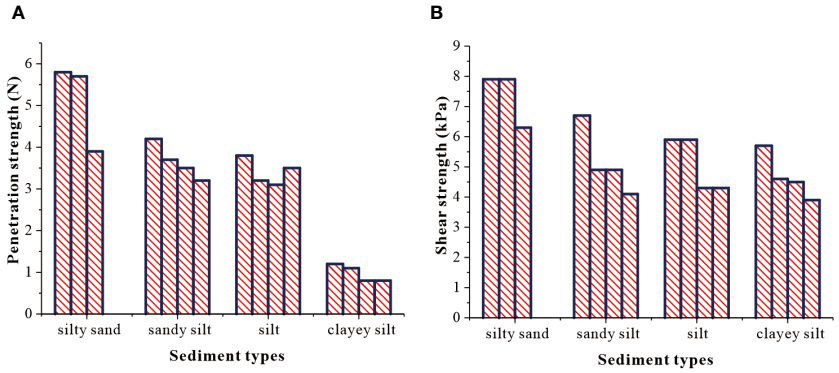

FIGURE 6
Mechanical properties of different types of sediment samples: **(A)** penetration strength; **(B)** shear strength.

middle values, with insignificant differences between them, whereas clayey silt sediments had very low penetration strengths and high shear strengths. The distributions of the mechanical properties of these sediments could also be obtained in the same manner for the laboratory measurements of the sediments from the southern Huanghai Sea (Meng et al., 2012). However, for the sediments in the north, the differences were particularly notable.

Combining the analyses shown in Figures 4–6 and research of Meng et al. (2012) in the southern Huanghai Sea, we identified four types of sediments – silty sand, sandy silt, silt and clayey silt, which could be divided into three categories for measurement in the laboratory. Among them, silty sand constituted a category, sandy silt and silt could be grouped into a single category and clayey silt was the final category. Comparatively, sandy silt and silt have small differences in their particle sizes (i.e., sand content, clay content, average particle size and sorting coefficient), physical properties (i.e., wet bulk density, dry bulk density, water content, porosity, plasticity index and permeability) and mechanical properties (i.e., penetration and shear strength). In this study, the sediment samples were classified according to Shepard's ternary diagram used for classification according to the Marine Investigation Regulations (GB/T12763.8-2007). In marine geotechnical engineering, sediments are divided into sand, silt and clay according to their plasticity indices (Jia et al., 2011). According to the plasticity index method used in marine geotechnical engineering, there are four types of sediments in the study area, as classified according to the Marine Investigation Regulations, which can be broadly divided into the aforementioned three categories. Among them, silty sand and sandy silt can be roughly classified as sand, while silt and clay are classified as such.

4.5 Microstructures of different sediments

The microstructural characteristics of sediments are important factors that determine their physical mechanics and engineering properties, and also have important impacts on their acoustic properties. In this work, three microscopic structures of different magnifications (×100, ×800 and ×1500) were examined by electron microscopy in the sediments from the northern Huanghai Sea and Bohai Sea. The typical microstructure electron microscope images of four different sediment samples are shown in Figure 7. This microscope images represent the dried particles alignment of different sediments.

Silty sand had a sedimentary structure based on sand particles, and silt particles supplemented to become the skeleton, with a small amount of clay filling in. It can be seen from the upper panel of Figure 7 that the samples of silty sand had large skeletal particles and their tendency toward a preferred orientation is obvious. The fine particles are filled and attached to larger particles with large pores, which can be approximated as a single grain structure (Hamilton and Bachman, 1982). The content of the sand in sandy silt was less than that of the silty sand, and the content of fine grain sizes increased. It can be seen from the second panel (row) of Figure 7 that the particle sizes of the sedimentary skeleton were much smaller than in the silty sand, with no clear trend of particle orientation. Additionally, the sediments shown in this panel exhibit moderate roundness, and the voids are filled with more fine-grained particles, while also being attached to the skeleton, with more and smaller pores. The sand content in the silt was even lower, and the main component was silt; the clay content increased relative to the sandy silt. It can be seen from the second panel from the bottom in Figure 7 that the abundance of large particles that make up the skeleton is greatly reduced, and there is an obvious grain orientation. The silt grains exhibit poor roundness, and a large number of fine particles fill in and attach to the skeleton, with more and smaller pores than in the sandy silt. Finally, the sand content in clayey silt was very small, as the main components were fine-grained particles and clay. As can be seen from the bottom panel of Figure 7, the clayey silt forms and approximate bundled sheet structure (Hamilton and Bachman, 1982; Meng et al., 2012), wherein large particles are completely surrounded by fine particles, which become aggregates owing to complex physicochemical interactions.

The observation of the microstructural characteristics of sediments involves relatively matured research methods; however, the physical models of sediment geotechnical and acoustic behaviours and properties based on such microstructures are currently lagging behind. Techniques for measuring the porosity

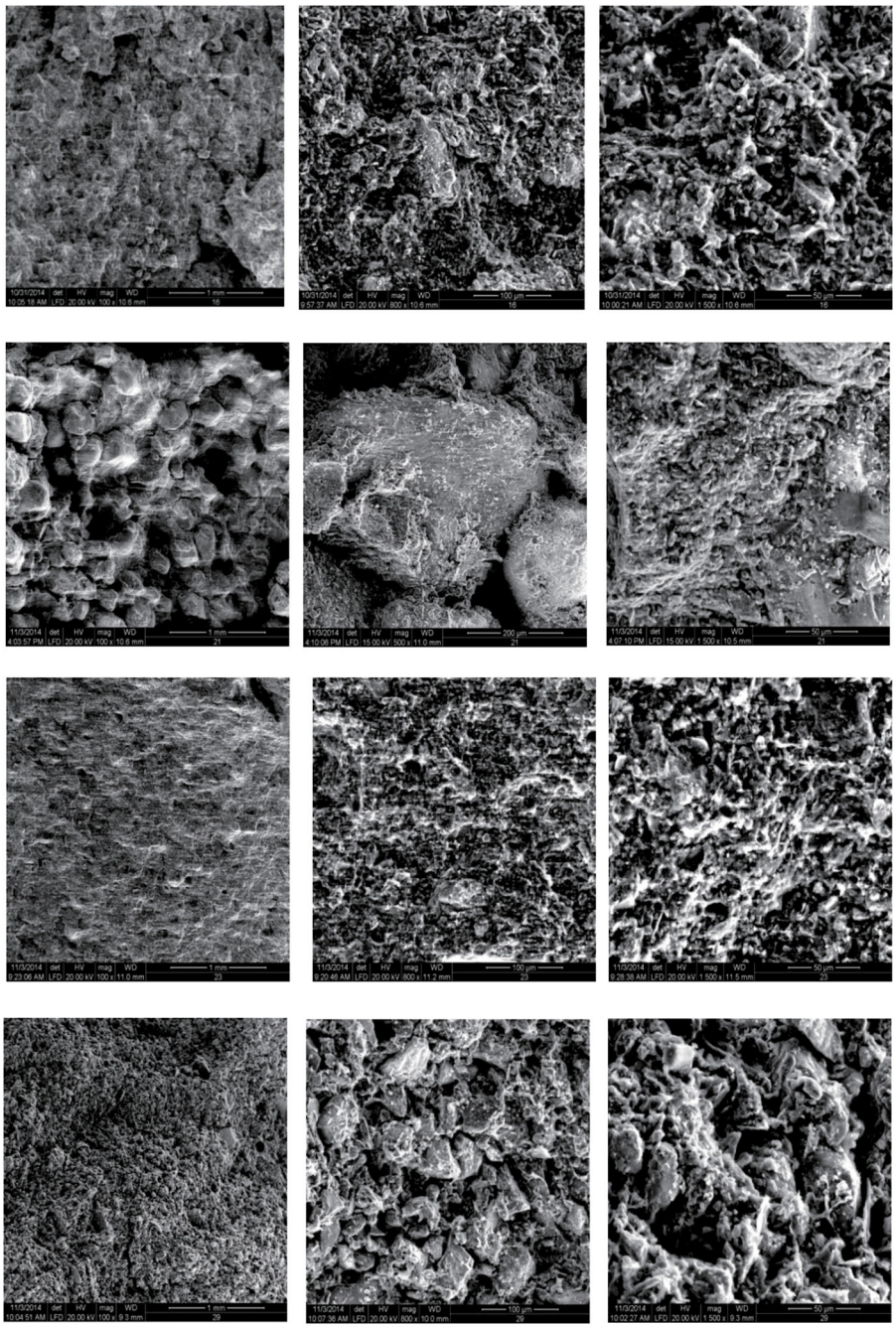

FIGURE 7
Microstructures of (upper row) silty sand, (upper middle row) sandy silt, (lower middle row) silt and (lower row) clayey silt samples at 100, 800 and 1500 times magnification.

sediments from microstructural images have now become possible. Changes in the clay microstructure during consolidation have also been studied and linked to changes in the shape, alignment and spatial arrangement or distribution of clay crystals and aggregates (Zheng et al., 2014). It is also now possible to predict sediment permeability based on the size of the pores pathways observed and the amount and degree of interconnection among pores (Vaughan et al., 2002). Nevertheless, models for predicting compressional or shear wave velocities based on sediment structure and the physicochemical interactions between sediment grains and pore fluids have remained unsuccessful, and much research is still required (B.H. Liu et al., 2013).

5 Discussion

Physical characteristics and the conditions of the depositional environment are two major factors affecting the acoustic properties

of marine sediments. Meanwhile, the influence of the sedimentary environment on these properties is also largely based on the physical characteristics of the sediments. Changes in environmental conditions that may affect the physical properties of sediments include changes in temperature and pressure during the collection of the sample, as well physical disturbances during sample transport. For shallow sea sediments, the effect of deep-water stress (i.e., depressurisation) on geoacoustic properties is negligible (Li et al., 2008; Wang et al., 2008). Here, we discuss the factors and mechanisms influencing sound velocity measurement errors in the laboratory and on the deck for samples from the Huanghai and Bohai seas with respect to the effects of temperature and physical disturbance during the process of sample transport.

5.1 Deviation of sound velocities measured in the laboratory and on the deck

Based on the comparative analysis of the sound velocities measured on the deck and the laboratory for four types of sediments collected from the northern Huanghai and Bohai seas (i.e., silty sand, sandy silt, silt and clayey silt), we found the thresholds of V_{p-f}/V_{p-l}, which ranged from 0.92–0.94, 0.90–0.92, 0.98–0.99 and from 0.99–1.01, respectively (Figure 8). According to our comparative analyses, the V_{p-f}/V_{p-l} values of the four types of sediment in the southern Huanghai Sea are generally within the thresholds of the northern Huanghai Sea and Bohai Sea, and their deviations are less than 5%, which demonstrates that the calculated threshold range of V_{p-f}/V_{p-l} in this study is statistically significant.

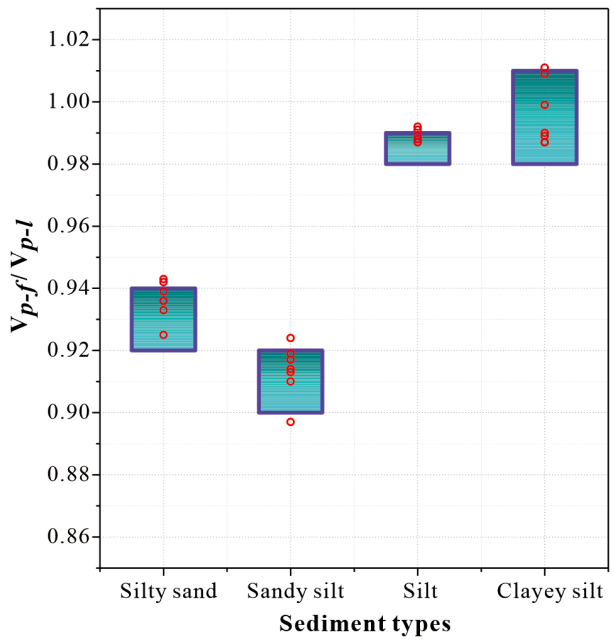

FIGURE 8
Contrasting sound velocity measurements from the on-deck and laboratory between the northern Huanghai Sea and Bohai Sea (green rectangles) and the southern Huanghai Sea (red circles).

5.2 Influence of temperature on the deviation of sound velocity

Temperature is one of the most important factors affecting the sound field in the ocean. A clear theoretical system of its influence has now been formed. However, the influence of temperature on the acoustic properties of seafloor sediments is still in the stage of semi-qualitative analysis and a clear understanding of the mechanism of influence has not yet been formed.

Hamilton (1971, 1972) concluded that the acoustic properties of pore water in sediments are the most sensitive to temperature changes and are also the main factors that control the acoustic properties of sediments with temperature. Zou et al. (2008) found three trends in sound velocities with temperature based on temperature-controlled physical model experiments in a laboratory; these were: (1) the positive growth of sound velocity (STPIK), (2) the negative growth of sound velocity (STNIK) and (3) the fluctuation of sound velocity (STWK). Because the test samples for these three trends were all silt, with little differences in porosity, density or water content, it is difficult to clearly interpret these results in terms of the actual effect of such trends in sediment sound velocities with temperature. In this study, it was speculated that seafloor sediments have complex structures due to their different sedimentary histories (Hamilton, 1976; Lu et al., 2003), and the testes samples were all unconsolidated sediments with a loose structure. The difference between loose and unconsolidated structures composed of pore particles of different shapes and geometries leads to the complexity of the relative motions of seawater through pores and the solid-phase particles under thermal motion, possibly resulting in the formation of the three trends observed by Zou et al. (2008). In other words, the microstructure of loose sediments is a critical factor affecting the trends in sound velocity with temperature.

Based on the laboratory measurements of sound velocities with temperature for nine different types of samples, Zeng et al. (2009) showed that the sound velocity decreased with temperature in the order of sand > clay > silt, presumably because as temperature rises, changes in the seepage state cause the porosity of the sediment to increase, such that the seawater volume increases, resulting in a low sound velocity. Thus, sound velocity increases with temperature in the clayey sand and clayey sand–silt. It is speculated that in the clayey silt, moisture does not easily flow due to the high clay content. Furthermore, the composition of clay minerals and sands play an important role in the response of sediment sound velocities with temperature. In other words, the difference between the grain sizes of sedimentary components is the important factor influencing the variation of the sound velocity with temperature for different types of sediments. Hong et al. (2011) analysed the variation of seafloor sediment sound velocities with temperature in the South China Sea. The sound velocities of the sediments in this area varied slowly and exhibited obvious fluctuations, but the overall trend was almost linearly decreasing. We believe that the mechanism underling the effect of temperature on the sound velocity of seafloor sediments was equivalent to the comprehensive effect on the equivalent elastic modulus and density of the sediments.

In the temperature-controlled physical model experiments in laboratories, such as the studies of Zou et al. (2008) and Zeng et al. (2009), the range of temperatures measured has been 0–30°C, and the range of sound velocities has been 1300–1600 m/s. As for the temperature-controlled sound velocity measurement of samples from the South China Sea (Hong et al., 2011), the range of variation in the sound velocity was 1700–1880 m/s within a similar temperature range as for the aforementioned studies, and the variations in the sound velocities of different types of sediments differed. The measured sound velocities of different sediment samples varies within the range of 1400-1600 m/s over the measured temperature range (Meng et al., 2012). In the shipboard field and laboratory sound velocity measurements of sediment samples from the Huanghai and Bohai seas, the measurement temperature ranged from ~18.0–20.5°C, and the temperature difference in the same group was less than 3°C. Based on the present laboratory measurements of sediment sound velocity, it is assumed that temperature had little effect on the sound velocities measured (about 8 m/s), as such a small difference in temperature (≤2.5°C) can be neglected.

5.3 Influence of particle composition on the deviation of sound velocity

The particle size composition of seafloor sediments is one of the important parameters in seafloor sedimentology and soil mechanics, an important parameter can reflect the sedimentary origin, environment and processes of the sediments. Characterizing the size composition of sediments is important for laboratory analyses of seafloor sediment samples (Lu and Liu, 2008). Research of the relationship between the particle size composition and acoustic properties of seafloor sediments began in 1960s and 1970s. Akal (1972) and Hamilton (1976) extensively studied the effects of particle size on the sound velocities of seafloor sediments in the world oceans, and established the empirical relationships of grain size parameters, such as sand content, clay content and mean particle size, with their acoustic properties. In subsequent works, Liang and Lu (1983), Prasad (2002), X.L. Liu et al. (2013) and Kan et al. (2014) have analysed the effect of sediment particle size on the acoustic properties of shallow sediments in different marine areas, and established an empirical ground acoustic model that describes the relationship between sediment particle size and geoacoustic properties, which are suitable for different areas. These studies have revealed that the influence of sediment particle size on the acoustic properties of marine sediments has a clear mathematical relationship that may be quantified during macroscopic characterization. The deviations of on-site sound velocity measurements from laboratory measurements of different types of sediments have obvious differences with respect to their classification and particle size compositions, but what are the effects? What is the mechanism underlying such impacts? The answers to these two questions need to be understood from the point of view of marine soil mechanics to understand the mechanism that causes the deviation between laboratory and on-site sound velocity measurements.

From Figure 3 and Figure 8, it can be seen that the silty sand, sandy silt, clayey silt and silt samples from the Huanghai and Bohai seas have significantly different V_{p-f}/V_{p-l} ranges, while for the same type of sediments, the V_{p-f}/V_{p-l} is concentrated within a narrow range and the deviation is small. The results show that the V_{p-f}/V_{p-l} value of silty sand is similar to that of sandy silt, both of which are notably less than 1.0. The V_{p-f}/V_{p-ll} of the silt is also less than but closer to 1.0, while for clayey silt, values both greater than and less than 1.0 exist. From the V_{p-f}/V_{p-ll} value classifications, silty sand and sandy silt can be grouped into one class, while the classes for silt and clayey silt remain discrete. Based on the characteristics of the particle size components of sediment samples in this study, and according to the Shepard's classification method of Marine Investigation Regulations (GB/T12763.8-2007) and the plasticity index method of marine geotechnical engineering, silty sand and sandy silt can be roughly classified as sand, and silt and clayey silt can be classified as such.

For superficial sediments, the external environmental factors that cause errors in the shipboard and laboratory acoustics tests are the changes in the temperature of sediment samples and the vibration of sediment samples during transport. From the analyses described in section 5.2, it can be assumed that the change in temperature had little effect on the errors of either on-site or laboratory acoustics tests of sediment samples in this study. Therefore, the impact of vibration during the transport of sediment samples can be taken as the main factor causing the deviation of the laboratory-measured velocities from the on-site ones. As shown in Figure 3 and Figure 8, the influence of vibration during the transport of sediment samples obviously differed between silty sand and sandy silt, and between silt and clayey silt. Based on analogous analyses in marine sediment surveys and marine geotechnical classification methods, the difference in the above influencing mechanisms could be analysed from the perspective of marine soil mechanics.

In the study of marine soil mechanics, sandy soil has the characteristic of micro-vibrational liquefaction, and clay exhibits obvious thixotropic characteristics under the action of dynamic forces. As the transitional soil between sand and clay, silt has both the liquefaction characteristics of sandy soil and the thixotropic characteristics of clay (Jia et al., 2011). The liquefaction of sand refers to the phenomenon that the saturated sand entered a liquid state under the action of vibration; due to the increase of pore water pressure, the sand changes from a solid state to a liquid state from the decrease in the effective stress. The mechanism is the saturated fine sand has a tendency to move and become denser under vibrational forces, wherein the stress migrates from the sand framework to the water, and due to the poor penetration of fine sand, the pore water pressure will increase sharply. When the pore water pressure reaches the total stress value, the effective stress declines to 0. The particles will then be suspended in the water, and the sand will liquefy (Liu et al., 2017). After a period of time following liquefaction, the drainage and consolidation processes will occur, resulting in more intense consolidation (Li et al., 2008). Meanwhile, the thixotropic property of clay is such that when the structure of clay is disturbed, the electric double layer is destroyed, resulting in reduced strength. However, with the increase of

standing time, a new equilibrium is formed among the soil particles, ions and water molecules, and the soil strength recovers gradually. Nevertheless, the recovered characteristics generally do not differ greatly from the initial sediment strength; this property is called soil thixotropy.

Based on the analyses presented here, it can be inferred that silty sand and sandy silt both have the dynamic liquefaction characteristics of sandy soils, such that the liquefaction and re-consolidation processes that occur during sample transport are important mechanisms that lead to significantly higher laboratory sound velocities than those recorded on the deck. Clayey silt has the dynamic thixotropy characteristic of clay, and the thixotropic resumption process during sample transport is also an important mechanism that leads to significantly higher laboratory sound velocities than those from the on-deck. With the dual characteristics of liquefaction and thixotropy, the processes of liquefaction, re-consolidation and thixotropic resumption of silt–sand occurring in the process of sample transport are the important factors that lead to significantly higher laboratory sound velocities than those measured on the deck for silts. The dual characteristics of silt–sand, with dynamic liquefaction–thixotropy, determine that its V_{p-f}/V_{p-l} ranges from those of sandy silt and silty sand to that of clayey silt.

Particle size is the main factor that affects the dynamic liquefaction and thixotropic properties of sands, silts and clays (Zheng et al., 2011), and indirectly affects the V_{p-f}/V_{p-l} of silty sand, sandy silt, silt and clayey silt. Based on a comparative analysis of the on-deck- and laboratory-measured sound velocities in the sediment samples from the northern Huanghai and Bohai seas, it can be concluded that the V_{p-f}/V_{p-l} of the silt samples was the least affected by the particle size composition, while those of sandy silt and silty sand were the most affected (Figure 9). For the V_{p-f}/V_{p-l} of clayey sand, different granularity parameters have different influences. In the sample tests performed in this study, the clay content of clayey silt was more concentrated, so it was difficult to judge the influence of clay content on its V_{p-f}/V_{p-l}. However, we can clearly point out that the sorting coefficient and sand content had significant impacts (Figures 9B–D).

Based on the microstructural observations, it was found that both the silty sand and sandy silt had large skeletal particles, tendencies for preferred grain orientations and the fine particles were filled and attached to larger particles (Figure 7 upper row and upper middle row). The large and small particles and their combined arrangements can greatly affect the infiltration and drainage of sediments, thus affecting their liquefaction and re-consolidation, and the resultant change in V_{p-f}/V_{p-l}. The clayey silt had an approximately bundled sheet structure (Hamilton and Bachman, 1982), with large particles that were completely surrounded by fine particles, some of which became aggregates owing to complex physicochemical interactions (Figure 7 lower row). For clayey silts with relatively concentrated clay contents, the effects of sand content and particle size on the electric double layer and the microstructure of the aggregates were relatively prominent. Therefore, the variations in the sand content and sorting coefficients had significant effects on the thixotropic properties of the clayey silt, which in turn affected its V_{p-f}/V_{p-l}. As a feature of dynamic liquefaction, re-consolidation and thixotropic resumption, particle size parameters exhibit a coupled effect on the dynamic characteristics of silty sand, making it difficult to determine which particle size factor had a significant impact. This is also an important reason that the V_{p-f}/V_{p-l} of the silt was obviously higher than those of the sandy silt and silty sand.

5.4 Influence of physical properties on the deviation of sound velocity

Based on the discussion and analyses in sections 5.2 and 5.3, it has now been shown that the dynamic liquefaction and re-consolidation and the dynamic thixotropy resumption processes of sediment samples are the important external factors that lead to the differences between the on-site and laboratory sound velocity measurements of sediments in the Huanghai and Bohai seas. External environmental conditions often affect the acoustic properties of sediments by changing the sedimentary characteristics of their properties, which acts as a trigger mechanism, as the physical properties of sediments are important internal factors that determine their acoustic properties (B.H. Liu et al., 2013). Numerous studies have shown that there are relatively clear mathematical relationships among bulk density, water content, porosity and other physical properties of sediments and their sound velocities (Hamilton and Bachman, 1982; Bachman, 1985; Orsi and Dunn, 1990; Kim et al., 2001; B.H. Liu et al., 2013). At present, the consistent research results obtained have shown that the larger the bulk density, the lower the water content, the smaller the porosity and the higher the sound velocity of the sediment.

In this study, the physical properties of sediment samples from on-site were not measured. However, comparative analyses of the on-deck- and laboratory-measured physical properties of a large number of sediments collected by Li et al. (2013) in the southern Huanghai Sea showed that the wet bulk density of sediments measured in the laboratory is generally higher than that of sediments measured on the deck, and the laboratory measurements of water content are generally lower than those obtained on site. The results presented here are closely related to the dynamic liquefaction and re-consolidation of the samples of silty sand, sandy silt and silt during transport. After the sediment sample was liquefied for a period of time, the pore water was drained and re-consolidation (i.e., compaction) occurred, which led to the aforementioned changes in physical properties. From Figure 10, it can be seen that there are still some measurement data that show that the laboratory measurements were not much different from the on-site index. These data are the result of sediment samples exhibiting dynamic thixotropy, such as clayey silt. For sediment samples with thixotropy resumption, little water loss and no significant changes in wet bulk density were observed during the dynamic–static change. Therefore, a comparative analysis of the measured data from the southern Huanghai Sea confirms that liquefaction, re-consolidation and the resumption of thixotropy in sediment samples affect their V_{p-f}/V_{p-l} values based on changes in sediment physical properties.

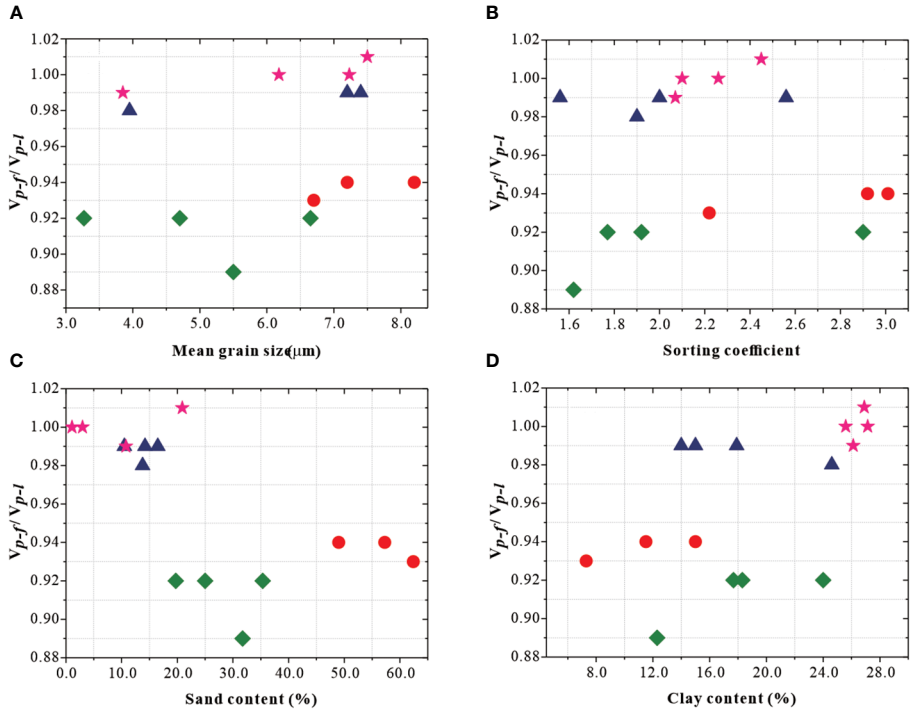

FIGURE 9
Variation in the on-deck- and laboratory-measured sound velocities (V_{p-f}/V_{p-l}) with particle size: **(A)** mean grain size; **(B)** sorting coefficient; **(C)** sand content; **(D)** clay content in different types of sediments in the study area. Circles denote silty sand; diamonds represent sandy silt; triangles represent silt and stars denote clayey silt.

In order to further analyse the factors that may influence the differences in the sound velocities between the those measured in the laboratory and the on-deck for the sediments from the Huanghai and Bohai seas, we statistically analysed the relationship between the physical parameters measured in the laboratory and V_{p-f}/V_{p-l}. Due to the limitations of on-site testing of the physical properties of sediment samples, the description of the relationship between the sound velocities and the physical properties of sediment samples in this sedimentary acoustic study, a laboratory measurement index was adopted (Hamilton, 1972; Lu and Liu, 2008; Meng et al., 2012; B.H. Liu et al., 2013), Therefore, in this study, the physical properties of sediment samples were not tested on-site, and only the effects of physical parameters measured in the laboratory on V_{p-f}/V_{p-l} were analysed. (Figure 11).

Because different types of sediments differ substantially in their physical properties, and different types of sediments were represented by fewer samples, the impacts of the physical properties of different types of sediment on V_{p-f}/V_{p-l} were not separately analysed. From a broad perspective, the impacts of the lab-measured bulk density (wet and dry bulk density), water content and plasticity index on V_{p-f}/V_{p-l} was more pronounced than those of laboratory-measured porosity and permeability

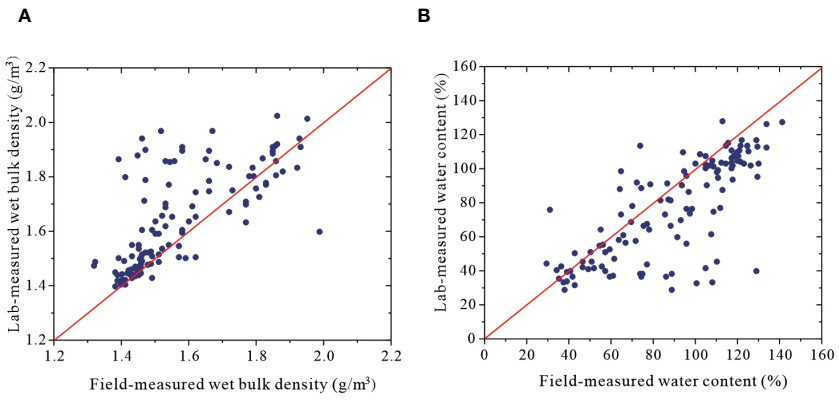

FIGURE 10
Comparison of the bulk densities **(A)** and water contents of sediments measured on the deck and in the laboratory **(B)** (Li et al., 2013).

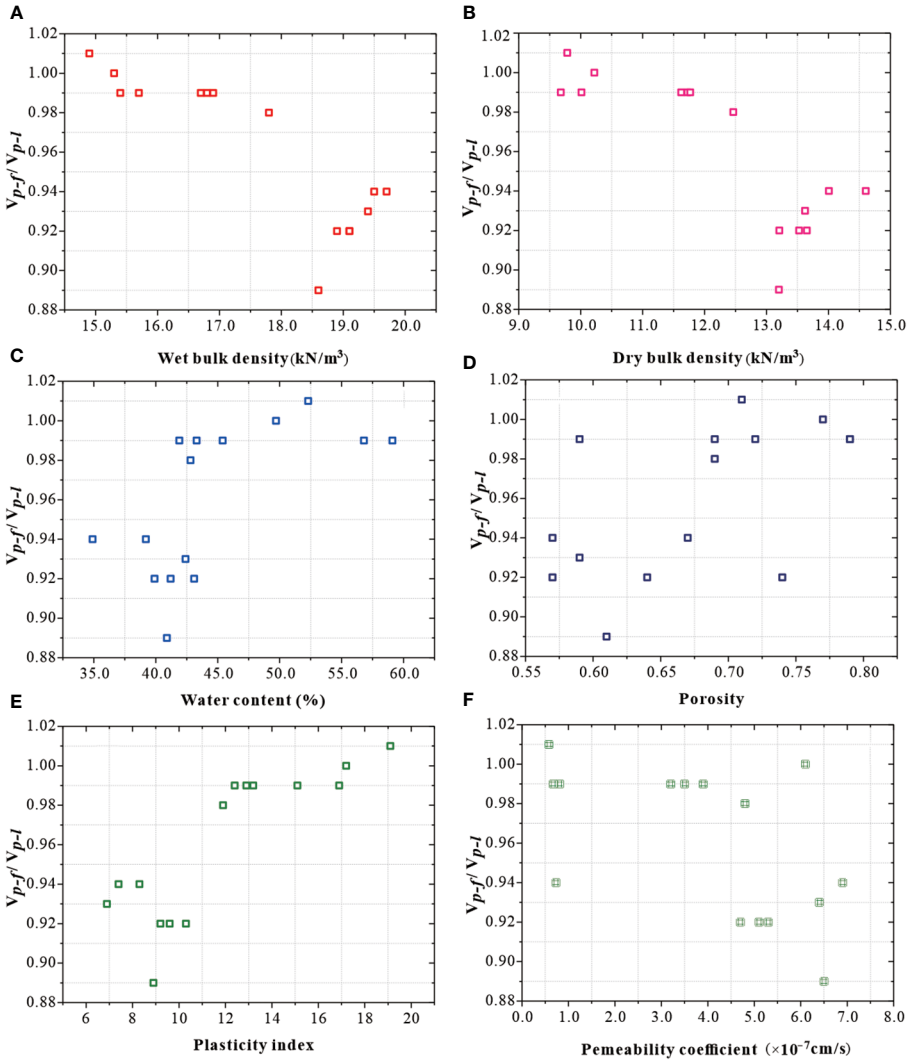

FIGURE 11
Variation of V_{p-f}/V_{p-l} with the physical parameters of different types of sediment in the study area: **(A)** wet bulk density; **(B)** dry bulk density; **(C)** water content; **(D)** porosity; **(E)** plasticity index; **(F)** permeability coefficient.

(Figure 11). The V_{p-f}/V_{p-l} decreased with the increase of bulk density when the wet bulk density was lower than 18.0 kN/m^3 and the dry bulk density was lower than 13.0 kN/m^3. When the wet bulk density was higher than 18.0 kN/m^3 and the dry bulk density was higher than 13.0 kN/m^3, V_{p-f}/V_{p-l} increased with increasing bulk density (Figures 11A, B). Additionally, when the water content was above 40.0%, V_{p-f}/V_{p-l} showed a significant positive correlation with water content (Figure 11C). When the plasticity index was higher than 9.0, V_{p-f}/V_{p-l} also showed a significant positive correlation with the plasticity index (Figure 11D).

Porosity is one of the most important physical parameters, and also has exhibited the most significant relationship with sound velocity statistics in previous empirical acoustic models used for studying the sound velocities and physical properties of sediments (Pan et al., 2006; Meng et al., 2012; Kan et al., 2014). However, the effect of porosity on V_{p-f}/V_{p-l} is not significant, which shows that the absolute value of the sediment pore size is an important parameter that affects the sound velocity. However, the effect of the absolute value of the sediment pore size on the difference between the velocities measured on-site and those measured in the laboratory is not obvious. In our analyses, it could be seen that compaction and decreases in the porosity of sediments during dynamic liquefaction and re-consolidation were the important factors influencing the V_{p-f}/V_{p-l} of silty sand, sandy silt and silt. It can be inferred that the variation of porosity under dynamic actions is also likely to be an important factor affecting V_{p-f}/V_{p-l}, which needs further study.

Based on a comparative analysis of the physical properties of sediments from the southern Huanghai Sea measured on site (i.e., shipboard) and in the laboratory, it was found that the large bulk density and high water content measured in the laboratory indicated that the values measured on the deck were also generally high. In the process of dynamic liquefaction, re-consolidation and thixotropy, changes in water content and bulk density are also large (Meng et al., 2012). Therefore, the effect of laboratory-measured bulk density and water content on V_{p-f}/V_{p-l}

can represent the effect of bulk density and water content on V_{p-f}/V_{p-l}. The plasticity index of sediments is a physical indicator determined by the sediment particle size, and is independent of sediment disturbances. The effect of the plasticity index on V_{p-f}/V_{p-l} can represent sediment type. Comparative analyses showed that the effect of the particle size (Figure 9) and plasticity index (Figure 11) on V_{p-f}/V_{p-l} is consistent, which therefore demonstrates that the two classification methods, Shepard's ternary diagram of Marine Investigation Regulations (GB/T12763.8-2007) and the plasticity index of sediments in marine geotechnical engineering, are different in approach but equally satisfactory in their results in terms of the influence on V_{p-f}/V_{p-l} in the Huanghai and Bohai seas.

6 Conclusions

We compared the deviations between the sound velocities of seafloor sediments measured on-site and in the laboratory (V_{p-f}/V_{p-l}), and their mechanisms were analysed by combining the on-site and laboratory measurements obtained from a surveying voyage in the southern Huanghai Sea in 2009 with the on-site and laboratory measurements acquired in 2014 from the northern Huanghai Sea and Bohai Sea. There were different degrees of deviations in the sound velocities of on-site and laboratory measurements in the Huanghai Sea and Bohai Sea sediment samples. The deviations between different sediment types were significant. Among them, the ratio of V_{p-f}/V_{p-l} was in the range of ~0.90–0.92 for sandy silt, ~0.92–0.94 for silty sand, ~0.98–0.99 for silt and ~0.99–1.01 for clayey silt.

Changes in temperature and disturbance during the transport of the samples were the key environmental factors causing deviations to exist in the measured sound velocities. Among them, the dynamic liquefaction, re-consolidation and thixotropic resumption processes that occurred during transport and the standing of samples were the most important dynamical mechanisms of acoustic deviations, all of which were caused by disturbances during sample transport. Sandy silts and silty sands exhibited dynamic liquefaction and re-consolidation, while the clayey silts exhibited thixotropy and resumption and the silts showed dynamic liquefaction, re-consolidation, thixotropy and then resumption. The dynamic formation mechanisms of the deviations between on-deck- and laboratory-measured sound velocities were the changes in the properties of sediments by external actions. Sediment porosity was not an important factor; however, the values of bulk density, water content and the plasticity index had significant impacts on the differences between measured velocities[1].

Data availability statement

The raw data supporting the conclusions of this article will be made available by the authors, without undue reservation.

Author contributions

BL: Funding acquisition, Writing – original draft, Writing – review & editing. JZ: Data curation, Writing – original draft, Writing – review & editing. JW: Writing – original draft, Writing – review & editing. XL: Funding acquisition, Investigation, Writing – original draft, Writing – review & editing. LS: Data curation, Writing – review & editing.

Funding

The author(s) declare financial support was received for the research, authorship, and/or publication of this article. This work was supported by the National Natural Science Foundation of China (42022052, U2006202, 42176191), the Shandong Provincial Natural Science Foundation (ZR2020YQ29, ZR2022YQ40), and the Basic Scientific Fund for National Public Research Institutes of China (2022S01).

Conflict of interest

The authors declare that the research was conducted in the absence of any commercial or financial relationships that could be construed as a potential conflict of interest.

Publisher's note

References

Akal, T. (1972). The relationship between the physical properties of underwater sediments that affect bottom reflection. *Mar. Geol.* 13, 251–260. doi: 10.1016/0025-3227(72)90054-0.

Bachman, R. T. (1985). Acoustic and physical property relationships in marine sediments. *J. Acoustical Soc. America* 78, 616–623. doi: 10.1121/1.392429.

Baldwin, K. C., Celikkol, B., and Silva, A. J. (1981). Marine sediment acoustic measurement system. *Ocean Eng.* 8, 481–488. doi: 10.1016/0029-8018(81)90013-5.

Best, A. I., Huggett, Q. J., and Harris A, J. K. (2001). Comparison of in *situ*and laboratory acoustic measurements on Lough Hyne marine sediment. *J. Acoustic Soc. America* 110, 695–709. doi: 10.1121/1.1382616.

Chadwick, W. W., Dziak, R. P., Haxel, J. H., Embley, R. W., and Matsumoto, H. (2012). Submarine landslide triggered by volcanic eruption recorded by in *situ*hydrophone. *Geological Soc. America* 40, 51–54. doi: 10.1130/G32495.1

Clearman, W. M. (2007). *Measurement and correlation of directional permeability and forchheimer's inertial coefficient of micro porous structures used in pulse tube cryocoolers* (Atlanta, Georgia, USA: Georgia Institute of Technology).

Fu, S. S., Tao, C., Prasad, M., Wilkens, R. H., and Fraser, L. N. (2004). Acoustic properties of coral sands, Waikiki, Hawaii. *J. Acoustical Soc. America* 115, 2013–2020. doi: 10.1121/1.1689340.

Hamilton, E. L. (1956). Low sound velocities in high-porosity sediments. *J. Acoustical* 28, 16–19. doi: 10.1121/1.1908208.

Hamilton, E. L. (1965). Sound speed and related physical properties of sediments from Experimental Mohole (Guadalupe Site). *Geophysics* 30, 257–261. doi: 10.1190/1.1439566.

Hamilton, E. L. (1971). Elastic properties of marine sediments. *J. Geophysics Res.* 76, 6350–6366. doi: 10.1029/JB076i002p00579.

Hamilton, E. L. (1972). Compressional wave attenuation in marine sediments. *Geophysics* 37, 620–646. doi: 10.1190/1.1440287.

Hamilton, E. L. (1976). Variations of density and porosity with depth in deep-sea sediments. *J. Sedimentol. Petroleum* 46, 280–300. doi: 10.1306/212F6F3C-2B24-11D7-8648000102C1865D

Hamilton, E. L., and Bachman, R. T. (1982). Sound velocity and related properties of marine sediments. *J. Acoustical Soc. America* 72, 1891–1904. doi: 10.1121/1.388539.

Han, T. C., Liu, B. H., Kan, G. M., Meng, X. M., and Ding, Z. J. (2011). Joint elastic-electrical properties of sediments in the Yellow Sea. *Sci. China Earth Sci.* 3, 1–8. doi: 10.1007/s11430-011-4335-6

Hong, G., Wu, B. H., and Zou, D. P. (2011). Experimental study on acoustic characteristics of seafloor sediment on effects of temperature. *J. Trop. Oceanogr.* 30, 70–73. doi: 10.11978/j.issn.1009-5470.2011.06.070

Hou, Z. Y., Guo, C. S., and Wang, J. Q. (2013). Surface sediments acoustic velocity and porosity correlation in Nansha sea area abyssal region. *Mar. Sci.* 37, 77–82.

Hou, Z. Y., Guo, C. S., Wang, J. Q., Li, H. Y., and Li, T. G. (2014). Tests of new *in-situ*seabed acoustic measurement system in Qingdao. *Chin. J. Oceanol. Limnol.* 32, 1172–1178. doi: 10.1007/s00343-015-4013-1.

Jia, Y. G., Shan, H. X., Yang, X. J., Meng, X. M., Chang, F. Q., and Zheng, J. W. (2011). *Sediment dynamics and hazards in Yellow River Delta* (Beijing: Science Press).

Kan, G. M., Liu, B. H., and Zhao, Y. X. (2011). Self-contained in *situ*sediment acoustic measurement system based on hydraulic-driving penetration. *High Technol. Letter* 17, 311–316.

Kan, G. M., Su, Y. F., and Liu, B. H. (2014). Properties of acoustic impendance of seafloor sediments in the middle area of the Southern Yellow Sea. *J. Jilin Univ. (Earth Sci. Edition)* 1, 19–26.

Kim, D. C., Sung, J. Y., Park, S. C., Lee, G. H., Choi, J. H., Kim, G. Y., et al. (2001). Physical and acoustic properties of shelf sediments, the South Sea of Korea. *Mar. Geol.* 179, 39–50. doi: 10.1016/S0025-3227(01)00200-6.

Kraft, B. J., Mayer, L. A., Simpkin, P., Lavoie, P., Jabs, E., Lynskey, et al. (2002). "Impact of Littoral Environmental Variability of Acoustic Predictions and Sonar Performance," in *Calculation of in* situ*acoustic wave properties in marine sediments*, 123–130. (Springer, Dordrecht).

Lei, H. Y., and Xiao, S. F. (2002). Research on soil structure characteristics and its quantitative parameter through pocket penetrometer. *J. Tianjin Univ.* 35, 718–722.

Li, F. F., Cui, Q. L., Li, M., Zhou, Q., and Zou, G. T. (2008). Acoustic velocity of water under high temperature and high pressure: validity of the equation of state of water. *China J. High Pressure Phys.* 22, 281–285.

Li, G. B., Kan, G. M., Meng, X. M., Liu, B. H., and Han, G. Z. (2013). Effects of the condition changes on the laboratory acoustic velocity measurements of seafloor sediments. *Adv. Mar. Sci.* 31, 211–218.

Liang, Y. B., and Lu, B. (1983). Acoustic-physical parameters of seafloor sediments of a low velocity continental shelf area. *Trop. Oceanol.* 2, 191–201.

Liang, Y. B., and Lu, B. (1991). Marine sediment acoustics, physics, and mechanics. *Advance Earth Sci.* 6, 42–43.

Liu, B. H., Han, T. C., Kan, G. M., and Li, G. B. (2013). Correlations between the in *situ*acoustic properties and geotechnical parameters of sediments in the Yellow Sea, China. *J. Asian Earth Sci.* 77, 83–90. doi: 10.1016/j.jseaes.2013.07.040.

Liu, X. L., Jia, Y. G., Zheng, J. W., and Shan, H. X. (2017). An experimental investigation of wave-induced sediment responses in a natural silty seabed: New insights into seabed stratification. *Sedimentology* 64, 508–529. doi: 10.1111/sed.12312.

Liu, X. L., Jia, Y. G., Zheng, J. W., and Yang, X. J. (2013). Consolidation of sediments discharged from the Yellow River: Implications for sediment erodibility. *Ocean Dynamics* 63, 371–384. doi: 10.1007/s10236-013-0599-z.

Liu, X. L., Lu, Y., Yu, H. Y., Ma, L. K., Li, X. Y., Li, W. J., et al. (2022). *In-situ*observation of storm-induced wave-supported fluid mud occurrence in the subaqueous Yellow River delta. *J. Geophysical Res.: Oceans* 127, e2021JC018190. doi: 10.1029/2021JC018190

Lu, B., Huang, S. J., and Li, G. X. (2003). Vertical variations of core sound velocity: evidence of paleooceanographic history since the Pleistocene epoch. *Mar. Georesources &. Geotechnol.* 21, 63–71. doi: 10.1080/716100485

Lu, B., and Liang, Y. B. (1994). Statistical correlation between physical parameters and sound velocity of marine sediments in the southeast coast of China. *Sci. China: Chem. Life Sci. Geol.* 24, 110–114.

Lu, B., and Liu, Q. (2008). Grain and pore factors in acoustic response of seafloor sediments. *J. Trop. Oceanogr.* 27, 23–30.

Mccann, C., Sothcott, J., and Best, A. I. (2013). A new laboratory technique for determining the compressional wave properties of marine sediments at sonic frequencies and in *situ*pressures. *Geophysical Prospecting* 62, 97–116. doi: 10.1111/1365-2478.12079

Meng, X. M., Li, G. B., Han, G. Z., and Kan, G. M. (2015). Sound velocity and related properties of seafloor sediments in the Bering Sea and Chukchi Sea. *Acta Oceanologica Sin.* 34, 75–80. doi: 10.1007/s13131-015-0669-9.

Meng, X. M., Liu, B. H., Kan, G. M., and Li, G. B. (2012). An experimental study on acoustic properties and their influencing factors of marine sediment in the southern Huanghai Sea. *Acta Oceanologica Sin.* 34, 74–83.

Orsi, T. H., and Dunn, D. A. (1990). Sound velocity and related physical properties of fine-grained abyssal sediments from the Brazil Basin (South Atlantic Ocean). *J. Acoustic Soc. America* 88, 1536–1542. doi: 10.1121/1.400311.

Pan, G. F., Ye, Y. C., Lai, X. H., Chen, X. S., and Lv, X. F. (2006). Shear wave velocity of seabed sediment from laboratory measurements and its relationship with physical properties of sediment. *Acta Oceanologica Sin.* 28, 64–69.

Prasad, M. (2002). Acoustic measurements in unconsolidated sands at low effective pressure and overpressure detection. *Geophysics* 67, 405–412. doi: 10.1190/1.1468600.

Richardson, M. D., and Briggs, K. B. (1996). *In situ*and laboratory geoacoustic measurements in soft mud and hard-packed sand sediments: Implications for high-frequency acoustic propagation and scattering. *Geo-Marine Lett.* 16, 196–203. doi: 10.1007/BF01204509.

Shepard, F. P. (1954). Nomenclature based on sand-silt-clay ratios. *J. Sedimentary Petrology* 24, 151–158. doi: 10.1306/D4269774-2B26-11D7-8648000102C1865D

Tao, C. H., Deng, X. M., Li, H. X., Zhou, J. P., Jin, X. B., Fu, S. S., et al. (2009). Development of *in- situ*marine sediment geo-acoustic measurement system with real-time and multi frequencies (the Second Generation). *China Ocean Eng.* 23, 769–778.

Vaughan, W. C., Easley, D. H., and Lavoie, D. L. (2002). Averageing pore statistics of two-dimensional images for predicting permeability. *J. Hydraulic Eng.* 128, 1002–1007. doi: 10.1061/(ASCE)0733-9429(2002)128:11(1002).

Wang, J., Li, G., Liu, B., Kan, G. M., Sun, Z. W., Meng, X. M., et al. (2018). An experimental study of the ballast in *situ*Sediment acoustic measurement system in south China sea. *Mar. Georesources Geotechnol.* 36, 515–521. doi: 10.1080/1064119X.2017.1348413.

Wang, Q., Liu, C. Y., Wu, Y. Z., Zhang, L., and Li, H. S. (2008). Relation between the acoustic characters of sea bottom sediment and the seawater depth. *Appl. Acoustics* 27, 217–221.

Wang, Y., Liu, R., and Su, J. L. (1996). *Marine Geography in China* (Beijing: Science Press).

Xu, Y., Li, P., Li, P., Du, J., Liu, L. J., Gao, W., et al. (2017). The difference analysis of physical-mechanical properties of sediments in the central South Yellow Sea and Zhe-Min coastal area in China. *Acta Oceanol. Sin.* 36, 77–85. doi: 10.1007/s13131-017-1000-8.

Yang, J., Tang, D., and Williams, K. L. (2008). Direct measurement of sediment sound speed in Shallow Water'06. *J. Acoustical Soc. America* 124, EL116–EL121. doi: 10.1121/1.2963038.

Zeng, J. Y., Zou, D. P., Wu, B. H., and Zhang, W. F. (2009). Acoustic signal processing and spectrum analysis of seafloor sediment under temperature perturbation. *J. Trop. Oceanogr.* 28, 80–88.

Zhang, S. Y. (1997). Geo-acoustics: the important discipline to study seabed environment. *Physics* 26, 280–285.

Zheng, J., Jia, Y., Liu, X., and Shan, H. X. (2014). Sediment characteristics as a function of variable hydrodynamics in a tidal flat of the Yellow River Delta, China. *J. Offshore Mechanics Arctic Eng.* 136, 1–12. doi: 10.1115/1.4025547.

Zheng, J. W., Liu, B. H., Kan, G. M., Liu, X. L., Li, G. B., and Pei, Y. L. (2017). Correlation between sediment acoustics and geotechnical properties in Jiaozhou bay. *J. Chongqing Jiaotong Univ. (Natural Science)* 36, 57–63.

Zheng, J., Shan, H., Jia, Y., Liu, X. L., and Hou, W. (2011). Field tests and observation of wave loading influence on erodibility of silty sediments in Huanghe Estuary, China. *J. Coast. Res.* 27, 706–717.

Zhou, X., Li, H., He, J., Wang, Q., and Zhang, X. (2008). Design of multi-segment in *situ*soil sampler testing bulk density. *Trans. Chin. Soc. Agric. Eng.* 24, 127–130.

Zou, D. P., Wu, B. H., and Lu, B. (2008). Acoustic inversion models of physical parameters of seabed sediments. *Acta Oceanologica Sin.* 30, 17–23.

frontiers | Frontiers in Marine Science

TYPE Original Research
PUBLISHED 02 April 2024
DOI 10.3389/fmars.2024.1377474

OPEN ACCESS

EDITED BY
Dong-Sheng Jeng,
Griffith University, Australia

REVIEWED BY
Qi Zhang,
Shanghai Jiao Tong University, China
Pan Hu,
Western Sydney University, Australia

*CORRESPONDENCE
Tingkai Nian
tknian@dlut.edu.cn

RECEIVED 27 January 2024
ACCEPTED 20 March 2024
PUBLISHED 02 April 2024

CITATION
Jiao H, Guo X, Fan N, Wu H and Nian T (2024) An undrained dynamic strain-pore pressure model for deep-water soft clays from the South China Sea.
Front. Mar. Sci. 11:1377474.
doi: 10.3389/fmars.2024.1377474

An undrained dynamic strain-pore pressure model for deep-water soft clays from the South China Sea

Houbin Jiao[1], Xingsen Guo[2], Ning Fan[3,4], Hao Wu[5] and Tingkai Nian[1]*

[1]State Key Laboratory of Coastal and Offshore Engineering, Dalian University of Technology, Dalian, China, [2]Department of Civil, Environmental, Geomatic Engineering, University College London, London, United Kingdom, [3]College of Civil Engineering and Architecture, Wenzhou University, Wenzhou, China, [4]Key Laboratory of Engineering and Technology for Soft Soil Foundation and Tideland Reclamation of Zhejiang Province, Wenzhou, China, [5]Department of Geotechnical Engineering, Nanjing Hydraulic Research Institute, Nanjing, China

With the increasing use of oceans for engineering purposes, such as the installation of suction anchors and pipelines, the stability of seabed structures has become a pivotal concern and is intricately linked to the characteristics of seabed soils. This study focuses specifically on deep-sea soft clay, a predominant seabed soil type distinguished by its high water content, thixotropy, and low permeability. These clays are vulnerable to destabilization and damage when disturbed, thereby posing threats to seabed installations. While the existing literature extensively examines the cyclic behavior of clay, considering factors such as the pore pressure response and strain and deformation characteristics, there is a notable gap in research addressing the behavior of deep-sea soft clay under comprehensive stress levels and prolonged cyclic loading. In this study, cyclic shear tests of the natural marine clay of the South China Sea were conducted, and the cyclic stress ratio (*CSR*), overpressure consolidation ratio (*OCR*), consolidation ratio (K_c), and loading frequency were varied. It was found that the *CSR*, *OCR*, and K_c significantly impact the cumulative dynamic strain in deep-sea soft clay during undrained cyclic dynamic tests. Higher *CSR* values lead to increased dynamic strain and structural failure risk. Subsequently, a dynamic strain-dynamic pore pressure development model was proposed. This model effectively captures the cumulative plastic deformation and dynamic pore pressure development, showing correlations with the *CSR*, *OCR*, and K_c, thus providing insights into the deformation and pore pressure trends in deep-sea clay under high cyclic dynamic loading conditions. This research not only furnishes essential background information but also addresses a critical gap in understanding the behavior of deep-sea soft clay under cyclic loading, thereby enhancing the safety and stability of seabed structures.

KEYWORDS

deep-sea soft clay, undrained dynamic behavior, cyclic loading, cumulative dynamic strain, dynamic pore pressure, empirical model

1 Introduction

With the development and utilization of deep-sea resources, many engineering structures (e.g., the anchoring foundation of floating production platforms, submarine wellheads, and submarine pipelines) are fixed or laid to seabed soils (Guo et al., 2023a; Wang et al., 2024; Wu et al., 2024). The stability of these structures is closely related to the self-properties and responses of the seabed soils (Nian et al., 2021; Liu et al., 2023). The distribution of soft soils, which have physical and mechanical properties such as high water content, high thixotropy, low strength, and low permeability, is very common in deep-sea areas, according to survey and analysis results (Nian et al., 2018; Huang et al., 2021). Deep-sea soft soils are highly susceptible to destabilization and sliding due to external disturbances (Ren et al., 2018a; Fan et al., 2023; Guo et al., 2023b; Guo et al., 2024), especially for cyclic loading disturbances with high frequencies and load levels (usually caused by frequent seaquakes or earthquakes; for example, Figure 1 shows the seismic distribution situation around the Pacific Ocean). The low permeability of deep-sea soft soils results in the inability of water to drain out of the soils (i.e., in the undrained state) under cyclic loading, which generates excess pore water pressure and reduces the strength and bearing capacity of deep-sea seabed soils, threatening the safety and stability of deep-sea engineering structures (Andersen, 2009). Therefore, it is necessary to study the undrained deformation-pore pressure behavior of deep-sea soft soils under cyclic loading to ensure the safety and normal use of deep-sea engineering structures.

The dynamic response of soft soils under cyclic loading has been investigated in many studies (e.g., Moses et al., 2003; Li et al., 2011, 2014; Wang et al., 2017). In studies on the dynamic pore water pressure response of soils, several empirical and theoretical models have been proposed to describe the development of pore water pressure under cyclic loading based on cyclic triaxial test results (e.g., Li and Meissner, 2002; Nie et al., 2007; Ni et al., 2015), which can predict the pore pressure accumulation of soft soils under cyclic loading. Considering the low number of cyclic loadings (usually less than 2000) in previous studies, Ren et al. (2018b) conducted long-term low-stress horizontal cyclic loading tests to obtain a new empirical model describing the development of pore pressure in soft marine clay under long-term low-stress horizontal cyclic loading. Wang et al. (2021) carried out several principal stress axis rotation tests and found that the pore water pressure accumulation of soft clay is greatly affected by the intermediate principal stress coefficient. Through a series of dynamic cyclic shear tests, Jin et al. (2023) found that an increase in the cyclic stress ratio and the amplitude ratio of the shear stress accelerates pore water pressure accumulation and proposed a normalized model for predicting the variation in residual pore water pressure with the number of cycles.

Many studies have also been carried out on the strain and deformation behavior of soft soils under cyclic loading. Hyodo et al. (1992) found that the elastic strain of saturated clay was not significantly related to the value of the amplitude of the dynamic stress, but there was a corresponding relationship with the effective stress ratio through cyclic triaxial tests. Muhanna (1994) developed a simple model for assessing the elastic modulus and cumulative permanent strain of soft clay under cyclic loading through similar soil dynamic tests. Yang et al. (2012) revealed that the cyclic stress ratio was a key factor for the development of different deformations of marine soft clay under cyclic loading and proposed the concept of a critical cyclic stress ratio, below which the cumulative plastic deformation of the soil body gradually stabilized. Guo et al. (2013) found that the stress-strain hysteretic loop, resilient modulus, and permanent strain of soils were significantly correlated with the cyclic stress ratio and confining pressure by analyzing the results of a series of monotonic triaxial tests and long-term cyclic triaxial tests. Yang et al. (2012) and Lei et al. (2016) further reported that

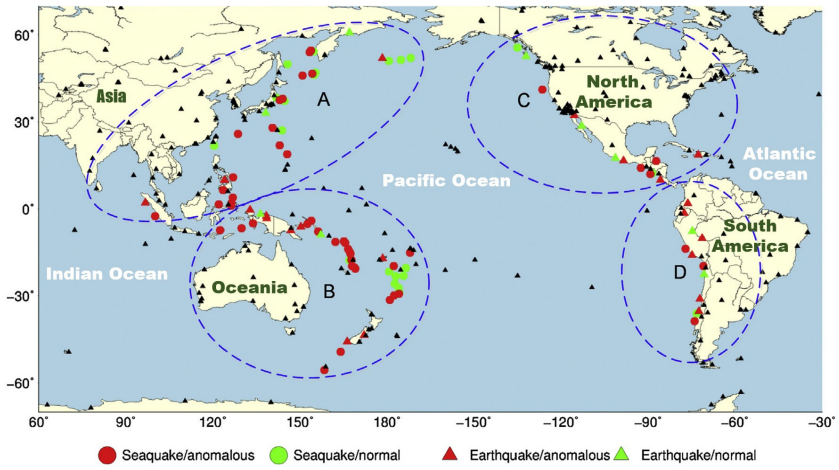

FIGURE 1
Distribution of 100 M7.0+ earthquakes in the Circum-Pacific seismic belt from 2006 to 2015 (sources from Li et al., 2018, where **(A)** refers to most parts of Southeast Asia, Taiwan Island, Japan, Kamchatka and the Aleutian Islands; **(B)** refers to New Guinea, the Solomon Islands, the Fiji Islands and New Zealand; **(C)** refers to Mexico and the west coast of Canada and America; **(D)** refers to the west coast of South America; and the black triangles signify the IGS stations).

cyclic loading accelerated the creep behavior of marine soft clay when the cyclic stress ratio was greater than the critical cyclic stress ratio, which adversely affected soil deformation. Lei et al. (2020) investigated the microscopic characteristics and deformation development of soft marine clay under cyclic loading using cyclic triaxial tests and scanning electron microscopy (SEM), discussed the relationship between microscopic parameters and the cumulative plastic strain of marine soft clay, and further established an empirical model of cumulative plastic strain involving microscopic parameters for assessing the deformation of marine soft clay.

In addition, in several previous studies, the pore pressure–deformation behavior of soft soils under cyclic loading and their relationships have also been investigated. For example, Ansal and Erken (1989) investigated the cyclic stress-strain-pore pressure and cyclic shear strength characteristics of clay under undrained conditions and proposed an empirical method for evaluating the cyclic yield strength of normally consolidated soils. Hyde et al. (1993) carried out a series of cyclic undrained triaxial tests on Ariake clay, and based on the results of the tests, relevant stability criteria for pore water pressures and strains at different cyclic stress levels were developed. Wang et al. (2013) conducted a series of high-cycle (50,000 cycles) triaxial tests on Wenzhou marine soft clay under different stress levels and confining pressures to study the development of strain and pore water pressure. These researchers proposed an equation for describing the relationship between the peak axial stress and the peak pore water pressure after 1000 cycles. Dai et al. (2021) found that the development of permanent pore pressure depends on the large initial shear stress ratio (*SSR*) and overpressure consolidation ratio (*OCR*), whereas the development of permanent dynamic strain is divided into three stages by a series of cyclic triaxial tests on marine soft clay with large initial *SSR* and *OCR*. Zhao et al. (2023) proposed a conceptual model of high-cycle, low-amplitude undrained loading containing shrinkage yield surfaces and swelling boundary surfaces to describe the weakening behavior induced by the increase in excess pore water pressure and the hardening effect induced by shrinkage plastic deformation, respectively.

In summary, although some valuable studies on the behavior of soft soils under cyclic loading have been conducted, to date, there have been relatively few studies on the *in situ* properties of deep-sea soft soils. In particular, there is still a gap in the studies that reveal the pore pressure-deformation behavior of deep-sea soft soils under cyclic loading, taking into account a more comprehensive stress level and long-term cyclic loading (such as earthquake action). In this study, we aim to reveal the dynamic pore pressure–deformation development behavior of deep-sea soft soils under strong and long-term cyclic loading and further propose a dynamic pore pressure–deformation equation applicable to typical deep-sea soft soils in the South China Sea.

2 Materials and methods

2.1 Soil properties and specimen preparation

The marine clay samples analyzed in this study were collected during a shared voyage in the northeastern part of the South China Sea and the Luzon Strait. This region, characterized by its unique location at the convergence of several tectonic plates, has a rich history of seismic activity and marine events (Liu, 1994; Wang et al., 2014). Its geological features offer a unique opportunity to study interactions between tectonic movements and marine geological processes. The study of these marine clays is pivotal for understanding the mechanics behind seismic occurrences, predicting future seismic activities, and formulating strategies for mitigating disaster risks. The sampling stations are located at the intersection of the Pearl River valley slope (Station S7A-3) and the Dongsha slope (Station D2-1), as depicted in Figure 2. These samples were retrieved by employing the gravity penetration method. The selected region is notably situated in an area characterized by seismic activity and frequent maritime occurrences.

The soil samples used in the test were obtained through the 2016 shared voyage plan for the northeastern South China Sea and the Luzon Strait by using the gravity sampling method. This

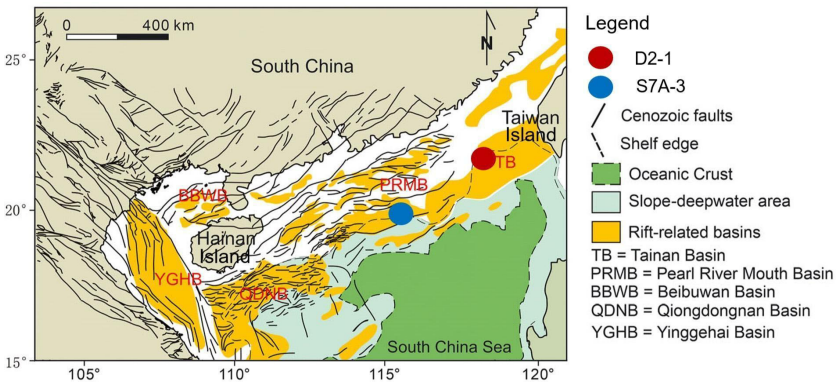

FIGURE 2
Sampling sites in the northern continental slope area of the South China Sea showing the major tectonic units (modified from Zhang et al., 2020).

sampling method can ensure that the sampling depth meets the test requirements and ensure the natural state of undisturbed soil samples to the greatest extent. The soil samples obtained by drilling consisted of shallow sensitive clay located at seabed depths ranging from 0 to 2.4 m, beneath water depths of 1,152 m (Station S7A-3) and 1,885 m (Station D2-1). The soil samples obtained by drilling were canned in polyvinyl chloride (PVC) pipes with a diameter of 10 cm. To facilitate transportation, each section was cut to 1 m. The cut soil samples were marked in turn, wrapped with fresh-keeping film, sealed with adhesive tape, and then sealed at both ends with pipe heads to ensure no loss of water. During the test period, the soil samples were kept in a constant temperature room. The collection, cutting, packaging, transportation, storage and other processes of the above soil samples minimize the disturbance caused by objective factors and effectively ensure the undisturbed nature of the soil samples.

The fundamental physical and mechanical properties of these undisturbed soil samples were determined through indoor soil testing, and the results are presented in Table 1. Analysis of these parameters reveals distinctive attributes of deep-sea marine clay in the South China Sea. The specific gravity (G_s) of the S7A-3 sample was found to be 2.62 g/cm^3, which was slightly greater than that of the D2-1 sample, which was 2.57 g/cm^3. This difference suggests a higher mineral content in the S7A-3 sample, possibly due to the localized geological composition. A remarkable difference was observed in the natural water content (ω_0), with the S7A-3 sample exhibiting a significantly higher value (121.04%) than the D2-1 sample (85.75%). This substantial disparity indicates a greater degree of saturation and potential pore-water interaction in the S7A-3 sample, which could have implications for its mechanical behavior under stress. The initial density (ρ_0) of the S7A-3 sample was 1.354 g/cm^3, whereas the D2-1 sample had a notably higher density of 1.523 g/cm^3. Correspondingly, the initial void ratio (e_0) for S7A-3 was 3.326, which was significantly greater than the value of 2.191 for Station D2-1. These measurements suggest a more loosely packed structure in the S7A-3 sample, potentially influencing its compressibility and shear strength. The liquid limit (ω_L) and plasticity index (I_p) of the S7A-3 sample were 55.85% and 31.42, respectively, compared to 51.01% and 32.35 for the D2-1 sample. These values indicate that both samples exhibit high plasticity. The compressibility factor (α_v) for S7A-3 was 3.217 MPa^{-1}, which is greater than the 2.283 MPa^{-1} of D2-1, indicating a greater susceptibility to volume change under load for the S7A-3 sample. Additionally, the undrained strength ($S_{u,0}$) of the S7A-3 sample was 19.58 kPa, substantially higher than the 12.31 kPa of D2-1, suggesting a greater resistance to shear under undrained conditions. The sensitivity (S_t) of the S7A-3 sample was 14.34, compared to 10.53 for the D2-1 sample. This higher sensitivity in the S7A-3 sample points to a more delicate structure, which could be more susceptible to disturbances. These characteristics are indicative of the unique structural properties inherent to marine clay under various environmental and loading conditions.

TABLE 1 Index properties of the deep-sea clay.

Index properties	S7A-3	D2-1
Specific gravity, G_s	2.62	2.57
Natural water content, ω_0 (%)	121.04	85.75
Initial density, ρ_0 (g/cm^3)	1.354	1.523
Initial void ratio, e_0	3.326	2.191
Liquid limit, ω_L (%)	55.85	51.01
Plasticity index, I_p	31.42	32.35
Compressibility factor, α_v (MPa^{-1})	3.217	2.283
Undrained strength, $S_{u,0}$ (kPa)	19.58	12.31
Sensitivity, S_t	14.34	10.53

The meticulous process of preparing and cutting marine clay samples for dynamic triaxial testing is a crucial step in ensuring the accuracy and reliability of the experimental results. As depicted in Figure 3 of the study, this process involves several key stages, each designed to preserve the integrity of the samples while preparing them for precise testing. The process begins with the *in situ* cylindrical soil samples, which are carefully sectioned into three equal parts. This initial sectioning is critical to ensure uniformity in size and properties across all test specimens. Each of these segments is then meticulously processed into cylindrical specimens. The dimensions of these specimens are strictly controlled, with a diameter of 39.1 mm and a height of 80 mm. These dimensions are chosen to fit the requirements of the dynamic triaxial testing apparatus. The precision in cutting these cylindrical specimens is achieved through the use of specialized equipment. This equipment ensures that each specimen maintains its integrity without inducing any additional stress or alteration to its natural state. Precision cutting is crucial for maintaining the natural structure and properties of marine clay, which are essential for accurate testing and analysis. Throughout the preparation and cutting process, great care is taken to preserve the natural moisture content and structural properties of the samples. This preservation is vital for maintaining the authenticity of the samples under *in situ* conditions. Once cut to the precise dimensions, the specimens are immediately prepared for dynamic triaxial testing.

2.2 Test scheme of the automated triaxial testing system

In this study, an automated triaxial testing system (ATTS), as shown in Figure 4, was employed to conduct consolidation and cyclic loading triaxial tests. This system, which is specifically designed and manufactured, accommodates the unique requirements of dynamic triaxial testing under both isotropic and anisotropic consolidation conditions. The ATTS applies vertical pressure through a highly precise load cell. This load cell is a crucial component, providing the necessary force to simulate vertical stress conditions on the soil specimens. The confining pressure, an essential parameter in triaxial testing, is generated within the system using an air pressure-type piston. This method of applying confining pressure allows for accurate simulation of the lateral stress conditions that are prevalent in subsurface environments. The axial displacements during the testing process are meticulously recorded using a linear

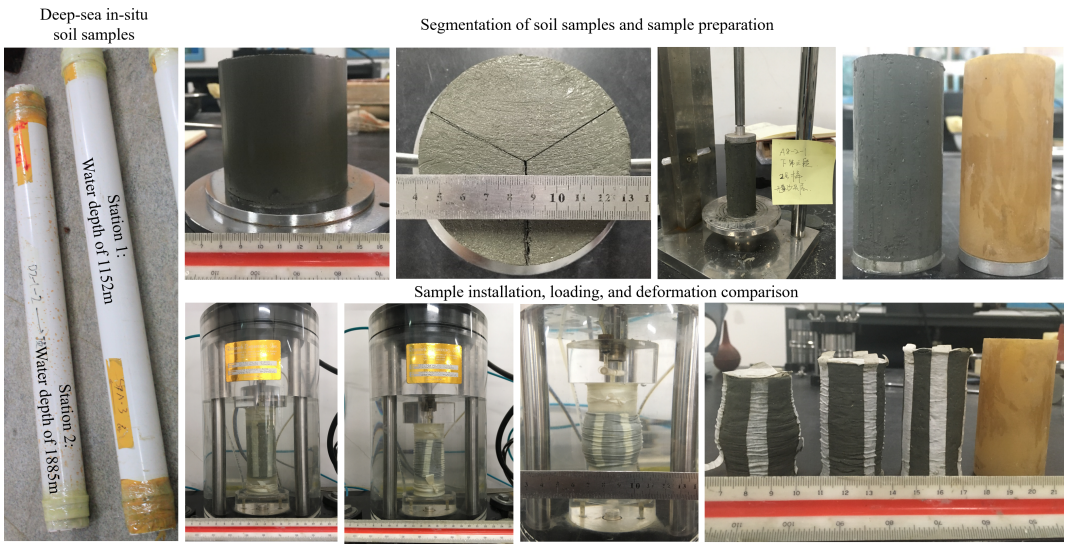

FIGURE 3
Deep-sea *in situ* clay samples and specimen preparation.

variable differential transformer (LVDT) axial actuator. The LVDT axial actuator offers high-resolution measurements of the specimen's deformation. The ATTS is also equipped with a pore water pressure transducer positioned at the center of the specimen's bottom.

The experimental scheme is presented in Table 2. A confining pressure of 150 kPa was maintained. The test specimens from Station S7A-3 were subjected to anisotropic consolidation with consolidation stress ratios of 1.0, 1.25, and 1.40, whereas the specimens from D2-1 were tested at a ratio of 1.25. The experiments were conducted using constant-amplitude half-sine wave cyclic loading at a frequency of 1.0 Hz. The condition for the end of the test is that the axial dynamic strain exceeds 25% or the number of loading times exceeds 2000. The number of loading cycles each specimen underwent varied, as indicated in Table 2. To

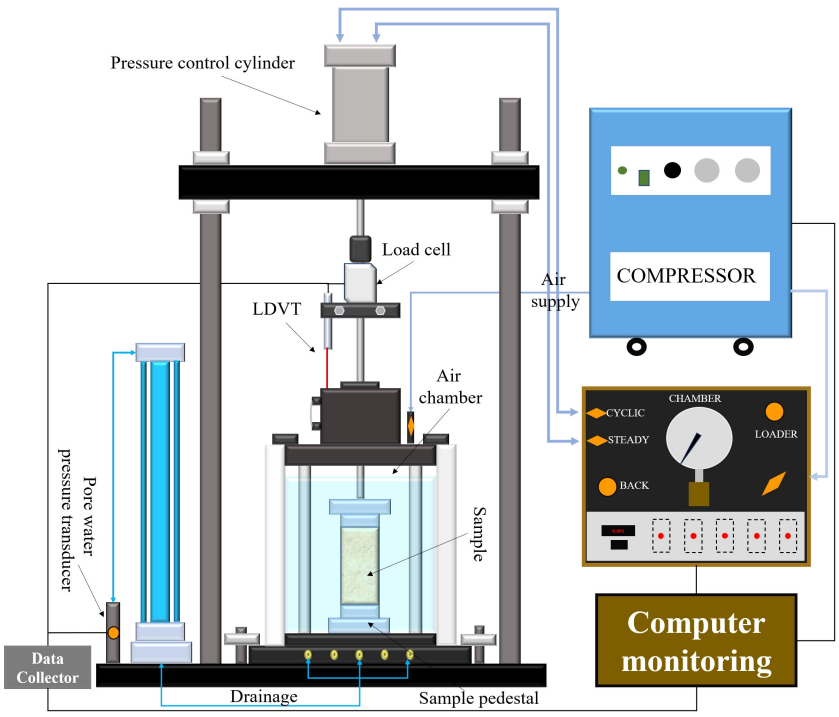

FIGURE 4
The ATTS testing system.

TABLE 2 Experimental conditions of the cyclic triaxial tests.

Station	Confining pressure, p'_0 (kPa)	*OCR*	Consolidation ratio, K_c	Cyclic stress ratio, *CSR*	No. of cycles, *N*
1 (S7A-3)	150	0.167	1.00	0.347, 0.367, 0.387	3742, 4792, 4261
		0.133	1.25	0.372, 0.394, 0.412	4134, 4224, 4408
		0.119	1.40	0.426, 0.435, 0.455, 0.477	4282, 4986, 1116, 576
	100	0.25	1.00	0.43, 0.49, 0.57	3000
	150	0.167		0.372, 0.463, 0.634	3000
	200	0.125		0.407, 0.483, 0.535	3000
2 (D2-1)	150	0.167	1.25	0.351, 0.406, 0.425, 0.434	2500

account for varying conditions of biased and isostatic consolidation, the cyclic stress ratio (*CSR*) was defined as per Formula (1):

$$CSR = \frac{\sigma_d}{2\sigma_c} = 3\sigma_d/[2(\sigma_1 + 2\sigma_3)] \quad (1)$$

where σ_d is the cyclic dynamic stress, σ_c is the average consolidation pressure, σ_1 is the axial consolidation pressure, and σ_3 is the lateral consolidation pressure.

3 Results and discussion

3.1 Cumulative evolution of the undrained dynamic strain

This section assesses the impact of the cyclic stress ratio (*CSR*), *OCR*, and consolidation stress ratio (K_c) on the accumulation of dynamic strain during undrained cyclic dynamic tests. Figure 5 illustrates the dynamic strain (ε_d) accumulations as the number of cycles increases under varying K_c and *OCR*. Overall, the evolution of the dynamic strain (ε_d) is closely linked to the peak value of the cyclic dynamic stress, i.e., the magnitude of the *CSR*. A higher *CSR* results in a greater dynamic strain, including resilient strain (ε_r) and permanent strain (ε_p), increasing the likelihood of structural failure of clay samples across all K_c. The critical cyclic stress ratio (CSR_{cr}) serves to distinguish the developmental trend of dynamic strain (ε_d) (Nian et al., 2020).

When the *CSR* is less than the CSR_{cr}, the dynamic strain initially increases and then stabilizes within a very few cycles, well before reaching 100 cycles. Ultimately, ϵ_d stabilizes at a lower level, consistently below 3% (refer to the black trend lines in Figures 5A–C, E, F. However, when the *CSR* exceeds the CSR_{cr}, the dynamic strain continues to increase during subsequent cyclic loading, particularly when the *CSR* is significantly greater than the CSR_{cr}. In such cases, the ε_d of the specimen rapidly surpasses 5% within the initial 10 cycles (refer to the blue trend lines in Figure 5). The impact of K_c on dynamic strain development during dynamic tests is depicted in Figures 5A–C. For a given *CSR*, a higher consolidation stress ratio leads to smaller strain growth trends. As illustrated by the black trend lines in Figure 5, a consistent strain growth pattern characterized by slow increases that tend to stabilize is exhibited at approximately 3%. With the same growth trend, as K_c increases from 1.0 to 1.25 and then to 1.40, the corresponding cyclic stress ratio increases from 0.347 to 0.412 and then to 0.426. This implies that under the same dynamic load, greater consolidation ratios result in less structural damage to marine clay and enhanced stability. Figures 5D–F illustrates the influence of the *OCR* on dynamic strain development during dynamic tests. The influence of *CSR* on dynamic strain aligns with the earlier discussion. In contrast to the effect of K_c on the dynamic strain, to achieve the same level of dynamic strain, the *OCR* decreases from 0.25 to 0.167 and further to 0.125, requiring an increase in the *CSR* from 0.43 to 0.463 or even 0.483. This reveals a converse outcome compared to K_c; under the same dynamic load, a smaller *OCR* results in reduced structural damage to marine clay and increased clay sample stability.

3.2 Cumulative dynamic strain model

Through fitting and analyzing the dynamic strain data, it is observed that the model (Equation (2)) based on the well-known classical Hardin-Drnevich model (Hardin and Drnevich, 1972) effectively captures the cumulative plastic deformation of deep-sea soft clay caused by dynamic stress:

$$\varepsilon_d = \frac{N^c}{a + bN^c} \quad (2)$$

where *a*, *b*, and *c* are parameters dependent on the stress path, stress state, and physical properties of the clay.

Considering the dynamic strain growth curve, it is reasonable to infer that parameter *c* depends on the physical properties of the clay, such as the water content, void ratio, particle size, and particle specific surface area. Ren et al. (2018), in conjunction with previous studies (referencing Monismith et al., 1975; Li and Selig, 1996), discovered that most values of parameter *c* fall within a narrow range of 0.18–0.82, with an average value of approximately 0.5. The fitting results for parameter *c* of the deep-sea clay in the South China Sea in this article are essentially consistent with previous findings, yielding an average value of 0.49, as illustrated in Figure 6.

An analysis of the cumulative curve of the corresponding changes shows that parameter *a* governs the initial strain of the

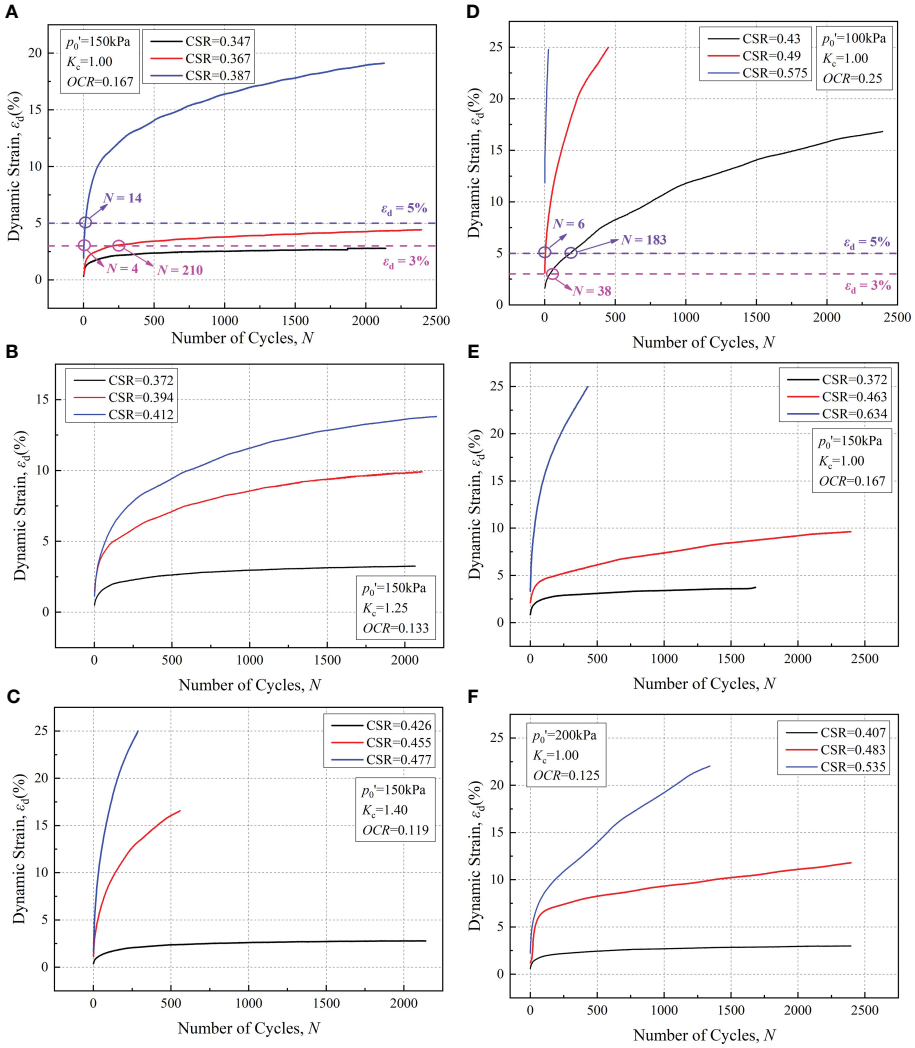

FIGURE 5
Dynamic strain evolution under different stress magnitudes [**(A–C)** under different consolidation ratios K_c (Nian et al., 2018); and **(D–F)** under different overpressure consolidation ratios *OCR* (Nian et al., 2020)].

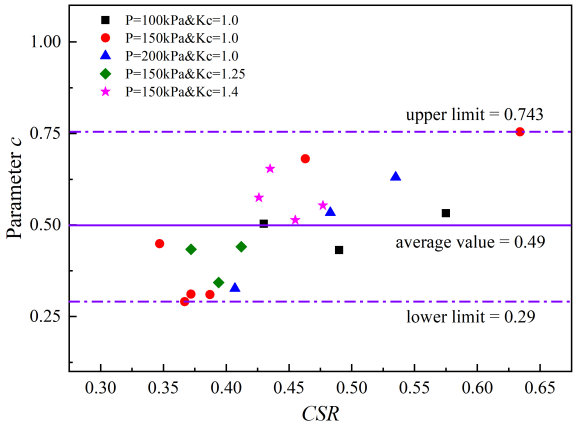

FIGURE 6
Effect of the stress state on parameter *c*.

clay, indicating the degree of difficulty for the clay to begin deforming. Additionally, experimental data of ϵ_d under different *CSR* values, varying initial mean effective stresses *P*, and different K_c values were utilized to derive parameters *a* and *b* in Equation (2) using the least squares method. The fitting revealed a robust correlation between parameter *b* and *CSR* (as illustrated in Figure 7), while parameter *a* exhibited a strong correlation with *CSR* and K_c. Their relationships were also determined. The influence of the *OCR* on the dynamic strain was found to be insignificant, and therefore, it is not reflected in the relationship equation. The correlation of parameters *a* and *b* in the fitting formula exceeded 90%, and the corresponding Equations (3) and (4) are as follows:

$$a = 2(\mathrm{E}-5)\ \ CSR^{-8.05}K_c^{16.30} \tag{3}$$

$$b = 0.0002CSR^{-6.4} \tag{4}$$

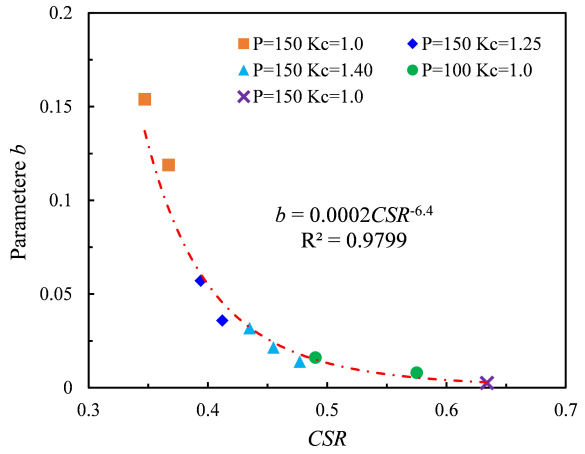

FIGURE 7
Effect of the stress state on parameter *b*.

To validate the applicability of the strain model and the fitting formula for model parameters, laboratory test results from Station-2 were compared with corresponding predicted outcomes from the model. Figure 8 shows the comparison between the model predictions for deep-sea clay and the dynamic strain results obtained from laboratory tests. The validation utilized deep-sea soft clay (Station-2) in the South China Sea, and its fundamental physical and mechanical properties are listed in Table 1. The test carefully considered the physical state, stress conditions, and applied dynamic loads of the clay to maintain consistency with the testing process at Station-1, minimizing human interference. In Figure 9, the experimental results and model predictions are represented by points and dashed lines, respectively. The predicted strain results from the model closely replicate the experimental data, demonstrating a high degree of fitting under sustained cyclic dynamic loading. The conditions corresponding to the four different *CSR* values encompass various development trends of the clay sample from stability to failure, all achieving a high level of reproducibility. This signifies that the model effectively characterizes the development curve of dynamic strain in deep-sea clay under dynamic loading. The control parameters *a* and *b* exhibit robust correlations with *CSR* and K_c. Furthermore, their relationships in this deep-sea clay are successfully validated.

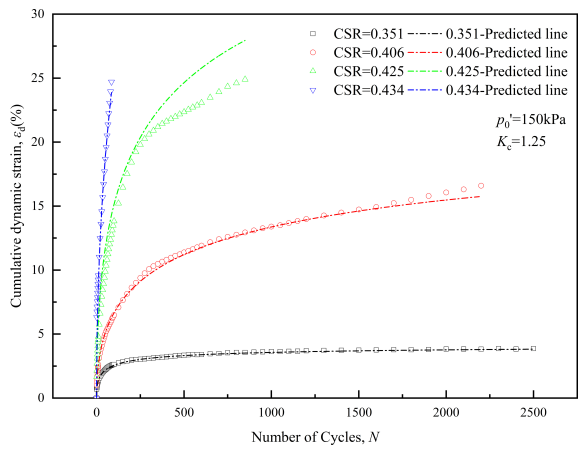

FIGURE 8
Comparison between model predictions and laboratory test results of cumulative dynamic strain for deep-sea clay.

3.3 Cumulation evolution of the undrained dynamic pore pressure

Figures 9A–C illustrates the accumulations of dynamic pore water pressure (u_d) with an increasing number of cycles under various K_c. Notably, in correspondence with dynamic strain development, the evolution of dynamic pore water pressure (u_d) is highly dependent on the peak value of cyclic dynamic stress, with minimal influence from the consolidation stress ratio. Across all dynamic triaxial tests, the pore water pressure exhibits rapid initial growth under dynamic loading, followed by a gradual decrease in the growth trend, ultimately stabilizing around a specific value. The final stability value is primarily determined by the peak value of the dynamic load and increases with increasing dynamic load. Moreover, regardless of the increase in the cyclic stress ratio and consolidation stress, the maximum stability value of the pore water pressure can only reach 120 kPa. This limitation arises from the constant confining pressure of 150 kPa applied in all dynamic load tests combined with the unique structural characteristics of the soft clay from the South China Sea.

Figures 9D–F demonstrates the impact of the *OCR* on the development of u_d during dynamic tests. The influence of *CSR* on u_d aligns with the earlier discussion. In contrast to the effect of the consolidation stress ratio K_c on u_d, under the same stress level, as the *OCR* decreases from 0.25 to 0.167 and further to 0.125, the maximum pore pressure ratio achievable by the sample decreases from 0.875 to 0.833 until 0.75. This reveals a starkly different outcome compared to K_c; that is, under the same dynamic load, a smaller *OCR* results in increased stability in the structural characteristics of marine clay, along with a lower limit for the dynamic pore water pressure u_d that the clay sample can attain.

3.4 Undrained dynamic pore pressure model

To address the issue of conventional pore pressure models showing a perpetual increase rather than reaching a plateau across loading cycles (*N*), Ren et al. (2018b) introduced a curve model tailored for cyclic dynamic loads to forecast the growth trajectory of undrained dynamic pore pressure. Given that the clay sample utilized in the study originates from soft clay in the deep sea of the South China Sea, which is subjected to an intricate seabed environment during sedimentation, the stress conditions and initial pore pressure characteristics inherent to this clay sample significantly differ from those of normally consolidated clay. To precisely predict the undrained pore pressure of the clay sample, we have made adaptive enhancements to the model proposed by Ren et al. (2018a). Specifically, by addressing the complex cyclic

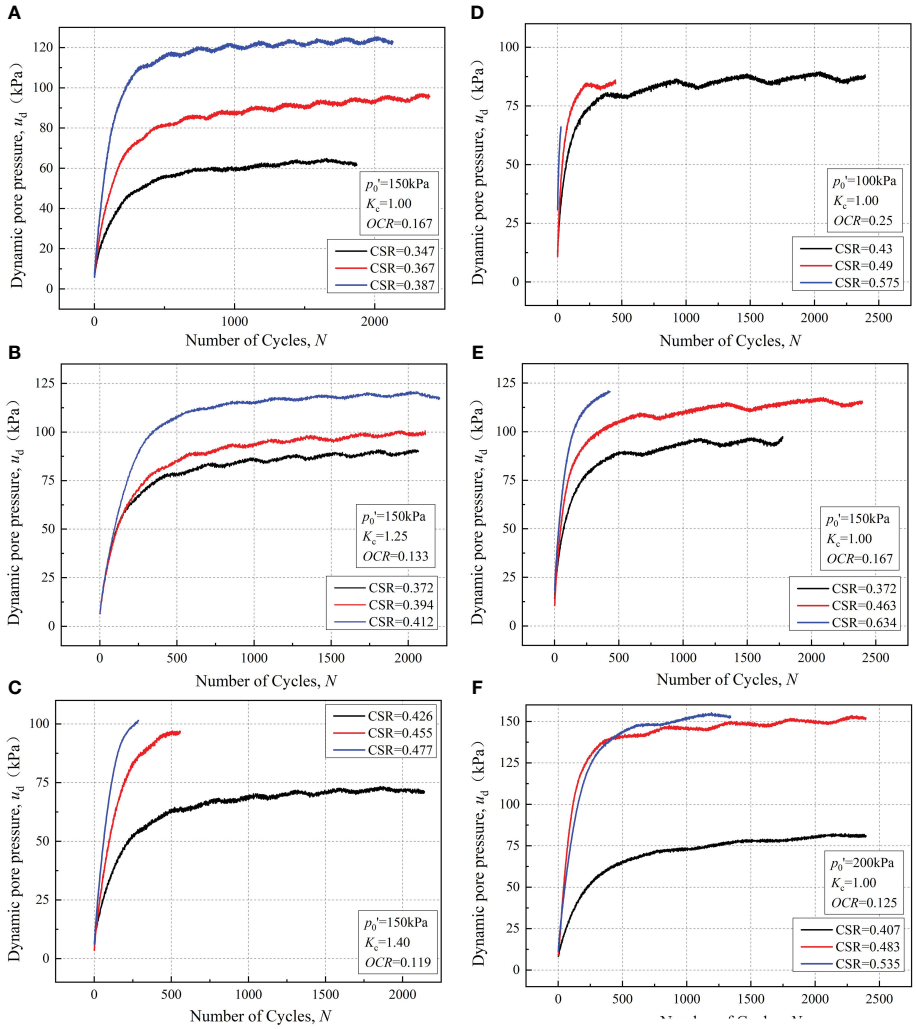

FIGURE 9
Accumulations of the dynamic pore water pressure under different stress magnitudes [**(A–C)** Station-1 under different K_c (Nian et al., 2018); **D–F** Station-2 under different *OCRs* (Nian et al., 2020)].

loads and initial pore pressure conditions considered in the experiment, we have derived a dynamic pore pressure model suitable for deep-sea clay in the South China Sea. The formulated model is expressed as follows:

$$u_d' = \frac{u_d}{p_0'} = D + \frac{N^C}{A + BN^C} \tag{5}$$

where u_d' is the dynamic pore pressure ratio; u_d is the dynamic pore pressure; P_0' is the initial mean effective stress; and *A*, *B*, *C*, and *D* are parameters that depend on the stress state and physical properties of the clay.

The relationship between the dynamic pore pressure and dynamic strain suggests that the factors governing strain also play a crucial role in determining the pore pressure. These factors include cyclic stress, effective confining pressure, and clay static strength. The model parameters are designed to capture the influence of these factors on the dynamic pore pressure. Ren et al. (2018) emphasized that the exponential parameter *C* characterizes the rate of pore pressure development, specifically how fast it increases with loading cycles. Importantly, *C* does not influence the generation of permanent pore pressure. On the other hand, the physical meaning of parameter *c* in the strain model has consistently maintained its interpretation. This implies that parameter *C* may solely depend on the inherent physical properties of the clay and should be independent of the stress state. This distinction clarifies the roles of *C* and *c*, reinforcing the model's ability to capture the nuanced behavior of pore pressure under dynamic loading conditions.

An examination of the relationship between parameter *C* and *CSR* reveals that parameter *C* shares the same physical meaning as parameter *c* in the strain model. It is solely dependent on the clay type and remains independent of the cyclic stress state. Consequently, for a given type of clay sample, parameter *C* should remain constant. In contrast to the fixed value of *C* (equal to 0.5) in Ren et al. (2018), the best-fit values for *C* for the deep-sea soft clay of the South China Sea under dynamic cyclic loading fall within the range of 0.73 to 1.34, as depicted in Figure 10. Their average value is 1.03, which closely aligns with 1.0. As a result, it is

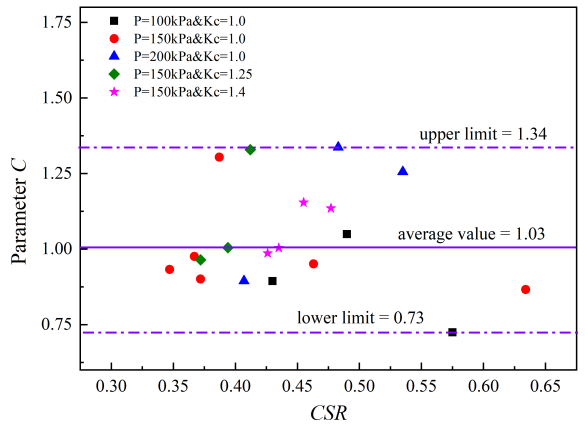

FIGURE 10
Effect of the stress state on parameter *C*.

recommended that Equation (5) be simplified to the following form (Equation (6)):

$$u_d' = D + \frac{N}{A + BN} \tag{6}$$

By employing the same fitting method as that used for the dynamic strain model parameters, the experimental dynamic pore pressure ($u_{d'}$) data under various *CSR*, *OCR*, and K_c values were utilized to determine parameters *A*, *B*, and *D* in Equation (5) through the least squares method. In contrast to parameters *a* and *b* in the dynamic strain fitting formula, the influence of the overpressure consolidation ratio on the dynamic pore pressure is significant. The fitting results reveal that parameters *A* and *D* exhibit a robust correlation with *CSR* and *OCR*, with correlation coefficients (R^2) of 97% and 90%, respectively. Parameter *B* demonstrates a strong correlation with *CSR*, with a correlation coefficient exceeding 90%, as depicted in Figure 11. The relationships Equations (7–9) are as follows:

$$A = 0.039CSR^{1.405}OCR^{-5.360} \tag{7}$$

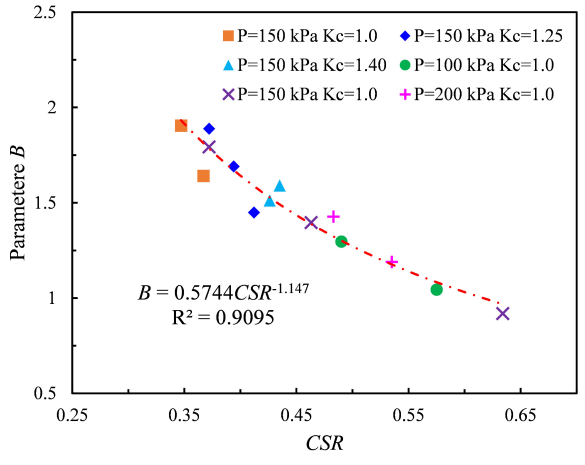

FIGURE 11
Effect of the stress state on parameter *B*.

$$B = 0.574CSR^{-1.147} \tag{8}$$

$$D = -0.006 + 0.258CSR^2 + 6.028OCR^3 \tag{9}$$

To validate the applicability of the strain model and the fitting formula for model parameters, the laboratory test results from Station-2 were compared with their corresponding predicted outcomes obtained from the model. Figure 12 shows a comparison between the model predictions for deep-sea clay and the laboratory test results of the dynamic pore pressure. In Figure 12, the experimental results and model predictions are represented by points and dashed lines, respectively. The dynamic pore pressure curves predicted by the model effectively replicate the experimental data, maintaining a high level of fitting under sustained cyclic dynamic loading. The conditions corresponding to four different cyclic stress ratios cover various development trends of the clay sample from stability to failure, all achieving a high level of reproducibility. This indicates that the model is effective in describing the dynamic pore pressure development curve of deep-sea clay under dynamic loading. The control parameters *A*, *B*, and *D* are strongly correlated with the cyclic stress ratio and the overpressure consolidation ratio. Their relationships in this deep-sea clay have been successfully validated.

3.5 Undrained dynamic strain–pore pressure model

The parameter *c*=0.5, derived from fitting cyclic triaxial test data of deep-sea soft clay, is integrated into a universal model capable of describing the cumulative dynamic strain trend under high cyclic dynamic loads. The dynamic strain formula for the South China Sea soft clay is obtained as follows:

$$\varepsilon_d = \frac{N^{0.5}}{a + bN^{0.5}} \tag{10}$$

Substituting Equation (10) into Equation (6), the relationship between the dynamic pore pressure ratio and cumulative dynamic strain (ε_d - $u_{d'}$) is expressed as:

$$u_d' = q + \frac{\varepsilon_d^2}{m + n(\varepsilon_d - p)^2} \tag{11}$$

Equation (11) reveals a hyperbolic relationship between the cumulative dynamic strain and accumulated dynamic pore pressure ratio for deep-sea soft clay under high cyclic dynamic loading conditions. This observation aligns with conclusions drawn by Yasuhara et al. (1982); Hyodo et al. (1992), and Ren et al. (2018). The experimental data support a strong hyperbolic relationship between ε_d and $u_{d'}$, with regression analyses consistently yielding correlation coefficients (R^2) exceeding 90%. Consequently, it can be concluded that Equation (11) effectively describes the relationship between ε_d and $u_{d'}$ for deep-sea soft clay in the South China Sea under high-frequency and strong-load dynamic cyclic loading conditions.

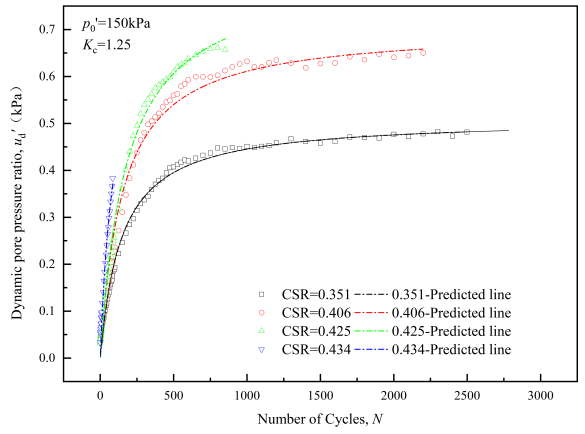

FIGURE 12
Comparison between model predictions and laboratory test results of dynamic pore pressure ratio for deep-sea clay.

Applying the same fitting method employed for the model parameters in Equations (2) and (5), we utilized experimental data of ϵ_d and u_d, under varying *CSR*, *OCR*, and K_c values to determine the parameters *m*, *n*, *p*, and *q* in Equation (11) through the least squares method. Unlike the parameters in the dynamic strain and dynamic pore pressure fitting formula, both K_c and *OCR* exert a significant influence on the parameters. The fitting analysis revealed a robust correlation between parameter *n* and *CSR* (as illustrated in Figure 13), while parameter *m* demonstrated a strong correlation with *CSR* and K_c, both with correlation coefficients exceeding 96%. Parameters *p* and *q* exhibited a robust correlation with *CSR* and *OCR*, achieving correlation coefficients (R^2) of 92% and 98%, respectively. The relationships Equations (12–15) are expressed as follows:

$$m = 1.8 * 10^6 CSR^{10.054} - 7.55K_c^{11.56} \quad (12)$$

$$n = 0.186CSR^{-3.915} \quad (13)$$

$$p = 20.372 + 23.197\mathrm{Ln}\ CSR + \frac{0.414}{OCR^2} \quad (14)$$

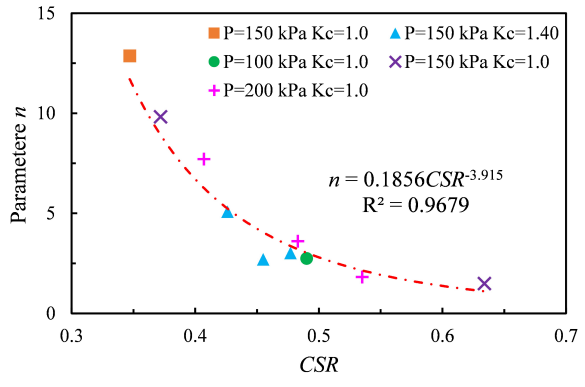

FIGURE 13
Effect of the stress state on parameter *n*.

$$q = -0.492 + 1.339CSR^2 + 93.674OCR^3 \quad (15)$$

Similarly, the experimental results from Station-2 were utilized to compare and validate the ε_d - u_d, model along with its parameter fitting formula, as illustrated in Figure 14. In Figure 14, the experimental results and model predictions are denoted by points and dashed lines, respectively. The dynamic strain-pore pressure curves predicted by the model effectively replicate the experimental data, maintaining a high level of fitting under sustained cyclic dynamic loading. The conditions corresponding to four different cyclic stress ratios cover various development trends of the clay sample from stability to failure, all demonstrating a high degree of reproducibility. Notably, the initial fitting deviation of the *CSR* = 0.425 test group is relatively large, likely due to unavoidable factors such as differences in the undisturbed soil samples and experimental errors. However, overall, the model effectively describes the ε_d - u_d' curve of deep-sea clay under dynamic loading. The control parameters *m*, *n*, *p*, and *q* exhibit strong correlations with the consolidation stress ratio, cyclic stress ratio, and overpressure consolidation ratio. These relationships in deep-sea clay have been successfully validated. This implies that with limited deep-sea soil samples, we can predict the deformation and pore pressure development trend of this soil type based on the ε_d - u_d' model, considering known working conditions such as the determined soil sample category, sedimentary history, stress state, and loading conditions.

4 Conclusions

This study comprehensively assessed the influence of *CSR*, *OCR*, and K_c on the cumulative evolution of dynamic strain during undrained cyclic dynamic tests in deep-sea soft clay. The key findings and conclusions are summarized as follows:

(1) The evolution of ε_d is closely linked to the peak value of the *CSR*. Higher *CSR* values result in greater dynamic strain, including ε_r and ε_p, increasing the likelihood of structural failure of clay samples across all K_c values. The CSR_{cr} distinguishes the developmental trend of dynamic strain. When the *CSR* is less than the CSR_{cr}, the dynamic strain stabilizes at a lower level within a few cycles. However, when the *CSR* exceeds the CSR_{cr}, the dynamic strain continues to increase, particularly when the *CSR* significantly surpasses the CSR_{cr}.

(2) The cumulative plastic deformation of deep-sea soft clay caused by dynamic stress is effectively captured by a model based on the classical Hardin-Drnevich model. The parameters in the model show strong correlations with *CSR* and K_c, and their relationships have been successfully validated through laboratory test results.

(3) The evolution of u_d is highly dependent on the peak value of the cyclic dynamic stress, with minimal influence from K_c. Smaller *OCR* values result in increased stability in the structural characteristics of marine clay, along with a lower limit for u_d that the clay sample can attain.

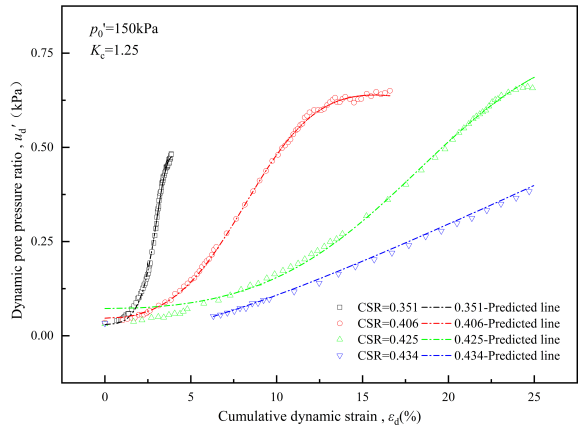

FIGURE 14
Comparison between the model predictions and laboratory test results of dynamic strain - pore pressure ratio for deep-sea clay.

(4) A dynamic pore pressure model tailored for deep-sea clay under high cyclic dynamic loads is proposed. The model parameters (A, B, and D) show strong correlations with CSR, OCR, and K_c, and the model effectively replicates the experimental data, demonstrating its applicability in describing the dynamic pore pressure development curve.

(5) The proposed model, which integrates the parameter c = 0.5, effectively describes the hyperbolic relationship between the cumulative dynamic strain and dynamic pore pressure ratio (ε_d - u_d') for deep-sea soft clay under high cyclic dynamic loading conditions. The control parameters (m, n, p, q) exhibit strong correlations with the consolidation stress ratio, cyclic stress ratio, and overpressure consolidation ratio, and the model effectively replicates the experimental data, indicating its potential for predicting the deformation and pore pressure development trend of deep-sea clay under known working conditions.

In conclusion, this comprehensive investigation provides valuable insights into the complex behavior of deep-sea soft clay under cyclic dynamic loading, offering practical implications for engineering applications and further research in geotechnical engineering.

Data availability statement

The original contributions presented in the study are included in the article/supplementary material. Further inquiries can be directed to the corresponding author.

Author contributions

HJ: Data curation, Formal analysis, Methodology, Visualization, Writing – original draft. XG: Investigation, Writing – review & editing. NF: Conceptualization, Writing – review & editing. HW: Conceptualization, Writing – review & editing. TN: Funding acquisition, Resources, Supervision, Writing – review & editing.

Funding

The author(s) declare financial support was received for the research, authorship, and/or publication of this article. This research is funded by the National Natural Science Foundation of China (Nos. 52079020 and 52108337).

Acknowledgments

We thank the Trial Voyage of Dongfanghong 2 Scientific Research Vessel for providing the clay samples.

Conflict of interest

The authors declare that the research was conducted in the absence of any commercial or financial relationships that could be construed as a potential conflict of interest.

Publisher's note

All claims expressed in this article are solely those of the authors and do not necessarily represent those of their affiliated organizations, or those of the publisher, the editors and the reviewers. Any product that may be evaluated in this article, or claim that may be made by its manufacturer, is not guaranteed or endorsed by the publisher.

References

Andersen, K. H. (2009). Bearing capacity under cyclic loading-offshore, along the coast, and on land. The 21st Bjerrum Lecture presented in Oslo, 23 November 2007. *Can. Geotech. J.* 46, 513–535. doi: 10.1139/T09-003

Ansal, M. A., and Erken, A. (1989). Undrained behavior of clay under cyclic shear stresses. *J. Geotech. Eng.* 115, 948–955. doi: 10.1061/(ASCE)0733-9410(1989)115:7(968)

Dai, M., Guo, L., Li, M. F., and Jin, T. (2021). The pore pressure generation and deformation of overconsolidated soft marine clay considering initial static shear effect. *Mar. Georesour. Geotechnol.* 40, 922–935. doi: 10.1080/1064119X.2021.1951406

Fan, N., Jiang, J. X., Nian, T. K., Dong, Y. K., Guo, L., Fu, C. W., et al. (2023). Impact action of submarine slides on pipelines: A review of the state-of-the-art since 2008. *Ocean Eng.* 286, 115532. doi: 10.1016/j.oceaneng.2023.115532

Guo, L., Wang, J., Cai, Y. Q., Liu, H. L., Gao, Y. F., and Sun, H. L. (2013). Undrained deformation behavior of saturated soft clay under long-term cyclic loading. *Soil Dynam. Earthquake Eng.* 50, 28–37. doi: 10.1016/j.soildyn.2013.01.029

Guo, X., Fan, N., Liu, Y., Liu, X., Wang, Z., Xie, X., et al. (2023b). Deep seabed mining: Frontiers in engineering geology and environment. *Int. J. Coal Sci. Technol.* 10, 23. doi: 10.1007/s40789-023-00580-x

Guo, X., Fan, N., Zheng, D., Fu, C., Wu, H., Zhang, Y., et al. (2024). Predicting impact forces on pipelines from deep-sea fluidized slides: A comprehensive review of key factors. *Int. J. Min. Sci. Technol.* doi: 10.1016/j.ijmst.2024.02.001

Guo, X., Liu, X., Li, M., and Lu, Y. (2023a). Lateral force on buried pipelines caused by seabed slides using a CFD method with a shear interface weakening model. *Ocean Eng.* 280, 114663. doi: 10.1016/j.oceaneng.2023.114663

Hardin, B. O., and Drnevich, V. P. (1972). Shear modulus and damping in soils: measurement and parameter effects (terzaghi leture). *J. Soil mechan. foundations division* 98, 603–624. doi: 10.1061/JSFEAQ.0001756

Huang, J., Jiao, W., Liu, J., Wan, S., Xiong, Z., Zhang, J., et al. (2021). Sediment distribution and dispersal in the southern South China Sea: Evidence from clay minerals and magnetic properties. *Mar. Geol.* 439, 106560. doi: 10.1016/j.margeo.2021.106560

Hyde, A. F. L., Yasuhara, K., and Hirao, K. (1993). Stability criteria for marine clay under one-way cyclic loading. *J. Geotech. Eng.* 119, 1771–1789. doi: 10.1061/(ASCE)0733-9410(1993)119:11(1771)

Hyodo, M., Yasuhara, K., and Hirao, K. (1992). Prediction of clay behaviour in undrained and partially drained cyclic triaxial tests. *Soils Foundations* 32, 117–127. doi: 10.3208/sandf1972.32.4_117

Jin, H. X., Pan, D. M., Guo, L., and Shi, L. (2023). Effect of cyclic shear stress ratio on cyclic behavior of clay under multidirectional shear loading. *Mar. Georesour. Geotechnol.* 20, 1–9. doi: 10.1080/1064119X.2023.2267042

Lei, H. Y., Liu, J. J., Liu, M., Zhang, Z. P., and Jiang, M. J. (2016). Effects of frequency and cyclic stress ratio on creep behavior of clay under cyclic loading. *Mar. Georesour. Geotechnol.* 35, 281–291. doi: 10.1080/1064119X.2016.1157659

Lei, H. Y., Xu, Y. G., Jiang, M. J., and Jiang, Y. (2020). Deformation and fabric of soft marine clay at various cyclic load stages. *Ocean Eng.* 195, 106757. doi: 10.1016/j.oceaneng.2019.106757

Li, J. A., Chen, S. X., Jiang, L. F., and Xiong, S. D. (2014). Experimental study on the influence of stress history on the dynamic characteristics of remolded red clay. *Chin. J. Geotech. Eng.* 36, 1657–1665. doi: 10.11779/CJGE201409012

Li, L. L., Dan, H. B., and Wang, L. Z. (2011). Undrained behavior of natural marine clay under cyclic loading. *Ocean Eng.* 38, 1792–1805. doi: 10.1016/j.oceaneng.2011.09.004

Li, T., and Meissner, H. (2002). Two-surface plasticity model for cyclic undrained behavior of clays. *J. Geotech. Geoenviron. Eng.* 128, 613–626. doi: 10.1061/(ASCE)1090-0241(2002)128:7(613)

Li, D., and Selig, E. T. (1996). Cumulative plastic deformation for fine-grained subgrade soils. *J. geotech. Eng.* 122, 1006–1013. doi: 10.1061/(ASCE)0733-9410(1996)122:12(1006)

Li, W., Yue, J. P., Guo, J. Y., Yang, Y., Zou, B., Shen, Y., et al. (2018). Statistical seismo-ionospheric precursors of M7.0+ earthquakes in Circum-Pacific seismic belt by GPS TEC measurements. *Adv. Space Res.* 61, 1206–1219. doi: 10.1016/j.asr.2017.12.013

Liu, Y. (1994). Neotectonic and Crustal Stableness. Beijing: Science Press, 1–271.

Liu, X., Wang, Y., Zhang, H., and Guo, X. (2023). Susceptibility of typical marine geological disasters: an overview. *Geoenviron. Disasters* 10, 10. doi: 10.1186/s40677-023-00237-6

Monismith, C. L., Ogawa, N., and Freeme, C. R. (1975). Permanent deformation characteristics of subgrade soils due to repeated loading. *Transport. Res. Rec.* 537.

Moses, G. G., Rao, S. N., and Rao, P. N. (2003). Undrained strength behaviour of a cemented marine clay under monotonic and cyclic loading. *Ocean Eng.* 30, 1765–2178. doi: 10.1016/S0029-8018(03)00018-0

Muhanna, A. S. H. (1994). A testing procedure and a model for resilient modulus and accumulated plastic strain of cohesive subgrade soils. North Carolina State University.

Ni, J., Indraratna, B., Geng, X., Carter, J. P., and Chen, Y. (2015). Model of soft soils under cyclicloading. *Int. J. Geomechan.* 5, 1–10. doi: 10.1061/(ASCE)GM.1943-5622.0000411

Nian, T. K., Jiao, H. B., Fan, N., and Guo, X. S. (2020). Microstructure analysis on the dynamic behavior of marine clay in the South China Sea. *Mar. Georesour. Geotechnol* 38, 349–362. doi: 10.1080/1064119X.2019.1573864

Nian, T., Jiao, H., Fan, N., Guo, X., and Jia, Y. (2018). Experiment on dynamic strain-pore pressure of soft clay in the northern slope of south China sea. *Yantu Lixue. Rock Soil Mech.* 39, 1564–1572. doi: 10.16285/j.rsm.2017.0887

Nian, T., Shen, Y., Zheng, D., and Lei, D. (2021). Research advances on the chain disasters of submarine landslides. *J. Eng. Geol.* 29, 1657–1675. doi: 10.13544/j.cnki.Jeg.2021-0815

Nie, Q., Bai, B., Hu, J., and Shang, W. (2007). The pore pressure model and undrained shear strength of soft clay under cyclic loading. *Rock Soil Mech.* 28, 724–729.

Ren, X. W., Xu, Q., Teng, J., Zhao, N., and Lv, L. (2018a). A novel model for the cumulative plastic strain of soft marine clay under long-term low cyclic loads. *Ocean Eng.* 149, 194–204. doi: 10.1016/j.oceaneng.2017.12.028

Ren, X. W., Xu, Q., Xu, C. B., Teng, J. D., and Lv, S. H. (2018b). Undrained pore pressure behavior of soft marine clay under long-term low cyclic loads. *Ocean Eng.* 150, 60–68. doi: 10.1016/j.oceaneng.2017.12.045

Wang, Y. K., Gao, Y. F., Guo, L., Cai, Y. Q., Li, B., Qiu, Y., et al. (2017). Cyclic response of natural soft marine clay under principal stress rotation as induced by wave loads. *Ocean Eng.* 129, 191–202. doi: 10.1016/j.oceaneng.2016.11.031

Wang, J., Guo, L., Cai, Y. Q., Xu, C. J., and Gu, C. (2013). Strain and pore pressure development on soft marine clay in triaxial tests with a large number of cycles. *Ocean Eng.* 74, 125–132. doi: 10.1016/j.oceaneng.2013.10.005

Wang, X., Li, S., Gong, Y., Liu, X., Suo, Y., and Dai, L. (2014). Active tectonics and its effects on gas-hydrates in Northern South China Sea. *Journal of Ji Lin University: Earth Science Edition* 44 (2), 419–431. doi: 10.13278/j.cnki.jjuese.201402102

Wang, Y. K., Wan, Y. S., Ruan, H., Yu, X., Shao, J. G., and Ren, D. B. (2021). Pore pressure accumulation of anisotropically consolidated soft clay subjected to complex loads under different stress paths. *China Ocean Eng.* 35, 465–474. doi: 10.1007/s13344-021-0043-y

Wang, Z., Zheng, D., Guo, X., Gu, Z., Shen, Y., and Nian, T. (2024). Investigation of offshore landslides impact on bucket foundations using a coupled SPH–FEM method. *Geoenviron. Disasters* 11, 2. doi: 10.1186/s40677-024-00266-9

Wu, T., Zhang, C., and Guo, X. (2024). Dynamic responses of monopile offshore wind turbines in cold sea regions: Ice and aerodynamic loads with soil-structure interaction. *Ocean Eng.* 292, 116536. doi: 10.1016/j.oceaneng.2023.116536

Yang, G., Yang, Q., Liu, W. H., and Zhang, K. (2012). Critical cyclic stress ratio of reconstituted silty clay under the cyclic loading. *J. Converge. Inf. Technol.* 7, 1–8. doi: 10.4156/jcit.vol7.issue23.1

Yasuhara, K., Yamanouchi, T., and Hirao, K. (1982). Cyclic strength and deformation of normally consolidated clay. *Soils Foundations* 22, 77–91. doi: 10.3208/sandf1972.22.3_77

Zhang, G., Shao, L., Qiao, P., Cao, L., Pang, X., Zhao, Z., et al. (2020). Cretaceous–Palaeogene sedimentary evolution of the South China Sea region: A preliminary synthesis. *Geol J.* 55, 2662–2683. doi: 10.1002/gj.3533

Zhao, C., Liu, J. M., Liu, H. M., Bian, X. C., and Chen, Y. M. (2023). A conceptual model for the shakedown response of soft clay to high-cycle, low-amplitude undrained loading. *Comput. Geotech.* 156, 105257. doi: 10.1016/j.compgeo.2023.105257

frontiers | Frontiers in Marine Science

TYPE Original Research
PUBLISHED 03 May 2024
DOI 10.3389/fmars.2024.1356302

OPEN ACCESS

EDITED BY
Xingsen Guo,
University College London, United Kingdom

REVIEWED BY
Xiangchun Wang,
China University of Geosciences, China
Qunshu Tang,
Zhejiang University, China
Yifan Huang,
Chinese Academy of Sciences (CAS), China

*CORRESPONDENCE
Lei Xing
xingleiouc@ouc.edu.cn

RECEIVED 15 December 2023
ACCEPTED 12 April 2024
PUBLISHED 03 May 2024

CITATION
Zhang H, Xing L, Zhou Q, Li Q, Han J and Liu K (2024) Correlation between acoustic velocity and physical parameters of sea floor sediments: a case study of the northern South China Sea.
Front. Mar. Sci. 11:1356302.
doi: 10.3389/fmars.2024.1356302

Correlation between acoustic velocity and physical parameters of sea floor sediments: a case study of the northern South China Sea

Hongmao Zhang[1], Lei Xing[1,2,3,4]*, Qingjie Zhou[5], Qianqian Li[1], Jiayi Han[1] and Kai Liu[5]

[1]Key Laboratory of Submarine Geosciences and Prospecting Techniques, Ministry of Education, College of Marine Geosciences, Ocean University of China, Qingdao, China, [2]Evaluation and Detection Technology Laboratory of Marine Mineral Resources, Qingdao National Laboratory for Marine Science and Technology, Qingdao, China, [3]National Engineering Research Center of Offshore Oil and Gas Exploration, Beijing, China, [4]Key Laboratory of Marine Geophysical Prospecting Technology of Qingdao, Qingdao, China, [5]Key Laboratory of Marine Geology and Metallogeny, First Institute of Oceanography, Ministry of Natural Resources (MNR), Qingdao, China

As the interface between seawater and the seabed, superficial sediments on the seabed are an important part of the marine acoustic field environment and are indispensable for marine resource investigations. Studying sediments several meters to hundreds of meters below the seafloor is highly valuable and important. This study processes and analyses the water depth, topography and bottom data and obtains the shallow bottom profile and topographic map of the northern continental slope of the South China Sea (SCS). The study analyzes the influence of physical parameter (including density, porosity, and grain size) on the acoustic velocity in sediments. Single-parameter and dual-parameter models are established to further examine this influence. The results show that porosity and density have greater influences on the acoustic velocity of sediments than does grain size. Finally, the acoustic properties of several typical stations with water depths are tested to analyze the variations in the acoustic properties of the shallow sediments in the northern SCS. The results show that the influence of each parameter on the prediction of the acoustic velocity of the sediment is in the following order: porosity>density>grain size. This study analyses and reveals the reason why the seafloor sediments in the local area cause the acoustic properties to change greatly. It may be caused by changes in the sediment type, lithology along with the depth. And the other reason is the development of interlayer in the land slope of the northern SCS.

KEYWORDS

the northern South China Sea, physical parameter, acoustic velocity, density, porosity, grain size

1 Introduction

The seafloor is an important boundary of the underwater acoustic field and is also an object of common concern for the disciplines of ocean acoustics, marine geology and marine geophysics (Jackson and Richardson, 2007). The acoustic properties of seafloor sediments are important factors affecting the propagation of acoustic waves in the ocean, and related research has important application value in the fields of military marine environment safeguarding, seafloor target detection, and seafloor resource exploration (Liu et al., 2019; Zhao et al., 2023). Research on acoustic properties based on sediments in different sea areas has involved the following steps: research on acoustic property testing methods (Wang et al., 2018; Xing et al., 2022a); research on acoustic propagation theory (Gassmann, 1951; Wood, 1964; Stoll, 1977); and research on the correlation between acoustic properties and physical parameters (Endler et al., 2016). Additionally, the acoustic properties of different sea areas (Xing et al., 2022b) and their empirical prediction equations for acoustic velocity have contributed to the progress of sedimentary acoustics.

Since seafloor sediments combine the acoustic properties of both the granular skeleton and pore fluid, their acoustic properties are more complex than those of media, such as seawater and rocks (Wood, 1941; Wang et al., 2018). Biot has created Biot's theory, which can be applied to porous elastic media, and can be used to study the transmission properties of acoustic waves in surface sediments on the seafloor (Biot, 1956a; Biot, 1956b). The Biot–Stoll model was established by Stoll based on the porous elasticity theory (Stoll, 1977); the elasticity theory based on Buckingham's Viscous Grain Shearing (VGS) model was established by Stoll based on the porous elasticity theory (Stoll, 1977); and the VGS model was established by Buckingham based on the elasticity theory (Buckingham and Richardson, 2002; Buckingham, 2005). These authors also attempted to model the acoustic properties of sediments from different perspectives.

The empirical equations for seafloor sediment acoustics are based on carrying out many actual measurements of the acoustic and physical properties of sediments. And equation determine the interrelationships between the sediments and the relevant parameters, such as physical properties. These relationships are among the main elements of current sediment acoustics research (Lu et al., 2010; Bae et al., 2014). Compared to acoustic propagation theories with many constraints, empirical equations for sediment acoustics have more obvious and outstanding advantages. And empirical equations have the advantages of being more convenient and less expensive to use. Moreover, this approach can be used to invert the values of certain sediment physical property parameters under certain difficult-to-measure conditions or under no conditions to measure sea conditions, which can provide an important basis for marine development and exploration, and national defense science and technology engineering construction. Orsi and Dunn (Orsi and Dunn, 1990, Orsi and Dunn, 1991) also used statistical methods to fit measured values and constructed equations for the prediction of ocean acoustic velocity with respect to porosity. Richardson (Richardson and Briggs, 1996), Fu (Fu et al., 2004) and others have investigated *in situ* measurement techniques to carry out observational experiments in many foreign waters in the United States and to study the relationship between the acoustic velocity and the physical properties of the seafloor sediments (Richardson et al., 2002; Richardson and Briggs, 2004).

Research and analyses of the relevant elements of China's coastal waters and many results from empirical equations for acoustics are available (Xing et al., 2021). Lu et al. (Lu and Liang, 1993) applied the Hamilton model (Hamilton, 1985) to study the coastal region of southeastern China and derived an acoustic velocity model for marine sediments on the shallow continental shelf off the coast of southeastern China. It can provide a better understanding of the acoustic properties of seafloor sediments in this region (Liu et al., 2013).

In this study, a combination of measured data and theoretical modeling is used to investigate the acoustic properties of sea floor sediments on the land slope of the northern SCS and the mechanisms influencing the acoustic velocity of the sediments. The acoustic and physical parameters of the samples retrieved from the sampling laboratory from the sea floor sediments are measured, and one-parameter and two-parameter equations applicable to the acoustic velocity-physical parameters are established based on the measured data. The study area is also divided into upper, middle and lower land slopes to fit equations suitable for different regions. Then this study analyzes the characteristics of the lateral distribution of sediment acoustic velocity. Finally, the discussion of the influence mechanism of sediment acoustic properties is carried out by integrating physical parameters and shallow bottom profile.

2 Regional overview and data analysis

2.1 Regional overview

The study area is in the northern part of the SCS within the range of 115°E~115.5°E, 19.2°N~20.1°N (as shown in Figure 1). The shelf of the northern SCS is basically a continuation of the shelf, and the topographic line is approximately parallel to the coastline, roughly spreading in the NNE–WNW direction. There is a gentle inclination from the shore to the sea, with a total area of approximately 2.13×10^5 km^2. Additionally, the total land slope is approximately 1,300 km in length, with widths varying within 126~265 km. Generally, the land slope is in the form of a striped area, which is a shape that is wider in the east than in the west and spreads in the NE direction. It is with a length of 900 km and a width of approximately 143~342 km. In addition, the average slopes are approximately 1.3°~ 2.3°, which are more than ten to dozens of times larger than the slopes of the continental shelf.

Sediment samples for this study were taken from the land slope of the northern SCS, and a gravity column sampler was used to

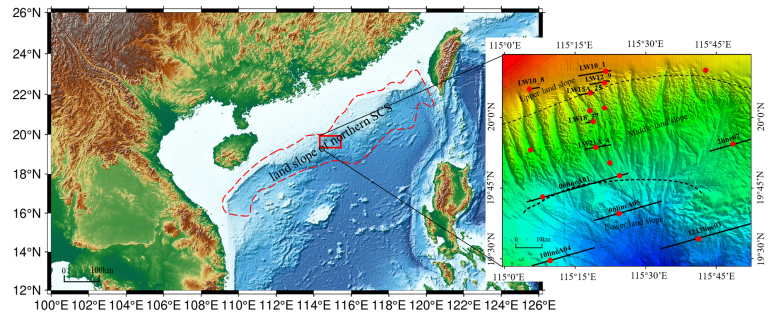

FIGURE 1
Location of the study area. The red box shows the study area, and the red dashed line is the range of the land slope of the northern SCS. The red dots are the sampling location. The black solid lines are the survey lines of shallow stratigraphic profile. The black dashed lines are the boundary of upper, middle, and lower land slope.

obtain sediment samples from a total of 17 stations with water depths ranging from 400 to 2500 m. The samples contain two 100 m drill holes, five 40 m drill cores, and 10 gravity column samples. The locations of the sampling sites are shown in Figure 1. The stations are widely distributed in various areas of the land slope.

Based on the slope and typical topographic features of the land slopes of the northern SCS, we can categorize the land slope into three zones: the upper land slope, the middle land slope, and the lower land slope (as shown in Figure 1). The slopes of the upper and middle land slopes range from 1° to 3°, while the lower land slope is in the range of 2° to 4°. Eleven typical shallow stratigraphic profiles are also selected. Specifically, LW10_1, LW10_8, LW12_9, and LW15A_25 are on the upper land slope of the study area. Changes in the topographic relief can be roughly observed in the profiles. The topographic changes in the upper land slope are gradual due to the proximity to the shelf. LW18_37, LW21A_4, 2line_07, and 06lineA01 are on the middle slope of the study area. Similarly, 06lineA05, 10lineA04 and 1213line03 are on the lower slope of the study area, and the middle and lower slope are close to the sea basin. Additionally, the various effects occurring in the area have made the topography of the area more undulating, and the topography and geomorphology are complicated.

2.2 Acoustic velocity measurements

For the indoor acoustic characterization of the sediment samples taken to the laboratory, the WSD-3 digital sonic instrument was used for the acoustic velocity measurements. During the measurement, the axial transmittance method is used. The acoustic waves are propagated through the transmitting and receiving transducers at the two ends of the sediment, and the propagation medium is the sediment between the transducers. The method uses a set of axial measurement devices, including a signal generator, a digital acoustic wave monitor, a test platform, and a transducer. Longitudinal transducers used to excite a single-frequency 3-5 period sinusoidal signal with a sampling rate of 5 MHz or 10 MHz. The acquired acoustic velocity is the average value of the sample in the length direction, and the accuracy of the measurement is ±5 m/s. The platform is measured accurately to 0.1 mm with calipers.

The acoustic velocity V and the acoustic attenuation coefficient α are calculated as Equation (1) and Equation (2):

$$V = \frac{L_s}{(t_s - t_0) \times 10^3} \tag{1}$$

$$\alpha = \frac{20 \times 10^3}{L_{s1} - L_{s2}} log_{10} \frac{E_{s1} E_{w2}}{E_{w1} E_{s2}} \tag{2}$$

where L_s is the length of the column sample from the land slope of the northern SCS, in mm. t_s is the travel time of the acoustic signal through the sea floor sediment, in μs. t_0 is the transducer zero-time correction, in μs. L_{s1} and L_{s2} are the lengths of the two sediment sections, respectively, in mm. E_{s1}, E_{s2}, E_{w1} and E_{w2} are the amplitudes of the acoustic signals that pass through shallow sediments and water of different lengths. The travel time of the acoustic signal in the sediment is read by the zero-crossing method, and the difference between the travel times of the signals in the two sections of sediment is calculated by the signal correlation method.

3 Data analysis and results for predicting the acoustic velocity sea floor sediments

3.1 Experimental data analysis

After the acoustic velocity of the sediment samples was measured and the sediment column sample was collected, the obtained experimental data were analyzed. A total of 80 sets of data were analyzed from 17 stations located in the study area: DZ01~DZ17. In the experimental process, in addition to unavoidable errors, there may also be manual errors. Some obvious measurement errors in the data are deleted and sorted and the study area is divided again. The following parameters can be obtained in the research area: the physical mechanics of the sediment samples and acoustic parameters. Table 1 shows that the sediment acoustic velocity measured at 100 kHz in the land slope of the northern SCS ranges from 1387 m/s to 1622 m/s. Lu et al

TABLE 1 Statistical table of the acoustic velocity and physical parameters.

Sample location	Type	Depth	Velocity	Density	Grain size	Porosity
	unit	m	m/s	g/cm^3	Φ	%
Upper land slope	Average	694.2	1533	1.725	3.9	56.42
	Maximum	778	1622	1.945	10.0	63.90
	Minimum	538	1447	1.471	1.3	45.00
Middle land slope	Average	1410	1479	1.525	6.2	67.27
	Maximum	1772	1516	1.721	8.5	79.00
	Minimum	965	1405	1.311	4.1	57.33
Lower land slope	Average	1944	1474	1.429	8.7	76.23
	Maximum	2032	1492	1.557	9.4	80.39
	Minimum	1842	1435	1.329	7.8	67.66
Area	Average	1274	1494	1.569	7.4	65.57
	Maximum	2032	1622	1.944	10.0	80.39
	Minimum	539	1405	1.311	1.3	45.00

(2006) measured the sediment acoustic velocity in the northern SCS to be 1420 m/s to 1880 m/s in 2006. Cheng et al (2011) measured the sediment acoustic velocity in the central part of the South Yellow Sea (SYS) to be 1427.7 m/s to 1594.8 m/s. Kan et al (2020) measured and analysed the sediment acoustic velocity in the sediment area of the middle SYS using an in-situ testing method (Kan et al., 2018) to be approximately 1433.7 m/s ~ 1607.6 m/s. The results of the acoustic velocity measurements in this paper are relatively accurate and reliable. The sediment acoustic impedance is an important parameter for determining the reflection from the seabed and is equal to the value of the acoustic velocity of the sediment multiplied by the sediment density. The values of the sediment acoustic impedance in the study area of this paper range from 1.906×10^5 g•cm^{-2}•s^{-1} ~ 3.099×10^5 g•cm^{-2}•s^{-1}.

3.2 Correlation between the acoustic velocity and physical parameters

The parameter equations are designed to describe the correlation between the acoustic velocity and a single physical parameter of the sea floor sediments. They can reflect the effect of the physical parameter on the acoustic velocity. Although the different physical parameters of sedimentation can be converted using the corresponding methods, seafloor sediment is a complex mixture. There is no way to accurately describe complex sediment with any one of these parameters. The single-parameter equations have limitations. In addition, there is no single correlation between the physical-mechanical properties of sediments and the longitudinal wave velocity. Therefore, it is necessary to analyze the multiparameter correlation of the sea floor sediments on the land slope of the northern SCS.

3.2.1 Porosity, density and acoustic velocity

The porosity, density, and acoustic velocity measured by sediment samples from 17 stations are used to establish a two-parameter model for the land slope with the porosity and density of the sediment as the independent variables and the acoustic velocity as the dependent variable, as shown in Figure 2. Figure 2 shows that the acoustic velocity of the sediment reaches a larger value when the porosity is lower and the density is greater, and the two-parameter equations are constructed according to the model in Figure 2 with the Equation (3):

$$Vp = 2230 - 11.61n - 580.9\rho + 0.07707n^2 + 214.3\rho^2 - 0.2528\rho n \quad (3)$$

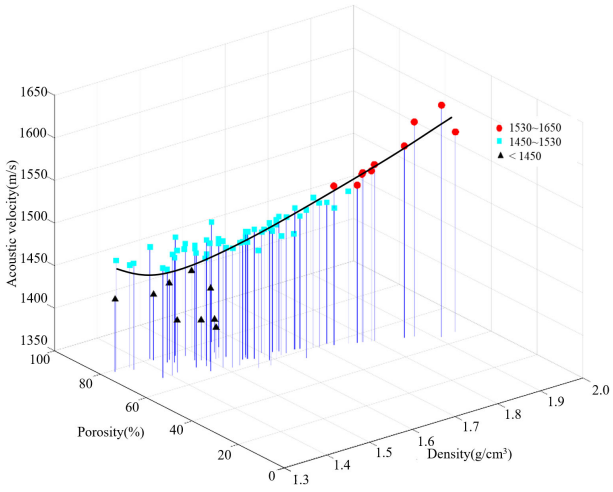

FIGURE 2
Porosity–density two-parameter acoustic velocity model. The solid line is the result of the two-parameter equation.

where V_p is the acoustic velocity, ρ is the density, and n is the porosity. The correlation coefficient r^2 equation is used to calculate the effect of fitting the variables of the prediction equation by using Equation (4):

$$r^2 = Cov\frac{(X, Y)}{\sigma_X \sigma_Y} \tag{4}$$

where X is the predicted data of the fitting equation, Y is the actual data, $Cov(X, Y)$ represents the covariance of X and Y, and σ is the variance. The larger the correlation coefficient is, the smaller the gap between the predicted results and the actual data. The correlation coefficient r^2 of this two-parameter equation is 0.9042, and the correlation coefficient is very high. In Figure 2, the black line shows the results of the two-parameter equations of the porosity and density.

3.2.2 Porosity, grain size and acoustic velocity

Using the measured porosity, grain size and acoustic velocity of the samples taken from the sea floor sediments, a two-parameter model is established. It is with the porosity and grain size of the sediments as the independent variables and the acoustic velocity as the dependent variable. The model is shown in Figure 3, and the model shows that when the measured porosity and grain size of the study area are lower, the sediment acoustic velocity reaches larger values. When the sediment acoustic velocity reaches a larger value, the two-parameter equation is constructed according to the model in Figure 3, and its relation is as Equation (5):

$$V_p = 1792 - 1.642n - 83.53Mz - 0.0039 - 2.322Mz^2 + 1.694nMz \tag{5}$$

where Mz is the grain size. The correlation coefficient r^2 of this two-parameter equation is 0.9102. In Figure 3, the black line shows the results of the two-parameter equations of the porosity and grain size.

3.2.3 Density, grain size and acoustic velocity

Similarly, a two-parameter model of sediments in this study area is established, with density and grain size as the independent variables and acoustic velocity as the dependent variable. The model diagram is shown in Figure 4. The sediment acoustic velocity increases with decreasing porosity and grain size. The two-parameter equations are constructed according to the model in Figure 4, and its relation is as Equation (6):

$$V_p = -125.3 + 138.2Mz + 1432\rho - 1.544Mz^2 - 268.3\rho^2 - 79.06\rho Mz \tag{6}$$

The correlation coefficient r^2 of this two-parameter equation is 0.9046, and the correlation coefficient is very high. In Figure 4, the black line shows the results of the two-parameter equations of the density and grain size.

3.3 Prediction equation of the acoustic velocity

Due to the complex topographic conditions on the slope of the northern SCS, this area experiences the greatest changes in water depth, topography, sediment type, and so on. It leads to large differences in the acoustic properties of the sediments in the upper and lower land slopes. The analysis of the study clarifies that the region shows a pattern of changes in the acoustic velocity according to the topography of the landscape. In the area of the upper slope where the water depth is less than 1000 m, the sediments in this area are influenced by the type of sediments on the continental shelf because of their proximity to the shelf, and the type of sediments is similar to that on the shelf. The sediments within the upper land slope are mainly silt and sand, gravels are even present in the sediments in individual areas, and shell fragments and coral fragments may also be present. Sediments on the upper land

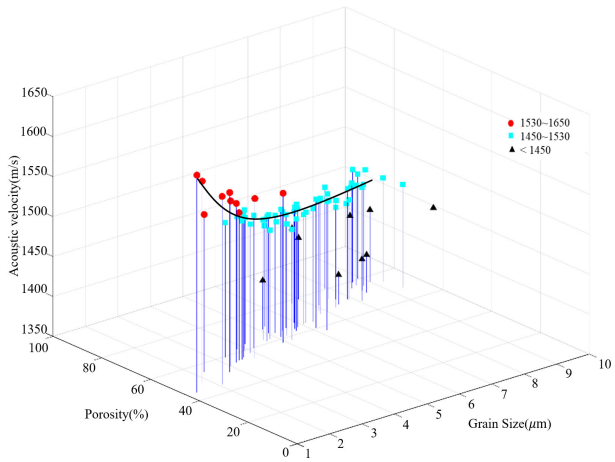

FIGURE 3
Porosity–grain size two-parameter acoustic velocity model. The solid line is the result of the two-parameter equation.

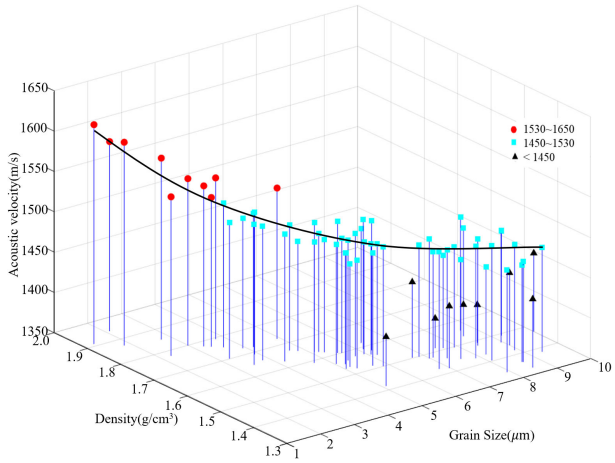

FIGURE 4
Density–grain-size two-parameter acoustic velocity model. The solid line is the result of the two-parameter equation.

slope have higher density and acoustic velocity, but there are some areas on the upper land slope that have sediments with low density and velocity.

The middle and lower land slopes with water depths greater than 1000 m are closer to the sea basin and are influenced by the sea basin. Thus, the types and properties of the sediments are similar to those in the sea basin area. The sediment types are mainly clayey silt, and the sediments in the middle and lower land slopes have higher water content, greater porosity, and lower density and acoustic velocity. Within the middle and lower land slopes, the topographic relief is highly variable, and most of the sediment transport occurs mainly in this region. Therefore, there are variations in the acoustic properties of the sediments within this wide area.

To analyze the regional distributions of the acoustic velocity, grain size, density, and water content of sea floor sediments based on the acoustic parameters measured from laboratory sediments and the grain size, porosity, density, and water content of the sediment samples measured by geotechnical tests (as shown in Figure 5). There is a certain pattern of change in the variation in the acoustic velocity and each physical parameter in the whole study area from the northern continental shelf to the southern sea. From north to south, the acoustic velocity varies from 1447~1622 m/s in the upper land slope to 1387~1516 m/s in the middle land slope and then to 1435~1492 m/s in the lower land slope. The variation is caused by the different types of sediment at different water depths. The sediments on the upper land slope in shallow water are generally coarser, less porous, and denser and possess higher acoustic velocities. The sediments on the middle and lower land slopes in deeper water are the opposite of those on the upper land slope. Thus, there is an overall trend toward gradual decreases. The average acoustic velocity on the upper land slope is generally greater than 1447 m/s, which is the high-velocity area in the region. The average acoustic velocities on the lower and middle land slopes are lower than 1447 m/s, and they are the lowest in the whole region. Sediment is composed of solid particles and porous seawater, and acoustic waves propagate between them. In addition, the bulk modulus and shear resistance of solid particles are generally greater than those of porous seawater, so the factor that has a stronger impact on the acoustic velocity is the grain size. It is generally believed that the larger the grain size is, the larger the solid particles in the skeleton of the sediment are and the greater the proportion of the sediment is. Thus, the porous seawater content of the sediments is lower, and the acoustic velocity is higher.

There are some differences in the topography and sedimentary layers between divided land slopes. To study the differences in the sediment acoustic velocity in different regions, prediction equations for the sediment acoustic velocity in different regions are constructed. Prediction equations of the acoustic velocity for the land slope of the northern SCS in the study area are established. Similarly, different regional acoustic velocity prediction models for the upper, middle and lower land slopes are established to study the regional acoustic properties of the sediments. In establishing the

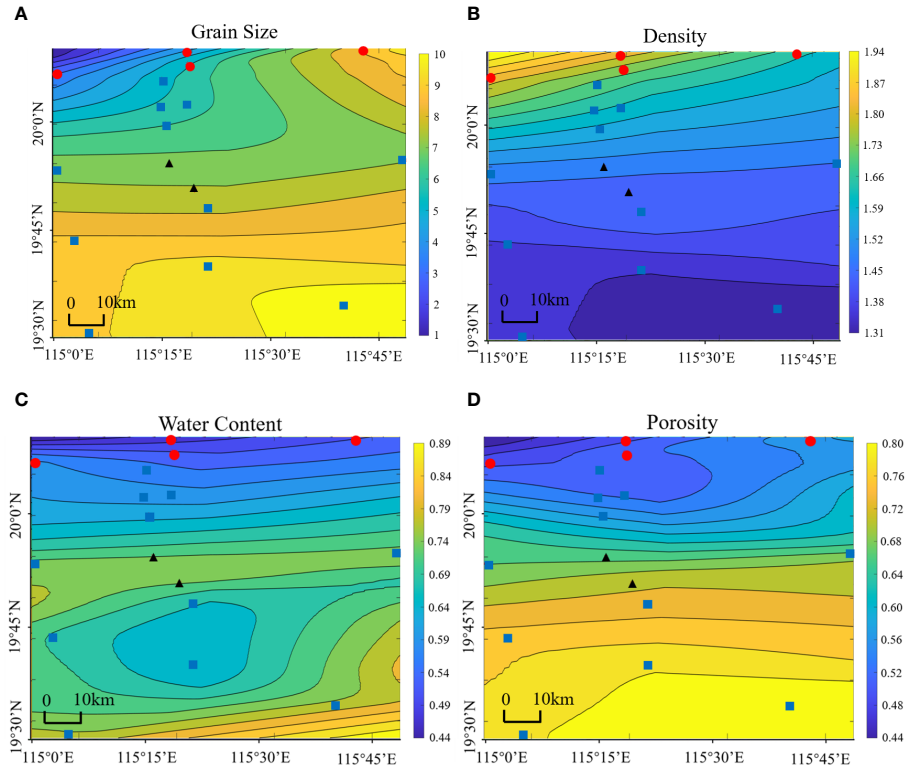

FIGURE 5
Distribution of parameters of sea floor sediments. **(A)** grain size, **(B)** density, **(C)** water content, and **(D)** porosity. The red dots are the samples where velocity is more than 1530 m/s. The blue boxes are the samples where velocity is between 1450 m/s and 1530 m/s. The black triangles are the samples where velocity is below 1450 m/s.

subregional prediction equations for the sediment acoustic velocity, one-parameter and two-parameter equations are established for the upper, middle and lower land slopes, and the equations and models are as follows.

3.3.1 Upper land slope

The sediments on the upper land slope are generally coarse, less porous, denser and possess higher acoustic velocities. Additionally, the acoustic velocity V_p of the sediments on the upper land slope has the following fitting relationships with porosity n, grain size Mz, and density ρ:

$$V_p = 0.1153n^2 - 5.0974n + 1870.1,\ r^2 \text{ is } 0.8216.$$

$$V_p = 2.2082Mz^2 - 42.519Mz + 1658.9,\ r^2 \text{ is } 0.8094.$$

$$V_p = 144.16\rho^2 - 179.17\rho + 1411.7,\ r^2 \text{ is } 0.8769.$$

The correlation coefficients of the above single-parameter equations established for each subregion of the land slope are greater than those established for the whole region, which means that the fitting effect is better. Therefore, the subregional single-parameter equations can better reflect the relationship between the acoustic velocity of the sediment in the upper land slope and the physical parameters.

The two physical parameter acoustic velocity equations for the sediments in the upper land slope are established as follows:

$$V_p = -2955 + 2.659n + 5229\rho + 0.1781n^2 - 1235\rho^2 - 16.12\rho n,\ r^2 \text{ is } 0.9281.$$

$$V_p = 1413 + 17.64n - 144.3Mz - 0.27n^2 - 2.362Mz^2 + 2.65nMz,\ r^2 \text{ is } 0.9116.$$

$$V_p = 8548 - 500.1Mz - 7328\rho + 12.84Mz^2 + 19.53\rho^2 + 231.5\rho Mz,\ r^2 \text{ is } 0.9263.$$

Therefore, the two-parameter model of the sediment acoustic velocity established in different zones also has high correlation coefficients and can be more accurately used to forecast the acoustic velocity of seafloor sediments, and the two-parameter equations fitted to different zones are more accurate than the two-parameter equations established for the whole area for practical applications.

3.3.2 Middle land slope

The sediments on the middle land slope are generally finer, more porous, less dense and possess lower acoustic velocities than the sediments on the upper land slope, and the following fitting relationship exists between the acoustic velocity V_p and physical parameters for the sediments on the middle land slope:

$$V_p = 0.027n^2 - 8.0052n + 1892.9,\ r^2 \text{ is } 0.4279.$$

$$V_p = 6.4974Mz^2 - 67.125Mz + 1320.9,\ r^2 \text{ is } 0.4914.$$

$$V_p = 608.92\rho^2 - 1677.9\rho + 2616.3,\ r^2 \text{ is } 0.4066.$$

The correlation coefficients of the fitted single-parameter prediction equations for the sediment acoustic velocity in the middle land slope are small and may be attributed to the large differences in the samples from the sampling sites on the middle land slope within the study area. Additionally, there are large differences in the porosity, grain size and density of the sediment. Additionally, slightly larger differences in the measurements of the sediment parameters from the same station on the middle land slope are found during the fitting process, which may be caused by measurement errors. The study area has a wide range of middle land slope, so it is possible that these differences are caused by the samples.

A two-parameter equation for the acoustic velocity and physics of the middle land slope sediments is constructed, and each expression is given below:

$$V_p = -1284 + 44.13n + 1855\rho - 0.1643n^2 - 246.4\rho^2 - 16.68\rho n,\ r^2 \text{ is } 0.7969.$$

$$V_p = 1471 + 6.183n - 25.04Mz - 0.1082n^2 - 2.323Mz^2 + 0.8041nMz,\ r^2 \text{ is } 0.726.$$

$$V_p = -3289 + 597.6Mz + 3880\rho - 16.01Mz^2 - 734.8\rho^2 - 266.1\rho Mz,\ r^2 \text{ is } 0.8229.$$

The correlation coefficients of the two-parameter model of the sediment acoustic velocity in the land slope divided into different areas are greatly improved compared with those of the single-parameter equations. Thus, the two-parameter model can be more accurately used for the prediction of the acoustic velocity of seafloor sediment.

3.3.3 Lower land slope

The sediments on the lower land slope are generally fine, porous, or less dense and possess a lower acoustic velocity than those on the upper land slope. Since there are fewer sampling points on the lower land slope, only DZ12, and DZ15 are considered, and since the sample data are limited, the establishment of single-parameter equations has little reference significance. The two-parameter equations of acoustic velocity V_p and physical parameters of the lower land slope sediment are established for the land slope of the northern SCS, and the expressions of these equations are as follows:

$$V_p = 2741 - 86.75n + 2550\rho + 0.6467n^2 - 647.2\rho^2 - 6.804\rho n,\ r^2 \text{ is } 0.437.$$

$$V_p = 4837 - 37.09n - 453.1Mz + 0.1433n^2 + 18.44Mz^2 + 1.769nMz,\ r^2 \text{ is } 0.2339.$$

$$V_p = 2143 - 421.1Mz + 369.5\rho + 38.55Mz^2 - 680.8\rho^2 - 183.1\rho Mz,\ r^2 \text{ is } 0.4241.$$

The correlation coefficient of the two-parameter model of the sediment acoustic velocity established for the lower land slope is small and has little reference value for accurately predicting the sediment acoustic velocity. Therefore, importantly, enough sampling points are necessary for comprehensive coverage when establishing equations for predicting the acoustic velocity.

4 Discussion

The sediments on the land slope of the northern SCS become consolidated and compacted as the depth of the sediments increases in the longitudinal direction due to geological movements and a series of changes. Therefore, sediments are characterized by changes in porosity and water content, with a tendency to increase in density, acoustic velocity, and acoustic impedance. However, for actual complex seabed sediments on the land slope, due to the changes in the burial depth, there are large differences in lithology. Thus, the acoustic velocities of the sea floor sediments on the land slope also change, and the distributions of the acoustic velocities in some places greatly differ from the overall distribution. This study examines and analyses the acoustic properties of the shallow sediments in the northern SCS. There are the differences that exist between the geological units of the different sediments through the acoustic properties by analyzing the acoustic properties of a few representative stations and bathymetric data.

4.1 Upper land slope

The upper land slope, where water depths are less than 778 m, is in the upper part of the study area and the land slope, closer to the shelf. The types of seafloor sediments are mainly silt and clayey silt. The seafloor sediments are generally characterized as follows: physical parameters, such as acoustic velocity and density, have a clear tendency caused by water depth, and there is also a clear change in acoustic properties in the vertical direction.

DZ03 is a station on the LW12_9 survey line and on the upper land slope. The seafloor sediments near the station are dominated by silty and clayey silt. As shown in the plot of the variation in each parameter with depth at station DZ03 in Figure 6, the seafloor

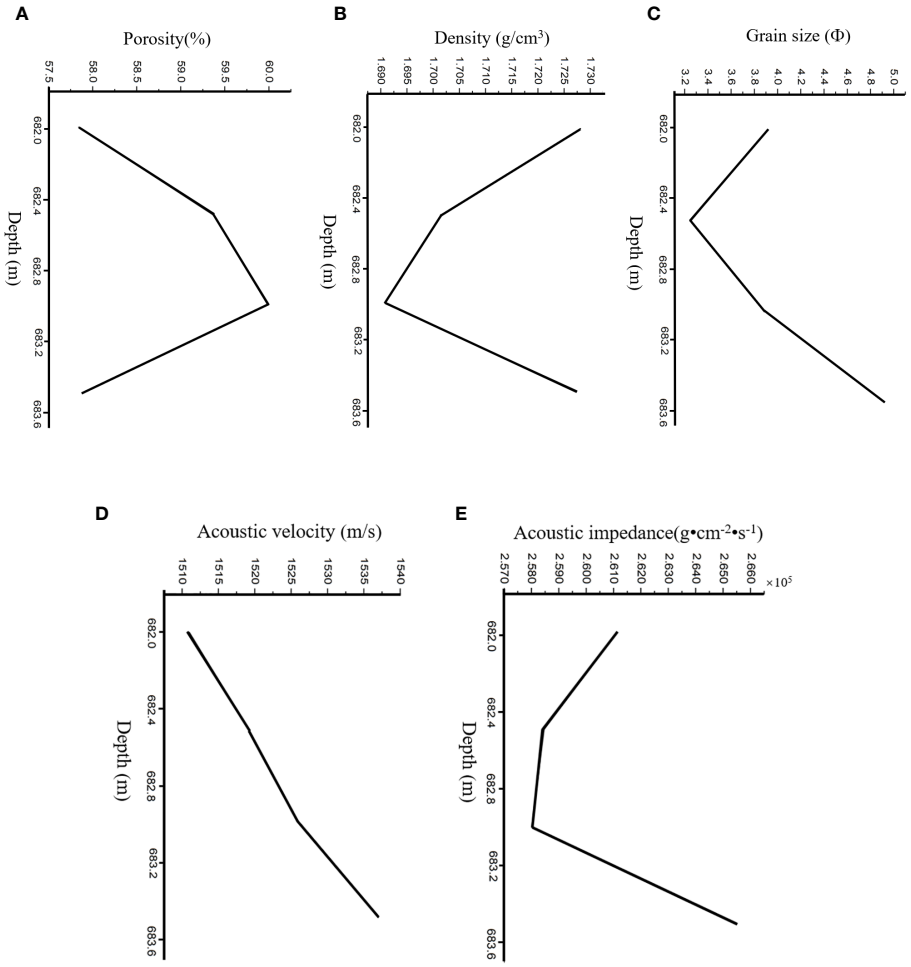

FIGURE 6
Variation in each parameter with depth at station DZ08. **(A)** porosity, **(B)** density, **(C)** grain size, **(D)** acoustic velocity, and **(E)** acoustic impendence.

sediments generally have a high acoustic velocity, a clear trend in density caused by water depth, and a clear change in acoustic properties in the vertical direction. The apparent variation reflects the complex sedimentary changes in the region and the development of coral reefs and coarse-grained detritus on the upper land slope. The presence of it also influences the gradients of the acoustic velocity and other parameters. It is not difficult to determine that the trend in acoustic impedance is similar to that in density from the graph of the trend in each parameter with water depth, and the trend in wave impedance can reflect reflective properties. Therefore, density has a greater influence on the sediment deposit layer in the upper land slope, which is reflected in the graph in which they have similar trends.

4.2 Middle land slope

The middle land slope, with water depths less than 1772 m, is in the middle of the study area and is in an intermediate region between the shelf and the basin. The area is more variable and more affected. The type of seafloor sediments in the middle land slope of the northern SCS is mainly silty clay, and the seafloor sediments are generally characterized as follows: parameters such as acoustic velocity and density exhibit small changes caused by water depth. There is a small change in the acoustic properties evident in the vertical direction, and the differences in the acoustic properties of the sediments between the stations are also relatively small.

DZ05 is a station on the LW10_8 survey line and is on the middle land slope. Figure 7 shows the variation in each parameter with depth at station DZ05. The seafloor sediments near this station are predominantly clayey silt. At the inflection point where the trend in the acoustic velocity changes significantly, the corresponding shallow stratigraphic profile is analyzed. Possibly, because of the variation in sediment type and lithology with burial depth, sea floor sediments cause the acoustic properties of the middle land slope to vary clearly with depth, where strata develop.

The trend in acoustic impedance is similar to that in density from the graph of the trend in each parameter with water depth, and the trend in wave impedance can reflect reflective properties. Therefore, density has a greater influence on the sediment deposit layer in the middle land slope, which is reflected in the graph in which they have similar trends.

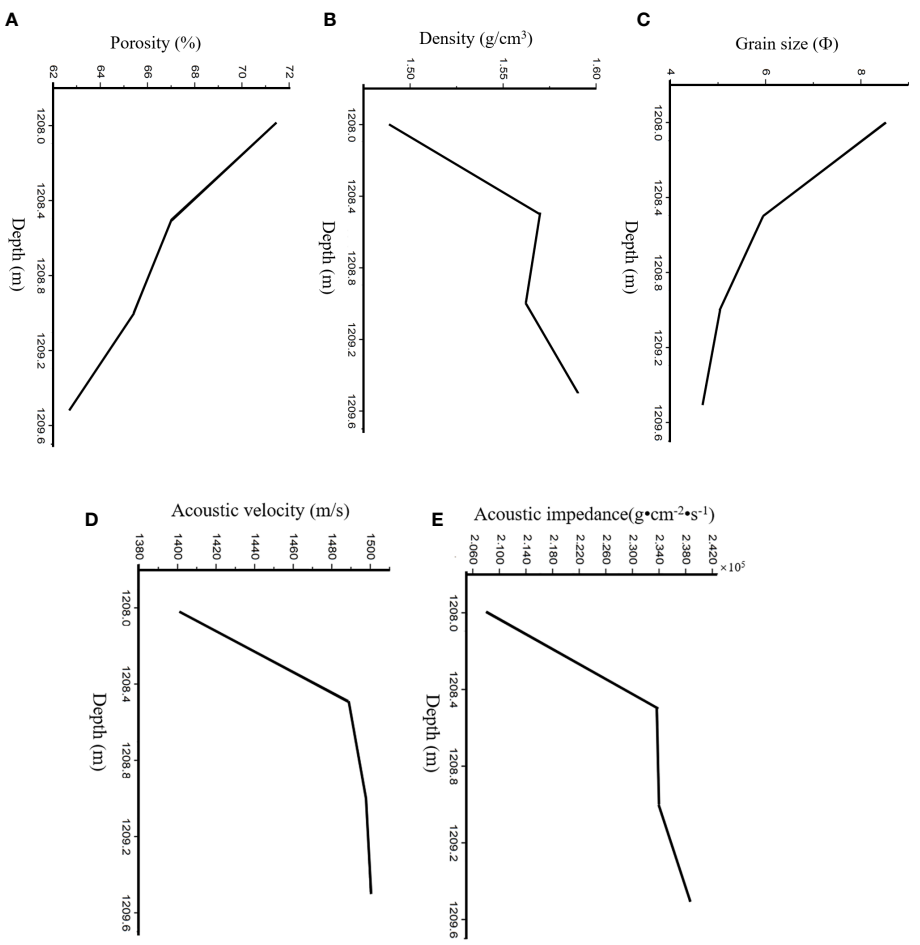

FIGURE 7
Variation in each parameter with depth at station DZ05. **(A)** porosity, **(B)** density, **(C)** grain size, **(D)** acoustic velocity, and **(E)** acoustic impendence.

4.3 Lower land slope

The lower land slope with water depths greater than 1842 m is in the lower part of the study area, closer to the sea basin, and is connected to the upper and middle land slopes. Thus, the variation in each parameter in this area is also more affected. The type of seafloor sediment in the lower land slope of the northern SCS is mainly silty clay, and the seafloor sediments generally have the following characteristics. Parameters such as acoustic velocity and density do not show significant trends caused by water depth. Moreover, there are small variations in the acoustic properties in the vertical direction, and the differences in the acoustic properties of the sediments between stations are also relatively small.

DZ12 is a station on the 06lineA05 survey line and is on the lower land slope. The complex sediment changes in the area are shown in the plot of each parameter with depth at station DZ12 in Figure 8.

At the inflection point, the trend of the acoustic velocity changes significantly. Based on the analysis of the depth of the corresponding profile, it is possible that the seafloor sediments still have large water depth variations in acoustic properties of the lower land slope due to local variations in sediment type, and lithology. The trend in acoustic impedance is similar to that in density based on the graph of the trend in each parameter with water depth, and the trend in wave impedance can reflect reflective properties. Therefore, density has a greater influence on the sediment deposit layer in the upper land slope, which is reflected in the graph in which they have similar trends.

5 Conclusion

The sediments of the land slope of the northern SCS are studied by testing and analyzing the acoustic velocity and physical parameters, and the main conclusions are as follows:

(1) The sediments in the study area are complex and include silt and silty clay, and the sediments in the area are generally characterized by a high-water content and high porosity. Overall, the highest acoustic velocity values are found in silt, and the lowest are found in silty clays, with a clear correlation between the sediment acoustic velocity and type.

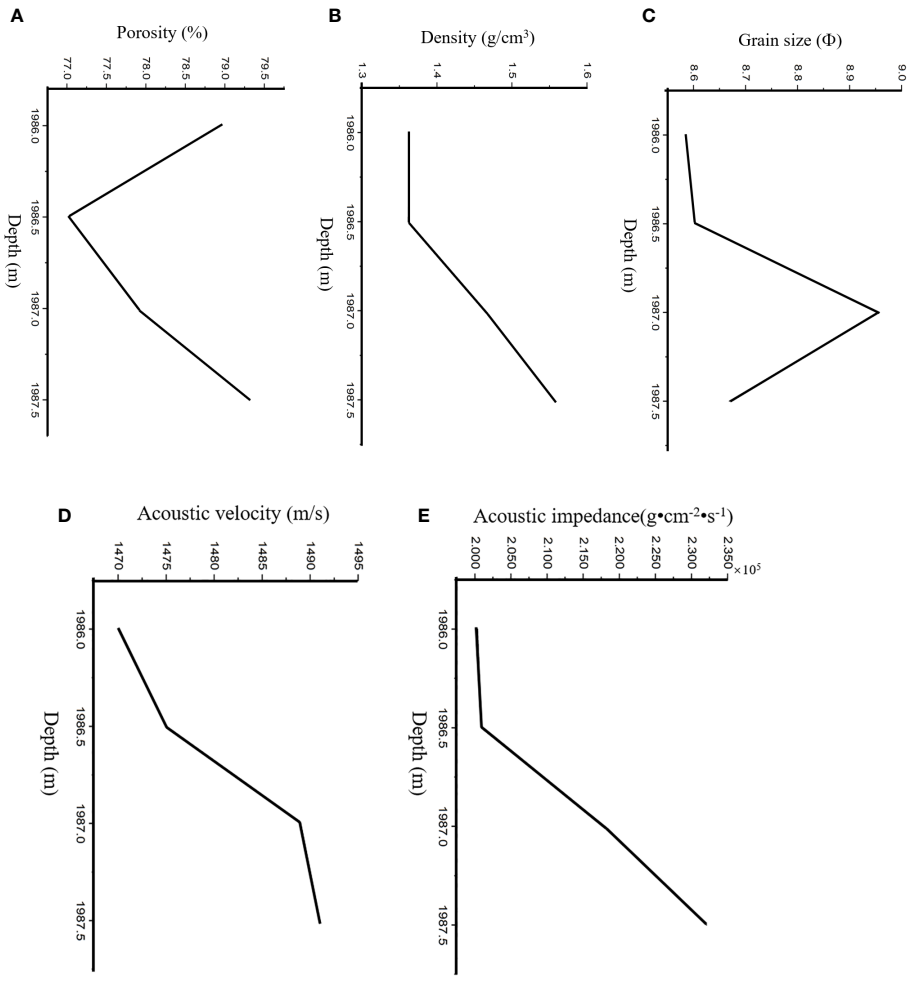

FIGURE 8
Variation in each parameter with depth at station DZ12. **(A)** porosity, **(B)** density, **(C)** grain size, **(D)** acoustic velocity, and **(E)** acoustic impendence.

(2) Correlation analysis of the physical parameters of the land slope sediment samples from the northern SCS with the acoustic properties of the samples from the laboratory tests revealed that the acoustic velocity of the samples from the laboratory tests correlated well with the density and porosity and, to a certain extent, with the grain size. The acoustic velocities at 100 kHz are 1387 m/s ~ 1622 m/s, which is in general agreement with the velocities reported in studies in other Chinese seas but lower than those predicted by the Hamilton model.

(3) To better study the relationships between each parameter (including density, porosity, and grain size) and the acoustic velocity in each subregion, this study also establishes single-parameter correlations and two-parameter equations suitable for the upper, middle and lower land slopes in each subregion. The analysis shows that the two-parameter correlation coefficients are greater than the single-parameter correlation coefficients. The control method is used to study the influence of each parameter on the acoustic velocity, and the results of the analysis show that porosity and density had greater influences on the acoustic velocity of the sediment. The influence of each parameter on the prediction of the acoustic velocity of the sediment is in the following order: porosity>density>grain size.

(4) Finally, several typical stations are selected to test and analyze the data of acoustic properties with water depth, and the changes in the acoustic properties of shallow sediment topography in the northern SCS seabed and the differences between different sedimentary geomorphological units are investigated. The variation in each parameter with depth at the study station to the corresponding position in the corresponding shallow stratigraphic profile shows the complex sediment changes in the region. And it is shown at the inflection points where the trend in the acoustic velocity changes significantly. In local area, acoustic properties changing greatly may be caused by changes in the sediment type, lithology along with the depth. And the interlayer developed the land slope of the northern SCS also may cause this change.

Data availability statement

The original contributions presented in the study are included in the article/supplementary materials, further inquiries can be directed to the corresponding author/s.

Author contributions

HZ: Writing – original draft, Methodology. LX: Funding acquisition, Writing – review & editing, Supervision. QZ: Data curation, Writing – review & editing. JH: Writing – original draft. QL: Writing – review & editing. KL: Writing – review & editing.

Funding

The author(s) declare financial support was received for the research, authorship, and/or publication of this article. This work is supported in part by the National Natural Science Foundation of China under grant 42276055; in part by the National Key Research and Development Program under grant 2022YFC2803503; in part by the Fundamental Research Funds for the Central Universities under grant 202262008; in part by Fujian Provincial Key Laboratory of Marine Physical and Geological Processes, (NO. KLMPG-22-08); and in part by the Natural Science Foundation of Shandong Province under grant ZR2022MD067.

Acknowledgments

The authors thank the reviewers for their constructive comments and suggestions, which significantly improved the quality of this paper.

Conflict of interest

The authors declare that the research was conducted in the absence of any commercial or financial relationships that could be construed as a potential conflict of interest.

Publisher's note

References

Bae, H. S., Kim, D. C., Lee, G. S., Kim, G. Y., Kim, S. P., Seo, Y. K., et al. (2014). Physical and acoustic properties of inner shelf sediments in the South Sea, Korea. *Quat. Int.* 344, 125–142. doi: 10.1016/j.quaint.2014.03.058

Biot, M. A. (1956a). Theory of propagation of elastic waves in a fluid-saturated porous solid. I. Low frequency range. *Acoust. Soc Am.* 28, 168–178. doi: 10.1121/1.1908239

Biot, M. A. (1956b). Theory of propagation of elastic waves in a fluid-saturated porous solid. II. Higher frequency range. *Acoust. Soc Am.* 28, 179–191. doi: 10.1121/1.1908241

Buckingham, M. J. (2005). Compressional and shear wave properties of marine sediments: comparisons between theory and data. *J. Acoust. Soc. Am.* 117 (1), 137–152. doi: 10.1121/1.1810231

Buckingham, M. J., and Richardson, M. D. (2002). On tone-burst measurements of sound speed and attenuation in sandy marine sediments. *IEEE J. Ocean. Eng.* 27, 429–453. doi: 10.1109/JOE.2002.1040929

Cheng, J. J., Fu, M. Z., Meng, X. M., Liu, L. J., Kan, G. M., and Liu, B. H. (2011). Correlation analysis of physical properties and compressional wave velocity of seafloor sediments from the central part of the south Yellow sea. *Periodical Ocean Univ. China.* 41, 331–336.

Endler, M., Endler, R., Wunderlich, J., Bobertz, B., Leipe, T., Moros, M., et al. (2016). Geo-acoustic modelling of late and postglacial sedimentary units in the Baltic Sea and their acoustic visibility. *Mar. Geol.* 376, 86–101. doi: 10.1016/j.margeo.2016.03.015

Fu, S. S., Tao, C. H., Prasad, M., Wilkens, R. H., and Frazer, L. N. (2004). Acoustic properties of coral sands, Waikiki, Hawaii. *J. Acoust. Soc. Am.* 115, 2013–2020. doi: 10.1121/1.1689340

Gassmann, F. (1951). Vierteljahrsschrift der Natruforschenden Gesellschaft in Zuric. *Uber die elastizitat poroser Medien. Vier. der Natur. Gesellschaft in Zurich*, Vol. 96. 1–23.

Hamilton, E. L. (1985). Acoustic velocity as a function of depth in marine sediments. *J. Acoust. Soc. Am.* 78, 1348–1355. doi: 10.1121/1.392905

Jackson, D. R., and Richardson, M. D. (2007). *High-frequency seafloor acoustics* (New York: Springer Science, Business Media). doi: 10.1007/978-0-387-36945-7

Kan, G., Cao, G., Wang, J., Li, G., Liu, B., Meng, X., et al. (2020). Shear wave speed of shallow seafloor sediments in the northern South China Sea and their correlations with physical parameters. *Earth Space Sci.* 7, e2019EA000950. doi: 10.1029/2019EA000950

Kan, G. M., Liu, B. H., Wang, J. Q., Meng, X. M., Li, G. B., Hua, Q. F., et al. (2018). Sound speed dispersion characteristics of three types of shallow sediments in the Southern Yellow Sea. *Mar. Georesour. Geotechnol.* 36, 853–860. doi: 10.1080/1064119X.2017.1392659

Liu, B. H., Han, T. C., Kan, G. M., and Liu, G. B. (2013). Correlations between the in situ acoustic properties and geotechnical parameters of sediments in the Yellow Sea, China. *J. Asian Earth Sci.* 77, 83-90. doi: 10.1016/j.jseaes.2013.07.040

Liu, B. H., Kan, G. M., Li, G. B., Yu, S. Q., Meng, X. M., Wang, J. Q., et al. (2019). *Seafloor sediments acoustic measurement techniques and application* (Beijing: Science Press).

Lu, B., and Liang, Y. B. (1993). Acoustic velocity and physical parameters relationship in marine sediments. *Mar. Sci., 06. (in Chinese).*

Lu, B., Li, G. X., Huang, S. J., and Zhang, F. S. (2006). The comparing of seabed sediment acoustic-physical properties in the Yellow Sea, the East China Sea and northern the South China Sea(in Chinese). *Ocean Technol.* 24, 28–33. doi: 10.3969/j.issn.1003-2029.2005.02.008

Lu, B., Liu, Q., and Li, G. X. (2010). Grain and pore factors in acoustic response to seafloor sediments. *Mar. Georesour. Geotechnol.* 28 (2), 115–129. doi: 10.1080/10641191003780724

Orsi, T. H., and Dunn, D. A. (1990). Acoustic velocity and related physical properties of fine grained abyssal sediments from the Brazil Basin (South Atlantic Ocean). *J. Acoust. Soc. Am.* 88, 1536–1542. doi: 10.1121/1.400311

Orsi, T. H., and Dunn, D. A. (1991). Correlations between acoustic velocity and related properties of glacio-marine sediments: Barents Sea. *Geo-Marine Lett.* 11, 79–83. doi: 10.1007/BF02431033

Richardson, M. D., and Briggs, K. B. (1996). *In situ* and laboratory geoacoustic measurements in soft mud and hard-packed sand sediments: Implications for high-frequency acoustic propagation and scattering. *Geo-Marine Lett.* 16, 196–203. doi: 10.1007/BF01204509

Richardson, M. D., Briggs, K. B., Bentley, S. J., Walter, D. J., and Orsi, T. H. (2002). The effects of biological and hydrodynamic processes on physical and acoustic properties of sediments off the Eel River, California. *Mar. Geol.* 182, 121–139. doi: 10.1016/S0025-3227(01)00231-6

Richardson, M. D., and Briggs, K. B. (2004). Empirical predictions of seafloor properties based on remotely measured sediment impedance. *High Frequency Ocean Acoustic Conference*. Melville, Louisiana, USA: AIP Pres 728, 12–21. doi: 10.1016/S0025-3227(01)00231-6

Stoll, R. D. (1977). Acoustic wave in ocean sediments. *Geophysics.* 42, 715–725. doi: 10.1190/1.1440741

Wang, J. Q., Liu, B. H., Kan, G. M., Li, G. B., Zheng, J. W., Meng, X. M., et al. (2018). Frequency dependence of sound speed and attenuation in fine-grained sediments from 25 to 250 kHz based on a probe method. *Ocean Eng.* 36, 515–521. doi: 10.1016/j.oceaneng.2018.04.078

Wood, A. B. (1941). *A Textbook Of Sound: Being An Account Of The Physics Of Vibrations With Special Reference To Recent Theoretical And Technical Developments* (USA: Macmillan).

Wood, A. B. (1964). *A Textbook of Sound. 3rd edition*. Ed. G. Bell (London: Sons Ltd.).

Xing, L., Li, Q. Q., Meng, Q. W., Liu, H. S., Wei, J., Lu, B. R., et al. (2022a). Enlightenment of the mariana fore-arc sedimentary basin evolution to the subduction process. *Acta GEOLOGICA SINICA-ENGLISH EDITION.* 96, 10. doi: 10.1111/1755-6724.14860

Xing, L., Lin, H. R., Zhang, D., Li, Q. Q., Zhou, H. W., and Liu, H. S. (2022b). Facial characteristics of air gun array wavelets in the time and frequency domain under real conditions. *J. Appl. Geophys.* 199, 104591. doi: 10.1016/j.jappgeo.2022.104591

Xing, L., Liu, X. Q., Liu, H. S., Qin, Z. L., and Ma, B. J. (2021). Research on the construction of a petrophysical model of a heterogeneous reservoir in the hydrate test area in the Shenhu area of the South China sea (SCS). *Geofluids* 2021, 1-19. doi: 10.1155/2021/5586118

Zhao, M. X., Liu, H. S., Wang, W. Q., Ma, Q., and Xing, L. (2023). Numerical study on mechanical properties and instability characteristics of sandy reservoir containing hydrate interlayer. *Ocean Eng.* 286. doi: 10.1016/j.oceaneng.2023.115694

frontiers | Frontiers in Marine Science

TYPE Original Research
PUBLISHED 17 May 2024
DOI 10.3389/fmars.2024.1370294

OPEN ACCESS

EDITED BY
Guangming Kan,
Ministry of Natural Resources, China

REVIEWED BY
Chunmei Yang,
Ministry of Natural Resources, China
Li He,
Chinese Academy of Sciences (CAS), China

*CORRESPONDENCE
Jee Woong Choi
choijw@hanyang.ac.kr
Hyoung Sul La
hsla@kopri.re.kr

RECEIVED 14 January 2024
ACCEPTED 29 April 2024
PUBLISHED 17 May 2024

CITATION
Lee DH, Han D-G, Choi JW, Son W, Yang EJ, La HS and Tang D (2024) Estimation of geoacoustic parameters and source range using airgun sounds in the East Siberian Sea, Arctic Ocean.
Front. Mar. Sci. 11:1370294.
doi: 10.3389/fmars.2024.1370294

Estimation of geoacoustic parameters and source range using airgun sounds in the East Siberian Sea, Arctic Ocean

Dae Hyeok Lee[1], Dong-Gyun Han[2,3], Jee Woong Choi[1,4]*, Wuju Son[5,6], Eun Jin Yang[5], Hyoung Sul La[5,6]* and Dajun Tang[7]

[1]Department of Marine Science and Convergence Engineering, Hanyang University ERICA, Ansan, Republic of Korea, [2]Research Center for Ocean Security Engineering and Technology, Hanyang University ERICA, Ansan, Republic of Korea, [3]Oceansounds Incorporation, Ansan, Republic of Korea, [4]Department of Military Information Engineering, Hanyang University ERICA, Ansan, Republic of Korea, [5]Division of Ocean and Atmosphere Sciences, Korea Polar Research Institute, Incheon, Republic of Korea, [6]Department of Polar Science, University of Science and Technology, Daejeon, Republic of Korea, [7]Applied Physics Laboratory, University of Washington, Seattle, WA, United States

Dispersion is a representative property of low-frequency sound propagation over long distances in shallow-water waveguides, making dispersion curves valuable for geoacoustic inversion. This study focuses on estimating the geoacoustic parameters using the dispersion curves extracted from airgun sounds received in the East Siberian Sea. The seismic survey was conducted in September 2019 by the icebreaking research vessel R/V Araon, operated by the Korea Polar Research Institute. A single hydrophone was moored at the East Siberian Shelf, characterized by nearly range-independent shallow water (<70 m) with a hard bottom. In the spectrogram of the received sounds, the dispersion curves of the first two modes were clearly observed. Utilizing a combination of warping transform and wavelet synchrosqueezing transform these two modes were separated. Then, the geoacoustic parameters, such as sound speed and density in the sediment layer, were estimated by comparing the two modal curves extracted at a source-receiver distance of approximately 18.6 km with the predictions obtained by the KRAKEN normal-mode propagation model. Subsequently, the distances between the airgun and the receiver system in the 18.6 to 121.5 km range were estimated through the comparison between the measured modal curves and the model replicas predicted using the estimated geoacoustic parameters.

KEYWORDS

seismic airgun sounds, dispersion curves, warping, geoacoustic inversion, East Siberian Sea, Arctic Ocean

1 Introduction

The East Siberian Sea remains one of the least studied areas in the Arctic Ocean due to its harsh climate characterized by heavy sea ice conditions. The topography of the East Siberian Shelf, located between the Chukchi Sea and the Laptev Sea, consists of a flat and shallow hard-bottom region that gradually slopes from southwest to northeast (Jakobsson et al., 2020). Approximately 70% of the waters have a water depth shallower than 50 m, with an average water depth of ~58 m (Outridge et al., 2008). Previous studies reported that the East Siberian Shelf is primarily composed of cemented subsea permafrost, which refers to a permanently frozen sedimentary layer (Brown et al., 1997; Romanovskii, 2004). This permafrost is overlaid by a relatively soft surficial layer consisting of a mixture of silt, sand, and stones (O'Regan et al., 2017; Jin, 2020; Han et al., 2023). As global warming accelerates in the Arctic region, significant environmental changes are occurring in the Arctic Ocean, leading to drastic changes in the underwater acoustic environment (Frisk, 2012; Mahanty et al., 2020; Duarte et al., 2021).

As part of research on these changes in the ocean environment, we have recently published two papers that present the outcomes of our studies on the underwater acoustical environment in the East Siberian Sea. In the first paper, Han et al. (2021) conducted measurements of long-term acoustic ambient noise in the East Siberian continental margin for a year, spanning from August 2017 to August 2018. Our analysis revealed that the spectrum level varied with seasons, exhibiting a strong negative correlation with changes in the sea ice concentration covering the sea surface. This pattern is likely attributed to increased ambient noise level due to exposure to underwater noise sources such as wind and rainfall as the sea ice on the sea surface melts in the summer. In addition, the utilization of airgun in seismic surveys in regions where sea ice has melted also contributed to the increase of ambient noise level. For example, during the one-year measurement period, the lowest sea ice concentration was in September, and underwater ambient noise during this period was approximately 16 dB higher than the annual average.

Underwater noise measurements were conducted again in the same region as the first measurement for about a year from August 2019 (Han et al., 2023). Additionally, from September 2 to 10, the R/V Araon, operated by the Korea Polar Research Institute (KOPRI), conducted a seismic airgun survey for underwater geological exploration. During this period, the airgun sounds at different source-receiver distances were unintentionally received by the receiver system. The received levels as a function of distance were compared with model predictions obtained from a broadband application of the range-dependent acoustic model (RAM) (Collins, 1993) based on the parabolic equation (PE). A two-layer geoacoustic bottom model, which was constructed based on core samples and sub-bottom profile survey data, was used as model input. The uppermost layer of the two-layer model was set to be mud composed of soft unconsolidated sediment less than 4 m thick with a sediment sound speed range of 1,424–1,471 m/s, sediment density range of 1.39–1.53 g/cm^3, and sediment attenuation coefficient range of 0.0793–0.1532 dB/λ, which are estimated using the geoacoustic relationships with mean grain size (Ainslie, 2010). The lower layer was set to the diamicton, of which the sound speed, density, and attenuation coefficient ranges were assumed to be 1,588–1,928 m/s, 1.82–2.55 g/cm^3, and 1.1006–0.9076 dB/λ, respectively. However, there was a significant difference between the measurements and the predictions, which became the motivation of this study. In this paper, the geoacoustic parameters of the site are estimated by comparing modal dispersion curves derived from the acoustic model predictions and the measurements.

In shallow water environments, long-range acoustic propagation is greatly influenced by geoacoustic parameters such as sound speed and density of the seafloor. Low-frequency sounds propagating over several kilometers in the ocean waveguides are dispersive in the time-frequency domain, which can be explained with normal mode theory as the sum of several modal components (Frisk, 1994; Jensen, 2011; Duncan et al., 2013; Keen et al., 2018). For this reason, the modal dispersion curves to be observed at the time-frequency domain of the received signal reflects the acoustic properties of the ocean waveguide, including the geoacoustic parameters, and therefore, it can be used to estimate the geoacoustic properties of the seafloor. In order to use the dispersion curves for geoacoustic parameter inversion, it is necessary to extract the dispersion curves for each mode from the spectrogram of the received signal, and then compare them with the simulated replicas obtained by the normal-mode-based propagation model. Recently, since warping transform was proposed as a good tool used for extracting the dispersion curves in the spectrogram (Bonnel et al., 2020), it has been applied to geoacoustic inversion studies in shallow water using various low-frequency broadband sound sources such as airgun, gunshot, light bulb, and whale call (Bonnel et al., 2013; Warner et al., 2015; Duan et al., 2016; Warner et al., 2016; Thode et al., 2017; Liu et al., 2020).

In this paper, we present the results of estimating geoacoustic parameters of the seafloor in the East Siberian Shelf. The modal dispersion curves of the first two modes were clearly observed in the spectrogram of the airgun sounds received at distances of several tens of km, and they were extracted using the warping transform combined with the wavelet synchrosqueezing transform. The genetic algorithm (Goldberg, 1989; Conn et al., 1997) was then applied to find the best-fit geoacoustic parameters by matching the extracted dispersion curves with the replicas predicted by the KRAKEN normal-mode program (Porter, 1992) within the search spaces of the geoacoustic parameters. Additionally, our geoacoustic inversion results were used to estimate the distance of sound source for distances from 18.6 km to 121.5 km.

2 Materials and methods

2.1 Acoustic measurements

Long-term underwater noise measurements were conducted in the East Siberian Shelf over the course of approximately one year, spanning from August 22, 2019 to August 13, 2020. An autonomous passive acoustic recorder (AURAL-M2, Multi-Electronique Inc.) was moored 13 m above the seafloor at location 74° 37.327'N, 174° 56.397'E in waters with a depth of approximately 70 m (Figure 1A).

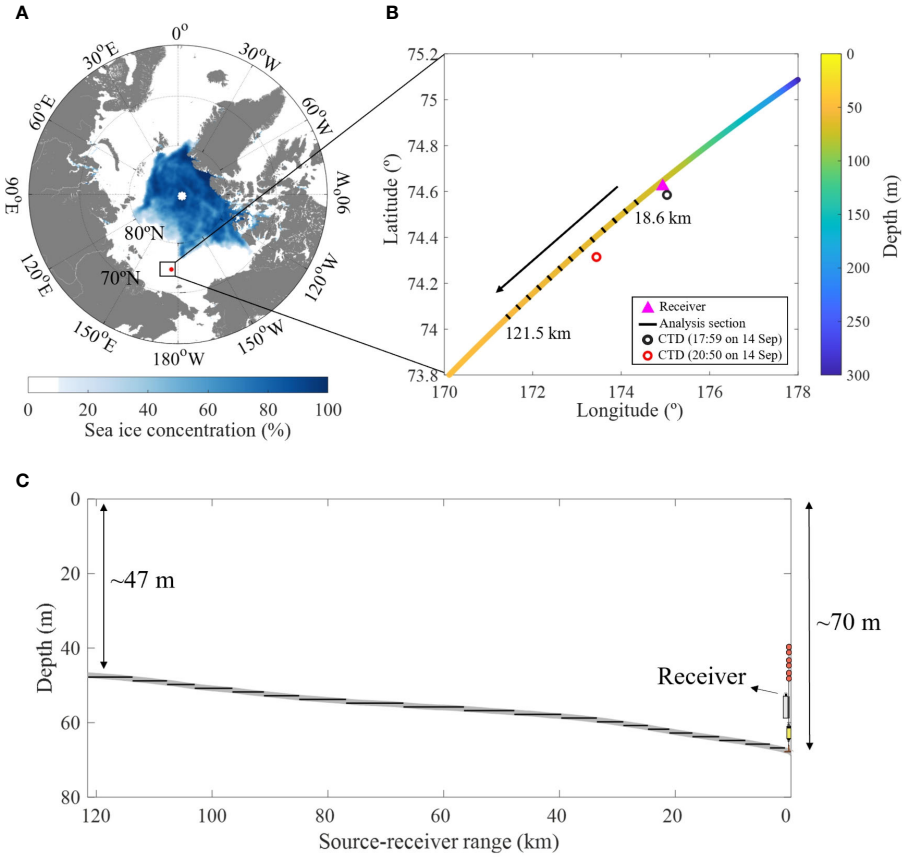

FIGURE 1
(A) Distribution map of sea ice concentration in the Arctic on September 9, 2019. Black box denotes the location of the measurement site. **(B)** The R/V Araon ship track. The colors on the ship track indicate bathymetry. The magenta triangle denotes the hydrophone mooring location, and the black and red open circles show the CTD cast locations. Acoustic data received at 18.6 km was applied to geoacoustic inversion, and the 13 sections (approximately 50 signals per section), represented by black bars on the ship tracks, were used to estimate the distance from the receiver system to sound source. **(C)** Range-dependent bathymetry along the source-receiver track. Black solid lines represent the range-independent segments, each based on a 1-m change in water depth.

Acoustic data were recorded for 10 minutes every hour at a sampling rate of 32,768 Hz. From September 2 to 10, 2019, the R/V Araon operated the airgun (GI-SOURCE 355, Sercel) for underwater geological survey in the Chukchi-East Siberian Continental Margin (Jin, 2020). Low-frequency impulsive airgun sounds were emitted by the airgun shots at approximately 11-s intervals while maintaining a constant firing depth of ~6 m. The waveform of the airgun shot, measured from a near-field hydrophone (AGH-7100-C, Geophysical Products Inc.) positioned approximately 1 m above the airgun, exhibited a spike-shaped pattern with a peak frequency of ~27 Hz and dominant energy concentrated below 300 Hz (Han et al., 2023).

During the seismic survey, the R/V Araon approached the receiver system from the northeast direction, coming closest at 15:47 on September 9, after which the vessel moved away in the southwest direction (Figure 1B). Notably, bathymetry in the northeast direction from the receiver exhibited range-dependent variations, while bathymetry in the southwest direction displayed minimal changes in water depth. Our current analysis focused on cases where the source moved away from the receiver in the southwest direction within a range-independent environment. It is important to note that when the source-receiver distance was less than 18.6 km, the energy of received signal exceeded the upper dynamic limit of the hydrophone, leading to signal truncation. Moreover, airgun data received at distances exceeding 121.5 km exhibited poor signal-to-noise ratio (SNR). Therefore, our analysis was confined to the range encompassed between these two distances.

2.2 Extraction of dispersion curves

Acoustic waves propagating in a waveguide exhibit dispersion as normal modes at different frequency propagate at different group velocities. Therefore, several dispersive modes with different frequency-dependent group velocities can be observed in the spectrogram of the received signal after propagating at least several kilometers in shallow water, and the group velocity $v_m(f)$ is calculated by Equation 1 (Frisk, 1994; Jensen, 2011; Bonnel et al., 2020):

$$v_m(f) = 2\pi \frac{\partial f}{\partial k_m(f)} \quad (1)$$

where, $k_m(f)$ is the horizontal wavenumber of mode m at frequency f. Therefore, the modal travel time t_m as a function of frequency over propagation range r is given by

$$t_m(f) = \frac{r}{v_m(f)} \tag{2}$$

Figure 2A shows the time series of the airgun sound received at a source-receiver distance of 18.6 km. Interestingly, arrivals that appear to be precursor arrivals were received before the water-borne arrivals. The precursor arrival is a signal that propagates primarily through the sediment layer and arrives prior to any water-borne arrival (Dahl and Choi, 2006; Choi and Dahl, 2007), and the observation of precursor arrivals in our measurements means that the sound speed in lower sediment layer might be faster than that in the water column. Figure 2B shows the spectrogram for water-borne arrivals corresponding to the red box in Figure 2A. The first two modes were clearly observable in the spectrogram. However, higher modes were not clearly visible.

In this study, the warping method was applied to extract each dispersion curve from the spectrogram. In normal mode theory, for an impulsive source signal propagating in a Pekris waveguide with a rigid bottom, the received signal as a function of time t can be expressed as (Jensen, 2011; Bonnel et al., 2020)

$$y(t) = \sum_{m=1}^{M} a_m(t) e^{j2\pi f_{cm}\sqrt{t^2-(\frac{r}{c_w})^2}} \tag{3}$$

where M is the mode number of propagating modes, a_m is the amplitude of mode m, c_w is the water sound speed, and f_{cm} represents the cutoff frequency of the m-th mode which can be calculated by $\frac{(2m-1)c}{4D}$, where D is the water depth. Note that the phase term of (Equation 3) is a non-linear function for time t. To linearize the non-linearity, we used $\sqrt{t^2+(\frac{r}{c_w})^2}$ as the warping function $h(t)$ under the assumption that the impulsive source signal propagates in an isovelocity waveguide. The warped signal $y_w(t)$ is calculated by

$$y_w(t) = \sqrt{|h'(t)|}\, y[h(t)] \tag{4}$$

where $h(t)$ is the warping function, $h'(t)$ is the time derivative of $h(t)$ (Bonnel and Chapman, 2011; Bonnel et al., 2020; Liu et al., 2020). Figure 2C shows the result of the warping transformation, in which the first two modes are well separated in the warped frequency.

Now that the two modes have distinct warped frequency bands, we extracted the first and second modes using a bandpass filter, as shown in Figures 3A, B, respectively. Each warped modes were then inversely warped by replacing $h(t)$ with $h(t)^{-1}= \sqrt{t^2-(\frac{r}{c_w})^2}$ in (Equation 4). As a next step, wavelet synchrosqueezing transform was applied to sharpen the time-frequency resolution of the dispersion curves of each mode (Daubechies et al., 2011; Thakur et al., 2013), and then time-frequency ridge tracking algorithm (Meignen et al., 2015; Iatsenko et al., 2016) was used to extract the maximum-energy ridges from wavelet synchrosqueezing transform results, and the results are shown in Figures 3C, D. Finally, the extracted dispersion curves were smoothed out using a 5-point moving average filter, with the results shown as red dashed lines in Figures 3C, D.

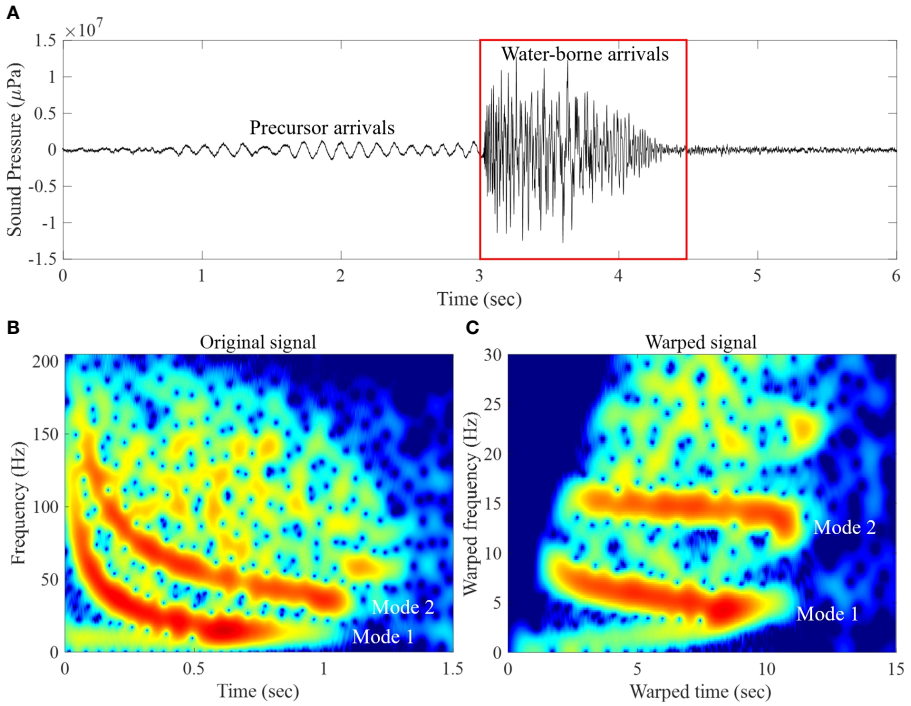

FIGURE 2
(A) Time series of the airgun sound received at the source-receiver distance of 18.6 km. **(B)** The spectrogram of the water-borne waveforms corresponding to the red box in **(A)**, which was obtained by the short-time Fourier transform using 512 fast Fourier transform points and 51-point Hamming window after decimation by a factor of 80. **(C)** Spectrogram of the warped signal.

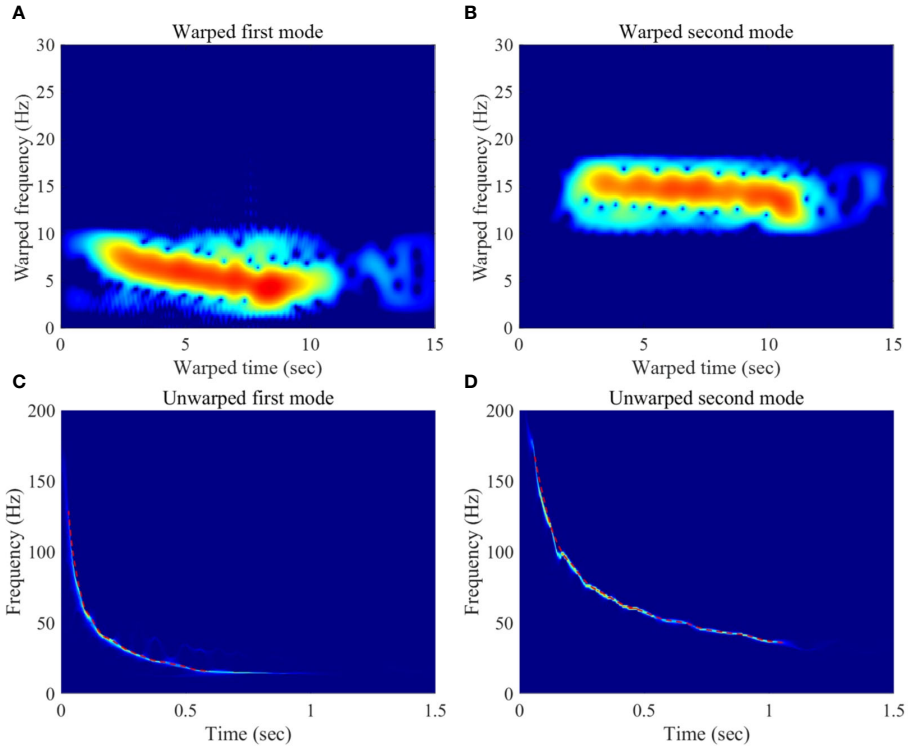

FIGURE 3
(A) Spectrograms of the warped first and **(B)** second modes extracted through bandpass filtering. **(C)** Dispersion curves obtained by the wavelet synchrosqueezing transform of the inverse-warped first and **(D)** second modes. Red dashed lines are the 5-point moving averaged output of the dispersion curves.

2.3 Geoacoustic inversion

The seafloor of the experimental site was flat with a water depth difference of only ~5 m from the receiver position to a point 18.6 km southwest. The sediment structure was reported to be composed of a thin layer of unconsolidated mud overlying the high-density sediment created by the grounding events of ice masses through the repeated advance and retreat of glaciers (Niessen et al., 2013; Dove et al., 2014; Han et al., 2023). The sound speed profile in the water column was measured using a conductivity-temperature-depth (CTD) cast on 14 September at points ~5 and ~56 km from the receiver (see the black and red open circles in Figure 1B), and the measurements showed that the sound speed profiles at two points were similar and distributed within the range of 1,438 and 1,448 m/s (Figure 4A).

In this study, a two-layer bottom model for geoacoustic parameter inversion was constructed based on the previous survey results (Han et al., 2023), as shown in Figure 4B. It was assumed that the ocean environment is range-independent, and the bottom consists of a homogeneous fluid sediment layer overlying a homogeneous fluid half-space. The genetic algorithm was used to estimate geoacoustic parameters by matching the extracted dispersion curves from the acoustic data with the replicas predicted by the KRAKEN acoustic propagation model. As mentioned in Section 2.1, the shortest range from the receiver position where the received signals were not truncated was 18.6 km, and at which point the water depth difference between the receiver and airgun positions was only ~ 5 m. Therefore, we used the data received at this point for geoacoustic parameter inversion.

Based on the two-layer bottom model, we estimated six unknown parameters including the layer thickness H, sound speed c_s and density ρ_s in the surficial sediment layer and sound speed c_b and density ρ_b of the basement, and the water depth D.

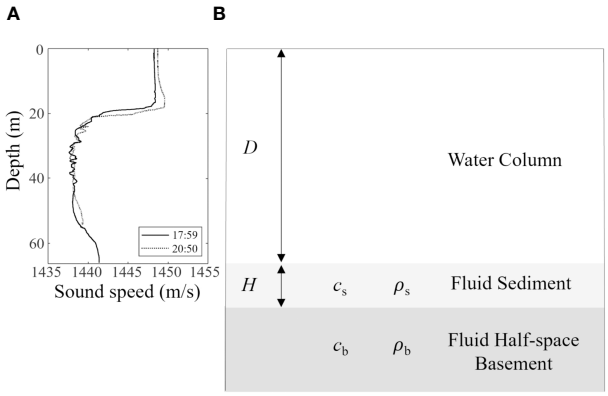

FIGURE 4
(A) Sound speed profiles at points ~5 (solid line) and ~56 km (dashed line) southwest of the receiver, which were measured at 17:59 and 20:50 on 14 September, respectively. **(B)** Two-layer geoacoustic bottom model constructed for the geoacoustic inversion process.

The sound speed profile measured at the point ~5 km from the receiver position was used as model input to run the KRAKEN acoustic propagation model. The search spaces for each parameter are shown in Table 1, which were set to sufficiently wide ranges based on previous survey results (Han et al., 2023). To create model replicas, the KRAKEN model was run in the frequency range between 16 and 130 Hz for mode 1 and 36 and 170 Hz for mode 2 at a 1-Hz interval. Then, the group velocity predictions as a function of frequency were converted to modal travel time for the source-receiver distance of 18.6 km by (Equation 2). To compare the modal travel times between the model replicas and those extracted dispersion curves from the acoustic data, each result was time-aligned by adjusting the arrival time for 130 Hz of the first mode to 0 on the time axis. Then, the least square method was used, in which the objective function to be minimized is given by

$$J(\mathrm{X}) = \sum_{m=1}^{M}\sum_{n=1}^{N_m}[t_m(f_n) - \hat{t}_m(f_n, \mathrm{X})]^2 \quad (5)$$

where M is the total number of modes used for the geoacoustic inversion, and M was set to 2 in this study. The vector $\mathrm{X} = \{H, c_s, \rho_s, c_b, \rho_b, D\}$. $t_m(f_n)$ and $\hat{t}_m(f_n, \mathrm{X})$ is the measured and modeled modal travel times, respectively. N_m is the total number of frequency segments used for the mode m.

To determine the optimal values of geoacoustic parameters, a global search was conducted using a genetic algorithm over the parameter search spaces. The genetic algorithm parameters were set as follows: a population size of 64, a crossover fraction of 0.8, and a mutation probability of 0.05 to prevent local minima. The algorithm terminated either when the number of generations reached 300 or when the objective function no longer decreased within an additional 60 generations from the generation that achieved the best result.

3 Results

3.1 Inversion in range-independent environment

The best-fit values and their uncertainties for each parameter within the search space are presented in Table 1. The inversion results reveal a water depth of approximately 68.2 m, with a surficial sediment layer approximately 4.1 m in thickness overlaying a high-velocity basement. The surficial sediment exhibits an approximate sound speed of 1422.4 m/s and a density of about 1.58 g/cm^3. These results suggest that the estimated geoacoustic parameters of the surficial sediment layer closely align with our previous survey results (Han et al., 2023). Additionally, the underlying basement displays a sound speed of approximately 1733.6 m/s and a density of approximately 1.84 g/cm^3. Figure 5 shows the sensitivities of $J(\mathrm{X})$ to parameter variations around the optimal values of the six environmental parameters. A sensitivity plot for each parameter is created by calculating $J(\mathrm{X})$ within the search spaces while keeping other parameters at their optimal values. As expected, $J(\mathrm{X})$ is most sensitive to the sound speed of the lower sediment layer and water depth D, while the other parameters are relatively less sensitive in the inversion process. In the sensitivity results for the surficial layer thickness, 0 m represents a scenario where the sediment is not structured with two sediment layers but solely with a half-space. Figure 6 compares the measured modal curves with model replicas predicted using the inversion results for the first four modes. Although the mode-3 and 4 are not clearly visible in the measured spectrogram, the predictions of mode-1 and 2 are in good agreement with the corresponding measured modal curves.

As a subsequent step, the Bayesian approach was applied to estimate the uncertainties in geoacoustic parameter estimates derived from the inversion process. Let X and d denote the given vectors representing the six geoacoustic parameters and the measured data, respectively. Following Bayes' rule, the posterior probability density $P(\mathrm{X}|d)$ can be expressed as Equation 6 (Gerstoft and Mecklenbräuker, 1998; Dosso, 2002; Dosso and Dettmer, 2011)

$$P(\mathrm{X}|d) = \frac{P(d|\mathrm{X})P(\mathrm{X})}{P(d)} \quad (6)$$

where $P(\mathrm{X})$ is the prior distribution, and $P(d|\mathrm{X})$ is the conditional probability density of given vector X for the measured data d. $P(d)$ is the probability density of measured data d, acting as a normalizing factor. To calculate $P(\mathrm{X}|d)$, the prior distribution is assumed to be uniform within the search bounds of each parameter. The conditional probability density $P(d|\mathrm{X})$, interpreted as the likelihood function $L(\mathrm{X})$, is given by Equation 7

$$P(d|\mathrm{X}) = L(\mathrm{X}) \propto \exp[-J(\mathrm{X})] \quad (7)$$

TABLE 1 Search spaces and estimated optimal parameter values for environmental parameters applied in geoacoustic inversion in the range-independent environment.

Parameter	Unit	Search space	Estimated value	95% HPD credible intervals
Sediment thickness H	m	[1 10]	4.1	[3.2 5.1]
Sediment sound speed c_s	m/s	[1400 1500]	1422.4	[1411.3 1439.2]
Sediment density ρ_s	g/cm^3	[1.0 2.0]	1.58	[1.07 1.97]
Basement sound speed c_b	m/s	[1550 3000]	1733.6	[1720.6 1744.6]
Basement density ρ_b	g/cm^3	[1.3 3.0]	1.84	[1.32 2.65]
Water depth D	m	[60 75]	68.2	[67.3 69.4]

The final column presents parameter uncertainties, assessed via 95% Highest Probability Density (HPD) credible intervals.

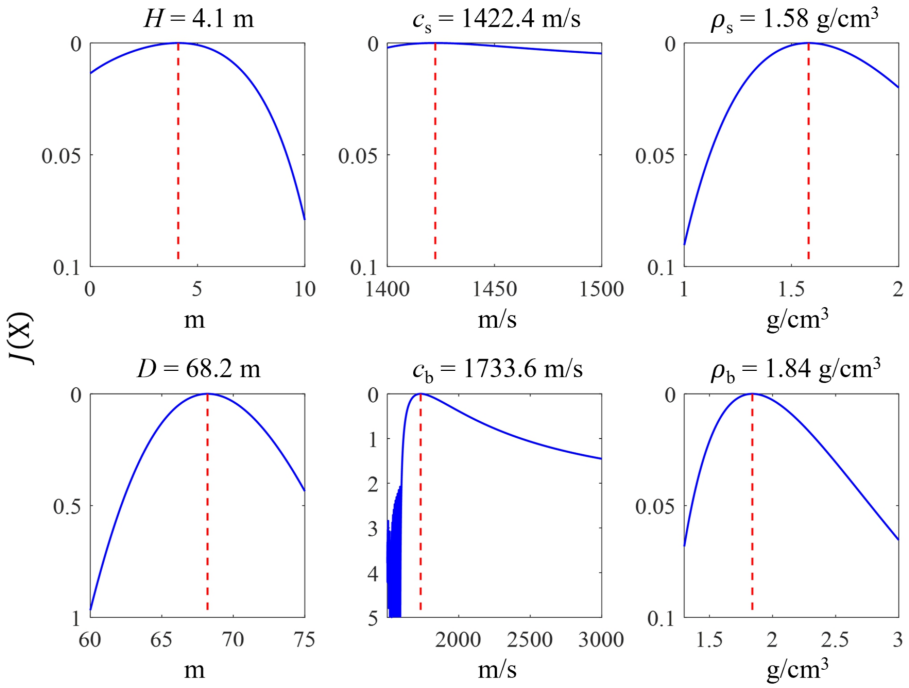

FIGURE 5
Sensitivity plots for each geoacoustic parameter. Red dashed lines are optimal values for each geoacoustic parameter. Note that the $J(X)$ scales of the c_b and D is different from those of other parameters.

where $J(X)$ represents the data misfit function (considered in section 2.3). Consequently, the posterior probability density can be written as Equation 8

$$P(X|d) = \frac{\exp[-J(X)]}{\int \exp[-J(X)]dX} \quad (8)$$

In this study, the Markov-chain Monte Carlo method utilizing Metropolis sampling (Metropolis et al., 1953; Hastings, 1970) was employed to estimate the marginal probability densities for each parameter. The inversion results were then utilized as initial values for the estimation. The sampling process involved 10,000 iterations using a proposal distribution in the form of a normal distribution, centered on the sampled results. Considering the parameter scale, the standard deviation of the proposal distribution for sound speed parameters was set to 1, while for the remaining parameters, it was set to 0.1. Subsequent to estimating the marginal probability densities for each parameter, parameter uncertainties were quantified using 95% Highest Probability Density (HPD) credible intervals (Bonnel et al., 2013; Gelman et al., 2013), as depicted in the last right column of Table 1.

Up to this point, we have derived estimates for geoacoustic parameters and water depth by comparing measured modal curves with model replicas for a source-receiver distance of 18.6 km. Conversely, if ocean environmental parameters, including geoacoustic parameters, are assumed to be known, the distance between the acoustic source and receiver can be estimated using the same method as described above. As indicated in section 2.1, reliable signals were received within the range of 18.6 and 121.5 km. Therefore, in this session, we estimate source-receiver distances for this range. Initially, assuming a range-independent environment, we executed the KRAKEN acoustic propagation model with input parameters comprising the estimated geoacoustic parameters and a water depth of 68.2 m. Subsequently, model replicas were generated for source-receiver distances ranging from 1 to 140 km at 1-m intervals. These replicas were compared with the measured modal curves extracted using the

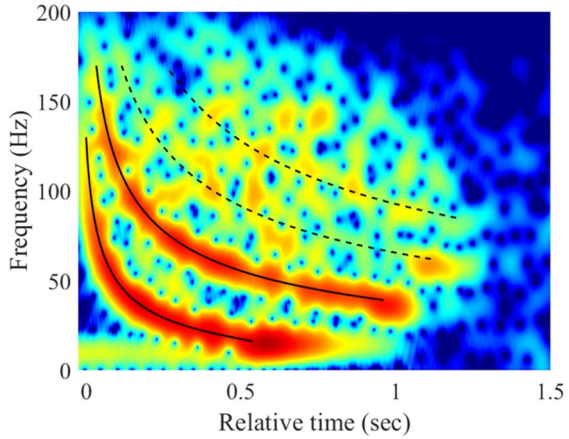

FIGURE 6
Comparison of dispersion curves between the modal curves in the measured spectrogram and the model replicas predicted using the estimated geoacoustic parameters. Black solid lines indicate the model replicas for the mode-1 and 2, which were used for the inversion process, and black dashed lines indicate the model replicas for mode-3 and 4.

same method outlined in section 2.2. Figures 7A, B illustrate the comparison between estimated source-receiver distances and those measured by GPS, along with their respective distance errors. Notably, distances estimated under the assumption of a range-independent environment (depicted by black open circles) exhibited increasing errors as the distance extended, in contrast to the actual distances measured by GPS. This discrepancy appears to be attributed to the gradual decrease in water depth from approximately 70 to 47 m as the source-receiver distance increases from 18.6 to 121.5 km. Consequently, the group velocity, as a function of frequency, decreases accordingly.

3.2 Inversion in range-dependent environment

To mitigate the discrepancy in the range-independent environment, we employ an adiabatic approximation for model propagation in the range-dependent environment (Jensen, 2011; Bonnel et al., 2022). The modeled modal travel times, denoted as $\hat{t}_m(f_n, \mathrm{X})$ in (Equation 5), are calculated by dividing the source-receiver distance into range-independent segments based on a 1-m change in water depth for the bottom bathymetry depicted in Figure 1C. The modal travel times for each segment are then summed using Equation 9

$$\hat{t}_m(f_n, \mathrm{X}) = \sum_{i=1}^{N_r} \frac{\Delta r_i}{v_m(r_i, f_n, \mathrm{X})} \tag{9}$$

Here N_r is the total number of range segments, Δr_i represents the range in the ith range segment, and $v_m(r_i, f_n, \mathrm{X})$ is the group velocity predictions of mode m as a function of frequency for the ith range segment.

Subsequently, the inversion process was reiterated for the source-receiver distance of 18.6 km, and the inversion results are presented in Table 2. The estimated geoacoustic parameters in the range-dependent environment exhibited consistency with those in the range-independent environment, falling within 95% HPD credible intervals, except for the thickness of the surficial sediment, estimated to be 5.3 m. the revised results indicate a surficial sediment layer with a thickness of approximately 5.3 m. The surficial sediment layer has an approximate sound speed of 1432.6 m/s and a density of about 1.41 g/cm^3. The underlying basement exhibits a sound speed of approximately 1737.6 m/s and a density of approximately 1.87 g/cm^3. Based on these optimal values, we now re-estimate the source-receiver distances to 121.5 km using the optimal values for the range-dependent environment. Consequently, as the source-receiver distance increased, the distance error–up to 30% in the range-independent environment was reduced to within 10%. It was assumed that the estimated geoacoustic parameters were independent of changes in water depth with distance, possibly explaining why the error could not be further reduced.

4 Summary and conclusion

Over the past few years, our research has focused on the underwater acoustic environment of the East Siberian Shelf, a region that remains one of the least studied in the Arctic Ocean. In our initial paper (Han et al., 2021), we reported on the seasonal variations in ambient noise levels, revealing a strong negative correlation with changes in sea ice concentration covering the sea surface. In our subsequent paper (Han et al., 2023), we aimed to understand the acoustic propagation characteristics of the East Siberian Shelf. This involved analyzing seismic airgun sounds propagating over tens of kilometers and comparing them with the model predictions obtained from a broadband application of the range-dependent acoustic model (RAM). In this acoustic model, a two-layer geoacoustic bottom structure, presented in the previous references, was used as model input. Interestingly, modal dispersion was observed in the spectrogram of the signal propagating over several kilometers, and this observation served as the motivation for this paper.

In this paper, we tried to estimate the geoacoustic parameter values for the two-layer geoacoustic bottom model by comparing the dispersion curves extracted from the replicas predicted by the KRAKEN normal-mode program with dispersion curves extracted from the acoustic data for the source-receiver distance of 18.6 km.

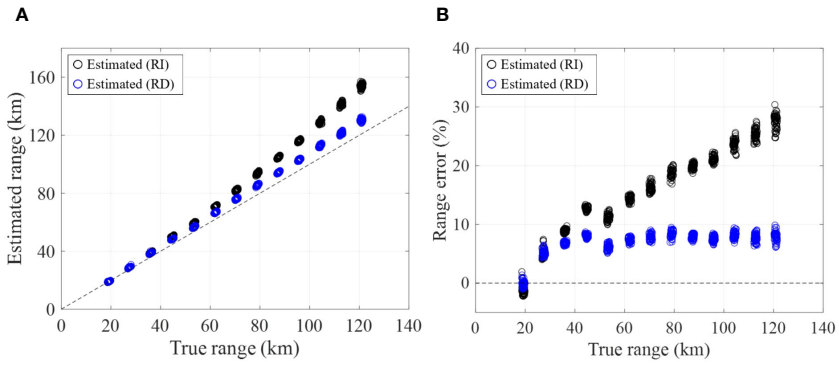

FIGURE 7
(A) Comparison of source-receiver distances measured by GPS (black dashed line) with distances estimated in range-independent bathymetry (black open circles) and distances estimated in range-dependent bathymetry (blue open circles). **(B)** Corresponding distance errors.

TABLE 2 Search spaces and estimated optimal parameter values for environmental parameters applied in geoacoustic inversion in the range-dependent environment.

Parameter	Unit	Search space	Estimated value	95% HPD credible intervals
Sediment thickness H	m	[1 10]	5.3	[4.1 6.4]
Sediment sound speed c_s	m/s	[1400 1500]	1432.6	[1421.1 1445.7]
Sediment density ρ_s	g/cm^3	[1.0 2.0]	1.41	[1.03 1.91]
Basement sound speed c_b	m/s	[1550 3000]	1737.6	[1727.9 1749.5]
Basement density ρ_b	g/cm^3	[1.3 3.0]	1.87	[1.32 2.70]

First, the inversion results, assuming a range-independent environment, revealed the best-fit values for the sediment sound speed and density in the surficial layer to be approximately 1422.4 m/s and 1.58 g/cm^3, respectively. For the lower layer, these values were estimated to be 1733.6 m/s and 1.84 g/cm^3, respectively and the surficial sediment thickness was estimated to be ~ 4.1 m. As mentioned in Section 1, previous studies have reported the presence of a soft, unconsolidated surficial sediment layer (less than 4 m thick) overlaying a glaciogenic overcompacted sediment layer (O'Regan et al., 2017; Jin, 2020). However, the surficial sediment parameters (H, c_s, ρ_s), including the basement density (ρ_b), exhibited limited sensitivity in predicting modal dispersion curves, as illustrated in Figure 5. This suggests that, within the frequency range of the airgun sound, the geoacoustic parameters of the soft surficial sediment may not significantly impact the modeling results.

Subsequently, the inversion results were applied to estimate source-receiver distances ranging from 18.6 to 121.5 km, employing the same method used for geoacoustic inversion. However, the estimated source-receiver distances exhibited increasing errors, reaching up to 30% as the distance increased. To mitigate the distance errors, we employed an adiabatic approximation for model propagation in the range-dependent environment. The modeled modal travel times were calculated by dividing the source-receiver distance into range-independent segments, each based on a 1-m change in water depth, and then summed. The inversion results demonstrated consistency with those obtained in the range-independent environment, except for the surficial sediment thickness, which was estimated to be ~ 5.3 m. Finally, the source-receiver distances were re-estimated using the geoacoustic parameters obtained under the range-dependent environment, resulting in a reduced distance error to within 10%. The simplification of sediment structure through a two-layer bottom geoacoustic model, as assumed in the study, might limit the accurate capture of depth variations relative to changes in sediment structure over distance. This limitation could contribute to the inability to further reduce distance error. Additionally, our study assumed the negligible shear wave effect on modal travel time, potentially posing another limitation in reducing distance errors. Potty and Miller (2020) reported that the impact of shear waves may intensify within the low-order mode Airy phase region, characterized by the minimum group velocity.

The estimation of the sediment attenuation coefficient was not undertaken in this study as this parameter does not influence modal travel time but rather affects modal amplitude. In Figure 6, it was observed that modes 3 and 4 are not distinctly visible in the measured spectrogram. The waveform, recorded by the near-field hydrophone, exhibited a spike-like signature, as depicted in Figure 3 of Han et al. (2023). The spectral peak of the airgun pulse was identified at approximately 27 Hz, beyond which the energy rapidly diminished, dropping to less than half around 100 Hz. Furthermore, the propagation of each mode is significantly influenced by the depth-dependent modal eigenfunctions. Figure 8 illustrates the depth-dependent modal eigenfunction for each mode at 100 Hz, within the frequency bands of mode 1–4. The modal amplitudes of modes 3 and 4, corresponding to the hydrophone depth, are smaller than those of modes 1 and 2. Lastly, the absence of ground truth

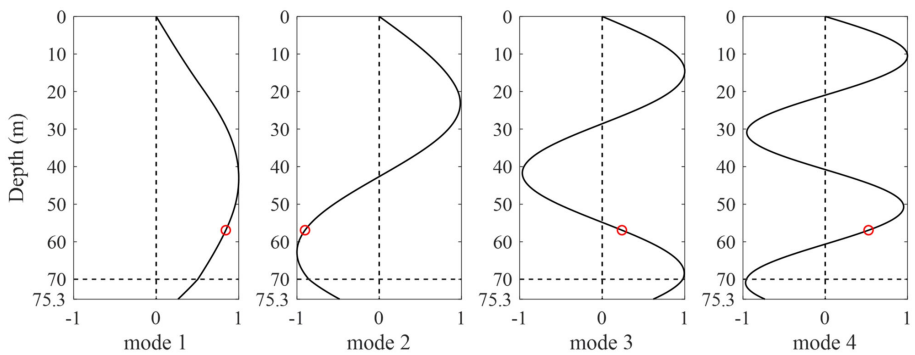

FIGURE 8
Depth-dependent modal eigenfunctions for modes 1–4 evaluated at 100 Hz. In each mode, the red circles represent modal eigenfunction amplitudes at the hydrophone depth.

data for comparison limits the ability to verify the reliability of the inversion results, given that the East Siberian Shelf is a poorly studied region. Despite these challenges, our inversion results hold value as they provide indirect information about the geoacoustic properties of the East Siberian Shelf.

Data availability statement

The original contributions presented in the study are included in the article/supplementary material. Further inquiries can be directed to the corresponding authors.

Author contributions

DL: Writing – review & editing, Writing – original draft, Methodology, Formal analysis, Data curation, Conceptualization. DH: Writing – original draft, Methodology, Data curation, Conceptualization. JC: Writing – review & editing, Writing – original draft, Validation, Supervision, Methodology, Funding acquisition, Formal analysis, Data curation, Conceptualization. WS: Writing – original draft, Investigation, Data curation, Conceptualization. EY: Writing – original draft, Investigation, Funding acquisition, Data curation, Conceptualization. HL: Writing – review & editing, Writing – original draft, Validation, Supervision, Methodology, Investigation, Funding acquisition, Formal analysis, Data curation, Conceptualization. DT: Writing – review & editing, Writing – original draft, Validation, Supervision, Methodology, Formal analysis.

Funding

The author(s) declare financial support was received for the research, authorship, and/or publication of this article. This research was supported by the Ministry of Oceans and Fisheries projects, entitled 'Korea-Arctic Ocean Warming and Response of Ecosystem (20210605)'. This work was also supported by the National Research Foundation of Korea (NRF) grant funded by the Korea government (MSIT) (2020R1A2C2007772).

Conflict of interest

Author DH was employed by company Oceansounds Incorporation.

The remaining authors declare that the research was conducted in the absence of any commercial or financial relationships that could be construed as a potential conflict of interest.

Publisher's note

References

Ainslie, M. (2010). *Principles of sonar performance modelling* (Berlin, Heidelberg: Springer Berlin Heidelberg: Imprint: Springer).

Bonnel, J., and Chapman, (2011). Geoacoustic inversion in a dispersive waveguide using warping operators. *J. Acoust Soc. Am.* 130, EL101–EL107. doi: 10.1121/1.3654580

Bonnel, J., Dosso, S. E., and Chapman, R. (2013). Bayesian geoacoustic inversion of single hydrophone light bulb data using warping dispersion analysis. *J. Acoust Soc. Am.* 134, 120–130. doi: 10.1121/1.4809678

Bonnel, J., Dosso, S. E., Goff, J. A., Lin, Y. T., Miller, J. H., Potty, G. R., et al. (2022). Transdimensional geoacoustic inversion using prior information on range-dependent seabed layering. *IEEE J. Oceanic Eng.* 47, 594–606. doi: 10.1109/JOE.2021.3062719

Bonnel, J., Thode, A., Wright, D., and Chapman, R. (2020). Nonlinear time-warping made simple: A step-by-step tutorial on underwater acoustic modal separation with a single hydrophone. *J. Acoust Soc. Am.* 147, 1897–1926. doi: 10.1121/10.0000937

Brown, J., Ferrians, O. J., Heginbottom, J. A., and Melnikov, E. S. (1997). *Circum-arctic map of permafrost and ground ice conditions* (Washington, D. C: U. S. Geological Survey). Available at: https://web.archive.org/web/20170226114554id_/https://pubs.usgs.gov/cp/45/report.pdf.

Choi, J. W., and Dahl, P. H. (2007). Spectral properties of the interference head wave. *J. Acoust Soc. Am.* 122, 146–150. doi: 10.1121/1.2743156

Collins, M. D. (1993). A split-step pade solution for the parabolic equation method. *J. Acoust. Soc Am.* 93, 1736–1742. doi: 10.1121/1.406739

Conn, A., Gould, N., and Toint, P. (1997). A globally convergent Lagrangian barrier algorithm for optimization with general inequality constraints and simple bounds. *Math. Comp.* 66, 261–288. doi: 10.1090/S0025-5718-97-00777-1

Dahl, P. H., and Choi, J. W. (2006). Precursor arrivals in the Yellow Sea, their distinction from first-order head waves, and their geoacoustic inversion. *J. Acoust Soc. Am.* 120, 3525–3533. doi: 10.1121/1.2363938

Daubechies, I., Lu, J., and Wu, H.-T. (2011). Synchrosqueezed wavelet transforms: An empirical mode decomposition-like tool. *Appl. Comput. Harmonic Anal.* 30, 243–261. doi: 10.1016/j.acha.2010.08.002

Dosso, S. E. (2002). Quantifying uncertainty in geoacoustic inversion. I. A fast Gibbs sampler approach. *J. Acoust Soc. Am.* 111, 129–142. doi: 10.1121/1.1419086

Dosso, S. E., and Dettmer, J. (2011). Bayesian matched-field geoacoustic inversion. *Inverse Problems* 27, 1–23. doi: 10.1088/0266-5611/27/5/055009

Dove, D., Polyak, L., and Coakley, B. (2014). Widespread, multi-source glacial erosion on the chukchi margin, Arctic ocean. *Quaternary Sci. Rev.* 92, 112–122. doi: 10.1016/j.quascirev.2013.07.016

Duan, R., Chapman, N. R., Yang, K., and Ma, Y. (2016). Sequential inversion of modal data for sound attenuation in sediment at the New Jersey Shelf. *J. Acoust. Soc Am.* 139, 70–84. doi: 10.1121/1.4939122

Duarte, C. M., Chapuis, L., Collin, S. P., Costa, D. P., Devassy, R. P., Eguiluz, V. M., et al. (2021). The soundscape of the Anthropocene ocean. *Science* 371, 1–10. doi: 10.1126/science.aba4658

Duncan, A. J., Gavrilov, A. N., McCauley, R. D., Parnum, I. M., and Collis, J. M. (2013). Characteristics of sound propagation in shallow water over an elastic seabed with a thin cap-rock layer. *J. Acoust. Soc Am.* 134, 207–215. doi: 10.1121/1.4809723

Frisk, G. V. (1994). *Ocean and seabed acoustics: a theory of wave propagation* (Englewood Cliffs, N.J: PTR Prentice Hall).

Frisk, G. V. (2012). Noiseonomics: The relationship between ambient noise levels in the sea and global economic trends. *Sci. Rep.* 2, 437. doi: 10.1038/srep00437

Gelman, A., Carlin, J. B., Stern, H. S., Dunson, D. B., Vehtari, A., and Rubin, D. B. (2013). *Bayesian data analysis. 3rd ed* (New York: Chapman and Hall/CRC). doi: 10.1201/b16018

Gerstoft, P., and Mecklenbräuker, C. F. (1998). Ocean acoustic inversion with estimation of a posteriori probability distributions. *J. Acoust. Soc Am.* 104, 808–819. doi: 10.1121/1.423355

Goldberg, D. E. (1989). *Genetic algorithms in search, optimization and machine learning* (Boston: Addison-Wesley).

Han, D.-G., Joo, J., Son, W., Cho, K. H., Choi, J. W., Yang, E. J., et al. (2021). Effects of geophony and anthrophony on the underwater acoustic environment in the East

Siberian Sea, Arctic ocean. *Geophysical Res. Lett.* 48, e2021GL093097. doi: 10.1029/2021GL093097

Han, D.-G., Kim, S., Landrø, M., Son, W., Lee, D. H., Yoon, Y. G., et al. (2023). Seismic airgun sound propagation in shallow water of the East Siberian shelf and its prediction with the measured source signature. *Front. Mar. Sci.* 14. doi: 10.3389/fmars.2023.956323

Hastings, W. K. (1970). Monte carlo sampling methods using markov chains and their applications. *Biometrika* 57, 97–109. doi: 10.1093/biomet/57.1.97

Iatsenko, D., McClintock, P. V. E., and Stefanovska, A. (2016). Extraction of instantaneous frequencies from ridges in time–frequency representations of signals. *Signal Process.* 125, 290–303. doi: 10.1016/j.sigpro.2016.01.024

Jakobsson, M., Mayer, L. A., Bringensparr, C., Castro, C. F., Mohammad, R., Johnson, P., et al. (2020). The international bathymetric chart of the arctic ocean version 4.0. *Sci. Data* 7, 176. doi: 10.1038/s41597-020-0520-9

Jensen, F. B. (2011). *Computational ocean acoustics* (New York: Springer). doi: 10.1007/978-1-4419-8678-8

Jin, Y. K. (2020) ARA10C cruise report: Korea- Russia East Siberian/Chukchi Sea research program. Available online at: http://library.kopri.re.kr/search/detail/CATTOT000000055761.

Keen, K. A., Thayre, B. J., Hildebrand, J. A., and Wiggins, S. M. (2018). Seismic airgun sound propagation in Arctic Ocean waveguides. *Deep Sea Res. Part I: Oceanographic Res. Papers* 141, 24–32. doi: 10.1016/j.dsr.2018.09.003

Liu, H., Yang, K., Ma, Y., Yang, Q., and Huang, C. (2020). Synchrosqueezing transform for geoacoustic inversion with air-gun source in the East China Sea. *Appl. Acoustics* 169, 107460. doi: 10.1016/j.apacoust.2020.107460

Mahanty, M. M., Latha, G., Venkatesan, R., Ravichandran, M., Atmanand, M. A., Thirunavukarasu, A., et al. (2020). Underwater sound to probe sea ice melting in the Arctic during winter. *Sci. Rep.* 10, 16047. doi: 10.1038/s41598-020-72917-4

Meignen, S., Gardner, T., and Oberlin, T. (2015). "Time-frequency ridge analysis based on the reassignment vector," in *23rd European Signal Processing Conference (EUSIPCO): IEEE*. 1486–1490.

Metropolis, N., Rosenbluth, A. W., Rosenbluth, M. N., Teller, A. H., and Teller, E. (1953). Equation of state calculations by fast computing machines. *J. Chem. Phys.* 21, 1087–1092. doi: 10.1063/1.1699114

Niessen, F., Hong, J. K., Hegewald, A., Matthiessen, J., Stein, R., Kim, H., et al. (2013). Repeated pleistocene glaciation of the East Siberian continental margin. *Nat. Geosci.* 6, 842–846. doi: 10.1038/ngeo1904

O'Regan, M., Backman, J., Barrientos, N., Cronin, T. M., Gemery, L., Kirchner, N., et al. (2017). The de long trough: a newly discovered glacial trough on the East Siberian continental margin. *Climate Past* 13, 1269–1284. doi: 10.5194/cp-13-1269-2017

Outridge, P. M., Macdonald, R. W., Wang, F., Stern, G. A., and Dastoor, A. P. (2008). A mass balance inventory of mercury in the Arctic Ocean. *Environ. Chem.* 5, 89–111. doi: 10.1071/EN08002

Porter, M. B. (1992). *"The KRAKEN normal mode program"* (Naval Research Lab Washington DC).

Potty, G. R., and Miller, J. H. (2020). Effect of shear on modal arrival times. *IEEE J. Oceanic Eng.* 45, 103–115. doi: 10.1109/JOE.48

Romanovskii, N. (2004). Permafrost of the east Siberian Arctic shelf and coastal lowlands. *Quaternary Sci. Rev.* 23, 1359–1369. doi: 10.1016/j.quascirev.2003.12.014

Thakur, G., Brevdo, E., Fučkar, N. S., and Wu, H.-T. (2013). The Synchrosqueezing algorithm for time-varying spectral analysis: Robustness properties and new paleoclimate applications. *Signal Process.* 93, 1079–1094. doi: 10.1016/j.sigpro.2012.11.029

Thode, A., Bonnel, J., Thieury, M., Fagan, A., Verlinden, C., Wright, D., et al. (2017). Using nonlinear time warping to estimate North Pacific right whale calling depths in the Bering Sea. *J. Acoust. Soc Am.* 141, 3059–3069. doi: 10.1121/1.4982200

Warner, G. A., Dosso, S. E., Dettmer, J., and Hannay, (2015). Bayesian environmental inversion of airgun modal dispersion using a single hydrophone in the Chukchi Sea. *J. Acoust. Soc Am.* 137, 3009–3023. doi: 10.1121/1.4921284

Warner, G. A., Dosso, S. E., Hannay, D. E., and Dettmer, J. (2016). Bowhead whale localization using asynchronous hydrophones in the Chukchi Sea. *J. Acoust. Soc Am.* 140, 20–34. doi: 10.1121/1.4954755

frontiers | Frontiers in Marine Science

TYPE Original Research
PUBLISHED 21 August 2024
DOI 10.3389/fmars.2024.1370274

OPEN ACCESS

EDITED BY
Guangming Kan,
Ministry of Natural Resources, China

REVIEWED BY
Vahid Tavakoli,
University of Tehran, Iran
Purna Sulastya Putra,
National Research and Innovation Agency (BRIN), Indonesia

*CORRESPONDENCE
Xinghui Cao
caoxinghui1982@163.com

RECEIVED 14 January 2024
ACCEPTED 30 July 2024
PUBLISHED 21 August 2024

CITATION
Zhen H, Cao X, Qu Z, Zou D, Xiong S, Song J and Guo H (2024) Sediment classification in the paleo-oceanic environment based on multi-acoustic reflectance characteristics in the Southern Tianshan Mountains. *Front. Mar. Sci.* 11:1370274. doi: 10.3389/fmars.2024.1370274

Sediment classification in the paleo-oceanic environment based on multi-acoustic reflectance characteristics in the Southern Tianshan Mountains

Huancheng Zhen[1], Xinghui Cao[1]*, Zhiguo Qu[2], Dapeng Zou[3], Shuai Xiong[1], Jiang Song[1] and Hao Guo[1]

[1]Xinjiang Key Laboratory of New Energy and Energy Storage Technology, Xinjiang Institute of Technology, Aksu, China, [2]College of Information and Communication Engineering, Harbin Engineering University, Harbin, China, [3]State Key Laboratory of Precision Electronic Manufacturing Technology and Equipment, School of Electromechanical Engineering, Guangdong University of Technology, Guangzhou, China

The grain size of sediments is a crucial parameter in sedimentology, with significant implications for submarine engineering and water conservancy projects. In this study, we developed an acoustic reflection measurement system using a self-developed, high-precision, high-frequency shallow stratigraphic profiler. The system's accuracy was validated with standard acrylic samples. Results showed that within the sediment grain size range of 0.3 to 2.5 mm, the acoustic reflection amplitude increased with grain size. However, distinguishing grain sizes between 0.1 and 0.3 mm from those between 1.0 and 1.5 mm based solely on reflection amplitude proved challenging. Notably, the differences in wavefront flare shapes between these grain sizes were readily apparent. Therefore, combining reflection peak amplitude with time-domain waveform analysis enables more precise sediment grain size classification.

KEYWORDS

sandy sediments, fine measurement, waveform characteristics, wide-band transducer, pulse compression

1 Introduction

Sediment classification is a prominent research topic in the fields of underwater acoustics and geology. Measuring the acoustic reflection characteristics of sediments serves as a crucial technical approach for investigating sediment classification. Establishing a correlation between the acoustic reflection characteristics of sediments and the types of sedimentation enables the inversion of sediment physical parameters. The process of

deriving physical parameters from acoustic parameters to classify sediments holds significant scientific importance for the theory of geoacoustic inversion (Jackson and Richardson, 2007; Li et al., 2021a; Wang J. et al., 2023).

The correlation between the acoustic reflection characteristics and physical properties of substrate sand and gravel has mainly been established through *in situ* measurements and laboratory studies (Hamilton, 1980; Liu et al., 2013; Zhengyu et al., 2015; Zhang et al., 2017; Li et al., 2021a; Li et al., 2021b). One direct method for obtaining underwater acoustic reflection characteristics is *in situ* measurement. For example, Zheng et al (2013). calculated seafloor reflection and attenuation coefficients based on seafloor profiles. Additionally, they quantitatively estimated the average grain size and corresponding sediment classification using the Biot model. However, this method can be costly and inefficient since the information about the seafloor only applies to discrete locations. Acoustic waves collected through sonar systems are a low-cost and effective means of detecting substrate structure and sediment type. For instance, the reflection coefficient (RC) estimated from acoustic echoes can be used to infer the mean grain size (Hamilton, 1970). Ji et al (2020) suggested that using acoustic remote sensing to classify seafloor siltation is an attractive method with a high coverage capacity and low cost compared to seafloor sampling. This research focuses on improving the accuracy of seafloor silt classification through backscattering intensity correction, sonar image quality enhancement, and classifier construction. The effectiveness and superiority of the selected optimal random forest (SORF) classifier were verified through comparison with the support vector machine (SVM) and random forest (RF) classifiers. The multi-beam echo sounding system records seafloor backscattering intensity data, which provide information about seafloor geological features. Acoustic inversion estimates the density of surface sediment layers, sediment sound velocity, and medium attenuation (Li et al., 2021b). Numerous studies have been conducted to identify various sediment types using acoustic echoes (Marsh and Brown, 2008; Fonseca et al., 2009). Moreover, there is a body of literature (Cui et al., 2021; Wang H. et al., 2023) utilizing deep learning methods for sediment classification. Anokye et al (2024). proposed a novel method for seafloor sediment classification using a multibeam echo sounder system and a convolutional neural network (CNN), thereby improving classification accuracy. Qin et al (2021). employed side-scanning sonar images in conjunction with different depths of a CNN. Pre-training the model using the greyscale CIFAR-10 dataset enables the transfer of parameters across a wide range of tasks, thereby improving the overall performance of the model and reducing the error rate of classification. However, in these studies (Wang J. et al., 2023; Wendelboe et al., 2023), the common practice is to first measure the acoustic properties of the sediments *in situ* and then sample them. The physical property parameters of the sediments are measured in the laboratory, and parameters such as the average grain size of the sediments are obtained. The extracted acoustic reflectance characteristics are based on the characteristic information of the mixed sediments. Fewer scholars have paid attention to the acoustic reflection characteristics of the fine distribution of particle sizes. Such research requires specific sediment grain sizes, which can be limited by sampling. Additionally, the use of sonar equipment with higher degrees of refinement is necessary for studying sediments with fine particle sizes. As a result, sediments with fine particle sizes have not been fully explored.

The study of specific sediments requires a sonar instrument capable of supporting refined measurements under laboratory conditions. Our laboratory has developed an in-house sonar that meets these requirements. This sonar instrument emits a very narrow beam, and in the mid- and high-frequency bands, the measurements are free from side-lobe interference. In contrast, general sonar equipment typically generates multipath interference from side lobes, which prevents clear echo distinction and complicates fine measurements in these frequency bands. To address this, we developed a unique transducer to support laboratory fine measurements.

Furthermore, the southern foothills of the Tianshan Mountain, where our study is located, were once a paleo-marine depositional environment (Song et al., 2016; Tao et al., 2023). Some studies suggest this region belongs to the Late Ediacaran-Early Cambrian stratigraphy (Chang et al., 2021), while others propose an Ordovician period (Zhang and Munnecke, 2016). The sandy sediments in this area exhibit good homogeneity of grain size due to natural sorting processes. Based on this, we screened six sandy sediment samples with grain sizes ranging from 0.1 to 2.5 mm using a standard sieve. Under laboratory conditions, we then used a high-frequency submersible sub-bottom profiler (HF-SSBP) to investigate the relationship between the sediments and acoustic reflection signals.

The remainder of this paper is organized as follows: Section 2 outlines the measurement principle and method. The experimental setup and sample preparation are detailed in Section 3. Section 4 presents the analysis and discussion of the data results. Finally, a concise summary is provided in Section 5.

2 Measurement methods

2.1 Measuring device

An iron water tank measuring 4 m × 2.5 m × 1.7 m was utilized in the experiment. The bottom of the tank was lined with a 100-mm-thick acrylic plate, which held the sediment samples in acrylic buckets. A small aerial crane was employed to lift the various test samples. The transducer and polyformaldehyde (POM) plate were connected and suspended from the iron frame at the top of the water tank. The POM plate was attached to the center of a fixed axis, allowing the transducer to move vertically and adjust its distance from the sediment surface. During testing, the transducer remained parallel to the sediment surface and was kept suspended directly above it. Figure 1 illustrates the schematic diagram of the measurement setup.

The experimental study is a mechanistic investigation of the relationship between sediment grain size and acoustic reflection. However, field sediments are typically mixtures of multiple grain sizes, complicating mechanistic studies. Therefore, sieving naturally sorted sediment grain sizes in the laboratory to study acoustic

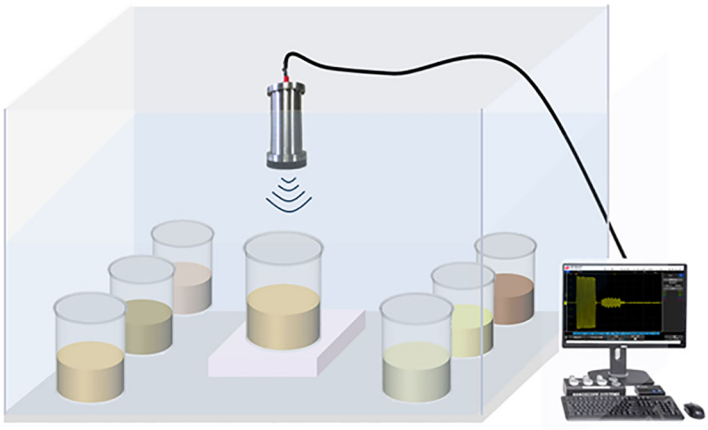

FIGURE 1
Schematic diagram of the measuring device.

reflection at different grain sizes is a fundamental aspect of understanding mixed grain sizes under field conditions.

2.2 Acoustic reflection signal processing

The HF-SSBP device utilizes a linear frequency modulation (LFM) signal as the transmit signal and receives an echo signal that is a superposition of multiple reflection signals in the time domain. This can make it difficult to distinguish between the interfaces of the sediments, acrylic, and water. By processing the raw data obtained using the shallow stratigraphic profiler with a pulse compression algorithm, it is possible to extract the reflection information at the interface between the water and sediment. First, the time-domain signal undergoes orthogonal demodulation. Next, the demodulated result is filtered using a low-pass filter to remove the signal's carrier frequency. Finally, the signal obtained from the low-pass filter is processed using the LFM signal as a matched filter, resulting in the computation of the interface reflection intensity. The pulse compression algorithm comprises several main steps. For more detailed information on the pulse compression algorithm, please refer to the literature (Curlander and Mcdonough, 1992).

$$\boldsymbol{s_{sin}(t) = s(t) \cdot H_{sin}} \tag{1}$$

$$\boldsymbol{s_{cos}(t) = s(t) \cdot H_{cos}} \tag{2}$$

$$\boldsymbol{S(t) = s_{sin}(t) \cdot P(t) \cdot j s_{cos} P(t)} \tag{3}$$

$$\boldsymbol{V(t) = S(t) \cdot M(t)} \tag{4}$$

Where: H_{sin} and H_{cos} are quadrature demodulation factors. (Equations 1, 2) are used to perform quadrature demodulation of the time-domain signal $S(t)$ to obtain the quadrature demodulation results $s_{sin}(t)$ and $s_{cos}(t)$ of the time-domain signal $s(t)$. Equation 3 represents the computational expression for the complex signal. $P(t)$ is the low-pass filter; $S(t)$ is the complex signal; and $M(t)$ is the matched filter; $V(t)$ represents the strength of reflection for a multilayer signal. Equation 4 represents the mathematical model for calculating the reflected intensity of the multilayer.

3 Experiments

3.1 Testing equipment

To investigate the acoustic echo signals of specific sediment grain sizes, we utilized an HF-SSBP (Cao et al., 2022). The HF-SSBP uses LFM signals with an operating carrier frequency of 110 kHz, a bandwidth of 30 kHz, and a coherent signal for echo reception. The transducer structure is a transceiver combination that employs a novel broadband design. It also incorporates very low side-lobe technology, resulting in a side-lobe to main-lobe ratio of −17.1 dB. To ensure that the transducer received reflective signals from all sediment surfaces, we selected an acrylic bucket with an appropriate diameter for the sediment samples. During the experiment, it was found that an acrylic bucket with a diameter of 30 cm could fully capture the acoustic signal, whereas buckets with diameters of 20 cm and 40 cm were less effective. Consequently, the experimental tests were conducted using a 30-cm-diameter bucket to ensure that all reflected signals originated from the sediment and not from other spatial reflections. This setup allowed for precise measurements even in confined spaces. Table 1 presents the device parameters.

3.2 Sample preparation

In order to conduct this experiment, samples of sandy sediment were collected from the Kumarik River basin. The sandy sediments in this area are transported by rivers. Due to the natural sorting effects of wind and other environmental factors, it was deemed appropriate to select naturally sorted sandy sediments, which are more representative of those formed in natural environments than man-made sand. However, the grain size of the naturally sorted sediments is not very uniform. Therefore, the sediments were further sieved into six grain sizes: 0.1-0.3 mm, 0.3-0.5 mm, 0.5-1.0 mm, 1.0-

TABLE 1 HF-SSBP parameter configuration.

Technical parameter	Index
Signal waveform	LFM
Bandwidth	30KHz
Carrier frequency	110KHz
3dB Beam width	5.8°
Wave beam sidelobe	-17dB
Transducer	Uniform wide band transmitter–receiver
Signal receiving form	Coherent

HF-SSBP, high-frequency submersible sub-bottom profiler; LFM, linear frequency modulation.

1.5 mm, 1.5-2.0 mm, and 2.0-2.5 mm, using a standard sieve in the laboratory. To remove very fine sand particles and clay attachments from the sediments, the sieved sediments were placed in a bucket and mixed with clean water. By repeatedly stirring and decanting the supernatant, most of the clay attached to the sediments was washed away after several repetitions. Finally, the grit was loaded into an acrylic bucket and stirred to settle. The resulting saturated sandy sediments, with a thickness of 8 cm, were placed in an acrylic bucket with a diameter and height of 300 mm. The thickness should not be too thin to avoid an unstable sound field and should not be too thick to prevent internal inhomogeneities and ensure strong echo information from the bottom of the sediment. These considerations help verify and calibrate the measurement results. The sediment samples were prepared in June 2023 and tested in October 2023 after a deposition time of approximately 90 days. Figure 2 shows the surface map of the sediment samples, illustrating the gradual increase in particle size and surface roughness across the six sediments.

4 Result and analysis

4.1 Test results and data processing

To verify the accuracy and stability of the measurement process, we placed an acrylic bottom with a depth of 10 cm at the bottom of the tank. We then measured the reflection signal from the transducer at intervals of 80 cm, 85 cm, 90 cm, 95 cm, 100 cm, and 105 cm from the surface of the acrylic. The data were processed using the pulse compression algorithm to extract the characteristic peaks. Two reflection peaks were observed: one at the interface between the water and acrylic, and the other at the interface between the acrylic and the bottom of the water tank. However, the amplitude of the reflection peak at the interface between the acrylic and the bottom of the water tank was stronger than that at the interface between the water and acrylic. This may be due to the strong reflection at the bottom of the water tank, resulting in a signal amplitude that exceeded that of the reflection between the water and acrylic interface. The reflected signal amplitude decreased linearly as the transducer moved away from the acrylic surface, indicating good accuracy and stability of the experimental process.

4.2 Time domain analysis

To analyze the effect of sediment grain size on the shape of the acoustic reflection signal echo, we examined the time-domain diagrams

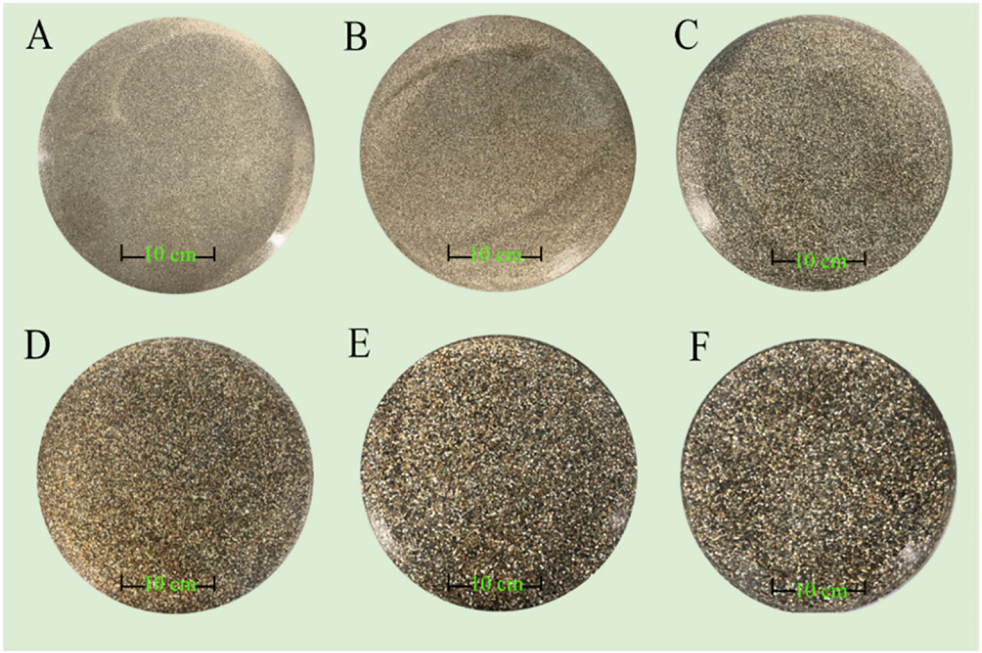

FIGURE 2
Six grain size sediment samples: **(A)** 0.1-0.3 mm; **(B)** 0.3-0.5 mm; **(C)** 0.5-1.0 mm; **(D)** 1.0-1.5 mm; **(E)** 1.5-2.0 mm; **(F)** 2.0-2.5 mm).

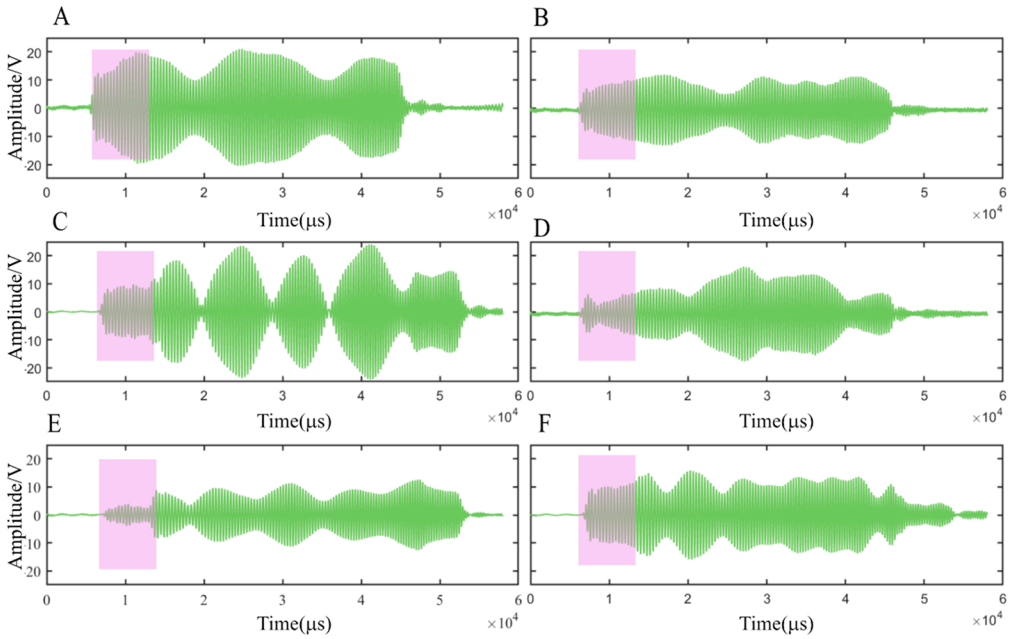

FIGURE 3
Time domain visualization of six particle sizes. **(A)** 0.1-0.3 mm; **(B)** 0.3-0.5 mm; **(C)** 0.5-1.0 mm; **(D)** 1.0-1.5 mm; **(E)** 1.5-2.0 mm; **(F)** 2.0-2.5 mm).

of the echo signals at the sediment surface 90 cm from the transducer. The time-domain diagrams of the six grain sizes are shown in Figure 3. The purple area in Figure 3 represents the initial 80 μs segment of the received signal following reflection by the sediment. Variations in the waveform within this region indicate sediment grain size differences. The reflection peak amplitude is relatively large for grain sizes A and F, and it gradually increases with increasing grain size for B, C, D, and E. For particle sizes A and B, the three echoes of the reflected signal are clearer. As particle size increases, the superposition trend of the three interfaces of the reflected echoes becomes more pronounced. The reflected echoes exhibit different wavefront flare shapes, with the angle of the wavefront flare being larger for several grain sizes, except for grain size E. This may be related to the porosity of the sediment and other factors.

5 Discussion

5.1 Six sediment reflection peaks

The characteristic reflection peaks of each grain size were extracted from the reflection signals of six sandy sediments using the pulse compression algorithm. The results are presented in Figure 4. The black line represents the first antipodal amplitude, the reflection peak at the water-sediment interface. The blue line represents the second antipodal amplitude, the reflection peak at the interface between the bottom of the sediment and the acrylic bucket. The red line represents the third antipodal amplitude, the reflection peak at the interface between the bottom of the tank and the acrylic bucket. These results are consistent with the pulse compression results shown in Figure 5, which illustrate the clear layering of the three interfaces. The reflection peak amplitude at the water-sediment interface is the strongest. As the distance between the sediment surface and the transducer surface increases, the reflection peaks at the water-sediment interface decrease to varying degrees. Figure 4C shows a situation where the amplitude of the third reflection peak (acrylic and the bottom of the water tank) is higher than those of the first and second reflection peaks. This could be due to the mutual interference between the bottom of the water tank, the acrylic, and the laboratory floor. It should be noted that our water tank was made of iron and was only 5 mm thick. Figures 4A–F show that the amplitude of the second peak is not stable. In Figures 4A, D, the second reflection peak is located between the first and third peaks. In Figures 4B, C, and F, the amplitude of the second reflection peak is the smallest. In Figure 4E, the difference in the amplitudes of the second and third peaks is not noticeable. Therefore, the first reflection peak is particularly valuable for studying sediments.

5.2 Analysis of the first reflection peak

To investigate the relationship between sediment grain size and reflection peak amplitude, we analyzed the extracted values of the first reflection peak amplitude and sediment grain size. The results are presented in Figure 6. In general, the amplitude of the first reflection peak increases with increasing sediment grain size. This trend is consistent with the findings of (Ivakin and Sessarego, 2007, Eleftherakis et al., 2014). in the high-frequency broadband range. However, grain sizes A (0.1–0.3 mm) and F (2.0–2.5 mm) do not exhibit an obvious amplitude correlation. This may be due to the positive correlation between reflection peak amplitude and grain size within a specific range of grain sizes. The findings of Hamilton (1972) are similar, indicating that acoustic attenuation is lower in coarse sand and clay sediments, but higher in fine sand and silt sediments.

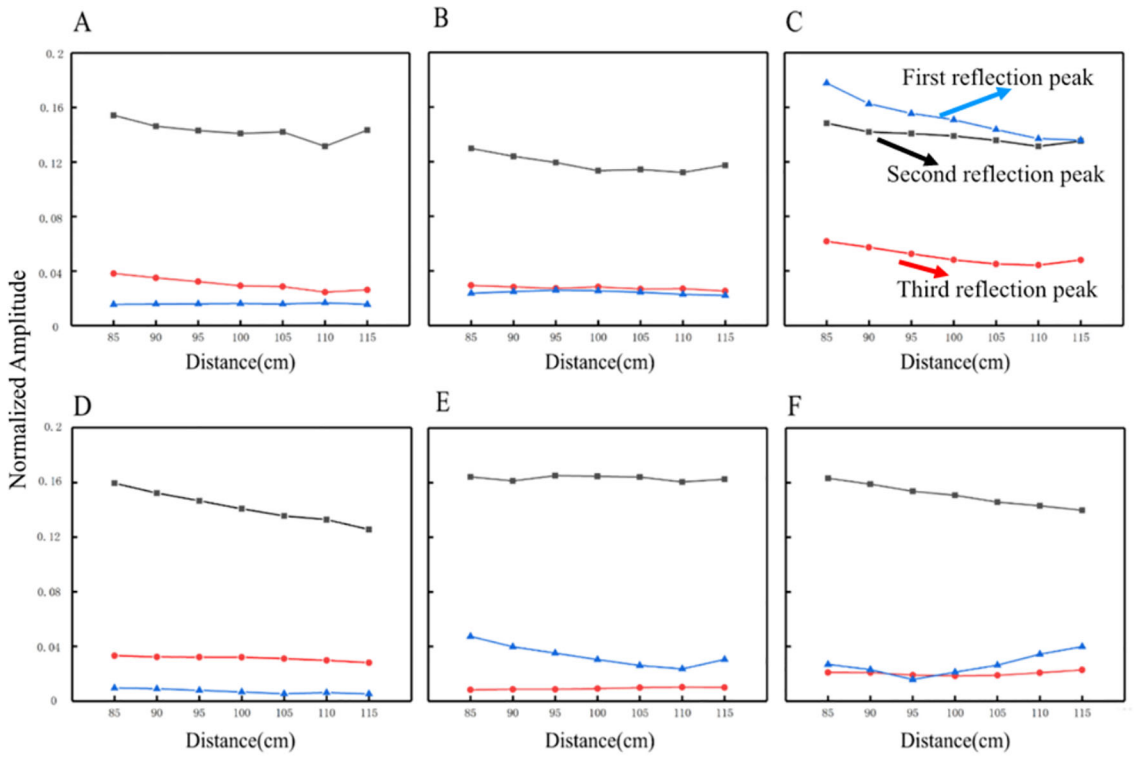

FIGURE 4
Reflectance peaks in sandy sediments of six grain sizes. **(A)** 0.1-0.3 mm; **(B)** 0.3-0.5 mm; **(C)** 0.5-1.0 mm; **(D)**1.0-1.5 mm; **(E)** 1.5-2.0 mm; **(F)** 2.0-2.5 mm.

As the sediment surface moves away from the transducer, the reflection peak amplitudes decrease to varying degrees. For particle size E, the reflection peak amplitude remains relatively stable. This may be because the acoustic emission signal of the sediment surface is less sensitive to distance changes at this particle size. The roughness of the sediment surface is caused by varying degrees of roughness.

5.3 Signal of the first reflection peak histogram

A calculation was performed based on the speed of sound in the sediment as presented in the literature (Park et al., 2023; Tian et al., 2023) and the thickness of the sediment as measured in the

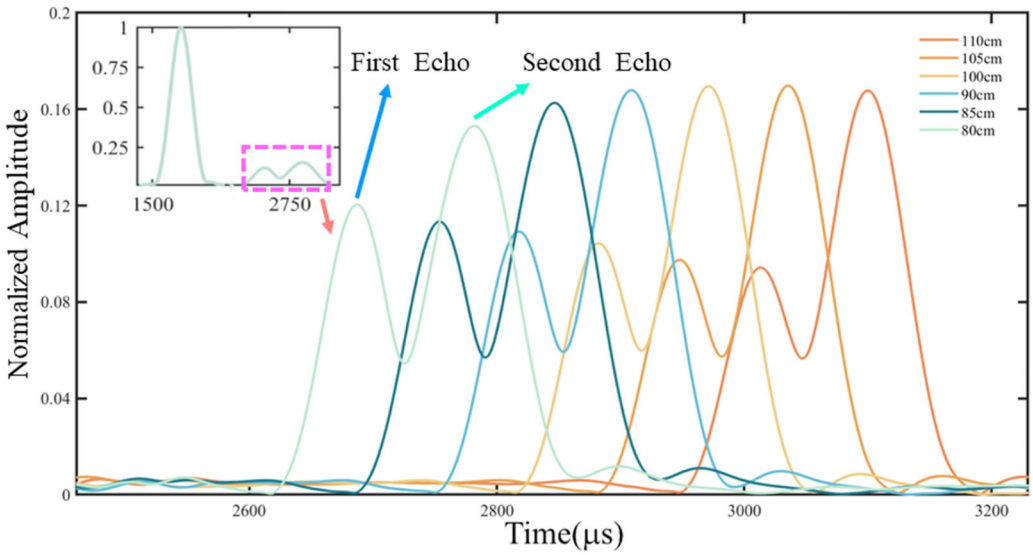

FIGURE 5
Waveforms of pulse compression of acoustic reflection signals from sandy sediments ranging in size from 1.0-1.5 mm.

10.3389/fmars.2024.1370274

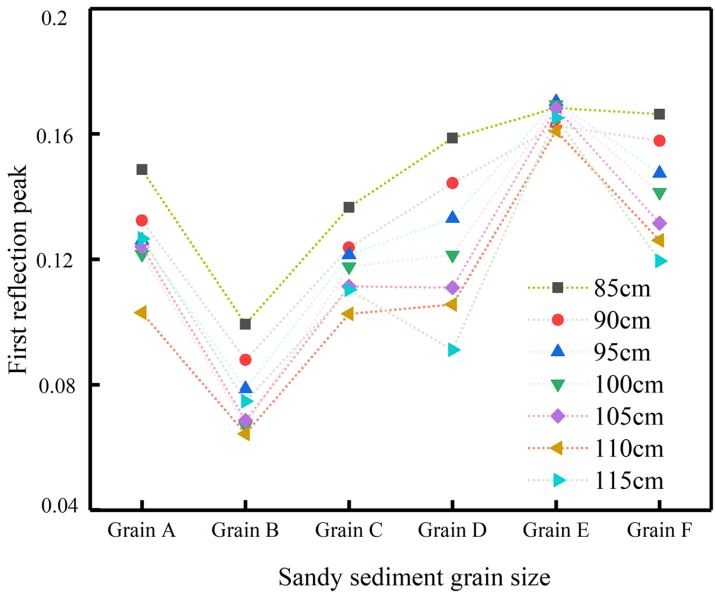

FIGURE 6
Peak amplitude of reflections at the water-sediment interface for six sediments.

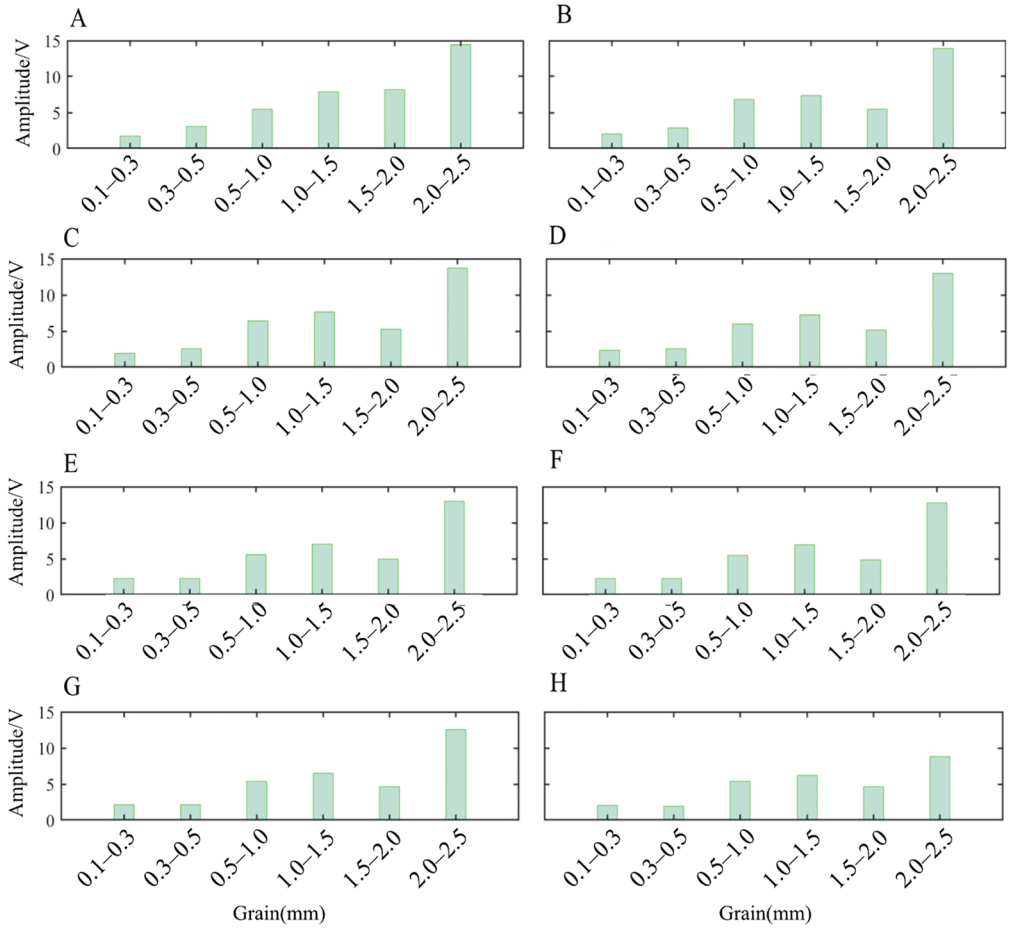

FIGURE 7
Histograms of 80 μs signals from six sandy sediments. **(A)** 80 cm; **(B)** 85 cm; **(C)** 90 cm; **(D)** 95 cm; **(E)** 110 cm; **(F)** 105 cm; **(G)** 110 cm; **(H)** 115 cm.

laboratory. This calculation yielded a one-way transmission propagation time of the sound wave in the sediment of 80 μs. By calculating the one-way propagation time of the sound wave in the sediment and the propagation time in the water, we can establish the time of the first wave of the signal reflected from the sediment surface. This allows us to determine the return signal of the sediment layer without interference. The mean value of the signal amplitude was plotted after extracting the 80 μs signal. The results are presented in Figure 7, which shows the consistency between the histogram of the 80 μs signal and the trend of the first wave of the time-domain echo signal.

5.4 Sediment classification

Figure 8 illustrates the first wave amplitude and waveforms of the reflection signals for six grain sizes of sandy sediments at different distances. It can be observed that the grain sizes of the sediments and the amplitude of the first reflection peaks are approximately positively correlated. Furthermore, the amplitude of the first reflection peaks increases gradually with the increase in sediment grain sizes. When the particle sizes are A, C, and D, the amplitude of the sediment reflection peaks exhibits minimal variation, whereas the time-domain waveforms show pronounced differences. As shown in the upper time-domain waveform in Figure 8, the beam opening angle is greater for particle size A. In contrast, particle sizes C and D exhibit smaller beam opening angles than A. The difference in reflected peak amplitude between particle sizes E and F is not particularly large, but the beam opening angle of the reflected waveform for particle size E is relatively small, while that for particle size F is relatively large. Therefore, the combination of acoustic reflection amplitude and echo waveform can be used to more finely distinguish sediment grain sizes.

6 Conclusions

The laboratory research on the acoustic reflection signals of sandy sediments with varying grain sizes revealed that the shallow low-level HF-SSBP is capable of precise measurements. In this study, we utilized this equipment to analyze six sandy sediments with different grain sizes in the laboratory. The following conclusions were reached:

(1) We independently developed the HF-SSBP used in the experiments, and this instrument can accurately and precisely measure sandy sediments in a small space. The equipment is capable of testing the accuracy and stability of the acoustic reflection echoes of sandy sediments in the laboratory.

(2) Six types of sediment with uniform grain sizes were obtained from sandy sediments using standard sieves. Their acoustic reflection echoes were then tested, and it was found that there was a positive correlation between the amplitude and grain size. The amplitude of the reflection peaks increased with increasing grain size.

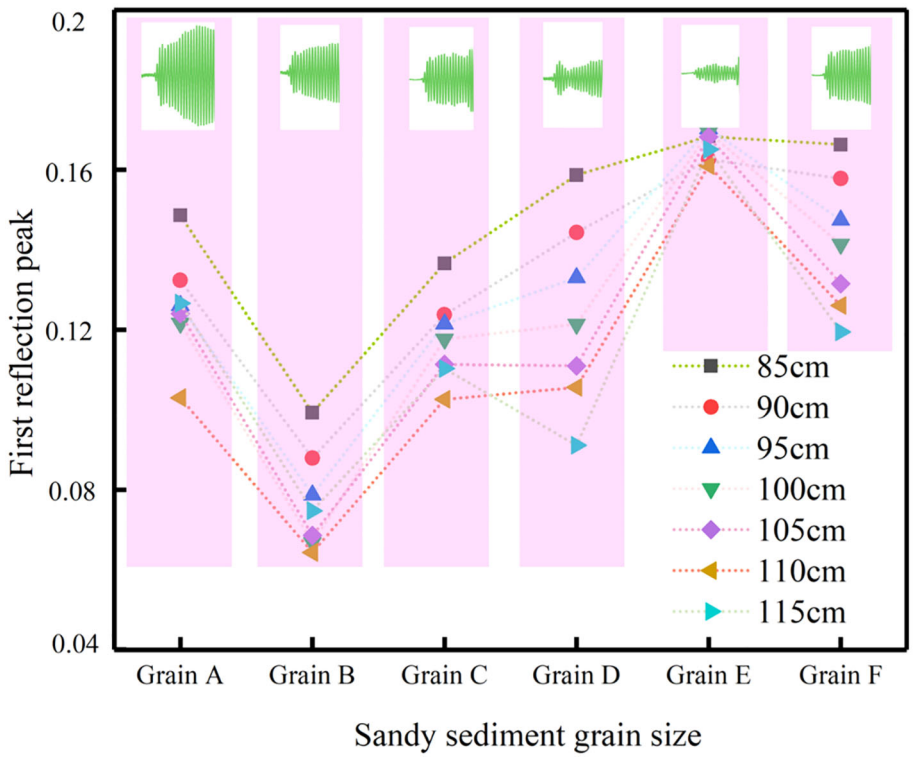

FIGURE 8
Classification of sediment particle size.

(3) By analyzing the amplitude of the reflection peaks and echo waveforms, sediment grain sizes can be distinguished in a more precise manner.

This study provides a valuable guide for the fine-grained classification of sediment grain size.

Data availability statement

The original contributions presented in the study are included in the article/supplementary material. Further inquiries can be directed to the corresponding author.

Author contributions

HZ: Data curation, Investigation, Writing – original draft, Writing – review & editing. XC: Funding acquisition, Project administration, Supervision, Writing – review & editing. ZQ: Data curation, Methodology, Software, Writing – review & editing. DZ: Conceptualization, Formal analysis, Supervision, Validation, Writing – review & editing. SX: Data curation, Investigation, Methodology, Writing – review & editing. JS: Data curation, Investigation, Writing – review & editing. HG: Data curation, Formal analysis, Investigation, Visualization, Writing – review & editing.

Funding

The author(s) declare financial support was received for the research, authorship, and/or publication of this article. This research was supported by the Natural Science Foundation of the Xinjiang Uygur Autonomous Region (grant numbers 2022D01C736 and 2022D01C348).

Conflict of interest

The authors declare that the research was conducted in the absence of any commercial or financial relationships that could be construed as a potential conflict of interest.

Publisher's note

References

Anokye, M., Cui, X., Yang, F., Fan, M., Luo, Y., and Liu, H. (2024). CNN multibeam seabed sediment classification combined with a novel feature optimization method. *Math. Geosciences* 56, 279–302. doi: 10.1007/s11004-023-10079-5

Cao, X., Zou, D., Qu, Z., Zhen, H., Cheng, H., and Wei, Z. (2022). Calibration and application of high-frequency submersible sub-bottom profiler for deep-sea surficial sediment measurement. *Mar. Georesources Geotechnology.* 41 (6), 671–681. doi: 10.1080/1064119X.2022.2086510

Chang, X., Hou, M., Woods, A., Chen, Z. Q., Liu, X., Liao, Z., et al. (2021). Late Ordovician paleoceanographic change: Sedimentary and geochemical evidence from Northwest Tarim and Middle Yangtze region, China. *Palaeogeography Palaeoclimatology Palaeoecol.* 562, 110070. doi: 10.1016/j.palaeo.2020.110070

Cui, X., Yang, F., Wang, X., Ai, B., Luo, Y., and Ma, D. (2021). Deep learning model for seabed sediment classification based on fuzzy ranking feature optimization. *Mar. Geology.* 432, 106390. doi: 10.1016/j.margeo.2020.106390

Curlander, J. C., and Mcdonough, R. N. (1992). Synthetic aperture radar: systems and signal processing. *Signal Process.* 29, 107–107. doi: 10.1016/0165-1684(92)90103-4

Eleftherakis, D., Snellen, M., Amiri-Simkooei, A., Simons, D. G., and Siemes, K. (2014). Observations regarding coarse sediment classification based on multi-beam echo-sounder's backscatter strength and depth residuals in Dutch rivers. *J. Acoust Soc. Am.* 135, 3305–3315. doi: 10.1121/1.4875236

Fonseca, L., Brown, C., Calder, B., Mayer, L., and Rzhanov, Y. (2009). Angular range analysis of acoustic themes from Stanton Banks Ireland: a link between visual interpretation and multibeam echosounder angular signatures. *Appl. Acoust.* 70, 1298–1304. doi: 10.1016/j.apacoust.2008.09.008

Hamilton, E. L. (1970). Sound velocity and related properties of marine sediments, North Pacific. *J. Geophys Res.* 75, 4423–4446. doi: 10.1029/JB075i023p04423

Hamilton, E. L. (1972). Compressional wave attenuation in seafloor sediments. *Geophysics* 37, 620–646. doi: 10.1190/1.1440287

Hamilton, E. L. (1980). Geoacoustic modeling of the sea floor. *J. Acoust Soc. Am.* 68, 1313–1340. doi: 10.1121/1.385100

Ivakin, A. N., and Sessarego, J.-P. (2007). High frequency broad band scattering from water-saturated granular sediments: Scaling effects. *J. Acoust Soc Am.* 122, 165–171. doi: 10.1121/1.2784534

Jackson, D. R., and Richardson, M. D. (2007). *High-frequency seafloor acoustics* (Berlin, Germany: Springer Science and Business Media). doi: 10.1007/978-0-387-36945-7

Ji, X., Yang, B., and Tang, Q. (2020). Seabed sediment classification using multibeam backscatter data based on the selecting optimal random forest model. *Appl. Acoust.* 167, 107387. doi: 10.1016/j.apacoust.2020.107387

Li, G. B., Hou, Z. Y., Wang, J. Q., Kan, G. M., and Liu, B. H. (2021a). Empirical equations of p-wave velocity in the shallow and semi-deep sea sediments from the south China Sea. *J. Ocean Univ China* 20, 532–538. doi: 10.1007/s11802-021-4476-y

Li, G. B., Wang, J. Q., Meng, X. M., Liu, B. H., Kan, G. M., Han, G. Z., et al. (2021b). Relationships between the ratio of sound speed and physical properties of surface sediments in the south yellow Sea. *Acta Oceanol Sin.* 40, 65–73. doi: 10.1007/s13131-021-1764-8

Liu, B., Han, T., Kan, G., and Li, G. (2013). Correlations between the *in situ* acoustic properties and geotechnical parameters of sediments in the yellow Sea, China. *J. Asian Earth Sci.* 77, 83–90. doi: 10.1016/j.jseaes.2013.07.040

Marsh, I., and Brown, C. (2008). Neural network classification of multibeam backscatter and bathymetry data from Stanton Bank (Area IV). *Appl. Acoust* 70, 1269–1276. doi: 10.1016/j.apacoust.2008.07.012

Park, J., Lee, J.-S., and Yoon, H.-K. (2023). Geoacoustic and geophysical data-driven seafloor sediment classification through machine learning algorithms with property-centered oversampling techniques. *Computer-Aided Civil Infrastructure Eng.* 39 (14), 1–17. doi: 10.1111/mice.13126

Qin, X., Luo, X., Wu, Z., and Shang, J. (2021). Optimizing the sediment classification of small side-scan sonar images based on deep learning. *IEEE Access* 9, 29417–29428. doi: 10.1109/Access.6287639

Song, D., Wang, T.-G., Deng, W., and Shi, S. (2016). Application of light hydrocarbons (C5–C7) in Paleozoic marine petroleum of the Tarim Basin, NW China. *J. Petroleum Sci. Eng.* 40, 57–63. doi: 10.1016/j.petrol.2016.01.009

Tao, Y., Gao, D., He, Y., Ngia, N. R., Wang, M., Sun, C., et al. (2023). Carbon and oxygen isotopes of the Lianglitage Formation in the Tazhong area, Tarim Basin: Implications for sea-level changes and palaeomarine conditions. *Geological J.* 58, 967–980. doi: 10.1002/gj.4637

Tian, Y., Chen, Z., Mo, Y., Xie, A., Huang, W., Wang, S., et al. (2023). Effects of physical properties on the compression wave speed of seafloor sediment in the South China Sea: Comparisons between theoretical models and measured data. *Front. Phys.* 11. doi: 10.3389/fphy.2023.1122617

Wang, J., Kan, G., Li, G., Meng, X., Zhang, L., Chen, M., et al. (2023). Physical properties and *in situ* geoacoustic properties of seafloor surface sediments in the East China Sea. *Front. Mar. Sci.* 10. doi: 10.3389/fmars.2023.1195651

Wang, H., Zhou, Q., Wei, S., Xue, X., Zhou, X., and Zhang, X. (2023). Research on seabed sediment classification based on the MSC-transformer and sub-bottom profiler. *J. Mar. Sci. Eng.* 11, 1074. doi: 10.3390/jmse11051074

Wendelboe, G., Hefner, T., and Ivakin, A. (2023). Observed correlations between the sediment grain size and the high-frequency backscattering strength. *JASA Express Lett.* 3, 026001. doi: 10.1121/10.0017107

Zhang, Y. X., Guo, C. S., Wang, J. Q., Hou, Z. Y., and Chen, W. J. (2017). Relationship between *in situ* sound volocity and granular characteristics of seafloor sediments in the Qingdao offshore region. *J. Oceanol Limnol* 35, 704–711. doi: 10.1007/s00343-017-5374-4

Zhang, Y., and Munnecke, A. (2016). Ordovician stable carbon isotope stratigraphy in the Tarim Basin, NW China. *Palaeogeography Palaeoclimatology Palaeoecol.* 458, 154–175. doi: 10.1016/j.palaeo.2015.09.001

Zheng, H. B., Yan, P., Chen, J., and Wang, Y-l. (2013). Seabed sediment classification in the northern South China Sea using inversion method. *Appl. Ocean Res.* 39, 131–136. doi: 10.1016/j.apor.2012.11.002

Zhengyu, H., Changsheng, G., Jingqiang, W., Wenjing, C., Yongtao, F., and Tiegang, L. (2015). Seafloor sediment study from south China Sea: acoustic & physical property relationship. *Remote Sens.* 7, 11570–11585. doi: 10.3390/rs70911570

frontiers | Frontiers in Marine Science

TYPE Original Research
PUBLISHED 21 November 2024
DOI 10.3389/fmars.2024.1377405

OPEN ACCESS

EDITED BY
Xingsen Guo,
University College London, United Kingdom

REVIEWED BY
Jiangong Wei,
Guangzhou Marine Geological Survey, China
Dapeng Zou,
Guangdong University of Technology, China
Xuesen Liu,
Ocean University of China, China
Piguang Wang,
Beijing University of Technology, China

*CORRESPONDENCE
Lei Guo
201894900036@sdu.edu.cn

RECEIVED 27 January 2024
ACCEPTED 13 August 2024
PUBLISHED 21 November 2024

CITATION
Wang C, Guo L, Jia L, Sun W, Xue G, Yang X and Liu X (2024) Development and application of a 3,000-m Seabed Cone Penetration Test and Sampling System based on a hydraulic drive.
Front. Mar. Sci. 11:1377405.
doi: 10.3389/fmars.2024.1377405

Development and application of a 3,000-m Seabed Cone Penetration Test and Sampling System based on a hydraulic drive

Cheng Wang[1], Lei Guo[1]*, Lei Jia[1], Wenxu Sun[1], Gang Xue[1], Xiuqing Yang[2] and Xiaolei Liu[3]

[1]Institute of Marine Science and Technology, Shandong University, Qingdao, China, [2]College of Oceanic and Atmospheric Sciences, Ocean University of China, Qingdao, China, [3]Shandong Provincial Key Laboratory of Marine Environment and Geological Engineering, Ocean University of China, Qingdao, China

The seabed surface is an important boundary for ocean exploration and foundation for ocean engineering construction. Accurate acquisition of seabed sediment mechanical properties and environmental parameters is critical to the development of marine resources and marine engineering. In this study, by designing the Seabed Cone Penetration Test (CPT) and Sampling System, multiparameter *in situ* testing and low-disturbance sampling of 3,000-m deep-sea seabed sediments are performed. Accounting for the stable penetration speed of the probe rod is the basis for ensuring the accuracy of the static penetration test results. The system adopts electrohydraulic proportional position control and a fuzzy proportional integral derivative (PID) controller to precisely control the position of the piston of the hydraulic circuit, which can improve the accuracy of the cone test data and reduce the interference of the sampling tube with the original sediment during the sampling process. Moreover, electrohydraulic co-simulation of the hydraulic control system was conducted with the AMESim and Simulink software, and the position control and speed control effects of the system were verified. The entire system was tested on site in the Shenhu Sea area of the South China Sea. This test successfully obtained nine *in situ* parameters, including physical and chemical parameters, for sediments within a depth range of 2.66 m on the seabed surface at a depth of 1,820 m. This system accurately and efficiently reflects the property characteristics of seafloor sediments in an *in situ* environment and can be widely used in marine engineering geological investigations.

KEYWORDS

seabed cone penetration test, multiparameter measurement, sediment sampling, seabed penetration platform, speed control, field application

1 Introduction

With the development and utilization of marine resources, seabed exploration and energy development have moved from the shallow sea to the deep sea, and an increasing number of marine projects have correspondingly been completed (Gubon, 1994; Leng et al., 2021; Liu and Li, 2021). In such projects, it is highly important to accurately determine the mechanical properties and environmental parameters of seabed sediments to enable the exploitation of marine mineral resources and construction of offshore engineering structures (Randolph, 2012; Cheng et al., 2018; Liu et al., 2022, 2023). There are two common methods used to measure the engineering mechanical properties of seafloor sediments: the first is to collect sediment samples from the seafloor and conduct laboratory analysis to determine their mechanical properties (Luo et al., 2016; Li and Chen, 2023); the second is *in situ* testing of the mechanical properties of seafloor sediments (Best et al., 1998; Zou and Kan, 2011). The experiment in the laboratory utilizing seafloor sediment sample is an effective traditional test method for studying the engineering properties of foundation sediment bodies. However, these methods have several problems, such as tedious measurement and distortion of test results, which cannot accurately reflect the real mechanical properties of the sediment body (Krage et al., 2014; Ganju et al., 2017). *In situ* testing is the direct mechanical testing of sediment in an *in situ* environment and includes methods such as penetration testing, shear testing, and other mechanical tests. Through the analysis of the mechanical test results, the mechanical properties of the sediment are obtained, which offers the advantages of rapid testing and small disturbance to the sediment layer, and the test results can better reflect the original state. Among them, the cone penetration test is the most commonly used *in situ* testing method. The technology works by pressing the probe installed with mechanics sensors into the seafloor sediment at a constant rate (the rate range is 0.02 m/s ± 10% according to the industry) and recording the cone tip resistance, side friction resistance, and pore water pressure with penetration depth (Yoshimura, 2013; Robertson, 2016). The seabed CPT equipment driven by the hydraulic penetration system is an important equipment for *in situ* detection of seabed sediment. The seabed penetration platform is lowered to the seabed through the photoelectric composite cable of vessel. The seabed penetration platform stably sits on the seabed and relies on its own weight to provide support and reaction forces. Then, the probe rod and probe are uniformly pressed into the sediment through a hydraulic drive. Because of the small diameter and high measurement range of the probe, precise measurement can be achieved for hard sediment layers such as sandy sediment and silty sediment. When the sediment is soft sediment, cone penetration test is difficult to accurately measure. Cone penetration test technology is now widely used in marine engineering geological exploration.

Four well-known companies, Fugro, Geomil, A.P. van den Berg in the Netherlands, and Datem in England, are leaders in researching marine static sounding technology (Seifert et al., 2008; Lunne, 2012; Lu et al., 2020). In 1965, the Dutch company Fugro developed the first underwater jack-up platform, CPT, denoted SEABULL. A MANTA-200 seabed CPT was produced by Geomil. The ROSON series seabed CPT produced by the company A.P. van den Berg began production in 1981. Datem, a British company, developed the Neptune series of CPT equipment in 2000.

In 2001, the drilling cone penetration test equipment developed by the Guangzhou Marine Geological Survey was the first hydraulic drive CPT equipment in China. In 2014, the CPT equipment was developed by the Key Laboratory of Marine Environmental Geological Engineering of Shandong Province. The working water depth of the equipment reached 20 m, and the maximum sounding depth was 10 m; these data were mainly applied to marine geological surveys in shallow coastal waters. In 2015, the Ocean University of China developed the SEEGeo equipment, a complex deep-sea engineering geology *in situ* long-term observation equipment, to carry out *in situ* long-term observations of ocean engineering geology (Ji et al., 2016). The Pene Vector-II seabed CPT was developed by Wuhan Panso Geological Prospecting Technology Co., Ltd (Zhang et al., 2022).

At present, the seabed CPT equipment mainly adopts hydraulic drive and hydraulic control technology to achieve uniform penetration of the probe rod. The power source is a key component of underwater equipment and provides energy and power to the mechanical system, such that many complex functions of underwater operation equipment can operate normally. Hydraulic drives offer many advantages, such as a high power-to-mass ratio, a compact structure, high reliability, and stepless speed regulation over a large range. Therefore, hydraulic drives have been widely used in underwater operation equipment (Chen et al., 2010; Luo and Zhang, 2011). The control technologies for underwater hydraulic systems can be divided into switch control, electrohydraulic proportional control, and electrohydraulic servo control (Xue et al., 2021). The seabed CPT equipment, such as CPTss and SEEGeo, penetrates the probe rod through a hydraulic drive and controls the motion process of the hydraulic cylinder through the electromagnetic on–off valve. The traditional on–off valve-controlled hydraulic system can only make the piston rod move to a predetermined position and cannot accurately control the speed of the piston rod. This hydraulic control system cannot overcome the influence of load changes on the penetration velocity effectively, and the ability to resist load disturbances is poor, which affects the accuracy of *in situ* tests. The Pene Vector-II equipment adopts an electrohydraulic proportional speed regulating valve to control the platform's penetration speed and introduces the fuzzy proportional integral derivative (PID) algorithm in the control to achieve a uniform and stable penetration speed of the probe pole under complex geological conditions and improve the accuracy of static contact detection test data (Zhang et al., 2022). The problems, such as poor speed stability and weak load disturbance rejection performance of the actuator in the hydraulic penetration system, are common in the working process of seabed CPT equipment.

This study investigates the Seabed Cone Penetration Test and Sampling System; analyzes and designs a corresponding mechanical structure, hydraulic transmission, and speed control strategy for the

hydraulic penetration platform; and demonstrates multiparameter *in situ* testing and low-disturbance sampling of 3,000-m-deep seabed sediments. The recordings are shown to accurately and efficiently reflect the characteristics of seabed sediments under *in situ* environmental conditions. First, a multifunctional and highly integrated penetration platform is designed from the structural form and driving mode to ensure the efficient and stable operation of the system in a complex marine environment. Then, a hydraulic control system under electrohydraulic proportional position control and fuzzy PID control is designed to improve the stability, rapidity, and accuracy of the hydraulic penetration system. The motion robustness and stability of the control scheme are discussed. It can be concluded that the fuzzy adaptive PID control scheme can effectively reduce the influence of variable loads on the penetration velocity, so as to ensure the stability of the penetration velocity under complex geological conditions. Finally, *in situ* tests were carried out in the Shenhu Sea area of the South China Sea from the research ship "Ocean Geology No. 9".

2 Materials and methods

2.1 Introduction of the Seabed Cone Penetration Test and Sampling System

The Seabed Cone Penetration Test and Sampling System combines the traditional cone penetration test with low-disturbance sampling techniques to accurately determine the mechanical properties of sediments and master the engineering properties of seabed sediment. The primary technical indices of this equipment are provided in Table 1, and its working principle is shown in Figure 1. The system can be divided into three parts: a seabed penetration platform, a CPT probe rod, and a sampling tube. These parts are described in detail as follows:

TABLE 1 Technical indices of the 3,000-m Seabed Cone Penetration Test and Sampling System.

Item	Parameter and technical indices
Platform size	Bottom outer circle diameter Φ1.8 m × height 1.8 m
Maximum working water depth	3,000 m
Equipment quality	1,600 kg (can add counterweight)
Continuous working time	≥6 h
Penetration force	≥12 kN
Penetration velocity	0.02 m/s ± 5% (adjustable)
CPT depth	≥4 m (note: related to geological strength)
Sampling depth	≥2.4 m (note: related to geological strength)
Communication mode	Photoelectric composite cable or coaxial cable, real-time communication
Power supply mode	Onboard charging, underwater battery power

1. The seabed penetration platform, as the vessel of the system, is used to carry the CPT probe rod and sampling tube. It achieves constant and stable penetration and withdrawal of the probe rod and sampling tube. Structural design was carried out on the penetration module, and static analysis was conducted on key components. At the same time, the hydraulic system has also been designed. A highly integrated carrier platform with reasonable structural strength and component quality layout is designed to ensure smooth and reliable operation of the platform on the seabed.
2. The CPT probe rod is an extension of conventional cone penetration test technology. A CPT probe, a resistivity sensor, a temperature sensor, and a multiparameter geochemical sensor are integrated on the probe rod, which can measure nine parameters *in situ*, including the physical, chemical, and mechanical parameters of sediments (Cui et al., 2023). Thus, this approach can accurately and efficiently reflect the property characteristics of seafloor sediments under *in situ* environmental conditions.
3. A sediment sampling tube is used to obtain sediment column samples. Through laboratory sediment tests, the sediment particle composition is analyzed to obtain stratigraphic and structural data in the investigation area. The results of the laboratory sediment sample analysis and the CPT *in situ* test are also able to be supplemented and corrected by each other.

2.1.1 Mechanical structure design of the seabed penetration platform

The seabed penetration platform is the underwater carrier of the whole system. Based on its main functional characteristics, the structural form and driving mode of the platform were considered. A multifunctional and highly integrated penetration platform has been designed to achieve an efficient and stable operation of the system in complex marine environments.

The seabed penetration platform adopts a hydraulic drive to realize the penetration and withdrawal of the probe rod and sampling tube. Additionally, the altimeter, attitude sensor, lighting, and camera are installed on the platform. The platform frame not only needs to provide installation and bearing space for the above instruments, but also needs to provide sufficient protection for them. To adapt the equipment to a variety of operating environments and facilitate its application in the sea, the platform frame is designed as a regular octagonal structure with two layers above and below it. The outer diameter of the bottom cross-section is Φ1.8 m, and the overall height of the equipment is 1.8 m.

The platform relies on its own weight to provide the reaction force during penetration. Therefore, equipment tilting due to insufficient dead weight or sinking deeper due to a large dead weight affects the authenticity of the measurement data. To satisfy this demand, skirt plates were installed around the base of the

10.3389/fmars.2024.1377405

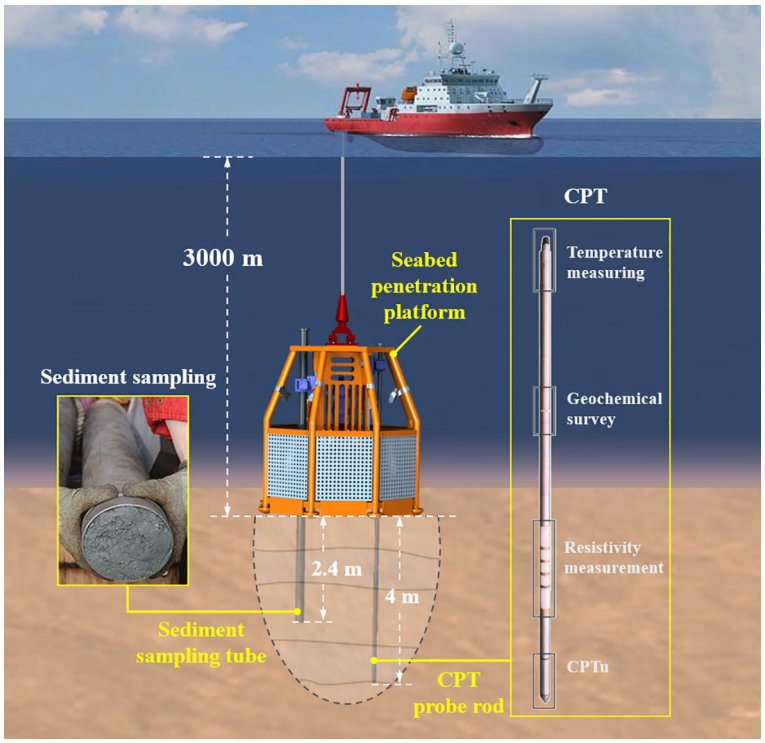

FIGURE 1
Seabed cone penetration test and sampling system.

equipment to increase the supporting area of the equipment when it touched the seabed. Moreover, a counterweight fixing slot was designed at the bottom of the platform, where counterweight blocks were placed to increase the overall weight of the equipment and improve its stability on the seabed. Considering these design requirements, the overall structure of the seabed hydrostatic penetration platform is shown in Figure 2.

To make the whole platform more compact and realize long-distance penetration, a penetration module with a single travel distance of 0.6 m was designed. This module can achieve reciprocating motion, mainly through the use of a column, a penetrating hydraulic cylinder, a clamping mechanism, and a transmission mechanism. The penetration module was designed with a stroke amplification mechanism that utilizes synchronous

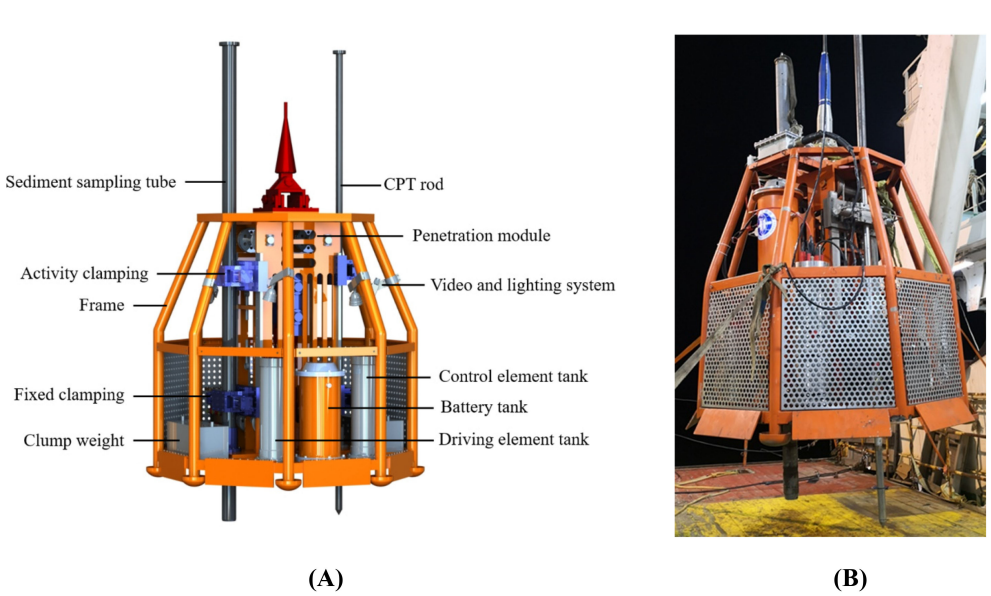

FIGURE 2
Seabed penetration platform: **(A)** Mechanical structure diagram; **(B)** picture of equipment used for field application.

steel wire ropes and pulley blocks to achieve the amplification of hydraulic cylinder stroke. The penetration side of the probe rod and the penetration side of the sampling tube were symmetrically installed on both sides of the column, corresponding to their respective transmission mechanisms and clamping mechanisms and sharing the same penetration hydraulic cylinder. The penetration module with reciprocating circulatory action and stroke amplification improves the efficiency and stability of the platform. The sediment sampling tube and probe rod are inserted in the same way, and the mechanism of penetrating module is analyzed based on the process of inserting the probe rod. Figure 3 shows the overall structure of the penetration module. The penetration force F_i of the probe rod is half of the driving force F_p of the hydraulic cylinder, and the single penetration stroke X_i of the probe rod is twice the maximum stroke X_p of the piston rod of the hydraulic cylinder. Therefore, the total stroke of the hydraulic piston rod is 0.3 m.

When the equipment inserts the probe rod into the seabed, the upper movable clamping mechanism clamps the probe rod, and the lower fixed clamping mechanism releases the probe rod. The piston rod of the penetrating hydraulic cylinder extends, and its output force and speed are transmitted by the steel wire rope and the pulley block. This steel wire rope drives the movable clamping mechanism fixed on the sliding seat to move downward together. Meanwhile, the displacement sensor in the hydraulic cylinder is used to measure the displacement of the piston rod in real time. After the completion of one penetration stroke, the lower fixed clamping mechanism clamps the probe rod, and the upper movable clamping mechanism is loosened. The piston rod of the penetrating hydraulic cylinder retracts, and the upper movable clamping mechanism returns to the initial position. The above actions are repeated to complete the penetration process.

2.1.2 Hydraulic penetration system

The working process of the penetration module has been described in detail above. The clamping hydraulic cylinder and the penetrating hydraulic cylinder are used as action actuators to realize the penetration, clamping, and pulling out of the probe rod and the sediment sampling tube.

The corresponding hydraulic principle diagram is shown in Figure 4. The hydraulic system mainly includes a DC motor, a hydraulic pump, a relief valve, an injection hydraulic cylinder, a clamping hydraulic cylinder, an accumulator, a pressure compensator, and other components. The mechanical energy of the DC motor is converted into pressure energy from the hydraulic oil through the hydraulic pump. Hydraulic oil is transported to the hydraulic cylinder through various control valves. Then, the hydraulic cylinder converts pressure energy into mechanical energy, causing the hydraulic cylinder to drive the load according to the specified action. The different uses of hydraulic cylinders can be divided into clamping mechanism hydraulic circuits and hydraulic injection circuits. Through the combination of the above two hydraulic circuits and execution actions, the cycle process of penetration and withdrawal action is realized.

2.1.3 Static analysis of the key components

The underwater working environment is complex. To ensure the reliability of the platform structure, the ANSYS Workbench software was used to perform static analysis on the key components of the platform. The stand column was made of stainless steel 316 L

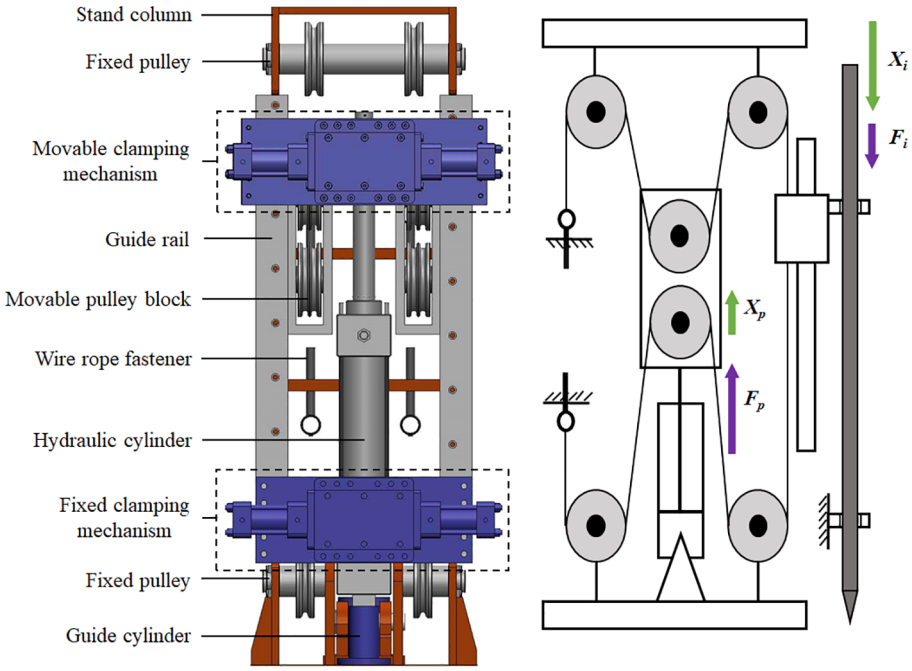

FIGURE 3
The structure and schematic diagram of the penetration module.

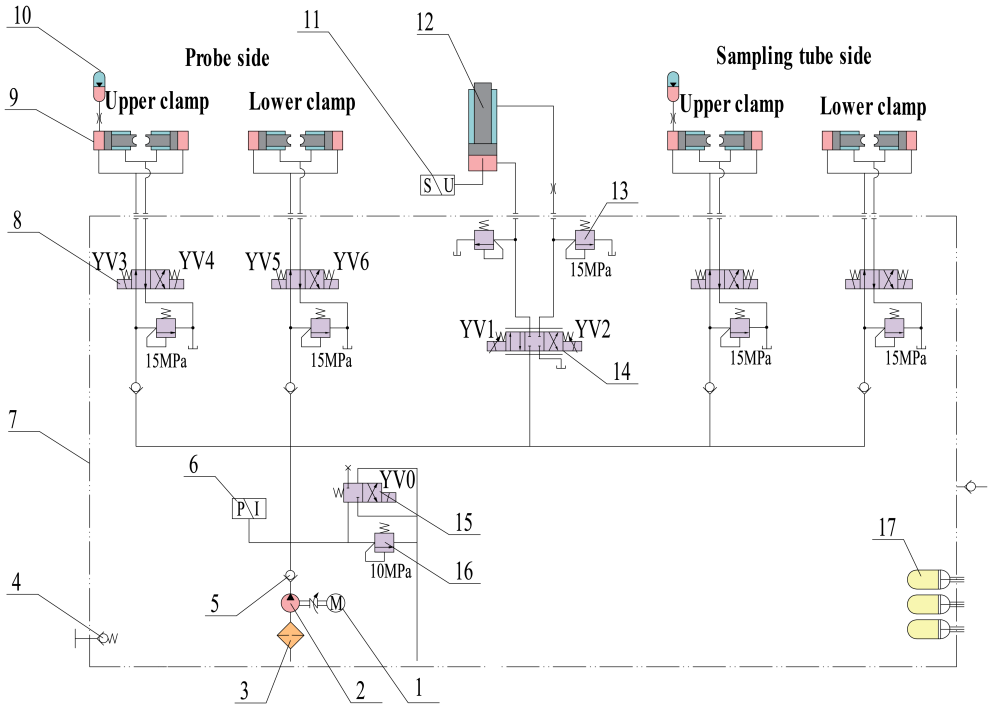

FIGURE 4
Hydraulic system schematic diagram. Note: 1, DC motor; 2, hydraulic pump; 3, oil filter; 4, oil valve; 5, check valve; 6, pressure sensor; 7, oil tank; 8/15, solenoid directional valve; 9, clamping hydraulic cylinder; 10, accumulator; 11, displacement sensor; 12, injection hydraulic cylinder; 13/16, relief valve; 14, proportional directional valve; 17, pressure compensator.

material, and the plate was designed with weight reduction holes. The stand column structure was subjected to the tension of the wire rope and the pressure of the penetrating hydraulic cylinder. To ensure the safety and reliability of the column frame, static analysis of the stand column was needed. To simplify the model, irrelevant components such as wire ropes, pulley blocks, and wire rope tensioners were removed. Figure 5A shows this simplified model. The column model material was set as stainless steel, and the grid elements were generated by static structuring in the commercial software ANSYS. Then, the load and constraint were applied, as shown in Figure 5B, according to the actual stress situation of the column.

Through finite element simulation analysis, the stress and strain distribution law of the column was obtained for a penetration force F_i = 12 kN. By observing the strain distribution, as shown in Figure 5C, and the stress distribution, as shown in Figure 5D, it is determined that the stand column will not fail and that the deformation meets the working requirements.

2.2 Penetration velocity stability

The penetration speed of the probe rod is an important control index of the cone penetration test. A penetration speed that is too fast, too slow, or unstable will lead to distortion of the measurement parameters. Most cone penetration test specifications at home and abroad require the probe to be pressed into the formation at a constant rate of 0.02 m/s ± 10% (Hardison, 2015). To ensure the uniformity and stability of the penetration speed of the probe rod under complex geological conditions and improve the accuracy of the static contact detection data, the hydraulic transmission system of the seabed penetration platform was studied first. The hydraulic system adopted an electrohydraulic proportional position control scheme. By utilizing the relationship between the speed and displacement, the speed of the hydraulic cylinder piston rod can be precisely controlled. Second, a fuzzy PID control method that can realize the online self-tuning of control parameters was established to effectively reduce the influence of variable loads on the penetration velocity. This method improves the control accuracy of the hydraulic system and ensures the accuracy of the seabed CPT data.

2.2.1 The proportional-valve-controlled electrohydraulic system

To ensure the stable operation of the penetration platform under the complex and harsh working environment of 3,000 m underwater, the hydraulic system adopted a proportional valve control cylinder position control scheme based on a quantitative pump. The proportional directional valve adjusts the size and direction of the output hydraulic oil flow and controls the speed and direction of the piston rod movement of the hydraulic cylinder based on throttling controls.

In the hydraulic penetration system, the actuator is the hydraulic cylinder, and the controlled object is the displaced piston rod. The displacement sensor converts the displacement

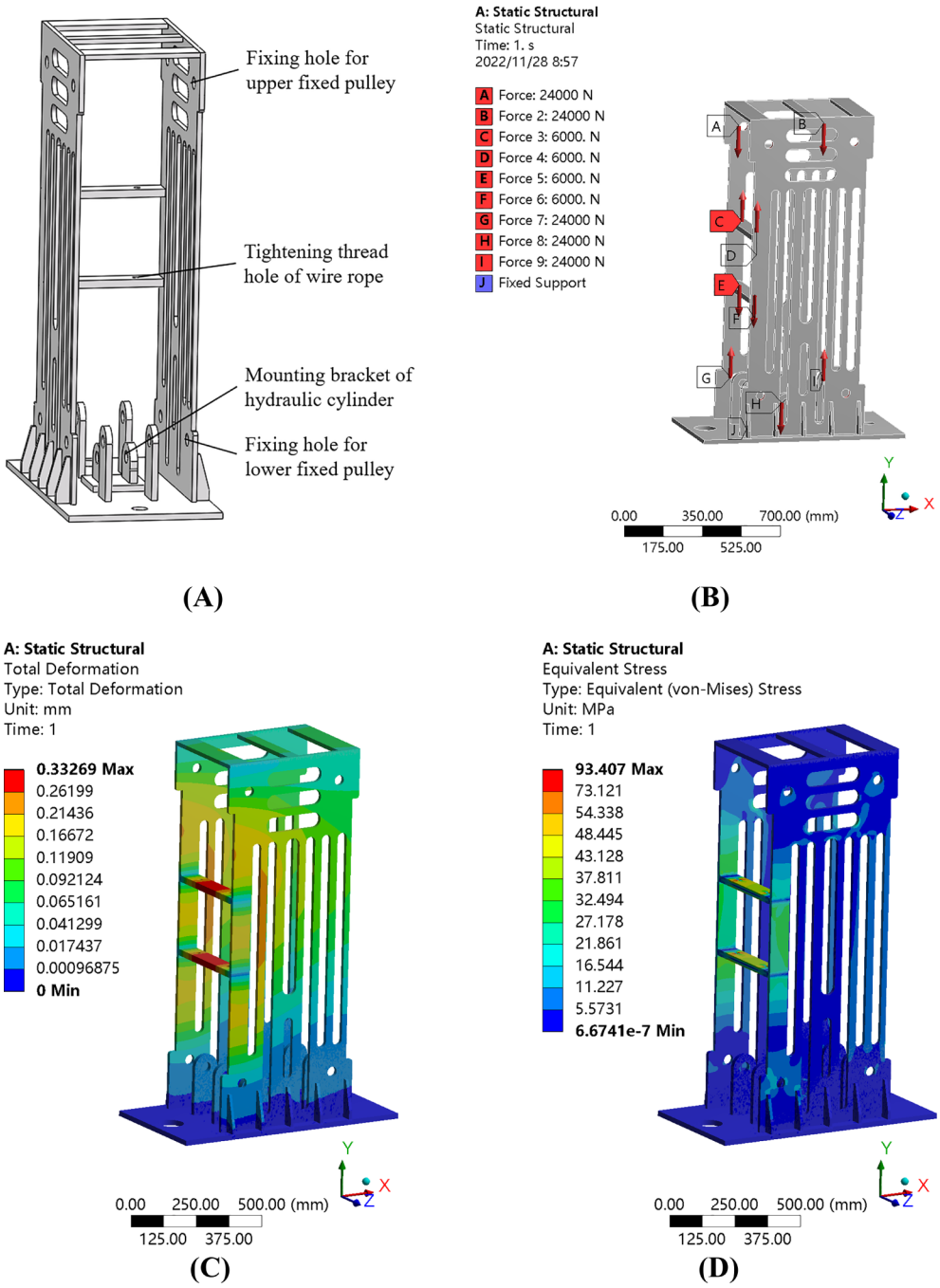

FIGURE 5
Static analysis of the stand column: **(A)** Structural diagram of the stand column. **(B)** Load distribution. **(C)** Strain distribution. **(D)** Stress distribution.

signal of the piston rod into an electrical signal and feeds it back to the control system. The control system generates an error signal by comparing the feedback signal and the input signal. This error signal is driven by a proportional amplifier to control the electrohydraulic proportional directional valve. The proportional directional valve regulates the flow rate of the hydraulic injection circuit, thereby accurately controlling the position of the hydraulic cylinder piston. Based on the relation between the speed and displacement, the movement speed of the piston rod is controlled. The position closed-loop control system is shown in Figure 6.

The establishment of an accurate mathematical model is the precondition for analyzing system performance. Based on the characteristics of an asymmetric hydraulic cylinder controlled by a four-way valve, a mathematical model of the hydraulic cylinder and load was established. The motion accuracy of the penetration process was emphasized during this process, so the analysis was conducted for the case when "$y > 0$." Accordingly, a mathematical model of the hydraulic cylinder and load was derived.

The flow rate equation for the three-position four-way proportional electromagnetic valve is as follows:

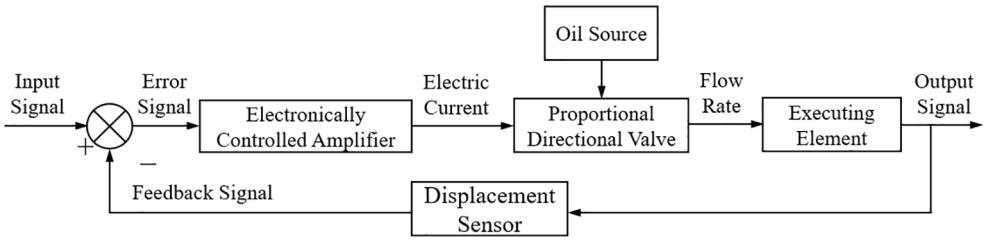

FIGURE 6
Position closed-loop control system structure block diagram.

$$q_L = A_1\frac{dy}{dt} + C_{ie}p_L + C_f p_s + \frac{V_t}{4\beta_e}\frac{dp_L}{dt} \tag{1}$$

where A_1 is the piston rod area in the no-rod cavity of the hydraulic cylinder, y is the displacement of the piston rod, C_{ie} is the equivalent leakage factor, p_L is the load pressure, C_f is the additional leakage factor, p_s is the oil source pressure, V_t is the equivalent total volume, and β_e is the effective bulk elastic modulus.

When the piston is extended, the balance equation between the output force and the load force of the hydraulic cylinder is as follows:

$$p_L A_1 = m_t\frac{d^2y}{dt^2} + B_p\frac{dy}{dt} + Ky + F_L \tag{2}$$

where m_t is the total mass of the piston and the load converted to the piston, B_p is the viscous damping coefficient of the piston and load, K is the load spring stiffness, and F_L is the external load when the piston rod is extended.

When the spool is shifted to the right, i.e., "$x_v > 0$", the linearized flow equation of the electrohydraulic proportional directional valve is as follows:

$$q_L = K_q x_v - K_c p_L \tag{3}$$

where K_q is the flow gain of the valve, x_v is the displacement of the valve core, and K_c is the flow-pressure coefficient of the valve.

After Laplace transforms of Equations 1–3, the total output displacement of the hydraulic cylinder under the action of spool displacement and an external load can be obtained:

$$Y(S) = \frac{\frac{K_q}{A_1}x_v - \frac{K_{ce}}{A_1^2}\left(1 + \frac{V_t}{4\beta_e K_{ce}}S\right)F_L}{S\left(\frac{S^2}{W_h^2} + \frac{2\xi_h}{W_h}S + 1\right)} \tag{4}$$

where

W_h is the hydraulic natural frequency, $W_h = \sqrt{\frac{4\beta_e A_1^2}{V_t m_t}}$;

K_{ce} is the total flow pressure coefficient, $K_{ce} = K_c + C_{ie}$; and

ξ_h is the hydraulic damping ratio, $\xi_h = \frac{K_{ce}}{A_1}\sqrt{\frac{\beta_e m_t}{V_t}} + \frac{B_p}{4A_1}\sqrt{\frac{V_t}{\beta_e m_t}}$.

The transfer function of the total output displacement of the hydraulic cylinder to the displacement x_v of the valve core is as follows:

$$\frac{Y(S)}{x_v} = \frac{{}^{K_q}/_{A_1}}{S\left(\frac{S^2}{W_h^2} + \frac{2\xi_h}{W_h}S + 1\right)} \tag{5}$$

The transfer function of hydraulic cylinder piston displacement of the external load force F_L is as follows:

$$\frac{Y(S)}{F_L} = \frac{-\frac{K_{ce}}{A_1^2}\left(1 + \frac{V_t}{4\beta_e K_{ce}}S\right)}{S\left(\frac{S^2}{W_h^2} + \frac{2\xi_h}{W_h}S + 1\right)} \tag{6}$$

2.2.2 Design of the fuzzy adaptive PID controller

To improve the stability of the penetration process and reduce the influence of uncertain factors in the seabed environment on the position control accuracy of the hydraulic system, a fuzzy adaptive PID control scheme was designed. This control scheme enables the hydraulic penetration system to maintain favorable position control accuracy and anti-load disturbance performance. Fuzzy control is a nonlinear intelligent control method first proposed by Professor Zadeh for computer digital control. Its greatest advantage is that it does not need to rely on the precise mathematical model of the controlled object and has favorable anti-interference ability for adjusting the parameter changes of the object (Pedrycz, 1993; Zadeh, 1996; Chen and Pham, 2001). Figure 7 shows the structure of the fuzzy PID controller.

The traditional PID control system is based on the error between the real-time data of the controlled object and a given expected value. By performing proportional, integral, and differential function operations on the error values, the result is used to control the controlled object.

The fuzzy adaptive PID controller takes the error "e" (the difference between the actual measured value and the expected value) and the error change rate "e_c" as the input and uses fuzzy control rules to adjust the three parameters of the PID controller in real time to adjust the size of the control quantity, adapt to complex and variable load conditions, and achieve the best control effect (Carvajal et al., 2000; Hu and Ying, 2001). The calculation formula of the fuzzy PID control parameters is as follows:

$$K_p = K_p^{'} + \Delta K_p \bullet K_1 \tag{7}$$

$$K_i = K_i^{'} + \Delta K_i \bullet K_2 \tag{8}$$

$$K_d = K_d^{'} + \Delta K_d \bullet K_3 \tag{9}$$

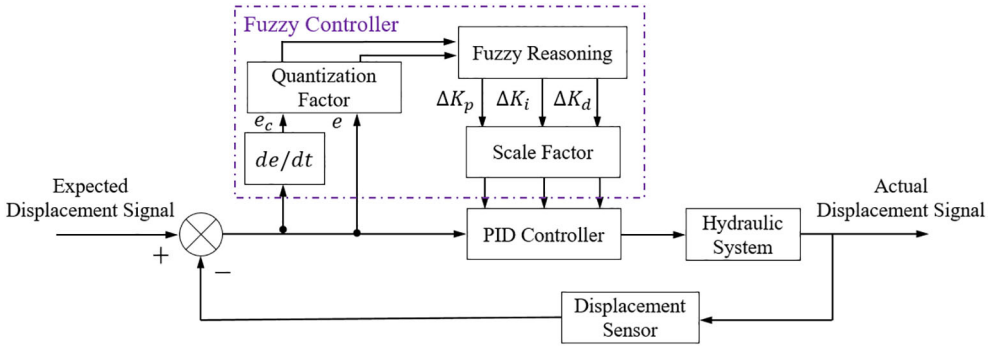

FIGURE 7
The structure diagram of the fuzzy adaptive PID controller.

where $K_p^{'}, K_i^{'}, K_d^{'}$ are the outputs of a conventional PID controller and K_1, K_2, K_3 are the adjustment factors of the final parameters ΔK_p, ΔK_i, ΔK_d of the fuzzy controller.

The working process of the fuzzy controller is divided into the following three steps. The first step implements the "fuzzification" process, which converts the exact input into the membership function of a fuzzy set. In the second step, the fuzzy control rules are formulated according to expert experience, and the fuzzy input values are added to a "fuzzy output" set composed of IF–THEN control rules to carry out fuzzy inference. In the third step, the precision processing of the fuzzy control quantity is the essence of obtaining the most representative and accurate control signal (Hu and Ying, 2001).

To improve the adaptability of the model to uncertain input parameters, the input and output parameters were divided into seven levels: NB, NM, NS, ZO, PS, PM, and PB. Considering the adjustment effect of the PID control parameters on the system, the fuzzy control rules shown in Table 2 are obtained.

The fuzzification process in fuzzy control is realized by a membership function. In practical engineering, triangular membership functions and Gaussian membership functions are mostly used. The expression of the triangular membership function is as follows:

$$f(x,a,b,c) = \begin{cases} 0 & x \le a \\ \frac{x-a}{b-a} & a \le x \le b \\ \frac{c-x}{c-b} & b \le x \le c \\ 0 & x \ge c \end{cases} \tag{10}$$

where a, b, and c are coefficients of the membership function.

The expression of the Gaussian membership function is as follows:

$$f(x) = e^{-\frac{(x-c)^2}{2\sigma^2}} \tag{11}$$

For the membership functions of the input and output of this system, PM, PS, ZO, NS, and NM adopted a triangular membership function, and for the fuzzy sets PB and NB, a Gaussian membership function was adopted.

Because the barycenter method has smooth output inference control, the barycenter method was used to accurately process the fuzzy control quantity, and its output value could be expressed as follows:

$$c_0 = \frac{\int vu(v)dv}{\int u(v)dv} \tag{12}$$

TABLE 2 Fuzzy control rule.

e / e_c	NB	NM	NS	ZO	PS	PM	PB
NB	PB/NB/PS	PB/NB/NS	PM/NM/NB	PM/NM/NB	PS/NS/NB	ZO/ZO/NM	ZO/ZO/PS
NM	PB/NB/PS	PB/NB/NS	PM/NM/NB	PS/NS/NM	PS/NS/NM	ZO/ZO/NS	NS/ZO/ZO
NS	PM/NB/ZO	PM/NM/NS	PM/NS/NM	PS/NS/NM	ZO/ZO/NS	NS/PS/NS	NS/PS/ZO
ZO	PM/NM/ZO	PM/NM/NS	PS/NS/NS	ZO/ZO/NS	NS/PS/NS	NM/PM/NS	NM/PM/ZO
PS	PS/NM/ZO	PS/NS/ZO	ZO/ZO/ZO	NS/PS/ZO	NS/PS/ZO	NM/PM/ZO	NM/PB/ZO
PM	PS/ZO/PB	ZO/ZO/NS	NS/PS/PS	NM/PS/PS	NM/PM/PS	NM/PB/PS	NB/PB/PB
PB	ZO/ZO/PB	ZO/ZO/PM	NM/PS/PM	NM/PM/PM	NM/PM/PS	NB/PB/PS	NB/PB/PB

2.3 Simulation analysis of the position control effect of the hydraulic system

To verify the effect of system position control and velocity control, a joint simulation of an electrohydraulic proportional position control system was carried out. The AMESim software and MATLAB/Simulink software were used to construct simulation models of the hydraulic part and the control part of the electrohydraulic proportional control system. Considering the proportional valve control electrohydraulic system as an example, the integrated AMESim and Simulink model of the hydraulic penetration system based on the fuzzy adaptive PID control scheme is shown in Figure 8A. The optimal PID control parameters $K_p^{'}$, $K_i^{'}$, $K_d^{'}$ are obtained by using the PID Tuner controller of Simulink. The physical model of the hydraulic system built in AMESim is shown in Figure 8B, and the main parameters of the model are shown in Table 3.

According to the working requirements of the hydraulic penetration platform, the displacement time curve of the piston

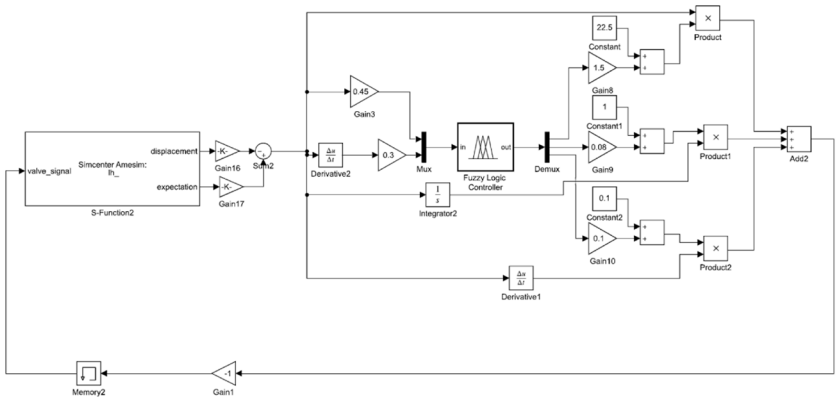

(A)

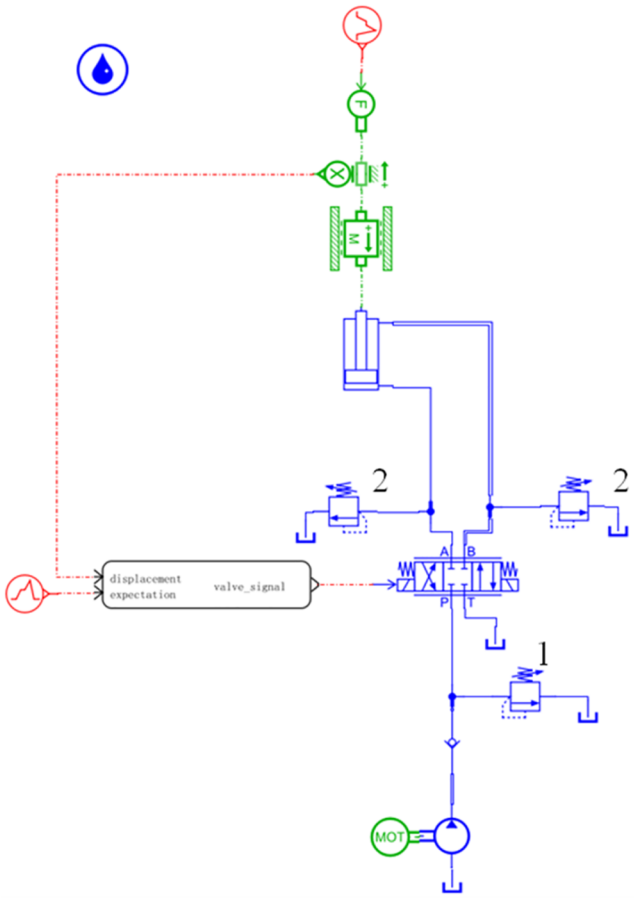

(B)

FIGURE 8
Simulation model: **(A)** Fuzzy adaptive PID control model. **(B)** The proportional valve-controlled hydraulic system model.

TABLE 3 The main parameters in the model.

Parameter name	Unit	Parameter value
Motor speed	r/min	1000
Pump displacement	mL/r	32
Relief valve 1 opening pressure	bar	100
Relief valve 2 opening pressure	bar	150
Proportional valve rated current	A	1.4
Proportional valve natural frequency	Hz	60
Proportional valve damping ratio	—	0.8
Hydraulic cylinder diameter	m	0.08
Hydraulic cylinder piston rod diameter	m	0.05
Total stroke of hydraulic cylinder	m	0.3
Hydraulic cylinder mass block	kg	400

rod is set in the simulation, as shown in Figure 9A. During the motion of the piston rod, an external load is applied to the piston rod to simulate the changes in resistance during penetration and withdrawal. The external load variation curve set in the AMESim hydraulic model is shown in Figure 9B.

2.4 Field application

To validate the working performance of the Seabed Cone Penetration Testing and Sampling System, two sea tests were carried out after the assembly and commissioning of the system. The first offshore test was conducted in the sea area of Guishan Island. Through practical operation at sea, the process of equipment layout, communication control, online monitoring, and equipment recycling has been further optimized. This offshore experiment successfully evaluated the physical and chemical properties of shallow surface sediments and sediment columns in the offshore area, providing rich practical systems for enabling far-reaching marine engineering applications.

The second sea test was located in the Shenhu Sea area of the South China Sea. The bottom layer is composed of soft and mostly silty sediments. The Shenhu Sea area is located inside the Baiyun Sag in the Pearl River Estuary Basin (Wu et al., 2022). The Baiyun Sag has abundant source rocks, and the characteristics of well-developed reservoirs and structural traps endow the Baiyun Sag with favorable geological conditions for oil and gas accumulation. Therefore, there are abundant marine oil and gas resources in the slope area of the Shenhu Sea area (Li et al., 2010).

Through at-sea testing, the application of the Seabed Cone Penetration Test and Sampling System was established; this test involved a series of evaluation, inspection, and testing processes, such as system assembly and debugging; equipment layout; and system underwater *in situ* testing and sampling tests. To ensure the smooth progress of the experiment, it is necessary to follow reasonable offshore testing procedures and operating methods. After the scientific research ship arrived at the scheduled sea trial site, the equipment was lowered to the seabed at a constant speed through the A-shaped hanger and dedicated winch at the stern of the ship. When the inclination angle of the equipment meets the working requirements of the system, the penetration test began. The operation instructions issued by the deck control system were transmitted to the underwater equipment through the optical cable. The seabed penetration platform inserted the CPT rod and sample tube into the sediment at a constant rate. During the penetration process, *in situ* detection data and underwater video signals were synchronously transmitted to the deck monitoring room through the optical cable and displayed in real time on the upper computer screen. At the same time, the platform attitude, hydraulic cylinder displacement, cone tip resistance, sidewall friction, pore water pressure, temperature, and other parameters were recorded at a frequency of 1 Hz.

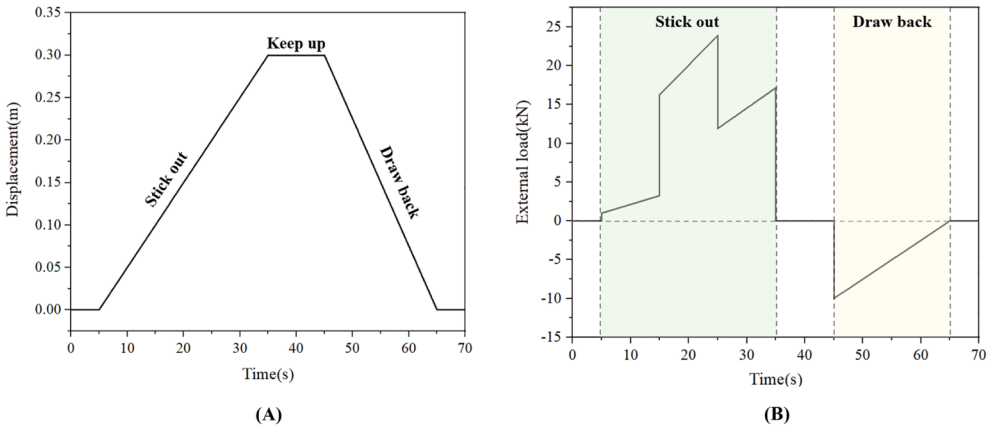

FIGURE 9
Input signals during simulation analysis: **(A)** Expected displacement curve of the piston rod. **(B)** External load change curve.

3 Results

3.1 Simulation results and comparative analysis

During the penetration process, the resistance of the probe rod varies with the depth of penetration and the type of sediment layer, which leads to the load on the hydraulic infiltration system changing over time, making the penetration speed of the probe rod unstable. To better analyze the speed control effect of the hydraulic system, a comparison was made between the control effects of the PID controller, fuzzy PID controller, and hydraulic system itself. The displacement, displacement error, and velocity curves of the hydraulic system were obtained via joint simulation, as shown in Figures 10A–C, respectively.

The displacement curve and displacement error curve demonstrate that there is a large error between the control displacement and the expected displacement of the hydraulic system itself without the action of an external controller. Under the action of the PID controller and fuzzy PID controller, the piston rod of the hydraulic cylinder moves according to the expected displacement. These simulation results show that the displacement error fluctuates when there is load disturbance, and each controller tries to eliminate the influence of load disturbance on the movement of the piston rod. Considering the load disturbance

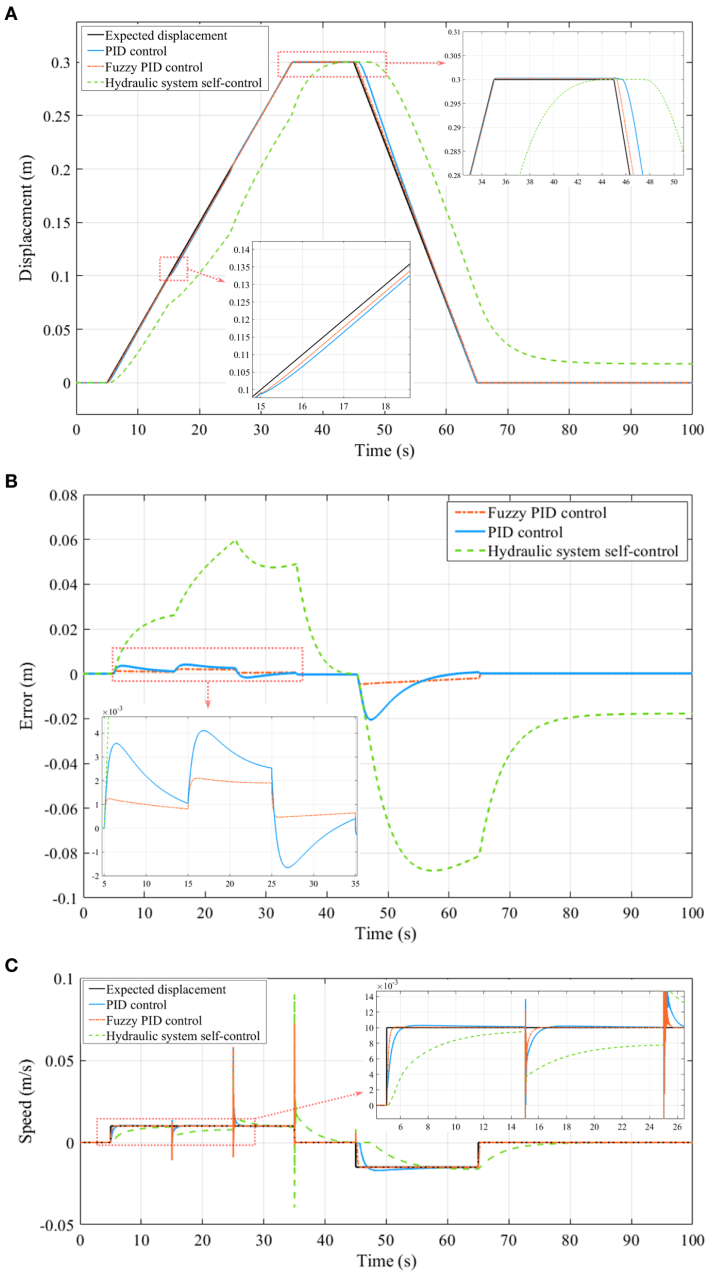

FIGURE 10
Electrohydraulic cosimulation results under load disturbance: **(A)** Displacement curve. **(B)** Displacement error curve. **(C)** Velocity curve.

when the simulation time is 15 s as an example, the displacement error of the piston rod under the PID controller is 4.1 mm, and the displacement error under the fuzzy PID controller is 2.05 mm. The displacement error of the fuzzy PID controller is 100% lower than that of the PID controller. The speed of the piston rod fluctuates within a small range, and the greater the change in the interference force is, the greater the fluctuation amplitude of the system, and the longer the time taken for the system to recover to the expected speed. As shown in Figure 10C, when the system is disturbed by the load, the fuzzy PID controller can control the speed of the hydraulic system quickly and accurately. In general, fuzzy PID control can significantly improve the control precision, dynamic performance, and robustness of the system.

3.2 Results of the field application

By analyzing the displacement of the hydraulic cylinder in the sea trial data, the displacement curve of the hydraulic cylinder during a single penetration process of the hydraulic system shown in Figure 11A is obtained. In this figure, the red line represents the displacement curve of the piston when the hydraulic cylinder drives the probe, and the blue line represents the displacement curve of the piston when the hydraulic cylinder pushes the sampling tube. The displacement curve of the hydraulic cylinder during the penetration process of the probe rod in Figure 11A shows that the movement speeds of the hydraulic cylinder piston and the probe rod are stable. After calculation, the average penetration speed of the probe is 0.0196 m/s, and the relative error between this speed and the ideal penetration speed is less than 3%. The penetration speed curve of the probe rod shown in Figure 11B was obtained through the displacement calculation of the hydraulic cylinder. The penetration speed is within the expected speed setting range of 5%, which meets the static penetration test standards. The penetration and withdrawal process of the sampling tube is also relatively stable, achieving the expected goals of the device design. The displacement and velocity curves show that the hydraulic system controlled by the electrohydraulic proportional valve and the fuzzy PID control strategy have favorable control accuracy and anti-interference ability. The speed control accuracy of the Seabed Cone Penetration Test and Sampling System fully meets the design and application requirements of seabed *in situ* exploration.

The sea test process was very smooth, and the physical and chemical properties of 2.66 m of sediment from the 1,820-m-deep seabed were successfully obtained. Figure 12 shows the onsite test data.

The characteristics of the sediment layer in the test area can be analyzed by using cone penetration test data. The cone tip resistance and sidewall friction resistance curves in a single sediment layer unit are composed of three parts: the initial section, the constant section, and the lag section (Garziglia, 2014). In the same sediment layer profile, the initial section and the lag section constitute a transition section between two adjacent sediment layers, and a certain position in the transition section is the mechanical boundary layer between the two sediment layers. The cone tip resistance and sidewall friction resistance curves shown in Figure 12A indicate that the sediment layer within the depth range of 2.66 m can be roughly divided into three layers. Previous studies have shown that environmental temperature has a significant impact on the electrical properties of sediments (Robert and Boyce, 1968; Nobes et al., 1986). As shown in the resistivity and temperature change curves in Figure 12C, the resistivity of the sediment is approximately negatively correlated with temperature. The pore water pressure、redox potential and pH、carbonate concentration and hydrogen sulfide concentration are shown in Figures 12B, D, E.

4 Discussion

4.1 The Seabed Cone Penetration Test and Sampling System

The system developed in this study can more accurately and comprehensively obtain various physical and chemical parameters of

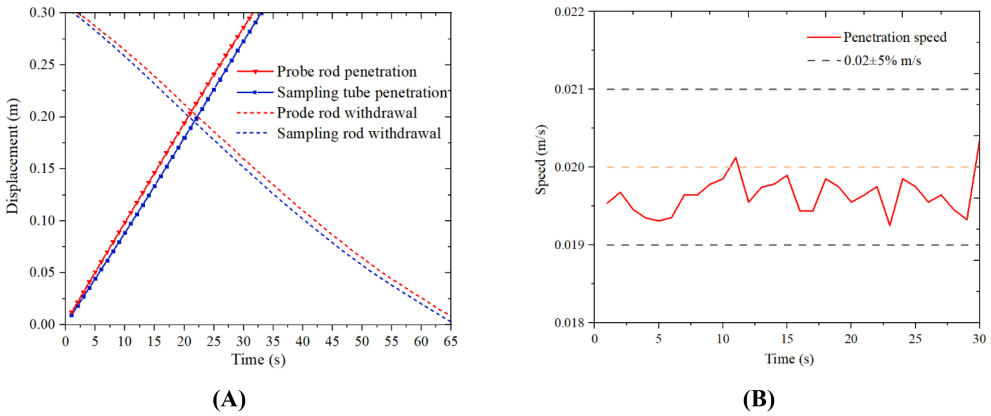

FIGURE 11
Displacement and velocity curves: **(A)** Displacement curve of the hydraulic cylinder. **(B)** Penetration speed curve of the probe rod.

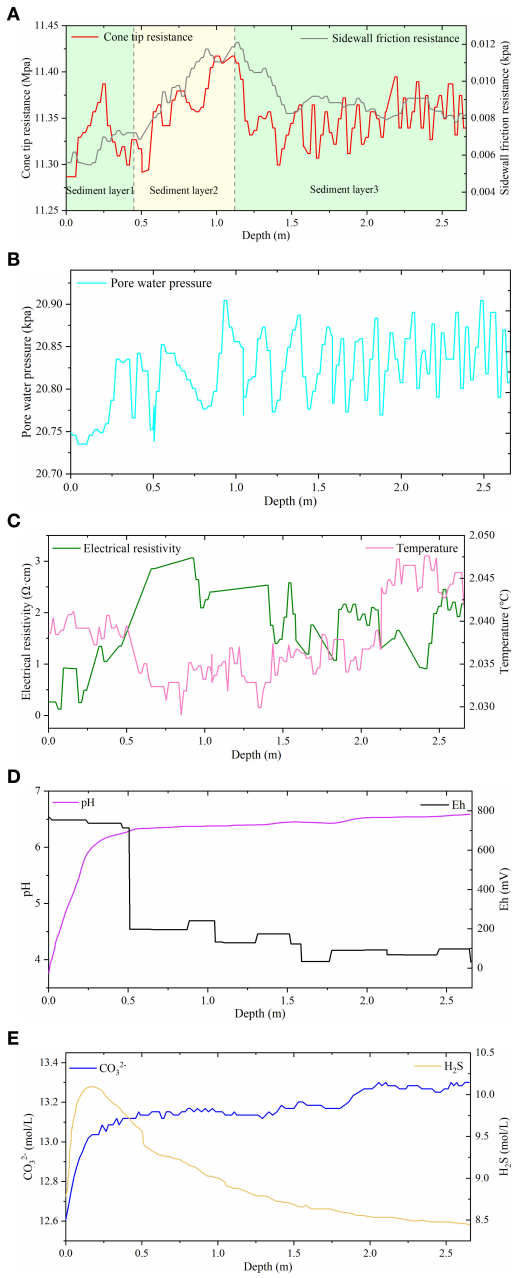

FIGURE 12
Variation in physical and chemical properties with depth within 2.66 m of the surface layer of marine sediments: **(A)** Cone tip resistance and sidewall friction resistance. **(B)** Pore water pressure. **(C)** Electrical resistivity and sediment temperature. **(D)** Redox potential and pH. **(E)** Carbonate concentration and hydrogen sulfide concentration.

sediments. More detailed physicochemical properties and environmental parameters of sediments are obtained by using multiparameter data. In addition, the combination of multiparameter *in situ* measurement and sampling technology improves the accuracy of sediment mechanics testing by mutual correction of the two test results.

4.2 Structure and penetration velocity stability of the seabed penetration platform

By conducting static simulation analysis on the key components of the seabed penetration platform, it is verified that its structural strength meets the working requirements. Meanwhile, during the on-site application of the sea trial, this platform has demonstrated advantages such as a stable structure, convenient use, and reliable functionality.

From the displacement and velocity curve of simulation and field application results, it can be seen that the hydraulic system controlled by the electro-hydraulic proportional valve and the fuzzy PID control strategy has good control accuracy and anti-interference ability. The penetration speed is within the expected speed setting range of 5%, which meets the cone penetration test standards. The speed control accuracy of the Seabed Cone Penetration Test and Sampling System fully meets the design requirements and the application requirements of seabed *in situ* exploration.

4.3 Study limitations

The application of CPT technology in marine engineering geological exploration in China is still in its early stages, mainly relying on foreign cone penetration test data analysis methods. In order to better obtain the mechanical properties of sediments, it is urgent to carry out a large number of field tests based on this equipment and rely on the marine geological environment of China. The analysis theory of static test results will be perfected, and a set of analytical methods and empirical formulas suitable for the characteristics of seafloor sediment in China will be formed.

The seabed penetration platform relies on its own weight to provide the reaction force during penetration. The maximum penetration capacity of the platform is therefore limited by its own weight. The future research direction is to study how to reduce the overall weight of the system while providing greater penetration force, such as the use of suction anchor technology to adsorb equipment to the seafloor.

5 Conclusions

In this study, a Seabed Cone Penetration Test and Sampling System for a 3,000-m-deep sea is designed and developed. The system can realize multiparameter *in situ* testing and low-disturbance sampling of seafloor sediments at a depth of 3,000 m, which can accurately and efficiently reflect the property characteristics of seafloor sediments under *in situ* environmental conditions. Based on the results of this study, the following are drawn.

1. To ensure the efficient and stable operation of the entire system in complex marine environments, a more compact,

stable, and reliable hydraulic penetration platform has been designed. The mechanical structure, hydraulic transmission, and speed control strategy of hydraulic outburst platforms were studied and validated.

2. Existing hydraulic systems for hydraulic penetration platforms mostly use traditional switch controls, which exhibit the problem of low control accuracy. The penetration platform designed in this study implements electrohydraulic proportional control technology to realize accurate speed control of the hydraulic cylinder penetration process and ensure the accuracy of the CPT test data.
3. A revised link is added to the electrohydraulic proportional position control system, and a fuzzy PID control strategy is adopted to improve the stability, speed, and accuracy of the hydraulic control system. This control strategy can effectively reduce the influence of variable loads on the penetration velocity to ensure the stability of the penetration velocity under complex geological conditions.

Through a series of offshore applications, the success of the Seabed Cone Penetration Test and Sampling System was verified. The results demonstrate that this approach can satisfy the needs of *in situ* deep-sea sediment detection and can be widely used in offshore engineering applications.

Data availability statement

The original contributions presented in the study are included in the article/Supplementary Material. Further inquiries can be directed to the corresponding author.

Author contributions

CW: Writing – review & editing. LG: Conceptualization, Writing – original draft, Writing – review & editing. LJ: Conceptualization, Methodology, Writing – review & editing. WS: Supervision, Writing – review & editing. GX: Methodology, Writing – original draft, Writing – review & editing. XY: Project administration, Writing – review & editing. XL: Conceptualization, Writing – review & editing.

Funding

The author(s) declare financial support was received for the research, authorship, and/or publication of this article. This research was funded by the National Natural Science Foundation of China (No.42477153), Laoshan Laboratory (No.LSKJ202203504), the National Natural Science Foundation of China (No. 42176057), the National Natural Science Foundation of China (NSFC) (U2006213), and the National Natural Science Foundation of China (42277138).

Acknowledgments

We would like to thank LG and XL for their guidance and everyone who contributed to this article.

Conflict of interest

The authors declare that the research was conducted in the absence of any commercial or financial relationships that could be construed as a potential conflict of interest.

The reviewer XL declared a shared affiliation with the authors XY and XL to the handling editor at the time of review.

Publisher's note

Supplementary material

The Supplementary Material for this article can be found online at: https://www.frontiersin.org/articles/10.3389/fmars.2024.1377405/full#supplementary-material

References

Best, A. I., Roberts, J. A., and Somers, M. L. (1998). A new instrument for making *in-situ* acoustic and geotechnical measurements in seafloor sediments. *Underwater. Technol.* 23, 123–131. doi: 10.3723/175605498783259182

Carvajal, J., Chen, G. R., and Gmen, H. (2000). Fuzzy PID controller: Design, performance evaluation, and stability analysis. *Inform. Sci.* 123, 249–270. doi: 10.1016/S0020-0255(99)00127-9

Chen, G. R., and Pham, T. T. (2001). *Introduction to Fuzzy Sets, Fuzzy Logic, and Fuzzy Control Systems* (Boca Raton: CRC Press), 193–197. doi: 10.1201/9781420039818

Chen, Q., Xing, X., Zhang, Z. G., and Yan, J. Y. (2010). Research on hydraulic self-leveling system of seabed-base of downhole CPT. *Ocean. Technol.* 29, 120–123. doi: 10.3969/j.issn.1003-2029.2010.01.027

Cheng, Y. R., Zeng, X., Li, X. Y., and Zheng, H. (2018). Analysis of sinking propertiess of deep-sea mining vehicles on soft sediment. *Min. Metallurgical. Eng.* 38. doi: 10.3969/j.issn.0253-6099.2018.06.009

Cui, Y. X., Guo, L., Liu, T., Yang, Z. N., Ling, X. Z., Yang, X. Q., et al. (2023). Development and application of the 3000 m-level multiparameter CPTu *in-situ* integrated test system. *Mar. Georesour. Geotec.* 41, 400–411. doi: 10.1080/1064119X.2022.2053008

Ganju, E., Prezzi, M., and Salgado, R. (2017). Algorithm for generation of stratigraphic profiles using cone penetration test data. *Comput. Geotech.* 90, 73–84. doi: 10.1016/j.compgeo.2017.04.010

Garziglia, S. S. (2014). Seafloor instabilities and sediment deformation processes: The need for integrated, multi-disciplinary investigations. *Mar. Geol.* 352, 183–214. doi: 10.1016/J.MARGEO.2014.01.005

Gubon, F. (1994). Development and management of marine resources in the pacific islands region: an overview of some basic issues and constraints. *Ocean. Yearbook* 11, 409–425. doi: 10.1163/221160094X00230

Hardison, M. (2015). Correlation of engineering parameters of the presumpscot formation to the seismic cone penetration test (SCPTU). *Integr. Med. Res.* doi: 10.1016/j.imr.2015.09.001

Hu, B. G., and Ying, H. (2001). Review of fuzzy PID control techniques and some important issues. *Zidonghua. Xuebao/Acta. Automatica. Sin.* 27, 567–584.

Ji, F. D., Jia, Y. G., Liu, X. L., Guo, L., Zhang, M. S., and Shan, H. X. (2016). IN SITU MEASUREMENT OF THE ENGINEERING MECHANICAL PROPERTIES OF SEAFLOOR SEDIMENT. *Mar. Geol. Quaternary. Geol.* 36, 191–200. doi: 10.16562/j.cnki.0256-1492.2016.03.019

Krage, C. P., Dejong, J. T., and Schnaid, F. (2014). Estimation of the coefficient of consolidation from incomplete cone penetration test dissipation tests. *J. Geotech. Geoenviron.* 141, 06014016. doi: 10.1061/(ASCE)GT.1943-5606.0001218

Leng, D. X., Shao, S., Xie, Y. C., Wang, H. H., and Liu, G. J. (2021). A brief review of recent progress on deep sea mining vehicle. *Ocean. Eng.* 228, 108565. doi: 10.1016/j.oceaneng.2020.108565

Li, G., Moridis, G. J., Zhang, K., and Li, X. S. (2010). Evaluation of gas production potential from marine gas hydrate deposits in shenhu area of South China sea. *Energ. Fuel.* 24, 6018–6033. doi: 10.1021/ef100930m

Li, Y. H., and Chen, P. Y. (2023). Temperature effect on undrained mechanical properties of hydrate-bearing clayey silts in the South China sea. *Energy And. Fuels.* 37, 13025–13033. doi: 10.1021/acs.energyfuels.3c01971

Liu, J. W., and Li, X. S. (2021). Recent advances on natural gas hydrate exploration and development in the South China sea. *Energ. Fuel.* 35, 7528–7552. doi: 10.1021/acs.energyfuels.1c00494

Liu, X. L., Lu, Y., Yu, H. Y., Ma, L. K., Li, X. Y., Li, W. J., et al. (2022). *In-situ* observation of storm-induced wave-supported fluid mud occurrence in the subaqueous yellow river delta. *J. Geophys. Res.: Oceans.* 127, e2021JC018190. doi: 10.1029/2021JC018190

Liu, X. L., Wang, Y. Y., Zhang, H., and Guo, X. S. (2023). Susceptibility of typical marine geological disasters: an overview. *Geoenvironmental. Disasters.* 10, 10. doi: 10.1186/s40677-023-00237-6

Lu, Y., Duan, Z., Zheng, J., Zhang, H., Liu, X., and Luo, S. (2020). "Offshore cone penetration test and its application in full water-depth geological surveys," in *IOP Conference Series: Earth and Environmental Science* (Beijing, China), 570. doi: 10.1088/1755-1315/570/4/042008

Lunne, T. (2012). The Fourth James K. Mitchell Lecture: The CPT in offshore soil investigations - a historic perspective. *Geomechanics. Geoeng.* 7, 75–101. doi: 10.1080/17486025.2011.640712

Luo, T. T., Song, Y. C., Zhu, Y. M., Liu, W. G., Liu, Y., Li, Y. H., et al. (2016). Triaxial experiments on the mechanical properties of hydrate-bearing marine sediments of South China Sea. *Mar. Petroleum. Geol.* 77, 507–514. doi: 10.1016/J.MARPETGEO.2016.06.019

Luo, G. S., and Zhang, G. P. (2011). Study on walking control strategy for hydraulic system of seabed tracked mining vehicle. *J. Hunan. Agric. Univ.* 37, 111–114. doi: 10.3724/SP.J.1238.2011.00111

Nobes, D. C., Villinger, H., Davis, E. E., and Law, L. K. (1986). Estimation of marine sediment bulk physical properties at depth from seafloor geophysical measurements. *J. Geophys. Res. Atmospheres.* 91, 14033–14043. doi: 10.1029/JB091iB14p14033

Pedrycz, W. (1993). Fuzzy control and fuzzy systems. *Res. Stud. Press.*, 28–36. doi: 10.1016/s0925-2312(96)90014-4

Randolph, M. F. (2012). *Offshore Geotechnics - The Challenges of Deepwater Soft Sediments* (geotechnical special publication). doi: 10.1061/9780784412138.0010

Robert, E., and Boyce, (1968). Electrical resistivity of modern marine sediments from the Bering Sea. *J. Geophys. Res.* 73, 4759–4766. doi: 10.1029/JB073i014p04759

Robertson, P. K. (2016). Cone penetration test (CPT)-based soil behaviour type (SBT) classification system - an update. *Can. Geotech. J.* 53, 1910–1927. doi: 10.1139/cgj-2016-0044

Seifert, A., Stegmann, S., Mörz, T., Lange, M., Wever, T., and Kopf, A. (2008). *In situ* pore-pressure evolution during dynamic CPT measurements in soft sediments of the western Baltic Sea. *Geo-Mar. Lett.* 28, 213–221. doi: 10.1007/s00367-008-0102-x

Wu, S. Y., Liu, J., Xu, H. N., Liu, C. L., Ning, F. L., Chu, H. X., et al. (2022). Application of frequency division inversion in the prediction of heterogeneous natural gas hydrates reservoirs in the Shenhu Area,South China Sea. *China Geol.* 5, 251–266. doi: 10.31035/cg2021074

Xue, G., Liu, Y. J., Guo, L., and Liu, B. H. (2021). Optimization on motion-robust and energy-saving controller for hydraulic penetration system of seabed equipment. *Proc. Inst. Mechanical. Eng. Part M.: J. Eng. Maritime. Environ.* 235, 792–808. doi: 10.1177/1475090220970425

Yoshimura, H. (2013). Interpretation of density profile of seabed sediment from nuclear density cone penetration test results. *Soils. Found.* 53, 671–679. doi: 10.1016/j.sandf.2013.08.005

Zadeh, L. A. (1996). *A rationale for fuzzy control* (United States: Cambridge University Press, Cambridge, England).

Zhang, W., Chen, Q., Xia, L. Q., and Li, T. (2022). Penevector marine multifunctional geological sampling/testing integrated equipment. *Int. J. Wireless. Mobile. Computing.* 23, 211. doi: 10.1504/ijwmc.2022.10052537

Zou, D. P., and Kan, G. M. (2011). Application study on *in-situ* acoustic measurement system of seafloor sediments. *Sensor. Lett.* 9, 1507–1510. doi: 10.1166/sl.2011.1655

Frontiers in Marine Science

Explores ocean-based solutions for emerging global challenges

The third most-cited marine and freshwater biology journal, advancing our understanding of marine systems and addressing global challenges including overfishing, pollution, and climate change.

Discover the latest Research Topics

See more →

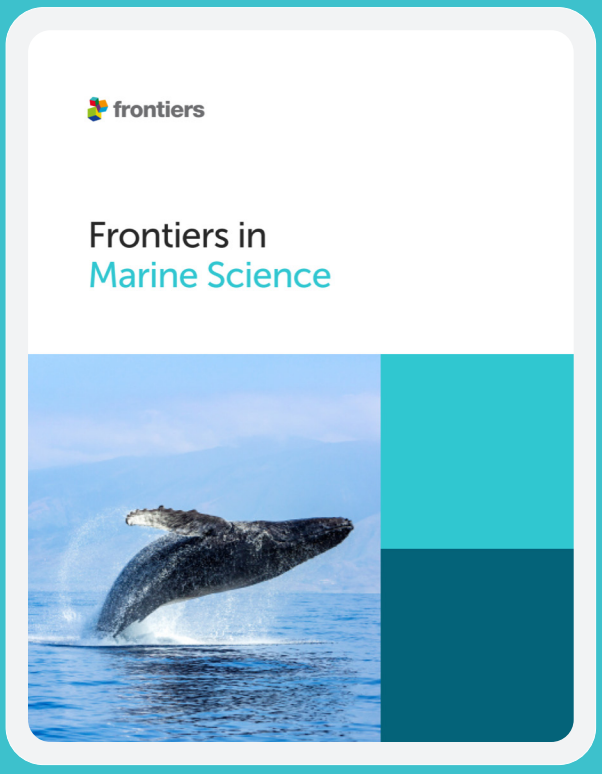

Frontiers

Avenue du Tribunal-Fédéral 34
1005 Lausanne, Switzerland
frontiersin.org

Contact us

+41 (0)21 510 17 00
frontiersin.org/about/contact